

UNIVERSITY NAME

DOCTORAL THESIS

**Non-linear structure formation in models
beyond LCDM**

Author:

Santiago CASAS CASTRO

Supervisor:

Dr. Valeria PETTORINO

*A thesis submitted in fulfillment of the requirements
for the degree of Doctor in Physics*

in the

Research Group Name
Department or School Name

March 4, 2017

Declaration of Authorship

I, Santiago CASAS CASTRO, declare that this thesis titled, "Non-linear structure formation in models beyond LCDM" and the work presented in it are my own. I confirm that:

- This work was done wholly or mainly while in candidature for a research degree at this University.
- Where any part of this thesis has previously been submitted for a degree or any other qualification at this University or any other institution, this has been clearly stated.
- Where I have consulted the published work of others, this is always clearly attributed.
- Where I have quoted from the work of others, the source is always given. With the exception of such quotations, this thesis is entirely my own work.
- I have acknowledged all main sources of help.
- Where the thesis is based on work done by myself jointly with others, I have made clear exactly what was done by others and what I have contributed myself.

Signed:

Date:

"Thanks to my solid academic training, today I can write hundreds of words on virtually any topic without possessing a shred of information, which is how I got a good job in journalism."

Dave Barry

UNIVERSITY NAME

Abstract

Faculty Name

Department or School Name

Doctor in Physics

Non-linear structure formation in models beyond LCDM

by Santiago CASAS CASTRO

The Thesis Abstract is written here (and usually kept to just this page). The page is kept centered vertically so can expand into the blank space above the title too...

Contents

Declaration of Authorship	iii
Abstract	vii
1 Overview of Standard Cosmology	1
1.1 The framework of General Relativity	1
1.1.1 The equivalence principle and geometry	1
1.1.2 The Einstein-Hilbert action and the field equations	1
1.1.3 The Newtonian limit	1
1.2 The standard cosmological model	1
1.2.1 Friedmann equations	2
1.2.2 Distances	2
1.2.3 The Λ CDM paradigm	2
1.2.4 The cosmological constant problem	2
1.2.5 Linear perturbations	2
1.3 Early Universe	2
1.3.1 Cosmic Microwave Background Radiation	2
1.3.2 Inflation	3
2 Dark Energy and Modified Gravity	5
2.1 Universal coupling to matter	5
2.1.1 Quintessence	5
2.1.2 f(R) Theories	5
2.1.3 Horndeski Theory	5
2.1.4 Effective Field Theory of Dark Energy	7
2.2 Non-universal coupling	7
2.2.1 Coupled Dark Energy	7
2.2.2 Growing Neutrino Quintessence	7
2.2.3 Non-universal couplings in EFT	7
3 Statistics in Cosmology	9
3.1 Correlation functions and the power spectrum	9
3.2 Likelihood and the Bayesian approach	9
3.3 Fisher Matrix formalism	9
3.4 The Fisher Matrix Code	9
3.4.1 Methodology of Fisher forecasts	9
3.4.1.1 The observed power spectrum	10
3.4.1.2 Derivatives of the observed power spectrum	11
3.4.1.3 Projecting back to the fundamental cosmological parameters	13
3.4.1.4 The Alcock-Paczynski-Effect	14
3.4.2 Marginalization	15
3.4.3 Validation of the code within the Euclid collaboration	15
3.4.4 Extensions of the Fisher matrix approach to higher orders	16

4	Linear and non-linear Modified Gravity forecasts	17
4.1	Introduction	17
4.2	Parameterizing Modified Gravity	18
4.2.1	Parameterizing gravitational potentials in discrete redshift bins	19
4.2.2	Parameterizing gravitational potentials with simple smooth functions of the scale factor	20
4.3	The power spectrum in Modified Gravity	21
4.3.1	The linear power spectrum	21
4.3.2	Non-linear power spectra	22
4.3.2.1	Halofit	23
4.3.2.2	Prescription for mildly non-linear scales including screening	24
4.4	Fisher Matrix forecasts	25
4.4.1	Future large scale galaxy redshift surveys	26
4.4.2	Galaxy Clustering	27
4.4.3	Weak Lensing	28
4.4.4	Covariance and correlation matrix and the Figure of Merit	30
4.4.5	CMB <i>Planck</i> priors	31
4.5	Results: Euclid forecasts for redshift binned parameters	32
4.5.1	Euclid Galaxy Clustering Survey	33
4.5.2	Euclid Weak Lensing Survey	34
4.5.3	Combining Euclid Galaxy Clustering and Weak Lensing, with <i>Planck</i> data	35
4.5.4	Decorrelation of covariance matrices and the Zero-phase Component Analysis	36
4.5.4.1	ZCA for Galaxy Clustering	37
4.5.4.2	ZCA for Weak Lensing	40
4.5.4.3	ZCA for Weak Lensing + Galaxy Clustering + CMB <i>Planck</i> priors	42
4.6	Modified gravity with simple smooth functions of the scale factor	44
4.6.1	Modified Gravity in the late-time parameterization	44
4.6.1.1	Galaxy Clustering in the linear and mildly non-linear regime	44
4.6.1.2	Weak Lensing in the linear and mildly non-linear regime	45
4.6.1.3	Combining Weak Lensing and Galaxy Clustering	45
4.6.1.4	Forecasts in Modified Gravity for SKA1, SKA2 and DESI	47
4.6.2	Modified Gravity in the early-time parameterization	52
4.6.2.1	Galaxy Clustering, Weak Lensing and its combination	52
4.6.2.2	Other Surveys: DESI-ELG, SKA1 and SKA2	54
4.6.3	Testing the effect of the Hu-Sawicki non-linear prescription on parameter estimation	54
4.7	Conclusions	57
4.8	Transformation of primary variables in Modified Gravity	59
4.8.1	Late time parameterization	59
4.8.2	Early time parameterization	60
4.9	Derivatives of the Power Spectrum with respect to μ and η	61
4.10	Other Decorrelation Methods	62
4.10.0.1	Principal Component Analysis	62

4.10.0.2 Cholesky decomposition	63
4.11 Weight matrices coefficients	64
4.12 The Kullback-Leibler divergence	66
5 Fitting and forecasting coupled dark energy in the non-linear regime	69
5.1 Introduction	69
5.2 Coupled Dark Energy	71
5.3 The CoDECS simulations	72
5.4 Extracting the power spectrum at small scales	72
5.5 Fitting functions	72
5.5.1 The net effect of the DM-DE coupling at non-linear scales	72
5.5.2 Generating the fitting functions	72
5.5.3 Fitting functions and cosmological parameters	72
5.6 Non-linear power spectrum and error estimation	72
5.7 Fisher Matrix method	72
5.7.1 Galaxy Clustering	72
5.7.1.1 Including sources of error in the Fisher formalism	73
5.7.1.2 Systematic bias on cosmological parameters	74
5.7.1.3 Choice of the k_{max} integration limit in the Fisher formalism	76
5.7.2 Weak Lensing	76
5.7.3 Adding non-linear corrections to the power spectrum	77
5.8 Results	78
5.8.1 Galaxy clustering	78
5.8.1.1 Variation of the k_{max} integration limit	79
5.8.2 Weak lensing	81
5.8.3 Combined results	83
5.9 Conclusions	83
5.10 Parameters of the fitting models M2 and M7	86
6 The non-linear evolution of matter perturbations	87
6.1 Standard perturbation theory and higher orders	87
6.2 The non-linear standard equations in Fourier space	87
6.2.0.1 The field notation	89
6.2.1 Solving for the general scale dependent linear propagator	90
6.2.2 The linear propagator in the Horndeski case	92
6.2.3 Assuming a constant $\mu \neq 1$ for the 1-loop quantities	94
6.3 The Evolution Equation for the Power Spectrum	94
6.3.1 The 1PI functions in the Horndeski constant $\mu \neq 1$ case	96
6.3.2 Method of implementation	98
6.4 Numerical approaches	99
6.4.1 N-body simulations	99
6.4.2 Fitting formulae and prescriptions	99
7 Growing Neutrino Quintessence	101
7.1 Introduction	101
7.2 Growing neutrinos with varying coupling	102
7.3 Numerical treatment of growing neutrino cosmologies	104
7.3.1 Modified Boltzmann code	104
7.3.2 N-body simulation	106
7.4 Lump dynamics and the low mass - high mass divide	108

7.5	Cosmological evolution in the light neutrino regime	112
7.6	heating of the neutrino fluid	114
7.7	Gravitational Potentials of Neutrino Lumps	118
7.8	Conclusions	120
7.9	Initial parameters for generating the models in nuCMB and in the N-Body simulation	121
7.10	The effective and observed equation of state of dark energy	122
8	Conclusions	125
A	Appendix Title Here	127
	Bibliography	129

List of Figures

- 4.1 The Modified Gravity functions μ and η as a function of redshift z for each of the models considered in this work, evaluated at the fiducials specified in Table 4.1. In light long-dashed blue lines, the ‘redshift binned model’ (Eqns. 4.6-4.8). In short-dashed red lines the late-time parameterization (Eqns. 4.9-4.10) and in green solid lines the early-time parameterization (Eqns. 4.11-4.12). Finally the medium-dashed orange line represents the standard Λ CDM model (GR) for reference. 21
- 4.2 **Left:** matter power spectra computed with MG-CAMB (linear) and MG-CAMB+Halofit (non-linear), illustrating the impact of non-linearities at different scales. As an illustrative example, MG in this plot corresponds to the fiducial model in the late-time parametrization defined in Eq. (4.9). All curves are computed at $z = 0$. The green solid line is the GR fiducial in the non-linear case, the blue long-dashed line is also GR but in the linear case. The short-dashed red line is the MG fiducial in the non-linear case and the medium-dashed brown line the MG fiducial in the linear case. **Right:** in order to have a closer look at small scales, we plot here the ratio of the MG power spectrum to the GR power spectrum for the linear (blue solid) and non-linear (red short-dashed) cases separately. The blue solid line compared to the horizontal grey dashed line, shows the effect of Modified Gravity when taking only linear spectra into account. While the red dashed line, which represents the non-linear case, shows that the ratio to GR presents clearly a bump that peaks around $k \approx 1.0 \text{ h/Mpc}$, meaning that the power spectrum in MG differs at most 4% from the non-linear power spectrum in GR. We will see later that we are able to discriminate between these two models using future surveys, especially when non-linear scales ($k \gtrsim 0.1 \text{ h/Mpc}$) are included. 24

- 4.3 The ratio of the Modified Gravity non-linear power spectrum using the HS prescription by Hu and Sawicki, 2007 (P_{nlHS}) with respect to the GR+Halofit fiducial non-linear power spectrum P_{HGR} , for different values of c_{nl} (left panel) and s (right panel), illustrated in Eqns.(4.13, 4.14). The value $c_{\text{nl}} = 0$ (green solid line) corresponds to MG+Halofit P_{HMG} . All curves are calculated at $z = 0$. **Left:** We show the ratio for $c_{\text{nl}} = \{0.5, 1.0, 10, 10^8\}$, plotted as short-dashed red, medium-dashed blue, short-dashed brown and medium-dashed purple lines respectively. When $c_{\text{nl}} \rightarrow \infty$, Eqn. (4.13) corresponds to the limit of P_{HGR} and therefore the ratio is just 1. The effect of the HS prescription is to grasp some of the features of the non-linear power spectrum at mildly non-linear scales induced by Modified Gravity, taking into account that at very small scales, a screening mechanism might yield again just a purely GR non-linear power spectrum. The parameter c_{nl} interpolates between these two cases. **Right:** in this panel we show the effect of the parameter s , for $s = \{0, 0.33, 0.66, 1\}$ (short-dashed red, medium-dashed blue, short-dashed brown and long-dashed purple, respectively). Both parameters need to be fitted with simulations in order to yield a reliable match with the shape of the non-linear power spectrum in Modified Gravity, as it was done in Zhao, Li, and Koyama, 2011 and references therein. The grey dashed line marks the constant value of 1. 26
- 4.4 Correlation matrix \mathbf{P} defined in (4.27) obtained from the covariance matrix in the MG-binning case, for a Galaxy Clustering Fisher forecast using Euclid Redbook specifications. **Left panel:** Linear forecasts. Here there are strong positive correlations among the μ_i and η_i parameters and anti-correlations between $\ln 10^{10} A_s$ and the μ_i parameters, as well as between μ_i and η_i . The FoC in this case is ≈ 65 . (see Eqn. (4.29) for its definition). **Right panel:** Non-linear forecasts using the HS prescription. Interestingly, the anti-correlations between $\ln 10^{10} A_s$ and μ_i have disappeared, as well as the correlations among the μ_i parameters. The FoC is in this case ≈ 32 , meaning that the variables are much less correlated than in the linear case. This is due to the fact that taking into account non-linear structure formation breaks degeneracies between the primordial amplitude parameter and the modifications to the Poisson equation. 33
- 4.5 Correlation matrix obtained from the covariance matrix in the MG-binning case, for a Weak Lensing Fisher Matrix forecast using Euclid Redbook specifications. **Left panel:** linear forecasts. Strong anti-correlations are present between the μ_i and the η_i parameters for the same value of i in 2,3,4,5. The amplitude $\ln(10^{10} A_s)$ parameter is mostly uncorrelated except with η_1 . The FoC (4.29) in this case is approximately 69. **Right panel:** non-linear forecasts using the HS prescription. Here the same trend as in the linear case is present, with just subtle changes. The FoC in this case is about 32, meaning that the variables are indeed less correlated than in the linear case. The parameter $\ln(10^{10} A_s)$ is effectively not correlated to other parameters, and the anti-correlation of μ_i and the η_i for the same value of the index i is present in the first three bins. The anti-correlation between these two sets of parameters is expected, since WL is sensitive to the Weyl potential Σ , which is a product of μ and η 35

- 4.6 Entries of the matrix W that relates the q_i parameters to the original p_i ones, after applying the ZCA decorrelation of the covariance matrix in the linear and non-linear GC cases. This matrix shows for each new variable q_i on the vertical axis, the coefficients of the linear combination of parameters μ_i , η_i and A_s that give rise to that variable q_i . The red (blue) colors, indicate a large (small) contribution of the respective variable on the horizontal axis. **Left panel:** linear forecast for Euclid Redbook specifications. **Right panel:** non-linear forecast for Euclid Redbook specifications, using the HS prescription. In both cases one can observe that most q_i parameters have only small or negligible contributions from μ_5 and η_5 , which are found to be the less constrained bins. 38
- 4.7 Results for a Euclid Redbook GC survey, with redshift-binned parameters, before and after applying the ZCA decorrelation. Each panel shows the 1σ fully marginalized errors on the primary parameters p_i (green dashed lines), and the 1σ errors on the decorrelated parameters q_i (orange solid lines). **Left:** linear forecasts, performed using linear power spectra up to a maximum wavenumber $k_{\max} = 0.15h/\text{Mpc}$. **Right:** non-linear forecasts using non-linear spectra with the HS prescription up to a maximum wavenumber $k_{\max} = 0.5h/\text{Mpc}$. In the linear case, the errors on the decorrelated q_i parameters are about 2 orders of magnitude smaller than for the primary parameters, while in the non-linear HS case, the improvement in the errors is of one order of magnitude. This means that applying a decorrelation procedure is worth even when non-linearities are considered. In both cases for GC, the least constrained parameters are μ_5 and η_5 , corresponding to $2.0 < z < 2.5$ 39
- 4.8 Best constrained modes for a Euclid Redbook GC survey, with μ and η binned in redshift, after transforming into uncorrelated q parameters via ZCA. Each of the four best constrained parameters q_i , shown in the panels, is a linear combination of the primary parameters p_i . The q_i in the legends are ordered from left to right, from the best constrained to the least constrained. 39
- 4.9 Entries of the matrix W that relates the q_i parameters to the original p_i ones, after applying the ZCA decorrelation of the covariance matrix in the linear and non-linear WL cases. This matrix shows for each new variable q_i on the vertical axis, the coefficients of the linear combination of parameters μ_i , η_i and A_s that give rise to that variable q_i . The red (blue) colors, indicate a large (small) contribution of the respective variable on the horizontal axis. **Left panel:** linear forecast for Weak Lensing Euclid Redbook specifications. **Right panel:** non-linear forecast for Weak Lensing Euclid Redbook specifications, using the HS prescription. As for GC, most q_i parameters have only small or negligible contributions from μ_5 and η_5 , which are found to be the less constrained bins. 40

- 4.10 Results for a Euclid Redbook WL survey, with redshift-binned parameters, before and after applying the ZCA decorrelation. Each panel shows the 1σ fully marginalized errors on the primary parameters p_i (green dashed lines), and the 1σ errors on the decorrelated parameters q_i (orange solid lines). **Left:** Linear forecasts, performed with an $\ell_{\max} = 1000$ and linear matter power spectra. **Right:** Non-linear forecasts using the non-linear HS prescription, up to an $\ell_{\max} = 5000$. The errors in the non-linear HS case, are about 1 order of magnitude smaller than in the linear case. For the best constrained q_i parameters, the decorrelated errors are up to 2 orders of magnitude smaller than the corresponding fully marginalized parameters on the parameters p_i 41
- 4.11 Best constrained modes for a Euclid Redbook WL survey, with μ and η binned in redshift, after transforming into uncorrelated q parameters via ZCA. Each of the four best constrained parameters q_i , shown in the panels, is a linear combination of the primary parameters p_i . q_i in the label are ordered from the best constrained to the least constrained. 41
- 4.12 Results for the combined forecasts of Euclid Redbook GC+WL using the non-linear HS prescription together with the addition of *Planck* CMB priors. **Left panel:** correlation matrix obtained from the covariance matrix in the MG-binning case. Red (purple blue) colors represent strong positive (negative) correlations. The structure of this matrix is considerably diagonal, except for the strong anti-correlations of the pair (μ_i, η_i) for $i = \{1, 2, 3, 4, 5\}$, which resembles the correlations found for the WL case alone (see Figure 4.5). However, the sub-block of standard cosmological parameters is now much more diagonal and shows less correlations than in the GC (Fig. 4.4) or WL cases. The natural FoC (defined in 4.29) in this case is ≈ 22 , showing that the variables are much less correlated than in the two previous cases. **Right panel:** entries of the matrix W for the ZCA decorrelation of the covariance matrix. This matrix shows for each new variable q_i on the vertical axis, the coefficients of the linear combination of parameters μ_i and η_i that give rise to that variable q_i . The red (blue) colors, indicate a large (small) contribution of the respective variable on the horizontal axis. 43
- 4.13 **Left:** the 1σ fully marginalized errors on the primary parameters p_i (green dashed lines), and the 1σ errors on the decorrelated derived parameters q_i (yellow solid lines). As opposed to the GC or WL cases (figs.4.7,4.10), here the decorrelated errors are much more similar to the standard errors. This is due to the fact that in the GC+WL+*Planck* combination, the cosmological parameters are not so strongly correlated. **Right:** best constrained modes for a Euclid Redbook GC+WL case using the non-linear HS prescription and adding a CMB *Planck* prior. Each panel shows the four best constrained parameters q_i . Each of them is a linear combination of the primary parameters p_i . The best constrained modes are sums $a\mu_i + b\eta_i$ for $i = \{1, 2, 3\}$ and positive values a and b 43

- 4.14 Fisher Matrix marginalized contours ($1, 2\sigma$) for the Euclid space mission in the late-time parameterization using mildly non-linear scales and the HS prescription. Green lines represent constraints from a Galaxy Clustering survey, pink lines stand for the Weak Lensing observables, and orange lines represent the GC+WL+*Planck* combined confidence regions. **Upper Left:** contours for the fully marginalized errors on η and μ . **Upper Right:** contours for the fully marginalized errors on Σ and μ . **Lower Left:** contours for the fully marginalized errors on μ and Ω_b . **Lower Right:** contours for the fully marginalized errors on Σ and $\ln(10^4 A_s)$. The fact that the combination of GC, WL and *Planck* breaks many degeneracies in the 7-dimensional parameter space, explains why the combined contours (yellow) have a much smaller area. Notice that in this parametrization, GC measures mostly μ and WL constrains mostly just Σ 50
- 4.15 1σ fully marginalized errors on the parameters $\{\Omega_m, \Omega_b, h, \ell A_s, n_s, \mu, \eta, \Sigma\}$ for the late-time parameterization of MG obtained by forecasts on Galaxy Clustering (non-linear HS) (top left panel), Weak Lensing (non-linear HS) (top right panel), the combinations GC+WL (linear) (middle left) and GC+WL+*Planck* (linear) (middle right) and the combinations GC+WL (non-linear HS) (bottom left) and GC+WL+*Planck* (non-linear) (bottom right). In the GC case, the surveys considered are SKA2 (blue), SKA1-SUR (green), Euclid Redbook (purple) and DESI-ELG (orange). For forecasts including WL, only Euclid, SKA1 and SKA2 are included. Although the 1σ constraints on the standard parameters are overall weaker for WL than for GC, Weak Lensing surveys perform better on Modified Gravity parameters. Comparing the different surveys, Euclid and SKA2 perform similarly well for the WL observable alone, if non-linearities are included. Notice that SKA1-SUR performs better than Euclid on the η and Σ parameters, because it can measure better at lower redshifts. Including the *Planck* prior, the GC+WL combination for Euclid and SKA2 constrains all parameters at much better than percent accuracy. Detailed specifications of the different surveys are explained in the text. 51
- 4.16 1σ and 2σ fully marginalized confidence contours on the parameters μ and η , for 3 different surveys combining Galaxy Clustering (GC) and Weak Lensing (WL): Euclid, SKA1-SUR and SKA2 and for GC only: DESI-ELG, all in the late-time (left panel) and early-time (right panel) parameterizations of sections 4.6.1 and 4.6.2, respectively. As explained in the main text, the constraints are parameterization-dependent, especially on η , where in the late-time scenario GC alone is not able to constrain it, while in the early-time scenario GC can constrain both μ and η 52

4.17 Fisher Matrix marginalized forecasted contours (1σ , 2σ) for the Euclid Redbook satellite in the early-time parameterization using mildly non-linear scales and the HS prescription. Green lines represent constraints from the Galaxy Clustering survey, pink lines stand for the Weak Lensing observables, and orange lines represent the GC+WL+ <i>Planck</i> combined confidence regions. Upper left: contours for the fully marginalized errors on η and μ . Upper right: contours for the fully marginalized errors on Σ and μ . Lower left: contours for the fully marginalized errors on μ and Ω_b . Lower right: contours for the fully marginalized errors on Σ and $\ln 10^{10} A_s$. Notice that in this parameterization, GC and WL are able to constrain both μ and η or Σ on their own.	53
4.18 Same as Fig.4.15 but for the early-time parameterization (Eqns. 4.11,4.12) The 1σ fully marginalized constraints on the parameters are weaker for WL than for GC, which is a consequence of the higher correlation among variables for the Weak Lensing observable.	55
4.19 Effect of the c_{nl} and s parameters on the 1σ marginalized error of the μ (left panel) and the η (right panel) parameters in the MG late-time parametrization for a Euclid Galaxy Clustering forecast with Redbook specifications. The colored contours show the percentage discrepancy when departing from the benchmark case $c_{\text{nl}} = 1$ and $s = 1$ (marked with a black arrow) to all other points in the $c_{\text{nl}}\text{-}s$ space. The red (blue) contours signal the regions of maximum positive (negative) discrepancy. For example in the left panel, choosing c_{nl} and s in the red region, will yield a 1σ marginalized error on μ which is 90% larger than in the benchmark case (see Table 4.4 for the benchmark forecast). For the standard Λ CDM cosmological parameters (not shown here) the discrepancy is smaller than 4% for all choices of c_{nl} and s	56
4.20 Same as Fig.4.19 but for a Weak Lensing Euclid forecast using Redbook specifications. In the left panel, choosing c_{nl} and s in the red region, will yield a 1σ marginalized error on μ which is 60% larger than in the benchmark case (see Table 4.4 for the benchmark forecast). In the right panel we see that for the MG parameter Σ the maximum positive and negative discrepancy is only of about 6%. The maximum and minimum discrepancy for the MG parameter η is of -15% and 50%. This means that the parameter Σ (defined as the lensing Weyl potential, and therefore directly constrained by Weak Lensing) is much less sensitive to changes in the non-linear prescription parameters.	56
4.21 Derivatives of the matter power spectrum $P(k, z)$ w.r.t. the MG parameters μ and η in the late-time parametrization.	61
4.22 Derivatives of the matter power spectrum $P(k, z)$ w.r.t. the MG parameters μ and η in the early-time parametrization.	61
4.23 Left: weight matrix W for PCA. Right: 1σ fully maximized errors on the primary parameters p (blue lines) and the errors on the uncorrelated derived parameters q (orange lines). Notice how all the important information is constrained in as few variables as possible, namely the last elements of q_i	63

4.24 Left: weight matrix W for the Cholesky decorrelation. Right: 1σ fully maximized errors on the primary parameters p (blue lines) and the errors on the uncorrelated derived parameters q (orange lines). Notice how in this case, because of the upper triangular construction, the new variables $q_{9,10,11}$ are equivalent to $\eta_{3,4,5}$. The parameter A_s is decorrelated in the non-linear HS case for GC, therefore it is almost equivalent to q_1 as was also the case in ZCA (compare with Fig. 4.6)	64
4.25 KL div mat	67
5.1 Change of the 1σ fully marginalized error on the set of cosmological parameters p_i for a galaxy clustering Fisher forecast, as a function of the maximum mode k_{max} used as a cutoff in the Fisher matrix integration. When increasing the maximum k_{max} the errors on the parameters get steadily smaller, especially when going from linear ($k \approx 0.1h/\text{Mpc}$) to mildly non-linear ($k \approx 0.3h/\text{Mpc}$) scales. The vertical dashed grey lines, mark the half and the full Nyquist frequencies.	80
5.2 Marginalized confidence contour regions $1,2,3\sigma$ for β^2 and h . The plots correspond to a comparison between linear (green-dashed lines) and non-linear (red-solid lines) scales for GC (left) and WL (right) using the scale cutoff at $k_{Ny}/2$	80
5.3 Variation in the 1σ fully marginalized errors for each cosmological parameter p_i as a function of the maximum multipole used in the weak lensing Fisher forecast. Increasing the observed multipole range improves considerably the determination of a parameter, especially on the coupling β^2 (red solid line) and the initial amplitude of perturbations $10^9 A_s$ (dashed green line). The double lines corresponding to each parameter, show how the error changes if a cut in the matter power spectrum $P(k)$ is performed at k_{Ny} (lower line) instead of a cut at $k_{Ny}/2$ (upper line, respectively). The vertical dashed grey lines mark the ℓ_{cut} at the peak of the first redshift bins for the cases $\ell_{cut, k_{Ny}/2}$ and $\ell_{cut, k_{Ny}}$	82
5.4 Marginalized confidence contour regions ($1,2,3\sigma$) for all cosmological parameters considered in this model. The blue dashed lines correspond to the WL Fisher forecast, while the green dashed lines correspond to the GC Fisher forecast both in our reference case. The red solid lines correspond to the combined Fisher matrix forecast. For combinations of the parameter β^2 , WL and GC have similar figures of merit, but different orientations, while for other combinations of cosmological parameters, the estimation is dominated by the GC Fisher matrix estimation.	84

- 7.1 Snapshots of the number density contrast of neutrinos $\delta n_\nu(\vec{x}) \equiv n_\nu(\vec{x})/\bar{n}_\nu - 1$ at different times. **Left:** Model M2, at scale factors $a = 0.45, 0.7, 0.75$ and 0.95 from top to bottom. The overdensity oscillates between values close to 1 (represented as yellow tones) at early times, where there are no lumps, to values close to 10 (dark blue and purple tones), where several concentrated lumps form at intermediate times. At later times lumps dissolve and the overdensity decreases back to values close to unity. **Right:** Model M4, at scale factors: $a = 0.35, 0.42, 0.53$ and 0.64 from top to bottom. The neutrino lumps start growing at early times and merge progressively into larger and more concentrated structures. At the end, almost all neutrinos are attracted to a single very massive lump. 110
- 7.2 Snapshots of the neutrino overdensity field $\delta_\nu(\vec{x})$ for models M4 (top left) and M6 (bottom left) at scale factors of $a = 0.64$, and 0.62 , respectively. In these models, neutrino lumps cluster into large stable structures with a high concentration, starting from a bottom-up approach, as was shown for model M4 in fig. 7.1. Neutrino structures occupy large parts of the simulation box, corresponding to scales of ~ 50 Mpc. At these scale factors, the forces introduced by the cosmon coupling are too strong to be resolved by our numerical approach and our simulation breaks down. 112
- 7.3 Evolution of $\Omega_{\phi+\nu}$ (blue lines) and Ω_ν (orange lines) for Model M2, compared between the linear output from nuCMB (dashed lines) and the non-linear calculation of the N-body simulation (solid lines). The total cosmon-neutrino fluid has the same background evolution in the simulation as in the linear calculation. The neutrino energy density is somewhat larger in the simulation and shows a phase-shift in its oscillations, as discussed in the text. 114
- 7.4 Equation of state of the combined neutrino-cosmon fluid $w_{\phi+\nu}$ (blue) and equation of state of neutrinos w_ν (orange). We compare the linear output (dashed lines) to the non-linear one obtained from the N-body simulation (solid lines) for model M2. This model has a time averaged RMS mass $\langle m_\nu \rangle(a_l) = 0.164$, where $a_l = 0.9$ in the label denotes the center of the time interval $a = [0.8 - 1.0]$ used to take the average. For w_ν , the linear output does not capture the oscillating equation of state of neutrinos due to the formation of structures, while for $w_{\phi+\nu}$, both codes agree relatively well. At late times the equation of state predicted by the simulation has a somewhat higher value and is phase-shifted due to the heating of the neutrino fluid. . . 115

- 7.5 Neutrino mass \bar{m}_ν (average over simulation volume) in model M2 (firebrick red line) and model M1 (dodger blue line), as a function of the scale factor a , for the N-body simulation. The horizontal lines, show the time averaged RMS value at a late time $a_l = 0.9$, denoting the center of the time interval of $[0.8 : 1.0]$ considered for taking the average. For model M2, the time averaged neutrino mass is $\langle m_\nu \rangle(a_l) = 0.164$ (blue dashed lines), while for model M1 it is somewhat smaller $\langle m_\nu \rangle(a_l) = 0.120$ (red dashed lines). One can observe that the oscillation frequency is higher for the smaller $\langle m_\nu \rangle$ mass and the peaks are higher for the larger $\langle m_\nu \rangle$. The present neutrino masses of the two models calculated in linear theory differ by an order of magnitude, on the contrary the time averaged masses are very close to each other. 116
- 7.6 Distribution of the momenta of the neutrino particles in the simulation, for two different times, $a = 0.75$ (purple shade) and $a = 1.0$ (orange shade), compared against a Fermi-Dirac distribution with a temperature given by the mean of the distribution (dashed lines). **Left:** For model M1 the Fermi-Dirac fits very well for temperatures of $\bar{T} = 0.018\text{eV}$ and $\bar{T} = 0.077\text{eV}$ for each scale factor respectively. **Right:** For model M2 the fit is also good, the corresponding temperatures being $\bar{T} = 0.018\text{eV}$ and $\bar{T} = 0.065\text{eV}$. The CMB photon temperature is $2.35 \times 10^{-4}\text{eV}$, this means that the non-linear cosmoneutrino interactions heat the neutrino background by more than a factor 100. 117
- 7.7 Power spectra of the total gravitational potential Φ_t (blue lines) and of the neutrino contribution Φ_ν (orange lines) for model M2 and model M5 at the scale factors $a = 0.40$ (solid lines) and $a = 0.65$ (dashed lines), as a function of scale. Model M2 has an RMS time averaged neutrino mass $\langle m_\nu \rangle(a_e) = 0.07$, where $a_e = 0.5$ stands for the central time in the interval $a = [0.4 - 0.6]$ used to take the average. Model M5 has in the same interval a higher RMS mass of $\langle m_\nu \rangle(a_e) = 0.40$. In the first model, Φ_t at large scales is of the order of 10^{-5} , while Φ_ν is 3 to 4 orders of magnitude smaller at both cosmological times. For model M5, in which neutrino lumps are stable and growing, one sees that at large scales, the total Φ_t starts with a value of 10^{-5} at $a = 0.4$, but reaches 10^{-4} at later times. At $a = 0.65$ the neutrino contribution is dominant and neutrino structures have migrated from small scales to large scales, as can be seen from the dip in Φ_ν at modes between $k = 0.2 - 1.0 \text{ h/Mpc}$ 118
- 7.8 Power spectra of the matter gravitational potential Φ_m (blue lines) and of the neutrino contribution Φ_ν (orange lines) at two different scales, $k = 0.016$ (solid lines) and $k = 0.116$ (dashed lines) as a function of scale factor a with two different scales on the top and bottom axis. For model M2 the matter gravitational potential Φ_m is at most 10^{-5} at all times, while the neutrino contribution is 2-3 orders of magnitude smaller and displays time oscillations. In clear contrast, the neutrino contribution from model M5 for very large scales, reaches and dominates over the matter contribution for $a \gtrsim 0.5$ and pushes the total Φ to high values that would be ruled out by observations, see also fig. 7.7. The RMS neutrino mass has been taken in the same interval range as for fig.7.7, where $a_e = 0.5$ 119

- 7.9 **Left:** Line plot through the main diagonal of the simulation box, for model M2 at $a = 0.75$. The negative of the neutrino contribution to the gravitational potential Φ_ν (blue dot-dashed lines) oscillates between $\pm 1.0 \times 10^{-7}$. This is correlated to the neutrino density contrast (black lines) and the number density contrast $\delta n_\nu = n_\nu(\vec{x})/\bar{n}_\nu - 1$ (orange dashed lines) reaching values of up to 1.5. **Right:** Snapshot of the same simulation, showing a equipotential contour of the gravitational potential, for $\Phi_\nu = +1.0 \times 10^{-7}$ in yellow, and the small but dense neutrino lumps in blue, purple and red, corresponding to density contrasts δn_ν of 1.5, 2.0 and 4.0 respectively. 120
- 7.10 Different $w(z)$ curves in the case of model M1 computed with the N-body simulation and compared to linear theory. The red dashed lines represent w_{DE} computed from the Hubble function which is an output of the linear code nuCAMB. The solid orange line, representing $w_{\nu+\phi}$ is computed using the standard pressure and density outputs from the simulation. The blue dots stand for some set of computed values of $w_{DE}(z)$ obtained from the Hubble function calculated entirely within the N-body simulation. Due to numerical noise in the oscillating derivatives of $E(z)$, there is some scatter in the e.o.s. obtained in this case. 124

List of Tables

4.1	Fiducial values for the Modified Gravity parameterizations and the redshift-binned model of μ and η used in this work. The DE related parameterization contains two extra parameters E_{11} and E_{22} with respect to GR; the early-time parametrization depends on 4 extra parameters E_{11} , E_{12} , E_{22} and E_{21} with respect to GR; the redshift-binned model contains 10 extra parameters, corresponding to the amplitudes μ_i and η_i in five redshift bins. In this work we will use alternatively and for simplicity the notation $\ell\mathcal{A}_s \equiv \ln(10^{10}A_s)$. The fiducial values are obtained performing a Monte Carlo analysis of <i>Planck</i> +BAO+SNe+H ₀ (BSH) data Planck Collaboration, Ade, and others, 2016.	22
4.2	Specifications for the spectroscopic galaxy redshift surveys used in this work. The number density of tracers $n(z)$ and the galaxy bias $b(z)$, can be found for SKA in Santos et al., 2015 and for DESI in reference DESI Collaboration, Aghamousa, and others, 2016a.	28
4.3	Specifications for the Weak Lensing surveys Euclid, SKA1 and SKA2 used in this work. Other needed quantities can be found in the references cited in section 4.4.1. For all WL surveys we use a redshift range between $z = 0.5$ and $z = 3.0$, using 6 equi-populated redshift bins.	30
4.4	1σ fully marginalized errors on the cosmological parameters in the late-time parameterization of Modified Gravity for a Euclid Galaxy Clustering forecast (top), a Weak Lensing forecast (middle) and the combination of both probes (bottom): Modified Gravity is encoded in two of the three functions μ , η , Σ , which are reconstructed in the late-time parameterization defined in Eqns. (4.9,4.10). For each case, we also list the forecasted errors using a <i>Planck</i> +BSH prior. Linear forecasts are labeled by “lin”, and correspond to a cutoff $k_{\max} = 0.15h/\text{Mpc}$ for GC and $\ell_{\max} = 5000$ for WL; non-linear forecasts use the prescription described in sec. 4.3.2.2, are labeled by “nl-HS” and correspond to a cutoff of $k_{\max} = 0.5h/\text{Mpc}$ for GC and $\ell_{\max} = 5000$ for WL. in both cases, power spectra have been computed using the MGCB Boltzmann code. For completeness, we also show the GC+WL+ <i>Planck</i> case using the non-linear power spectra computed using Halofit only (nl-Halofit). In the last column, we show for each observation the Figure of Merit (FoM) relative to our base observable in this parametrization, which is GC(linear). GC(linear) has an absolute FoM of -0.94 in ‘nits’. We can see that in both GC and WL there is a considerable gain when including non-linear scales and <i>Planck</i> priors. The difference in the FoM between the non-linear HS prescription and the standard Halofit approach is quite small.	46

4.8	1- σ fully marginalized errors on the cosmological parameters and the two HS parameters c_{nl} and s for a Euclid Galaxy Clustering forecast, a Weak Lensing forecast and the combination of both in the late-time parameterization of Modified Gravity using non-linear scales and the HS prescription. In contrast to Table 4.4 (where c_{nl} and s had been fixed to the benchmark value) here we include c_{nl} and s as free parameters and marginalize over them. The MG FoM is computed relative to the same Euclid Redbook GC linear case, used previously. The errors and the MG FoM show the expected behavior of adding two nuisance parameters, and remain quite stable. All other naming conventions are the same as for Table 4.4. Remarkably, the combination of GC and WL is still able to constrain all Modified Gravity parameters at the level of 1-2 % after marginalizing over the non-linear parameters.	57
4.9	Summary of results for this work. For each studied model, we indicate where to find the explanations and where to find the main Fisher forecast results.	57
4.10	Coefficients of the Matrix W for the Euclid Redbook GC forecasted covariance matrix, using linear power spectra. The entries marked with red are those whose absolute values are larger than 0.25.	64
4.11	Coefficients of the Matrix W for the Euclid Redbook GC forecasted covariance matrix, using the non-linear HS prescription. The entries marked with red are those whose absolute values are larger than 0.25.	65
4.12	Coefficients of the Matrix W for the Euclid Redbook WL forecasted covariance matrix, using linear power spectra. The entries marked with red are those whose absolute values are larger than 0.25.	65
4.13	Coefficients of the Matrix W for the Euclid Redbook WL forecasted covariance matrix, using the non-linear HS prescription. The entries marked with red are those whose absolute values are larger than 0.25.	65
4.14	Coefficients of the Matrix W for the Euclid Redbook GC+WL case using the non-linear HS prescription and adding a CMB <i>Planck</i> prior. The entries marked with red are those whose absolute values are larger than 0.25.	66
5.1	The main parameters and normalizations of the three coupled DE models of the Codecs suite considered in the present work. The last column displays the corresponding valuem for the reference ΛCDM cosmology.	72
5.2	Systematic bias on the ΛCDM cosmological parameters evaluated at our fiducial model. The systematic bias is higher when probing smaller scales, where uncertainties in the non-linear power spectrum are higher. This highlights the importance of modelling correctly the non-linear power spectrum in order to analyze data. Using the wrong non-linear power spectrum produces statistical errors which are larger or of the same order as the statistical results.	75
5.3	Specifications for the Fisher Matrix of an Euclid-like galaxy clustering survey.	79
5.4	1- σ fully marginalized errors on the cosmological parameters of the model for a galaxy clustering Fisher forecast. Two cases are presented, a hard cutoff of the power spectrum at $k_{\text{max}} = k_{Ny}/2$, and a hard cut at k_{Ny}	79

5.5	Specifications for the Fisher Matrix of an Euclid-like weak lensing survey.	81
5.6	Redshift bins specifications for an Euclid-like weak lensing survey using equipopulated redshift bins in the range $0 \leq z \leq 3$ and the corresponding values for the cutoff applied in the multipoles ℓ at each redshift bin, for two different cases: scales larger than $k_1 = k_{Ny}/2$ and scales larger than $k_2 = k_{Ny}$	81
5.7	1- σ fully marginalized errors on the cosmological parameters of the model for a weak lensing Fisher forecast. Two cases are presented, a redshift-dependent cutoff $\ell_{cut, k_{Ny}/2}$ and a cutoff $\ell_{cut, k_{Ny}}$, corresponding to cutting off the non-linear power spectrum at the half and at the full Nyquist frequency (analogously to the GC case) as explained in the main text. As opposed to the GC case, going into smaller scales in a WL survey does bring a noticeable improvement.	82
5.8	1- σ fully marginalized errors on the cosmological parameters for WL, GC and the combined Fisher matrix WL+GC, using three different power spectra. Linear CDE : Using only information from the linear power spectrum for the CDE model up to a scale of $k = 0.1h/\text{Mpc}$. Linear CDE+Halofit : Using the linear power spectrum for CDE plus a non-linear correction using the latest Halofit from Takahashi et al., 2012. Non-linear CDE fitting functions : Using the fully non-linear power spectra for CDE obtained from the fitting functions and the emulator as explained in 5.5, which we regard as the most reliable description of the model in this range of scales. In all these cases we are using our reference Fisher forecasts corresponding to the cutoff at $k_{Ny}/2$	85
7.1	Table of parameters for the six models considered in this work. The top part refers to the output values computed with the linear nuCMB code. The bottom part refers to values computed within the N-body simulation. Quantities denoted with a subscript 0 are values at present time, $a = 1.0$. The $\langle m_\nu \rangle [a_1 : a_2]$ is the root mean squared (RMS) value of the neutrino mass in units of eV computed between $a = a_1$ and $a = a_2$. The same notation is also valid for $\langle w_{\nu\phi} \rangle [a_1, : a_2]$ corresponding to the equation of state of the combined cosmon and neutrino fluid which represents dynamical dark energy. a_{final} is the final time at which simulations were computed accurately. Therefore, for the models M3-M6 we cannot cite values of present time quantities or averages at times beyond a_{final} . The input values for nuCMB corresponding to all models can be found in table 7.2 of appendix 7.9.	107
7.2	Table of initial parameters for each model computed with nuCMB. \tilde{m}_ν is the neutrino mass amplitude used in the simulations, $\hat{r}_{\nu eV}$ is the neutrino mass units conversion factor between the simulations and nuCMB. V_i is the initial value of the cosmon potential.	121

- 7.3 Table of numerical parameters for each N-body simulation run. Several tests were performed varying these parameters, but the overall behavior for the purposes of this paper was the same. We also tested model M2 with grid sizes of 128 and 8 times the number of particles, not noticing any qualitative difference in the dynamics. Only deviations of the order of 10% in perturbation quantities were observed when varying the grid size or the number of particles. 122

List of Abbreviations

LSS	Large Scale Structure
BAO	Baryon Acoustic Oscillations
RSD	Redshift Space Distortions
SPT	Standard Perturbation Theory
RPT	Renormalized Perturbation Theory
EFT	Effective Field Theory
CDM	Cold Dark Matter
GNQ	Growing Neutrino Quintessence
GR	General Relativity
RDE	Radiation Dominated Era
MDE	Matter Dominated Era
EdS	Einstein-de Sitter

Physical Constants

Speed of Light $c = 2.997\,924\,58 \times 10^8 \text{ m s}^{-1}$ (exact)

List of Symbols

a	scale factor	
H_0	Hubble parameter	(km s ⁻¹ Mpc ⁻¹)
z	redshift	
Ω_b	Fraction of energy density in baryons	
Ω_c	Fraction of energy density in CDM	
Ω_m	Fraction of energy density in non-relativistic matter	
Ω_ν	Fraction of energy density in neutrinos	
Ω_r	Fraction of energy density in radiation	

Dedicated to ...

Chapter 1

Overview of Standard Cosmology

1.1 The framework of General Relativity

1.1.1 The equivalence principle and geometry

- The equivalence principle
- Manifolds and local flatness
- Physical relation equivalence principle -> local flatness
- The metric formalism
- The Levi-Civita connection
- Diffeomorphism invariance

1.1.2 The Einstein-Hilbert action and the field equations

$$S = \int dx^4 \sqrt{-g} (R - \Lambda) \quad (1.1)$$

$$R_{\mu\nu} + \frac{1}{2}g_{\mu\nu}R + g_{\mu\nu}\Lambda = 8\pi G T_{\mu\nu} \quad (1.2)$$

- Bianchi identities and the conservation of $T_{\mu\nu}$
- Lovelock's theorem

1.1.3 The Newtonian limit

- Gravitational potentials Φ and Ψ .
- Very simple explanation of Gauge choice
- Newtonian Gauge
- Smallness of gravitational potentials
- Remark for later that in GR $\Psi = \Phi$
- Weyl potential (lensing potential, null geodesics)

1.2 The standard cosmological model

- small discussion on how to define a cosmology
- Observer along timelike geodesic and foliation of spacetime

1.2.1 Friedmann equations

- Friedmann-Lemaître-Robertson-Walker metric
- 00 and ii components of Einstein equation
- First and second Friedmann equations
- Several ways of writing Hubble function for different species
- Background expansion, , RDE, MDE, $w(z)$

1.2.2 Distances

- definition of distances
- definition of Hubble time
- Horizons?

1.2.3 The Λ CDM paradigm

- Reasons for CDM
- Reasons for Lambda
- Baryons, neutrinos and other species

1.2.4 The cosmological constant problem

- small discussion on old and new cosmological constant problem
- fine tuning, naturalness, basic definitions

1.2.5 Linear perturbations

- Differentiate between linear perturbations in different eras, just shortly
- Linear perturbations in matter dominated eras, newtonian gauge
- Fluid equations, full and linearized

1.3 Early Universe

1.3.1 Cosmic Microwave Background Radiation

- Short introduction and importance of CMB
- Important constraints on parameters coming from CMB
- Constrain CDM alone
- Constrain initial power amplitude and tilt
- Constrain relativistic degrees of freedom

1.3.2 Inflation

- Inflation as a paradigm
- Flatness and horizon problems
- Inflation produces almost scale invariant spectrum

Chapter 2

Dark Energy and Modified Gravity

2.1 Universal coupling to matter

- define Jordan and Einstein frame
- write action in both cases
- write that in Universal coupling matter couples to the full $\sqrt{-g}$

2.1.1 Quintessence

- small introduction to quintessence, Ratra, Peebles, Wetterich, Luca
- different potentials, Brans-Dicke, Exponential potential

2.1.2 $f(R)$ Theories

- small intro to $f(R)$, Amendola, Felice, Tsujikawa
- write $f(R)$ as conformal transformation of quintessence (Valeria's paper)

2.1.3 Horndeski Theory

- Most general single scalar field theory, second order equations of motion, 4 dimensions, ghost-free
- 5 Lagrangians which can be parametrized with the α functions that give more physical insight.
- Quasistatic limit yields modifications of gravity that depend only on time and k^2 .

In a homogeneous and isotropic universe, the distance element assumes the form:

$$ds^2 = a(\tau)[-(1 + 2\Psi)d\tau^2 + (1 - 2\Phi)\delta_{ij}dx^i dx^j], \quad (2.1)$$

where the conformal time τ is related to the cosmic time t by $d\tau = dt/a(\tau)$ and Ψ and Φ are the two scalar gauge invariant gravitational potentials, related (modulo sign) to the Bardeen potentials.

Horndeski models include (almost) all theories with second order equations of motion in the fields and can be generically described with five functions of time. They include a variety of particular models studied in literature, characterised by a universal coupling to matter fields.

The Lagrangian can be written as ...

where ... is the matter Lagrangian and ... are arbitrary functions of the scalar field ϕ , whose canonical kinetic term is $X = -\frac{1}{2}\phi^{;\mu}\phi_{;\mu}$; the latter is also coupled to the Ricci scalar and the Einstein tensor.

In the following, we will adopt the conformal Newtonian gauge in the notation of (**MaBertschinger**), so that the gauge invariant potentials Ψ and Φ are also equal to the gravitational potentials in the Newtonian limit. In this formulation, the cold dark matter (CDM, c) perturbation equations for the density contrast δ and the velocity divergence θ can be written in Fourier space in the usual way:

$$\dot{\delta}(\tau, \mathbf{k}) = -(\theta(\tau, \mathbf{k}) - 3\Phi(\tau, \mathbf{k})) , \quad (2.2)$$

$$\dot{\theta}(\tau, \mathbf{k}) = -H\theta(\tau, \mathbf{k}) + k^2\Psi(\tau, \mathbf{k}) . \quad (2.3)$$

Derivating the first of the above equations with respect to τ and eliminating $\dot{\theta}$ and θ using both equations, one obtains the usual second order equation in time for the density contrast:

$$\ddot{\delta}(\tau, \mathbf{k}) = -(H\dot{\delta}(\tau, \mathbf{k}) - 3H\dot{\Phi}(\tau, \mathbf{k}) + k^2\Psi(\tau, \mathbf{k}) - 3\ddot{\Phi}(\tau, \mathbf{k})) . \quad (2.4)$$

In the following, we will stay within the quasi-static limit, i.e restrict to scales much smaller than the cosmological horizon ($k/aH \gg 1$) and well inside the Jeans length of the scalar field $c_s k \gg 1$, so that terms containing k dominate over terms containing time derivatives. In this case, Eq. 2.4 reduces to:

$$\ddot{\delta}(\tau, \mathbf{k}) + H\dot{\delta}(\tau, \mathbf{k}) + k^2\Psi(\tau, \mathbf{k}) = 0 . \quad (2.5)$$

The gravitational potential is then obtained from the Poisson equation, that relates the gravitational potential to matter and relativistic species in the universe, by perturbing the Einstein field equations to first order.

In Horndeski theories, in the quasi-static limit, the deviation of the gravitational potentials from General Relativity has a known scale dependence in the Poisson equation, given by (...):

$$\mu(k, a) \equiv -\frac{2k^2\Psi}{3\Omega_m\delta_m} = h_1 \left(\frac{1 + (k/k_*)^2h_5}{1 + (k/k_*)^2h_3} \right) \quad (2.6)$$

where h_1, h_3, h_5 are functions of time only. A similar expression, with different time dependent coefficients h_2, h_4 , holds for the gravitational slip η :

$$\eta(k, a) \equiv -\frac{\Phi}{\Psi} = h_2 \left(\frac{1 + (k/k_*)^2h_4}{1 + (k/k_*)^2h_5} \right) . \quad (2.7)$$

In this work we will consider all h_i functions as constants, for simplicity, although in general they are all functions of time. k_* is an arbitrary pivot scale, chosen at large scales close to the horizon, in order to fulfil the quasi-static limit.

As it can be seen from eqns. 2.6 and 2.7, the functions h_5 and h_3 are degenerate as well as h_4 and h_5 . Λ CDM case is recovered when $\mu = \eta = 1$, which implies $h_5 = h_4 = h_3$ and an amplitude $h_1 = h_2 = 1$.

In the following, we will focus on CDM perturbations and deal only with the function $\mu(k, a) = \mu(k)$ (although perturbations require two functions of time and scale to fully specify the model). In particular, we will test the following cases:

1. Scale independent μ with modified amplitude: $h_5 = h_3$ and $h_1 > 1$ or $h_1 < 1$.

2. Scale dependent μ with unity amplitude: $h_1 = 1$ and $h_5 > h_3$ or $h_5 < h_3$.
3. Scale dependent μ with modified amplitude: $h_1 \neq 1$ and $h_5 > h_3$ or $h_5 < h_3$.

In logarithmic space $\mu(k)$ is very close to a step function, as shown in figure ??, so that we will only use values for the h_i in which the difference of the minimum and the maximum is of the order of 15%, since otherwise we would impose a rather unrealistic structure formation.

2.1.4 Effective Field Theory of Dark Energy

- Another approach to construct a general model for dark energy based on the allowed symmetries in the action.
- Can be parametrized with the α functions.
- Allows in a simple way to create theories beyond Horndeski and to accommodate non-universal couplings.

2.2 Non-universal coupling

- Motivate dark energy, the coincidence problem and a dark sector interaction
- Explain why baryons should be uncoupled (Solar system constraints)

2.2.1 Coupled Dark Energy

- Introduce coupling at the energy momentum tensor
- Linear perturbations, gravitational bias DM-baryons, signatures in LSS, non-linear perturbations
- Talk about present constraints

2.2.2 Growing Neutrino Quintessence

- Motivate coupling to neutrinos (energy scale of DE and coincidence problem), particle physics seesaw mechanism perspective, non-relativistic neutrinos
- Background equations, linear perturbations and instabilities, failure of linear theory to take into account structures, lumps and backreaction
- Non-linear perturbations, simulations, neutrino lump dynamics, heating of neutrinos

2.2.3 Non-universal couplings in EFT

Paper by Gleyzes

Chapter 3

Statistics in Cosmology

3.1 Correlation functions and the power spectrum

- Gaussian random variables
- Statistical isotropy and homogeneity
- Correlation functions and power spectrum

3.2 Likelihood and the Bayesian approach

- Bayes Theorem
- Likelihood
- Priors, posteriors and evidence

3.3 Fisher Matrix formalism

- Approximation of the Gaussian likelihood at the minimum
- Ellipses and confidence contours
- Marginalization and maximization

3.4 The Fisher Matrix Code

- This serves as a manual for the Fisher Tools code.

3.4.1 Methodology of Fisher forecasts

- Derivatives of cosmological functions
- Integration or summation in k or ℓ space
- Alcock-Paczynski effect
- Redshift binning
- Shape, redshift and nuisance parameters
- Marginalization

3.4.1.1 The observed power spectrum

The observed power spectrum is built from the theoretical power spectrum $P(k, z)$ which depends on a vector of fundamental cosmological parameters θ_i and the following contributions:

1. The contribution from redshift space distortions and bias $b(z)$, known as the Kaiser formula, where $\beta(z) = f(z)/b(z)$ and $f(z)$ is the growth rate of density perturbations. Terms shown in green below.
2. The geometrical effect of the change of cosmological parameters (the so called Alcock-Paczynski-effect), where $H(z)$ is the hubble function and $D_A(z)$ is the angular diameter distance evaluated at a different set of cosmological parameters as $H_{fid}(z)$ and $D_A(z)_{fid}$ which are defined at the fiducial parameter values (the ratio $H_{fid}(z)/H(z)$ is clearly 1 if both are evaluated at the fiducial values). If this effect is taken fully into account, then k and μ also have to be affected by a geometrical term when evaluating the power spectrum at a different set of parameters. (see the AP-effect section 3.4.1.4 below). These terms are shown in red below.
3. The damping due to redshift errors σ_z and non-linear peculiar velocity dispersions $\sigma_v(z)$, which is the first order correction term to the Kaiser formula. Terms shown in magenta below.
4. Extra shot noise due to observational effects, which can be included in general with the term $P_s(z)$. Term in blue below.

$$P_{\text{obs}}(z, k, \mu; \theta) = P_s(z) + \frac{D_A^2(z)_{ref} H(z)}{D_A^2(z) H(z)_{ref}} b^2(z) (1 + \beta(z) \mu^2)^2 P(k, z) e^{-k^2 \mu^2 (\sigma_z^2 / H(z) + \sigma_v^2(z))} \quad (3.1)$$

If one wishes to place constraints on the normalization of the power spectrum, σ_8 , then $P(k, z)$ can be written as:

$$P(k, z) = \sigma_8^2 \tilde{P}(k, z) \quad (3.2)$$

where $\tilde{P}(k, z)$ is the normalized power spectrum. The normalization s_R of the power spectrum (which is equivalent to the variance smoothed over a scale R) is given by:

$$s_R = \frac{1}{2\pi^2} \int_{k_{min}}^{k_{max}} k^2 P(k, z=0) W_R^2(kR) \quad (3.3)$$

The window function smoothes $P(k, z)$ over the scale R and has the form: $W(x) = 3(\sin(x) - x \cos(x))/x^3$, where x is a dimensionless variable. This term comes from assuming spherical symmetry and performing the angle integration of the 3-D power spectrum $P(\vec{k})$. If one chooses $R = 8h^{-1}\text{Mpc}$ and $[k] = \text{h/Mpc}$, then we recover the usual $s_R = \sigma_8^2$. The normalization σ_8 is a quantity defined only in linear theory, which means that in eqn. 3.3 either $P(k, z)$ is linear or the integration limits are chosen in such a way that only the linear normalization is taken into account, so that usually one should take $k_{max} \approx 0.1$. The normalized power spectrum is simply:

$$\tilde{P}(k, z) = \frac{1}{s_R} P(k, z) \quad (3.4)$$

Due to the fact that σ_8 is a linear quantity, we can use it as an independent cosmological parameter, because we can rescale it arbitrarily before it is compared

with observations. It is then completely degenerate with the initial primordial amplitude of the power spectrum, \mathcal{A}_s , and one can replace one parameter by the other, fixing just one of both.¹

Furthermore if one wishes to express a linear power spectrum $P(k, z)$ in terms of the primordial power spectrum, the growth $G(z)$ and the transfer functions $T(k)$, one can write eqn. 3.2 as:

$$P(k, z) = \frac{\sigma_8^2}{s_R} G^2(z) T^2(k) k^{ns} \mathcal{A}_s \quad (3.5)$$

being careful to take either σ_8 or \mathcal{A}_s as a primordial parameter and not both. In the case in which \mathcal{A}_s is the cosmological parameter, the ratio $\frac{\sigma_8^2}{s_R}$ should be 1. The growth function $G(z)$ depends on the cosmological parameters θ_i and is defined to be normalized to unity today: $G(z = 0) = 1$. The quantity $\sigma_8^2 G^2(z) \equiv \sigma_8(z)$ can be defined accordingly and can be used as an independent and time-dependent cosmological parameter too.

3.4.1.2 Derivatives of the observed power spectrum

For the calculation of the Fisher matrix, one needs to take derivatives of the logarithm of the observed power spectrum $P_{\text{obs}}(k, z, \mu)$ at the central value \bar{z} of each redshift bin. (see equation for the Fisher matrix). There are two options here in terms of the practical and numerical approach:

- One calculates numerically:

$$\left. \frac{d \ln P_{\text{obs}}(\bar{z}, k, \mu; \theta_i)}{d \theta_i} \right|_{fid} = \frac{P_{\text{obs}}(\bar{z}, k, \mu; \theta_i^+) - P_{\text{obs}}(\bar{z}, k, \mu; \theta_i^-)}{2\varepsilon \theta_i^{fid} \times P_{\text{obs}}(\bar{z}, k, \mu; \theta_i^{fid})} \quad (3.6)$$

where θ_i^+ , θ_i^- represent the parameter θ_i evaluated at $\pm\varepsilon$ around the fiducial value θ_i^{fid} :

$$\theta_i^\pm = \theta_i^{fid} (1 \pm \varepsilon) \quad (3.7)$$

However this assumes that all functions inside $P_{\text{obs}}(\bar{z}, k, \mu; \theta_i)$ can be evaluated at θ_i^\pm . Since this is not the case for the bias $b(z)$, one needs to add a further intermediate variable (see section 3.4.2 below on marginalization).

¹One has to emphasize that this can only be done for linear power spectra, because if one takes nonlinear density fluctuations into account for calculating a non-linear $P(k, z)$, a different primordial amplitude of fluctuations has a non-linear effect at small scales in the so called “non-linear bump”. The degeneracy between \mathcal{A}_s and σ_8 is then broken.

- One uses intermediate variables, namely the functions in eqn. 3.1, which depend on θ_i , and with the help of the chain rule one can write:

$$\begin{aligned} \left. \frac{d \ln P_{obs}(\bar{z}, k, \mu; \theta_i)}{d \theta_i} \right|_{fid} &= \frac{\partial \ln P_{obs}(\bar{z}, k, \mu; \theta_i)}{\partial \ln P_s(\bar{z})} \frac{\partial \ln P_s(\bar{z})}{\partial \theta_i} + \frac{\partial \ln P_{obs}(\bar{z}, k, \mu; \theta_i)}{\partial \ln f(\bar{z})} \frac{\partial \ln f(\bar{z})}{\partial \theta_i} \\ &+ \frac{\partial \ln P_{obs}(\bar{z}, k, \mu; \theta_i)}{\partial \ln H(\bar{z})} \frac{\partial \ln H(\bar{z})}{\partial \theta_i} + \frac{\partial \ln P_{obs}(\bar{z}, k, \mu; \theta_i)}{\partial \ln D_A(\bar{z})} \frac{\partial \ln D_A(\bar{z})}{\partial \theta_i} \\ &+ \frac{\partial \ln P_{obs}(\bar{z}, k, \mu; \theta_i)}{\partial \ln P(k, \bar{z})} \frac{\partial \ln P(k, \bar{z})}{\partial \theta_i} + \frac{\partial \ln P_{obs}(\bar{z}, k, \mu; \theta_i)}{\partial \ln b(\bar{z})} \frac{\partial \ln b(\bar{z})}{\partial \theta_i} \\ &+ \frac{\partial \ln P_{obs}(\bar{z}, k, \mu; \theta_i)}{\partial k} \frac{\partial k}{\partial \theta_i} + \frac{\partial \ln P_{obs}(\bar{z}, k, \mu; \theta_i)}{\partial \mu} \frac{\partial \mu}{\partial \theta_i} \end{aligned} \quad (3.8)$$

where we have ignored the dependence on the damping terms of eqn. 3.1 for simplicity. The last two terms are non-vanishing if one takes the Alcock-Paczynski effect into account for k and μ , since they are affected by geometrical terms also (see AP-effect section 3.4.1.4 below).

One then has to calculate the intermediate derivatives of $\ln P_{obs}(z, k, \mu; \theta_i)$ with respect to P_s , D_A , H , f and b using eqn. 3.1. The logarithm of these quantities is used, because it simplifies considerably the equations. Notice that the growth $G(z)$ is inside the definition of $P(k, z)$ so it is not needed as an intermediate variable, however it can be also used if wanted. It is important to stress here that the derivatives are calculated at the *fiducial* value of the parameters, including the fiducial values of the cosmological functions. The fiducial value of the shot noise is zero, $P_s^{fid}(z) = 0$. And under this choice the derivatives are:

$$\frac{\partial \ln P_{obs}(\bar{z}, k, \mu; \theta_i)}{\partial \ln P_s(\bar{z})} = \frac{1}{P_{obs}(\bar{z}, k, \mu; \theta_i)} \quad (3.9a)$$

$$\frac{\partial \ln P_{obs}(\bar{z}, k, \mu; \theta_i)}{\partial \ln f(\bar{z})} = \frac{2\beta(\bar{z})\mu^2}{1 + \beta(\bar{z})\mu^2} \quad (3.9b)$$

$$\frac{\partial \ln P_{obs}(\bar{z}, k, \mu; \theta_i)}{\partial \ln b(\bar{z})} = \frac{2}{1 + \beta(\bar{z})\mu^2} \quad (3.9c)$$

$$\frac{\partial \ln P_{obs}(\bar{z}, k, \mu; \theta_i)}{\partial \ln H(\bar{z})} = 1 \quad (3.9d)$$

$$\frac{\partial \ln P_{obs}(\bar{z}, k, \mu; \theta_i)}{\partial \ln D_A(\bar{z})} = -2 \quad (3.9e)$$

$$\frac{\partial \ln P_{obs}(\bar{z}, k, \mu; \theta_i)}{\partial \ln P(k, \bar{z})} = 1 \quad (3.9f)$$

If for the moment and for simplicity we neglect the extra shot noise contribution P_s and the dependence of k and μ on the change of cosmological parameters (see AP-effect section below) we get for each derivative of $P_{obs}(k, \mu, z)$ with respect to a cosmological parameter θ_i :

$$\begin{aligned} \frac{d \ln P_{\text{obs}}(\bar{z}, k, \mu; \theta_i)}{d \theta_i} \Big|_{\text{fid}} &= \frac{\partial \ln P(k, \bar{z})}{\partial \theta_i} + \frac{\partial \ln H(\bar{z})}{\partial \theta_i} - 2 \frac{\partial \ln D_A(\bar{z})}{\partial \theta_i} \\ &+ \frac{2\beta(\bar{z})\mu^2}{1 + \beta(\bar{z})\mu^2} \frac{\partial \ln f(\bar{z})}{\partial \theta_i} + \frac{2}{1 + \beta(\bar{z})\mu^2} \frac{\partial \ln b(\bar{z})}{\partial \theta_i} \end{aligned} \quad (3.10)$$

We see that by using intermediate variables, the space of parameters to be evaluated for the Fisher matrix has been extended by 4 new terms (they could be more if P_{obs} depends on further cosmological functions):

$$\zeta = \left\{ 1, 1, -2, \frac{2\beta(\bar{z})\mu^2}{1 + \beta(\bar{z})\mu^2}, \frac{2}{1 + \beta(\bar{z})\mu^2} \right\} \quad (3.11)$$

The new “vector” of derivatives has the form:

$$\Theta = \left\{ \frac{\partial \ln P(k, \bar{z})}{\partial \theta_i}, 1, -2, \frac{2\beta(\bar{z})\mu^2}{1 + \beta(\bar{z})\mu^2}, \frac{2}{1 + \beta(\bar{z})\mu^2} \right\} \quad (3.12)$$

notice that θ_i is a vector also, so that this vector has a number of components equal to: $\dim(\Theta) = \dim(\theta) + 4$.

Since the Fisher matrix is a tensor product of a vector of derivatives, we can express it as:

$$F_{ij} \approx \frac{d \ln P_{\text{obs}}}{d \theta_i} \frac{d \ln P_{\text{obs}}}{d \theta_j} \approx (\Theta \otimes \Theta)_{ij} \quad (3.13)$$

However this is only valid at one single redshift bin and if one wants to add together Fisher matrices at different redshift bins, one has to take into account that each $D_A(\bar{z}_i)$, $H(\bar{z}_i)$, $f(\bar{z}_i)$ and $b(\bar{z}_i)$ is an independent parameter but we will come to that later.

3.4.1.3 Projecting back to the fundamental cosmological parameters

If one wishes to express the Fisher matrix just in terms of fundamental cosmological parameters again, then one needs to perform the variable transformation back using a so-called Jacobian. This can be seen more clearly if one expresses eqns. 3.8, 3.9 and 3.10 as:

$$\frac{d \ln P_{\text{obs}}(\mathbf{T}(\boldsymbol{\theta}))}{d \theta_i} = \frac{\partial \ln P_{\text{obs}}}{\partial \mathbf{T}_j} \frac{\partial \mathbf{T}_j}{\partial \theta_i} \quad (3.14)$$

where $\mathbf{T}_i = \{\ln P, \ln H, \ln D_A, \ln f, \ln b\}$ and $\partial P_{\text{obs}}/\partial \mathbf{T}_i = \zeta$ from eqn. 3.11. The Jacobian is then simply:

$$J = \frac{\partial \mathbf{T}_j}{\partial \theta_i} \quad (3.15)$$

The Fisher matrix

$$\tilde{F}_{ab} \approx (\zeta \otimes \zeta)_{ab} \approx \frac{\partial \ln P_{\text{obs}}}{\partial \mathbf{T}_a} \frac{\partial \ln P_{\text{obs}}}{\partial \mathbf{T}_b} \quad (3.16)$$

formed in the intermediate variables \mathbf{T} can be transformed to the usual one F by calculating:

$$F_{ab} \approx \frac{d \ln P_{obs}}{d\theta_a} \frac{d \ln P_{obs}}{d\theta_b} \approx \frac{\partial \ln P_{obs}}{\partial \mathbf{T}_j} \frac{\partial \mathbf{T}_j}{\partial \theta_a} \frac{\partial \ln P_{obs}}{\partial \mathbf{T}_j} \frac{\partial \mathbf{T}_j}{\partial \theta_b} = J^T \tilde{F} J \quad (3.17)$$

In the praxis however, for calculating the full Fisher matrix, one interchanges the first element of ζ by the first element $\partial F_1 / \partial \theta_i$ (corresponding to the derivatives of the power spectrum $P(k, z)$) since one needs to integrate values in k and z . That is why one uses the vector Θ from eqn. 3.12. In this case the Jacobian and the \tilde{F} do not look like the ones presented above. This is however, mathematically equivalent at this point.

3.4.1.4 The Alcock-Paczynski-Effect

The Alcock-Paczynski-effect (AP) reiles on the fact that the scales k and the direction cosines μ are changed by geometrical factors of distance, when the cosmological parameters are changed. This means that k and μ depend on $H(z)$ and $D_A(z)$ and therefore are also indirectly functions of the cosmological parameters θ_i . The AP formulas relating the fiducial values of k_{fid} and μ_{fid} to their transformed values are:

$$k_{AP} = R_{AP}(\mu; \theta) k_{fid} \quad (3.18)$$

$$\mu_{AP} = \frac{H(z; \theta)}{H(z; \theta_{fid})} \frac{\mu_{fid}}{R_{AP}(\mu; \theta)} \quad (3.19)$$

where the geometrical function R_{AP} is defined as:

$$R_{AP}(\mu; \theta) = \sqrt{\frac{[D_A(z; \theta) H(z; \theta) \mu_{fid}]^2 - [(D_A(z; \theta_{fid}) H(z; \theta_{fid})]^2 (\mu_{fid} - 1)}{[D_A(z; \theta) H(z; \theta_{fid})]^2}} \quad (3.20)$$

The last two terms of eqn. 3.8 come from the fact that now $k = k(H(z; \theta), D_A(z; \theta))$ and $\mu = \mu(H(z; \theta), D_A(z; \theta))$, so that one has to use the chain rule for the derivative of $P_{obs}(k, \mu, z; \theta)$:

$$\begin{aligned} \frac{\partial \ln P_{obs}(\bar{z}, k, \mu; H(z); \theta_i)}{\partial \ln H(z)} &= \frac{\partial \ln P_{obs}(\bar{z}, k, \mu; \theta_i)}{\partial \ln H(z)} \\ &+ \frac{\partial \ln P_{obs}(\bar{z}, k, \mu; \theta_i)}{\partial \mu} \frac{\partial \mu}{\partial \ln H(z)} + \frac{\partial \ln P_{obs}(\bar{z}, k, \mu; \theta_i)}{\partial k} \frac{\partial k}{\partial \ln H(z)} \end{aligned} \quad (3.21)$$

and similarly for the dependence on $D_A(z)$.

Now we can write down explicitly the intermediate derivatives (evaluated at the fiducial value as usual):

$$\frac{\partial \ln P_{obs}(\bar{z}, k, \mu; \theta_i)}{\partial k} = \frac{\partial \ln P(\bar{z}, k; \theta_i)}{\partial k} \quad (3.22)$$

$$\frac{\partial \ln P_{obs}(\bar{z}, k, \mu; \theta_i)}{\partial \mu} = \frac{4\beta(z)\mu}{1 + \beta(z)\mu^2} \quad (3.23)$$

and the derivatives of k and μ with respect to $\ln D_A$ and $\ln H$ are:

$$\frac{\partial \mu}{\partial \ln D_A(z)} = -\mu(\mu^2 - 1) \quad (3.24a)$$

$$\frac{\partial \mu}{\partial \ln H(z)} = -\mu(\mu^2 - 1) \quad (3.24b)$$

$$\frac{\partial k}{\partial \ln D_A(z)} = k(\mu^2 - 1) \quad (3.24c)$$

$$\frac{\partial k}{\partial \ln H(z)} = k\mu^2 \quad (3.24d)$$

The interesting thing about eqns.3.24 is that one can see that when evaluating the derivative of P_{obs} w.r.t a cosmological parameter, the scales k and the direction cosine angles μ get mixed, giving a very powerful probe of cosmology. Using this, the vectors that form the Fisher matrix (either ζ or Θ , depending on the choice) have to be extended in their indices corresponding to $\ln D_A$ and $\ln H$. So that they are now more complicated:

$$\Theta = \left\{ \frac{\partial \ln P(k, \bar{z})}{\partial \theta_i}, 1 + \frac{4\beta(z)\mu}{1 + \beta(z)\mu^2}(-\mu(\mu^2 - 1)) + \frac{\partial \ln P(\bar{z}, k; \theta_i)}{\partial k}k\mu^2, \right. \\ \left. -2 + \frac{4\beta(z)\mu}{1 + \beta(z)\mu^2}(-\mu(\mu^2 - 1)) + \frac{\partial \ln P(\bar{z}, k; \theta_i)}{\partial k}k(\mu^2 - 1), \frac{2\beta(\bar{z})\mu^2}{1 + \beta(\bar{z})\mu^2}, \frac{2}{1 + \beta(\bar{z})\mu^2} \right\} \quad (3.25)$$

However, using the procedure described above, one can see that the Fisher matrix will have the same dimensions and that the Jacobian will be the same as in eqn. 3.15.

3.4.2 Marginalization

When using the form of the observed power spectrum presented before, it is not always possible to “project back” the matrix \tilde{F} into the matrix F which contains only fundamental cosmological parameters. This is the case for the bias or the extra shot noise, since there we do not know how the derivatives $\partial \ln b(z)/\partial \theta_i$ or $\partial P_s(z)/\partial \theta_i$ look like, since those are observational and/or phenomenological quantities which do not yet have a model in terms of fundamental cosmological parameters. Therefore, these terms will always remain and cannot be expressed as a function of cosmological parameters and have to be either fixed or marginalized over. In terms of the Fisher matrix F_{ij} , the marginalization is performed easily by removing from the inverse F_{ij}^{-1} all rows and columns corresponding to the index of the quantity to marginalize. More about this will be explained later on.

3.4.3 Validation of the code within the Euclid collaboration

- 4 Steps: from the basics to the more complicated
- Shape parameters, z-observables and non-diagonal terms
- WL: Cases

3.4.4 Extensions of the Fisher matrix approach to higher orders

- Taylor expansion of the Fisher matrix
- Fisher tensors
- Variations in parameter space

Chapter 4

Linear and non-linear Modified Gravity forecasts

4.1 Introduction

Future large scale structure surveys will be able to measure with percent precision the parameters governing the evolution of matter perturbations. While we have the tools to investigate the standard model, the next challenge is to be able to compare those data with cosmologies that go beyond General Relativity, in order to test whether a fluid component like Dark Energy or similarly a Modified Gravity scenario can better fit the data. On the theoretical side, while many Modified Gravity models are still allowed by type Ia supernova (SNIa) and Cosmic Microwave Background (CMB) data Planck Collaboration, Ade, and others, 2016; structure formation can help us to distinguish among them and the standard scenario, thanks to their signatures on the matter power spectrum, in the linear and mildly non-linear regimes (for some examples of forecasts, see Amendola and others, 2013; Casas et al., 2015; Bielefeld, Huterer, and Linder, 2014).

The evolution of matter perturbations can be fully described by two generic functions of time and space Kunz, 2012; Amendola et al., 2013, which can be measured via Galaxy Clustering and Weak Lensing surveys. In this work we want to forecast how well we can measure those functions, in different redshift bins.

While any two independent functions of the gravitational potentials would do, we follow the notation of Planck Collaboration, Ade, and others, 2016 and consider μ and η : the first modifies the Poisson equation for Ψ while the second is equal to the ratio of the gravitational potentials (and is therefore also a direct observable Amendola et al., 2013). We will consider forecasts for the planned surveys Euclid, SKA1 and SKA2 and a subset of DESI, DESI-ELG, using as priors the constraints from recent *Planck* data (see also Alonso et al., 2016; Hojjati et al., 2012; Baker and Bull, 2015; Bull, 2015; Gleyzes et al., 2016 for previous works that address forecasts in Modified Gravity).

In section 4.2 we define μ and η and parameterize them in three different ways. First, in a general manner, we let these functions vary freely in different redshift bins. Complementarily, we also consider two specific parameterizations of the time evolution proposed in Planck Collaboration, Ade, and others, 2016. Here, we also specify the fiducial values of our cosmology for each of the parameterizations considered. Section 4.3 discusses our treatment for the linear and mildly non-linear regime. Linear spectra are obtained from a modified Boltzmann code Hojjati, Pogosian, and Zhao, 2011; the mild non-linear regime (up to $k \sim 0.5 h/\text{Mpc}$) compares two methods to emulate the non-linear power spectrum: the commonly used Halofit Smith et al., 2003; Takahashi et al., 2012, and a semi-analytic prescription to

model the screening mechanisms present in Modified Gravity models Hu and Sawicki, 2007. In section 5.7 we explain the method used to produce the Fisher forecasts both for Weak Lensing and Galaxy Clustering. We explain how we compute and add the CMB *Planck* priors to our Fisher matrices. Section 4.5 discusses the results obtained for the redshift binned parameterization both for Galaxy Clustering and for Weak Lensing in the linear and non-linear cases. We describe our method to decorrelate the errors in section 4.5.4. The results for the other two time parameterizations are instead discussed in sections 4.6.1 and 4.6.2, both for Weak Lensing and Galaxy Clustering in the linear and mildly non-linear regimes. To test the effect of our non-linear prescription, we show in section 4.6.3 the impact of different choices of the non-linear prescription parameters on the cosmological parameter estimation.

4.2 Parameterizing Modified Gravity

In linear perturbation theory, scalar, vector and tensor perturbations do not mix, which allows us to consider only the scalar perturbations in this paper. We work in the conformal Newtonian gauge, with the line element given by

$$ds^2 = -(1 + 2\Psi)dt^2 + a^2(1 - 2\Phi)dx^2 . \quad (4.1)$$

Here Φ and Ψ are two functions of time and scale that coincide with the gauge-invariant Bardeen potentials in the Newtonian gauge.

In theories with extra degrees of freedom (Dark Energy, DE) or modifications of General Relativity (MG) the normal linear perturbation equations are no longer valid, so that for a given matter source the values of Φ and Ψ will differ from their usual values. We can parameterize this change generally with the help of two new functions that encode the modifications. Many different choices are possible and have been adopted in the literature, see e.g. Planck Collaboration, Ade, and others, 2016 for a limited overview. In this paper we introduce the two functions through a gravitational slip (leading to $\Phi \neq \Psi$ also at linear order and for pure cold dark matter) and as a modification of the Poisson equation for Ψ ,

$$-k^2\Psi(a, k) \equiv 4\pi Ga^2\mu(a, k)\rho(a)\delta(a, k) ; \quad (4.2)$$

$$\eta(a, k) \equiv \Phi(a, k)/\Psi(a, k) . \quad (4.3)$$

These expressions define μ and η . Here $\rho(a)$ is the average dark matter density and $\delta(a, k)$ the comoving matter density contrast – we will neglect relativistic particles and radiation as we are only interested in modeling the perturbation behaviour at late times. In that situation, η , which is effectively an observable Amendola et al., 2013, is closely related to modifications of GR Saltas et al., 2014; Sawicki et al., 2016, while μ encodes for example deviations in gravitational clustering, especially in redshift-space distortions as non-relativistic particles are accelerated by the gradient of Ψ .

When considering Weak Lensing observations then it is also natural to parameterize deviations in the lensing or Weyl potential $\Phi + \Psi$, since it is this combination that affects null-geodesics (relativistic particles). To this end we introduce a function $\Sigma(t, k)$ so that

$$-k^2(\Phi(a, k) + \Psi(a, k)) \equiv 8\pi Ga^2\Sigma(a, k)\rho(a)\delta(a, k) . \quad (4.4)$$

Since metric perturbations are fully specified by two functions of time and scale, Σ is not independent from μ and η , and can be obtained from the latter as follows:

$$\Sigma(a, k) = (\mu(a, k)/2)(1 + \eta(a, k)) . \quad (4.5)$$

Throughout this work, we will denote the standard Lambda-Cold-Dark-Matter (Λ CDM) model, defined through the Einstein-Hilbert action with a cosmological constant, simply as GR. For this case we have that $\mu = \eta = \Sigma = 1$. All other cases in which these functions are not unity will be labeled as Modified Gravity (MG) models.

Using effective quantities like μ and η has the advantage that they are able to model *any* deviations of the perturbation behaviour from Λ CDM expectations, they are relatively close to observations, and they can also be related to other commonly used parameterization Pogosian et al., 2010 On the other hand, they are not easy to map to an action (as opposed to approaches like effective field theories that are based on an explicit action) and in addition they contain so much freedom that we normally restrict their parameterisation to a subset of possible functions.

This has however the disadvantage of loosing generality and making our constraints on μ and η parameterization-dependent. In this paper, we prefer to complement specific choices of parameterizations adopted in the literature (we will use the choice made in Planck Collaboration, Ade, and others, 2016) with a more general approach: we will bin the functions $\mu(a)$ and $\eta(a)$ in redshift bins with index i and we will treat each μ_i and η_i as independent parameters in our forecast; we will then apply a variation of Principal Component Analysis (PCA), called Zero-phase Component Analysis (ZCA). This approach has been taken previously in the literature by Hojjati et al., 2012, where they bin μ and η in several redshift and k -scale bins together with a binning of $w(z)$ and cross correlate large scale structure observations with CMB temperature, E-modes and polarization data together with Integrated Sachs-Wolfe (ISW) observations to forecast the sensitivity of future surveys to modifications in μ and η . In the present work, we will neglect a possible k -dependence, we will focus on Galaxy Clustering (GC) and weak lensing (WL) surveys and we will show that there are important differences between the linear and non-linear cases; including the non-linear regime generally reduces correlations among the cosmological parameters. In the remainder of this section we will introduce the parameterizations that we will use.

4.2.1 Parameterizing gravitational potentials in discrete redshift bins

As a first approach we neglect scale dependence and bin the time evolution of the functions μ and η without specifying any parameterized evolution. To this purpose we divide the redshift range $0 \leq z \leq 3$ in 6 redshift bins and we consider the values $\mu(z_i)$ and $\eta(z_i)$ at the right limiting redshift z_i of each bin as free parameters, thus with the i index spanning the values $\{0.5, 1.0, 1.5, 2.0, 2.5, 3.0\}$. The first bin is assumed to have a constant value, coinciding with the one at $z_1 = 0.5$, i.e. $\mu(z < 0.5) = \mu(z_1)$ and $\eta(z < 0.5) = \eta(z_1)$. The $\mu(z)$ function (and analogously $\eta(z)$) is then reconstructed as

$$\mu(z) = \mu(z_1) + \sum_{i=1}^{N-1} \frac{\mu(z_{i+1}) - \mu(z_i)}{2} \left[1 + \tanh \left(s \frac{z - z_{i+1}}{z_{i+1} - z_i} \right) \right], \quad (4.6)$$

where $s = 10$ is a smoothing parameter and N is the number of binned values. We assume that both μ and η reach the GR limit at high redshifts: to realize this, the last $\mu(z_6)$ and $\eta(z_6)$ values assume the standard Λ CDM value $\mu = \eta = 1$ and both functions are kept constant at higher redshifts $z > 3$.

Similarly, the derivatives of these functions are obtained by computing

$$\mu'(\bar{z}_j) = \frac{\mu(z_{i+1}) - \mu(z_i)}{z_{i+1} - z_i}, \quad (4.7)$$

with $\bar{z}_j = (z_{i+1} + z_i)/2$, using the same $\tanh(x)$ smoothing function:

$$\frac{d\mu(z)}{dz} = \mu'(\bar{z}_1) + \sum_{j=1}^{N-2} \frac{\mu'(\bar{z}_{j+1}) - \mu'(\bar{z}_j)}{2} \left[1 + \tanh \left(s \frac{z - \bar{z}_{j+1}}{\bar{z}_{j+1} - \bar{z}_j} \right) \right]. \quad (4.8)$$

In particular we assume $\mu' = \eta' = 0$ for $z < 0.5$ and for $z > 3$. We set the first five amplitudes of μ_i and η_i as free parameters, thus the set we consider is: $\theta = \{\Omega_m, \Omega_b, h, \ln 10^{10} A_s, n_s, \{\mu_i\}, \{\eta_i\}\}$, with i an index going from 1 to 5. We take as fiducial cosmology the values shown in Tab. 4.1 columns 5 and 6. We only modify the evolution of perturbations and assume that the background expansion is well described by the standard Λ CDM expansion law for a flat universe with given values of Ω_m , Ω_b and h .

4.2.2 Parameterizing gravitational potentials with simple smooth functions of the scale factor

As an alternative approach, we assume simple specific, time parameterizations for the μ and η MG functions, adopting the ones used in the *Planck* analysis Planck Collaboration, Ade, and others, 2016. We neglect here as well any scale dependence:

- a parameterization in which the time evolution is related to the dark energy density fraction, to which we refer as ‘late-time’ parameterization:

$$\mu(a, k) \equiv 1 + E_{11} \Omega_{\text{DE}}(a) , \quad (4.9)$$

$$\eta(a, k) \equiv 1 + E_{22} \Omega_{\text{DE}}(a) ; \quad (4.10)$$

- a parameterization in which the time evolution is the simplest first order Taylor expansion of a general function of the scale factor a (and closely resembles the $w_0 - w_a$ parametrization for the equation of state of DE), referred to as ‘early-time’ parameterization, because it allows departures from GR also at high redshifts¹:

$$\mu(a, k) \equiv 1 + E_{11} + E_{12}(1 - a) , \quad (4.11)$$

$$\eta(a, k) \equiv 1 + E_{21} + E_{22}(1 - a) . \quad (4.12)$$

The late-time parameterization is forced to behave as GR ($\mu = \eta = 1$) at high redshift when $\Omega_{\text{DE}}(a)$ becomes negligible; the early time one allows more freedom as the amplitude of the deviations from GR do not necessarily reduce to zero at high redshifts. Both parameterizations have been used in Planck Collaboration, Ade, and others, 2016. In Bull, 2015; Gleyzes et al., 2016; Alonso et al., 2016 the

¹Notice that our early-time parametrization is called ‘time-related’ in Planck Collaboration, Ade, and others, 2016.

authors used a similar time parameterization in which the Modified Gravity parameters depend on the time evolution of the dark energy fraction. In Bull, 2015 an extra parameter accounts for a scale-dependent μ : their treatment keeps η (called γ in their paper) fixed and equal to 1; it uses linear power spectra up to $k_{\max}(z)$ with $k_{\max}(z=0) = 0.14/\text{Mpc} \approx 0.2 \text{ h/Mpc}$. In Gleyzes et al., 2016 the authors also use a combination of Galaxy Clustering, Weak Lensing and ISW cross-correlation to constrain Modified Gravity in the Effective Field Theory formalism Gubitosi, Piazza, and Vernizzi, 2013. In Bellini et al., 2016 and Alonso et al., 2016 a similar parameterization was used to constrain the Horndeski functions Bellini and Sawicki, 2014 with present data and future forecasts respectively, in the linear regime.

For the late-time parameterization, the set of free parameters we consider is: $\theta = \{\Omega_m, \Omega_b, h, \ln 10^{10} A_s, n_s, E_{11}, E_{22}\}$, where E_{11} and E_{22} determine the amplitude of the variation with respect to ΛCDM . As fiducial cosmology we use the values shown in Table 4.1, columns 1 and 2, i.e. the marginalized parameter values obtained fitting these models with recent *Planck* data; notice that these results differ slightly from the *Planck* analysis in Planck Collaboration, Ade, and others, 2016 for the same parameterization, because we don't consider here the effect of massive neutrinos.

For the early time parameterization we have E_{11} and E_{21} which determine the amplitude of the deviation from GR at present time ($a = 0$) and 2 additional parameters (E_{12}, E_{22}), which determine the time dependence of the $\mu(a)$ and $\eta(a)$ functions for earlier times. The fiducial values for this model, obtained from the *Planck*+BSH best fit is given in columns 3 and 4 of Table 4.1.

FIGURE 4.1: The Modified Gravity functions μ and η as a function of redshift z for each of the models considered in this work, evaluated at the fiducials specified in Table 4.1. In light long-dashed blue lines, the ‘redshift binned model’ (Eqns. 4.6-4.8). In short-dashed red lines the late-time parameterization (Eqns. 4.9-4.10) and in green solid lines the early-time parameterization (Eqns. 4.11-4.12). Finally the medium-dashed orange line represents the standard ΛCDM model (GR) for reference.

4.3 The power spectrum in Modified Gravity

4.3.1 The linear power spectrum

In this work we will use linear power spectra calculated with MGMCAMB Zhao et al., 2009; Hojjati, Pogosian, and Zhao, 2011, a modified version of the Boltzmann code CAMB Lewis, Challinor, and Lasenby, 2000. We do so, as MGMCAMB offers the possibility to input directly any parameterization of μ and η without requiring further assumptions: MGMCAMB uses our Eqns. (4.2) and (4.3) in the Einstein-Boltzmann system of equations, providing the modified evolution of matter perturbations, corresponding to our choice of the gravitational potential functions. Non-relativistic particles like cold dark matter are accelerated by the gradient of Ψ , so that especially the redshift space distortions are sensitive to the modification given by $\mu(a, k)$. For relativistic particles like photons and neutrinos on the other hand, the combination of $\Phi + \Psi$ (and therefore Σ) enters the equations of motion. The impact on the matter power spectrum is more complicated, as the dark matter

Late time		Early time		Redshift Binned	
Parameter	Fiducial	Parameter	Fiducial	Parameter	Fiducial
Ω_c	0.254	Ω_c	0.256	Ω_c	0.254
Ω_b	0.048	Ω_b	0.048	Ω_b	0.048
n_s	0.969	n_s	0.969	n_s	0.969
$\ln 10^{10} A_s$	3.063	$\ln 10^{10} A_s$	3.091	$\ln 10^{10} A_s$	3.057
h	0.682	h	0.682	h	0.682
E_{11}	0.100	E_{11}	-0.098	μ_1	1.108
E_{22}	0.829	E_{12}	0.096	μ_2	1.027
		E_{21}	0.940	μ_3	0.973
		E_{22}	-0.894	μ_4	0.952
				μ_5	0.962
				η_1	1.135
				η_2	1.160
				η_3	1.219
				η_4	1.226
				η_5	1.164

TABLE 4.1: Fiducial values for the Modified Gravity parameterizations and the redshift-binned model of μ and η used in this work. The DE related parameterization contains two extra parameters E_{11} and E_{22} with respect to GR; the early-time parametrization depends on 4 extra parameters E_{11} , E_{12} , E_{22} and E_{21} with respect to GR; the redshift-binned model contains 10 extra parameters, corresponding to the amplitudes μ_i and η_i in five redshift bins. In this work we will use alternatively and for simplicity the notation $\ell\mathcal{A}_s \equiv \ln(10^{10} A_s)$. The fiducial values are obtained performing a Monte Carlo analysis of *Planck+BAO+SNe+H₀* (BSH) data Planck Collaboration, Ade, and others, 2016.

density contrast is linked via the relativistic Poisson equation to Φ . In addition, an early-time modification of Φ and Ψ can also affect the baryon distribution through their coupling to radiation during that period. As already mentioned above, we will not consider the k -dependence of μ and η in this work and our modifications with respect to standard GR will be only functions of the scale factor a .

4.3.2 Non-linear power spectra

As the Universe evolves, matter density fluctuations (δ_m) on small scales ($k > 0.1$ h/Mpc) become larger than unity and shell-crossing will eventually occur. The usual continuity and Euler equations, together with the Poisson equation become singular Bernardeau et al., 2001; Bernardeau, 2013, therefore making a computation of the matter power spectrum in the highly non-linear regime practically impossible under the standard perturbation theory approach. However, at intermediate scales of around $k \approx 0.1 - 0.2$ h/Mpc, there is the possibility of calculating semi-analytically the effects of non-linearities on the oscillation patterns of the baryon acoustic oscillations (BAO). There are many approaches in this direction, from renormalized perturbation theories Crocce and Scoccimarro, 2006b; Blas et al., 2016; Taruya and Hiramatsu, 2008 to time flow equations Pietroni, 2008; Anselmi and Pietroni, 2012, effective or coarse grained theories Carrasco, Hertzberg, and Senatore, 2012; Baumann et al., 2012; Pietroni et al., 2011; Manzotti et al., 2014 and many others. This direction of research is important, since from the amplitude and

widths of the first few BAO peaks, one can extract more information from data and break degeneracies among parameters, especially in Modified Gravity.

Computing the non-linear power spectrum in standard GR is still an open question, and even more so when the Poisson equations are modified, as it is in the case in Modified Gravity theories. A solution to this problem is to calculate the evolution of matter perturbations in an N-body simulation Springel, 2005; Fosalba et al., 2013; Takahashi et al., 2012; Lawrence et al., 2010; Heitmann et al., 2014, however, this procedure is time-consuming and computationally expensive.

Because of these issues, several previous analyses have been done with a conservative removal of the information at small scales (see for example the *Planck* Dark Energy paper Planck Collaboration, Ade, and others, 2016, several CFHTLenS analysis Heymans and others, 2013; Kitching and others, 2014 or the previous PCA analysis by Hojjati et al., 2012). However, future surveys will probe an extended range of scales, therefore removing non-linear scales from the analysis would strongly reduce the constraining power of these surveys. Moreover, at small scales we also expect to find means of discriminating between different Modified Gravity models, such as the onset of screening mechanisms needed to recover GR at small scales where experiments strongly constrain deviations from it. For these reasons it is crucial to find methods which will allow us to investigate, at least approximately, the non-linear power spectrum.

Attempts to model the non-linear power spectrum semi-analytically in Modified Gravity have been investigated for f(R) theories in Zhao, 2014; Taruya et al., 2014, for coupled dark energy in Casas et al., 2015; Saracco et al., 2010; Vollmer, Amendola, and Catena, 2014 and for growing neutrino models in Brouzakis et al., 2011. Typically they rely on non-linear expansions of the perturbations using resummation techniques based on Pietroni, 2008; Taruya and Hiramatsu, 2008 or on fitting formulae based on N-Body simulations Casas et al., 2015; Takahashi et al., 2012; Bird, Viel, and Haehnelt, 2011. A similar analysis is not available for the model-independent approach considered in this paper. In order to give at least a qualitative estimate of what the importance of non-linearities would be for constraining these Modified Gravity models, we will adopt in the rest of the paper a method which interpolates between the standard approach to non linear scales in GR and the same applied to MG theories.

4.3.2.1 Halofit

We describe here the effect of applying the standard approach to non linearities to MG theories. This is done using the revised Halofit Takahashi et al., 2012, based on Smith et al., 2003, which is a fitting function of tens of numerical parameters that reproduces the output of a certain set of Λ CDM N-body simulations in a specific range in parameter space as a function of the linear power spectrum. This fitting function is reliable with an accuracy of better than 10% at scales larger than $k \lesssim 1\text{h/Mpc}$ and redshifts in between $0 \leq z \leq 10$ (see Takahashi et al., 2012 for more details). This fitting function can be used within Boltzmann codes to estimate the non-linear contribution which corrects the linear power spectrum as a function of scale and time. We will use the Halofit fitting function as a way of approximating the non-linear power spectrum in our models even though it is really only valid for Λ CDM. In Fig. 4.2, the left panel shows a comparison between the linear and non-linear power spectra calculated by MGCAMB in two different models, our fiducial late-time model (as from Table 4.1) and GR, both sharing the same Λ CDM

parameters. At small length scales (large k), the non-linear deviation is clearly visible at scales $k \gtrsim 0.3 \text{ h/Mpc}$ and both MG and GR seem to overlap due to the logarithmic scale used. In the right panel, we can see the ratio between MG and GR for both linear and non-linear power spectra, using the same ΛCDM parameters $\{\Omega_m, \Omega_b, h, A_s, n_s\}$. We can see clearly that MG in the non-linear regime, using the standard Halofit, shows a distinctive feature at scales in between $0.2 \lesssim k \lesssim 2$. This feature however, does not come from higher order perturbations induced by the modified Poisson equations (4.2, 4.4), because Halofit, as explained above, is calibrated with simulations within the ΛCDM model and does not contain any information from Modified Gravity. The feature seen here is caused by the different growth rate of perturbations in Modified Gravity, that yields then a different evolution of non-linear structures.

FIGURE 4.2: **Left:** matter power spectra computed with MGCAMB (linear) and MG CAMB+Halofit (non-linear), illustrating the impact of non-linearities at different scales. As an illustrative example, MG in this plot corresponds to the fiducial model in the late-time parametrization defined in Eq. (4.9). All curves are computed at $z = 0$. The green solid line is the GR fiducial in the non-linear case, the blue long-dashed line is also GR but in the linear case. The short-dashed red line is the MG fiducial in the non-linear case and the medium-dashed brown line the MG fiducial in the linear case. **Right:** in order to have a closer look at small scales, we plot here the ratio of the MG power spectrum to the GR power spectrum for the linear (blue solid) and non-linear (red short-dashed) cases separately. The blue solid line compared to the horizontal grey dashed line, shows the effect of Modified Gravity when taking only linear spectra into account. While the red dashed line, which represents the non-linear case, shows that the ratio to GR presents clearly a bump that peaks around $k \approx 1.0 \text{ h/Mpc}$, meaning that the power spectrum in MG differs at most 4% from the non-linear power spectrum in GR. We will see later that we are able to discriminate between these two models using future surveys, especially when non-linear scales ($k \gtrsim 0.1 \text{ h/Mpc}$) are included.

4.3.2.2 Prescription for mildly non-linear scales including screening

As discussed above, modifications to the Φ and Ψ potentials make the use of Halofit to compute the evolution at non linear scales unreliable. In order to take into account the non-linear contribution to the power spectrum in Modified Gravity, we investigate here a different method, which starts from the consideration that whenever we modify μ and η with respect to GR, we modify the strength of gravitational attraction in a way universal to all species: this means that, similarly to the case of scalar-tensor or $f(R)$ theories, we need to assume the existence of a non-perturbative screening mechanism, acting at small scales, that guarantees agreement with solar system experiments. In other words, it is reasonable to think that the non-linear power spectrum will have to match GR at sufficiently small scales, while at large scales it is modified. Of course, without having a specific model in mind, it remains arbitrary how the interpolation between the small scale regime and the large scale regime is done. In this paper, we adopt the Hu & Sawicki (HS) Parametrized Post-Friedmann prescription proposed in Hu and Sawicki, 2007, which was used for the case of $f(R)$ theories previously by Zhao, 2014. Given a

MG model, this prescription interpolates between the non-linear power spectrum in Modified Gravity (which is in our case just the linear MG power spectrum corrected with standard Halofit, P_{HMG}) and the non-linear power spectrum in GR calculated with Halofit (P_{HGR}). The resulting power spectrum will be denoted as P_{nlHS}

$$P_{\text{nlHS}}(k, z) = \frac{P_{\text{HMG}}(k, z) + c_{\text{nl}} S_{\text{L}}^2(k, z) P_{\text{HGR}}(k, z)}{1 + c_{\text{nl}} S_{\text{L}}^2(k, z)}, \quad (4.13)$$

with

$$S_{\text{L}}^2(k, z) = \left[\frac{k^3}{2\pi^2} P_{\text{LMG}}(k, z) \right]^s. \quad (4.14)$$

The weighting function S_{L} used in the interpolation quantifies the onset of non-linear clustering and it is constructed using the linear power spectrum in Modified Gravity (P_{LMG}). The constant c_{nl} and the constant exponent s are free parameters. In Figure 4.3 we show the ratio $P_{\text{nlHS}}/P_{\text{HGR}}$, which illustrates the relative difference between the non-linear HS prescription in MG and the Halofit non-linear power spectrum in GR, for different values of c_{nl} (left panel) and different values of s (right panel). The parameter c_{nl} controls at which scale there is a transition into a non-linear regime in which standard GR is valid (this can be the case when a screening mechanism is activated); s controls the smoothness of the transition and is in principle a model and redshift dependent quantity. When $c_{\text{nl}} = 0$ we recover the Modified Gravity power spectrum with Halofit P_{HMG} ; when $c_{\text{nl}} \rightarrow \infty$ we recover the non-linear power spectrum in GR calculated with Halofit P_{HGR} . In Zhao, 2014; Zhao, Li, and Koyama, 2011; Koyama, Taruya, and Hiramatsu, 2009, the c_{nl} and s constants were obtained fitting expression (4.13) to N-Body simulations or to a semi-analytic perturbative approach. In the case of $f(R)$, $s = 1/3$ seems to match very well the result from simulations up to a scale of $k = 0.5 \text{ h/Mpc}$ Koyama, Taruya, and Hiramatsu, 2009. A relatively good agreement up to such small scales is enough for our purposes. In the absence of N-Body simulations or semi-analytic methods available for the models investigated in this work, we will assume unity for both parameters, which is a natural choice, and we will test in Section 4.6.3 how our results vary for different values of these parameters, namely $c_{\text{nl}} = \{0.1, 0.5, 1, 3\}$ and $s = \{0, 1/3, 2/3, 1\}$. This will give a qualitative estimate of the impact of non-linearities on the determination of cosmological parameters.

4.4 Fisher Matrix forecasts

The Fisher matrix formalism (Tegmark et al., 1998; Seo and Eisenstein, 2007; Seo and Eisenstein, 2005) is one of the most popular tools to forecast the outcome of an experiment, because of its speed and its versatility when the likelihood is approximately Gaussian. Here we apply the Fisher matrix formalism to two different probes, Galaxy Clustering (GC) and Weak Lensing (WL), which are the main cosmological probes for the future Euclid satellite Mukherjee et al., 2008. The background and perturbations quantities we use in the following equations are computed with a version of MGCAMB Zhao et al., 2009; Hojjati, Pogosian, and Zhao, 2011 modified in order to account for the binning and the parameterizations described in Section 4.2.

FIGURE 4.3: The ratio of the Modified Gravity non-linear power spectrum using the HS prescription by Hu and Sawicki, 2007 (P_{nlHS}) with respect to the GR+Halofit fiducial non-linear power spectrum P_{HGR} , for different values of c_{nl} (left panel) and s (right panel), illustrated in Eqns.(4.13, 4.14). The value $c_{\text{nl}} = 0$ (green solid line) corresponds to MG+Halofit P_{HMG} . All curves are calculated at $z = 0$. **Left:** We show the ratio for $c_{\text{nl}} = \{0.5, 1.0, 10, 10^8\}$, plotted as short-dashed red, medium-dashed blue, short-dashed brown and medium-dashed purple lines respectively. When $c_{\text{nl}} \rightarrow \infty$, Eqn. (4.13) corresponds to the limit of P_{HGR} and therefore the ratio is just 1. The effect of the HS prescription is to grasp some of the features of the non-linear power spectrum at mildly non-linear scales induced by Modified Gravity, taking into account that at very small scales, a screening mechanism might yield again just a purely GR non-linear power spectrum. The parameter c_{nl} interpolates between these two cases. **Right:** in this panel we show the effect of the parameter s , for $s = \{0, 0.33, 0.66, 1\}$ (short-dashed red, medium-dashed blue, short-dashed brown and long-dashed purple, respectively). Both parameters need to be fitted with simulations in order to yield a reliable match with the shape of the non-linear power spectrum in Modified Gravity, as it was done in Zhao, Li, and Koyama, 2011 and references therein. The grey dashed line marks the constant value of 1.

4.4.1 Future large scale galaxy redshift surveys

In this work we choose to present results on some of the future galaxy redshift surveys, which are planned to be started and analyzed within the next decade. Our baseline survey will be the Euclid satellite Amendola and others, 2013; Laureijs and others, 2011. Euclid² is a European Space Agency medium-class mission scheduled for launch in 2020. Its main goal is to explore the expansion history of the Universe and the evolution of large scale cosmic structures by measuring shapes and redshifts of galaxies, covering 15000deg^2 of the sky, up to redshifts of about $z \sim 2$. It will be able to measure up to 100 million spectroscopic redshifts which can be used for Galaxy Clustering measurements and 2 billion photometric galaxy images, which can be used for Weak Lensing observations (for more details, see Amendola and others, 2013; Laureijs and others, 2011). We will use in this work the Euclid Redbook specifications for Galaxy Clustering and Weak Lensing forecasts Laureijs and others, 2011, some of which are listed in Tables 5.3 and 4.3 and the rest can be found in the above cited references.

Another important future survey will be the Square Kilometer Array (SKA)³, which is planned to become the world's largest radiotelescope. It will be built in two phases, phase 1 split into SKA1-SUR in Australia and SKA1-MID in South Africa and SKA2 which will be at least 10 times as sensitive. The first stage is due to finish observations around the year 2023 and the second phase is scheduled for 2030 (for more details, see Yahya et al., 2015; Santos et al., 2015; Raccanelli et al., 2015; Bull et al., 2015). The first phase SKA1, will be able to measure in an area of 5000deg^2 of the sky and a redshift of up to $z \sim 0.8$ an estimated number of about 5×10^6 galaxies; SKA2 is expected to cover a much larger fraction of the sky ($\sim 30000\text{deg}^2$), will yield much deeper redshifts (up to $z \sim 2.5$) and is expected to detect about 10^9 galaxies with spectroscopic redshifts Santos et al., 2015. SKA1 and

²<http://www.euclid-ec.org/>

³<https://www.skatelescope.org/>

SKA2 will also be capable of performing radio Weak Lensing experiments, which are very promising, since they are expected to be less sensitive to systematic effects in the instruments, related to residual point spread function (PSF) anisotropies Harrison et al., 2016. In this work we will use for our forecasts of SKA1 and SKA2, the specifications computed by Santos et al., 2015 for GC and by Harrison et al., 2016 for WL. The numerical survey parameters are listed in Tables 5.3 and 4.3, while the galaxy bias $b(z)$ and the number density of galaxies $n(z)$, can be found in the references mentioned above.

We will also forecast the results from DESI⁴, a stage IV, ground-based dark energy experiment, that will study large scale structure formation in the Universe through baryon acoustic oscillations (BAO) and redshift space distortions (RSD), using redshifts and positions from galaxies and quasars DESI Collaboration, Aghamousa, and others, 2016a; DESI Collaboration, Aghamousa, and others, 2016b; Levi et al., 2013. It is scheduled to start in 2018 and will cover an estimated area in the sky of about 14000deg^2 . It will measure spectroscopic redshifts for four different classes of objects, luminous red galaxies (LRGs) up to a redshift of $z = 1.0$, bright [O II] emission line galaxies (ELGs) up to $z = 1.7$, quasars (QSOs) up to $z \sim 3.5$ and at low redshifts ($z \sim 0.2$) magnitude-limited bright galaxies (BLGs). In total, DESI will be able to measure more than 30 million spectroscopic redshifts. In this paper we will use for our forecasts only the specifications for the ELGs, as found in DESI Collaboration, Aghamousa, and others, 2016a, since this observation provides the largest number density of galaxies in the redshift range of our interest. We cite the geometry and redshift binning specifications in Table 5.3, while the galaxy number density and bias can be found in DESI Collaboration, Aghamousa, and others, 2016a.

4.4.2 Galaxy Clustering

The distribution of galaxies in space is not perfectly uniform. Instead it follows, up to a bias, the underlying matter power spectrum so that the observed power spectrum P_{obs} (the Fourier transform of the real-space two point correlation function of the galaxy number counts) is closely linked to the dark matter power spectrum $P(k)$. The observed power spectrum however also contains additional effects like redshift-space distortions due to velocities and a suppression of power due to redshift-uncertainties. Here we follow Seo and Eisenstein, 2007, neglecting further relativistic and observational effects, and write the observed power spectrum as

$$P_{\text{obs}}(k, \mu, z) = \frac{D_{A,f}^2(z)H(z)}{D_A^2(z)H_f(z)} b^2(z)(1 + \beta_d(z)\mu^2)^2 e^{-k^2\mu^2(\sigma_r^2 + \sigma_v^2)} P(k, z) . \quad (4.15)$$

$P_{\text{obs}}(k, \mu, z)$ is the observed power spectrum as a function of the redshift z , the wavenumber k and of $\mu \equiv \cos \alpha$, where α is the angle between the line of sight and the 3D-wavevector \vec{k} . This observed power spectrum contains all the cosmological information about the background and the matter perturbations as well as corrections due to redshift-space distortions, geometry and observational uncertainties. In the formula, the subscript f denotes the fiducial value of each quantity, $P(k, z)$ is the matter power spectrum, $D_A(z)$ is the angular diameter distance, $H(z)$ the Hubble function and $\beta_d(z)$ is the redshift space distortion factor, which in linear theory is given by $\beta_d(z) = f(z)/b(z)$, with $f(z) \equiv d \ln G / d \ln a$ representing the linear growth rate of matter perturbations and $b(z)$ the galaxy bias as a function of

⁴<http://desi.lbl.gov/>

redshift, which we assume to be local and scale-independent. The exponential factor represents the damping of the observed power spectrum, due to two different effects: σ_z an error induced by spectroscopic redshift measurement errors, which translates into an uncertainty in the position of galaxies at a scale of $\sigma_r = \sigma_z/H(z)$ and σ_v which is the dispersion of pairwise peculiar velocities which are present at non-linear scales and also introduces a damping scale in the mapping between real and redshift space. We marginalize over this parameter, similarly to what Bull, 2015 and others have done, and we take as fiducial value $\sigma_v = 300\text{km/s}$, compatible with the estimates by Torre and Guzzo, 2012. We also include the Alcock-Paczynski effect Alcock and Paczynski, 1979, by which the k modes and the angle cosine μ perpendicular and parallel to the line-of-sight get distorted by geometrical factors related to the Hubble function and the angular diameter distance Ballinger, Peacock, and Heavens, 1996; Feldman, Kaiser, and Peacock, 1994.

We can then write the Fisher matrix for the galaxy power spectrum in the following form (Seo and Eisenstein, 2007; Amendola et al., 2012):

$$F_{ij} = \frac{V_{\text{survey}}}{8\pi^2} \int_{-1}^{+1} d\mu \int_{k_{\min}}^{k_{\max}} dk k^2 \frac{\partial \ln P_{\text{obs}}(k, \mu, z)}{\partial \theta_i} \frac{\partial \ln P_{\text{obs}}(k, \mu, z)}{\partial \theta_j} \left[\frac{n(z)P_{\text{obs}}(k, \mu, z)}{n(z)P_{\text{obs}}(k, \mu, z) + 1} \right]^2. \quad (4.16)$$

Here V_{survey} is the volume covered by the survey and contained in a redshift slice Δz and $n(z)$ is the galaxy number density as a function of redshift. We will consider the smallest wavenumber k_{\min} to be $k_{\min} = 0.0079\text{h/Mpc}$, while the maximum wavenumber will be $k_{\max} = 0.15\text{h/Mpc}$ for the linear forecasts and $k_{\max} = 0.5\text{h/Mpc}$ for the non-linear forecasts. In the above formulation of the Galaxy Clustering Fisher matrix, we neglect the correlation among different redshift bins and possible redshift bin uncertainties as was explored recently in Bailoni, Spurio Mancini, and Amendola, 2016, we will use for our forecasts the more standard recipe specified in the Euclid Redbook Laureijs and others, 2011.

Parameter	Euclid	DESI-ELG	SKA1-SUR	SKA2	Description
A_{survey}	15000 deg^2	14000 deg^2	5000 deg^2	30000 deg^2	Survey area in the sky
σ_z	0.001	0.001	0.0001	0.0001	Spectroscopic redshift error
$\{z_{\min}, z_{\max}\}$	{0.65, 2.05}	{0.65, 1.65}	{0.05, 0.85}	{0.15, 2.05}	Min. and max. limits for redshift bin
Δz	0.1	0.1	0.1	0.1	Redshift bin width

TABLE 4.2: Specifications for the spectroscopic galaxy redshift surveys used in this work. The number density of tracers $n(z)$ and the galaxy bias $b(z)$, can be found for SKA in Santos et al., 2015 and for DESI in reference DESI Collaboration, Aghamousa, and others, 2016a.

4.4.3 Weak Lensing

Light propagating through the universe is deflected by variations in the Weyl potential $\Phi + \Psi$, leading to distortions in the images of galaxies. In the regime of small deflections (Weak Lensing) we can write the power spectrum of the shear field as

$$C_{ij}(\ell) = \frac{9}{4} \int_0^\infty dz \frac{W_i(z)W_j(z)H^3(z)\Omega_m^2(z)}{(1+z)^4} [\Sigma(\ell/r(z), z)] P_m(\ell/r(z)). \quad (4.17)$$

In this expression we used Eqn. (4.4) to relate the Weyl potential to Σ and to the matter power spectrum P_m and we use the Limber approximation to write down the conversion $k = \ell/r(z)$, where $r(z)$ is the comoving distance given by

$$r(z) = c \int_0^z \frac{d\tilde{z}}{H(\tilde{z})}. \quad (4.18)$$

The indices i, j stand for each of the \mathcal{N}_{bin} redshift bins, such that C_{ij} is a matrix of dimensions $\mathcal{N}_{bin} \times \mathcal{N}_{bin}$. The window functions W_i are given by

$$W(z) = \int_z^\infty d\tilde{z} \left(1 - \frac{r(z)}{r(\tilde{z})}\right) n(\tilde{z}) \quad (4.19)$$

where the normalized galaxy distribution function is

$$n(z) \propto z^2 \exp\left(-(z/z_0)^{3/2}\right). \quad (4.20)$$

Here the median redshift z_{med} and z_0 are related by $z_{\text{med}} = \sqrt{2}z_0$. The Weak Lensing Fisher matrix is then given by a sum over all possible correlations at different redshift bins (Tegmark et al., 1998),

$$F_{\alpha\beta} = f_{\text{sky}} \sum_{\ell}^{\ell_{\text{max}}} \sum_{i,j,k,l} \frac{(2\ell+1)\Delta\ell}{2} \frac{\partial C_{ij}(\ell)}{\partial \theta_\alpha} \text{Cov}_{jk}^{-1} \frac{\partial C_{kl}(\ell)}{\partial \theta_\beta} \text{Cov}_{li}^{-1}. \quad (4.21)$$

The prefactor f_{sky} is the fraction of the sky covered by the survey. The upper limit of the sum, ℓ_{max} , is a high-multipole cutoff due to our ignorance of clustering and baryon physics on small scales, similar to the role of k_{max} in Galaxy Clustering. In this work we choose $\ell_{\text{max}} = 1000$ for the linear forecasts and $\ell_{\text{max}} = 5000$ for the non-linear forecasts (this cutoff is not necessarily reached at all multipoles ℓ , as what matters is the minimum scale between ℓ_{max} and k_{max} , as we discuss below; see also Casas et al., 2015). In Eqn. (5.14), Cov_{ij} is the corresponding covariance matrix of the shear power spectrum and it has the following form:

$$\text{Cov}_{ij}(\ell) = C_{ij}(\ell) + \delta_{ij} \gamma_{\text{int}}^2 n_i^{-1} + K_{ij}(\ell) \quad (4.22)$$

where γ_{int} is the intrinsic galaxy ellipticity, whose value can be seen in Table 4.3 for each survey. The shot noise term n_i^{-1} is expressed as

$$n_i = 3600 \left(\frac{180}{\pi}\right)^2 n_\theta / \mathcal{N}_{bin} \quad (4.23)$$

with n_θ the total number of galaxies per arcmin² and the index i standing for each redshift bin. Since the redshift bins have been chosen such that each of them contains the same amount of galaxies (equi-populated redshift bins), the shot noise term is equal for each bin. The matrix $K_{ij}(\ell)$ is a diagonal ‘‘cutoff’’ matrix, discussed for the first time in Casas et al., 2015 whose entries increase to very high values at the scale where the power spectrum $P(k)$ has to be cut to avoid the inclusion of uncertain or unresolved non-linear scales. We choose to add this matrix to have further control on the inclusion of non-linearities. Without this matrix, due to the redshift-dependent relation between k and ℓ , a very high ℓ_{max} would correspond at low redshifts, to a very high k_{max} where we do not longer trust the accuracy of the non-linear power spectrum. Therefore, the sum in Eqn. (5.14) is

limited by the minimum scale imposed either by ℓ_{\max} or by k_{\max} , which is the maximum wavenumber considered in the matter power spectrum $P(k, z)$. As we did for Galaxy Clustering, we use for linear forecasts $k_{\max} = 0.15$ and for non-linear forecasts $k_{\max} = 0.5$.

Parameter	Euclid	SKA1	SKA2	Description
f_{sky}	0.364	0.121	0.75	Fraction of the sky covered
σ_z	0.05	0.05	0.05	Photometric redshift error
n_θ	30	10	2.7	Number of galaxies per arcmin
γ_{int}	0.22	0.3	0.3	Intrinsic galaxy ellipticity
z_0	0.9	1.0	1.6	Median redshift over $\sqrt{2}$
N_{bin}	12	12	12	Total number of tomographic redshift bins

TABLE 4.3: Specifications for the Weak Lensing surveys Euclid, SKA1 and SKA2 used in this work. Other needed quantities can be found in the references cited in section 4.4.1. For all WL surveys we use a redshift range between $z = 0.5$ and $z = 3.0$, using 6 equi-populated redshift bins.

4.4.4 Covariance and correlation matrix and the Figure of Merit

The covariance matrix is defined for a d -dimensional vector p of random variables as

$$\mathbf{C} = \langle \Delta p \Delta p^T \rangle \quad (4.24)$$

with $\Delta p = p - \langle p \rangle$ and the angular brackets $\langle \rangle$ representing an expectation value. The matrix \mathbf{C} , with all its off-diagonal elements set to zero, is called the variance matrix V and contains the square of the errors σ_i for each parameter p_i

$$\mathbf{V} \equiv \text{diag}(\sigma_1^2, \dots, \sigma_d^2) . \quad (4.25)$$

The Fisher matrix \mathbf{F} is the inverse of the covariance matrix

$$\mathbf{F} = \mathbf{C}^{-1} . \quad (4.26)$$

The correlation matrix \mathbf{P} is obtained from the covariance matrix \mathbf{C} , in the following way

$$P_{ij} = \frac{C_{ij}}{\sqrt{C_{ii}C_{jj}}} . \quad (4.27)$$

If the covariance matrix is non-diagonal, then there are correlations among some elements of p . We can observe this also by plotting the marginalized error ellipsoidal contours. The orientation of the ellipses can tell us if two variables p_i and p_j are correlated ($P_{ij} > 0$), corresponding to ellipses with 45 degree orientation to the right of the vertical line or if they are anti-correlated ($P_{ij} < 0$), corresponding to ellipses oriented 45 degrees to the left of the vertical line.

To summarize the information contained in the Fisher/covariance matrices we can define a Figure of Merit (FoM). Here we choose the logarithm of the determinant, while another possibility would be the Kullback-Leibler divergence, which is a measure of the information entropy gain, see Appendix 4.12.

The square-root $\sqrt{\det(\mathbf{C})}$ of the determinant of the covariance matrix is proportional to the volume of the error ellipsoid. We can see this if we rotate our coordinate system so that the covariance matrix is diagonal, $\mathbf{C} = \text{diag}(\sigma_1^2, \sigma_2^2, \dots, \sigma_d^2)$, then $\det(\mathbf{C}) = \prod_i \sigma_i^2$ and $(1/2) \ln(\det(\mathbf{C})) = \ln \prod_i \sigma_i$ would indeed represent the logarithm of an error volume. Thus, the smaller the determinant (and therefore also $\ln(\det(\mathbf{C}))$), the smaller is the ellipse and the stronger are the constraints on the parameters. We define

$$\text{FoM} = -\frac{1}{2} \ln(\det(\mathbf{C})), \quad (4.28)$$

with a negative sign in front such that stronger constraints lead to a higher Figure of Merit. In the following, the value of the FoM reported in all tables will be obtained including only the dark energy parameters (i.e. the (μ_i, η_i) sub-block for the binned case and the (μ, η) sub-block in the smooth functions case), after marginalizing over all other parameters. The FoM allows us to compare not only the constraining power of different probes but also of the different experiments. As the absolute value depends on the details of the setup, we define the relative figure of merit between probe a and probe b : $\text{FoM}_{a,b} = -1/2 \ln(\det(\mathbf{C}_a)/\det(\mathbf{C}_b)) = \text{FoM}_a - \text{FoM}_b$ and we fix our reference case (probe b), for each parametrization, to the Galaxy Clustering observation using linear power spectra with the Euclid survey (labeled as ‘Euclid Redbook GC-lin’ in all figures and tables). The FoM has units of ‘nits’, since we are using the natural logarithm. These are similar to ‘bits’, but ‘nits’ are counted in base e instead of base 2.

An analogous construction allows us to study quantitatively the strength of the correlations encoded by the correlation matrix \mathbf{P} . We define the ‘Figure of Correlation’ (FoC) as:

$$\text{FoC} = -\frac{1}{2} \ln(\det(\mathbf{P})). \quad (4.29)$$

If the parameters are independent, i.e. fully decorrelated, then \mathbf{P} is just the unit matrix and $\ln(\det(\mathbf{P})) = 0$. Off-diagonal correlations will decrease the logarithm of the determinant, therefore making the FoC larger. From a geometrical point of view, the determinant expresses a volume spanned by the vector of (normalized) variables. If these variables are independent, the volume would be maximal and equal to one, while if they are strongly linearly dependent, the volume would be squeezed and in the limit where all variables are effectively the same, the volume would be reduced to zero. Hence, a more positive FoC indicates a stronger correlation of the parameters.

4.4.5 CMB *Planck* priors

Alongside the information brought by LSS probes, we also include CMB priors on the parameterizations considered. In order to obtain these, we analyze the binned and parameterized approaches described in Section 4.2 with the *Planck*+BSH combination of CMB and background (BAO+SN-Ia+ H_0) datasets discussed in the *Planck* Dark Energy and Modified Gravity paper Planck Collaboration, Ade, and others, 2016. We use a Markov Chain Monte Carlo (MCMC) approach, using the publicly available code COSMOMC Lewis and Bridle, 2002; Lewis, 2013, interfaced with our modified version of MGCB. The MCMC chains sample the parameter vector Θ which contains the standard cosmological parameters $\{\omega_b \equiv \Omega_b h^2, \omega_c \equiv \Omega_c h^2, \theta_{\text{MC}}, \tau, n_s, \ln 10^{10} A_s\}$ to which we add the E_{ij} parameters when we parameterize the time evolution of μ and η with continuous functions of the scale factor,

and the μ_i , η_i parameters in the binned case. On top of these, also the 17 nuisance parameters of the *Planck* analysis are included. From the MCMC analysis of the *Planck* likelihood we obtain a covariance matrix in terms of the parameters Θ . We marginalize over the nuisance parameters and over the optical depth τ since this parameter does not enter into the physics of large scale structure formation.

θ is usually the ratio of sound horizon to the angular diameter distance at the time of decoupling. Since calculating the decoupling time z_{CMB} is relatively time consuming, as it involves the minimization of the optical transfer function, COSMOMC uses instead an approximate quantity θ_{MC} based on the following fitting formula from Hu and Sugiyama, 1996

$$\begin{aligned} z_{\text{CMB}} = & 1048 \times (1 + 0.00124\omega_b^{-0.738}) \\ & \times (1 + 0.0783\omega_b^{-0.238}/(1 + 39.5\omega_b^{0.763})) \\ & \times (\omega_d + \omega_b)^{0.560/(1+21.1\omega_b^{1.81})} \end{aligned} \quad (4.30)$$

where $\omega_d \equiv (\Omega_c + \Omega_\nu)h^2$. The sound horizon is defined as

$$r_s(z_{\text{CMB}}) = cH_0^{-1} \int_{z_{\text{CMB}}}^{\infty} dz \frac{c_s}{E(z)} \quad (4.31)$$

where the sound speed is $c_s = 1/\sqrt{3(1 + \bar{R}_b a)}$ with the baryon-radiation ratio being $\bar{R}_b a = 3\rho_b/4\rho_\gamma$. $\bar{R}_b = 31500\Omega_b h^2(T_{\text{CMB}}/2.7\text{K})^{-4}$. However, CAMB approximates it as $\bar{R}_b a = 30000a\Omega_b h^2$.

Therefore we first marginalize the covariance matrix over the nuisance parameters and the parameter τ , which cannot be constrained by LSS observations. Then, we invert the resulting matrix, to obtain a *Planck* prior Fisher matrix and then use a Jacobian to convert between the MCMC parameter basis Θ_i and the GC-WL parameter basis θ_i . We use the formulas above for the sound horizon r_s and the angular diameter distance d_A to calculate the derivatives of θ_{MC} with respect to the parameters of interest. Our Jacobian is then simply (see Appendix 4.8 for details)

$$J_{ij} = \frac{\partial \Theta_i}{\partial \theta_j}. \quad (4.32)$$

4.5 Results: Euclid forecasts for redshift binned parameters

In this section we analyze the Modified Gravity functions $\mu(a)$ and $\eta(a)$, described in Section 4.2, when they are allowed to vary freely in five redshift bins.

For this purpose, we calculate a Fisher matrix of fifteen parameters: five for the standard Λ CDM parameters $\{\Omega_m, \Omega_b, h, \ln 10^{10} A_s, n_s\}$, five for μ (one for each bin amplitude μ_i) and five for η (one for each bin amplitude η_i), corresponding to the 5 redshift bins $z=\{0-0.5, 0.5-1.0, 1.0-1.5, 1.5-2.0, 2.0-2.5\}$. The fiducial values for all fifteen parameters were calculated running a Markov-Chain-Monte-Carlo with *Planck* likelihood data and can be found in Table 4.1.

We first show the constraints on our 15 parameters for Galaxy Clustering (GC) forecasts in subsection 4.5.1, while in subsection 5.7.2 we report results for Weak Lensing (WL). In subsection 4.5.3, we comment on the combination of forecasts for GC+WL together with *Planck* data. All forecasts are performed using Euclid Redbook specifications. Other surveys will be considered for the other two time

parameterizations in section 4.6.1.4 and 4.6.2.2. For each case, we show the correlation matrix obtained from the covariance matrix and argue that the redshift-binned parameters show a strong correlation, therefore we illustrate the decorrelation procedure for the covariance matrix in subsection 4.5.4 where we also include combined GC+WL and GC+WL+*Planck* cases.

4.5.1 Euclid Galaxy Clustering Survey

For the Galaxy Clustering survey, we give results for two cases, one using only linear power spectra up to a maximum wavevector of $k_{\max} = 0.15 \text{ h/Mpc}$ and another one using non-linear power spectra up to $k_{\max} = 0.5 \text{ h/Mpc}$, as obtained by using the HS parameterization of Eqn. (4.13). For the redshift-binned case, we will report forecasts only for a Euclid survey, using Euclid Redbook specifications which are detailed in section 4.4.2.

FIGURE 4.4: Correlation matrix \mathbf{P} defined in (4.27) obtained from the covariance matrix in the MG-binning case, for a Galaxy Clustering Fisher forecast using Euclid Redbook specifications. **Left panel:** Linear forecasts. Here there are strong positive correlations among the μ_i and η_i parameters and anti-correlations between $\ln 10^{10} A_s$ and the μ_i parameters, as well as between μ_i and η_i . The FoC in this case is ≈ 65 . (see Eqn. (4.29) for its definition). **Right panel:** Non-linear forecasts using the HS prescription. Interestingly, the anti-correlations between $\ln 10^{10} A_s$ and μ_i have disappeared, as well as the correlations among the μ_i parameters. The FoC is in this case ≈ 32 , meaning that the variables are much less correlated than in the linear case. This is due to the fact that taking into account non-linear structure formation breaks degeneracies between the primordial amplitude parameter and the modifications to the Poisson equation.

We calculate the Fisher matrix for the 15 parameters $\theta = \{\Omega_m, \Omega_b, h, \ln 10^{10} A_s, n_s, \mu_i, \eta_i\}$ where η_i and μ_i represent ten independent parameters, one for each function at each of the 5 redshift bins corresponding to the redshifts $z=\{0-0.5, 0.5-1.0, 1.0-1.5, 1.5-2.0, 2.0-2.5\}$. As a standard procedure, we marginalize over the unknown bias parameters. From the covariance matrix, defined previously in Eqn. (4.24), we obtain the correlation matrix P_{ij} defined in Eqn. (4.27) for the set of parameters θ_i . In Figure 4.4 we show the matrix P_{ij} in the linear (left panel) and non-linear-HS (right panel) cases. Redder (bluer) colors signal stronger correlations (anti-correlations).

A covariance matrix that contains strong correlations among parameter A and B, means that the experimental or observational setting has difficulties distinguishing between A and B for the assumed theoretical model, i.e. this represents a parameter degeneracy. Therefore if for example parameter A is poorly constrained, then parameter B will be badly constrained as well. The appearance of correlations among parameters is linked to the non-diagonal elements of the covariance matrix. Subsequently, this means that the fully marginalized errors on a single parameter, will be larger if there are strong correlations and will be smaller (closer to the value of the fully maximized errors) if the correlations are negligible.

In the linear case, μ_i and η_i parameters show correlations among each other, while the primordial amplitude parameter $\ln 10^{10} A_s$ exhibits a strong anti-correlation with all the μ_i . This can be explained considering that a larger growth of structures

in linear theory can also be mimicked with a larger initial amplitude of density fluctuations.

Interestingly, including non-linear scales in the analysis (right panel of Fig. 4.4) leads to a strong suppression of the correlations among the μ_i . Also the correlation between these and $\ln 10^{10} A_s$ is suppressed as a change in the initial amplitude of the power spectrum is not able to compensate for a modified Poisson equation when non-linear evolution is considered.

As discussed in Section 4.4.4, we can also express the difference between the correlation matrix of the linear forecast and the non-linear forecast in a more quantitative way, by computing the determinant of the correlation matrix, or equivalently the FoC (4.29). If the correlations were negligible, this determinant would be equal to one (and therefore its FoC would be 0), while if the correlations were strong, the determinant would be closer to zero with a corresponding large positive value of the FoC. For the linear forecast, the FoC is about 62, while for the non-linear forecast, it is much smaller at approximately 35. In Table ?? we show the 1σ constraints obtained on $\ln(10^{10} A_s)$ and on the μ_i and η_i parameters, both in the linear and non-linear cases for a Euclid Redbook GC survey (top rows). While linear GC alone ($k_{\max} = 0.15 \text{ h/Mpc}$) is not very constraining in any bin, the inclusion of non-linear scales ($k_{\max} = 0.5 \text{ h/Mpc}$) drastically reduces errors on the μ_i parameters: the first three bins in μ_i ($0 < z < 1.5$) are the best constrained, to less than 10%, with the corresponding η_i constrained at 20% by non-linear GC alone. This is also visible in the FoM which increases by 19 nits ('natural units', similar to bits but using base e instead of base 2), nearly 4 nits per redshift bin on average, when including the non-linear scales. The fact that the error on $\ln 10^{10} A_s$ improves from 90% to 0.68% shows that the decorrelation induced by the non-linearities breaks the degeneracy with the amplitude and therefore improves considerably the determination of cosmological parameters. This shows that it is important to include non-linear scales in GC surveys (and not only in Weak Lensing ones, which is usually more expected and will be shown in the next subsection).

4.5.2 Euclid Weak Lensing Survey

In the case of Weak Lensing, the linear forecast is performed with linear power spectra up to a maximum multipole $\ell_{\max} = 1000$, while the non-linear forecast is performed with non-linear spectra up to a maximum multipole of $\ell_{\max} = 5000$, as explained in section 5.7. Since we limit our power spectrum to a maximum in k -space, as explained in section 4.4.3, these multipole values are not reached at every redshift. Like for GC, also for WL it is very important to include information from the non-linear power spectrum, since in that range will lie most of the constraining power of next-generation surveys like Euclid. In Figure 4.5 we show the correlation matrices for the linear (left panel) and non-linear (right panel) Fisher Matrix forecasts. In this case, as opposed to the GC correlation matrices, it is not visually clear which case is more correlated than the other. At a closer look, in the linear case we can observe strong anti-correlations between the μ_j and η_j parameters for $j = 2, 3, 4, 5$ and an anti-correlation between η_1 and the primordial amplitude $\ln 10^{10} A_s$. In the non-linear case, the primordial amplitude parameter is effectively decorrelated from the Modified Gravity parameters, and the anti correlation between μ_j and the η_j affects the first three bins (effectively increasing degeneracies in the first bin). The anti-correlation between these two sets of parameters is expected, since WL is sensitive to Σ , which is a product of η and μ , c.f. Eqn. (4.5). The

decrease of correlation when going from the linear to the non-linear case is confirmed, also quantitatively, by the FoC: the one for the linear case is of ≈ 69 , larger than the one for the non-linear case ≈ 32 . Once again, the inclusion of non-linear scales breaks degeneracies, especially among the linear amplitude of the power spectrum and the MG parameters.

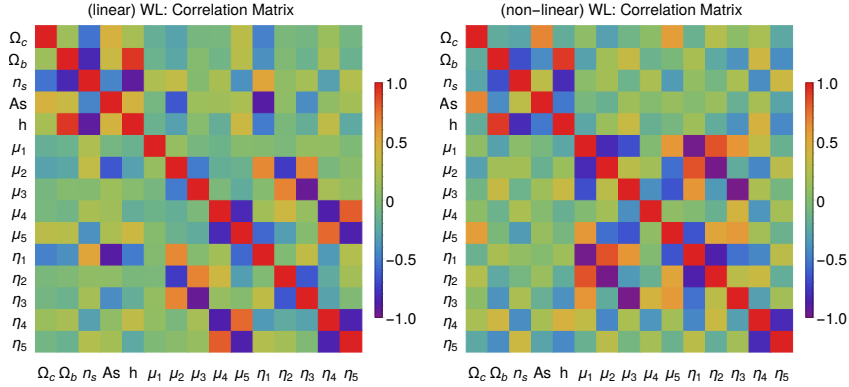


FIGURE 4.5: Correlation matrix obtained from the covariance matrix in the MG-binning case, for a Weak Lensing Fisher Matrix forecast using Euclid Redbook specifications. **Left panel:** linear forecasts. Strong anti-correlations are present between the μ_i and the η_i parameters for the same value of i in 2,3,4,5. The amplitude $\ln(10^{10}A_s)$ parameter is mostly uncorrelated except with η_1 . The FoC (4.29) in this case is approximately 69. **Right panel:** non-linear forecasts using the HS prescription. Here the same trend as in the linear case is present, with just subtle changes. The FoC in this case is about 32, meaning that the variables are indeed less correlated than in the linear case. The parameter $\ln(10^{10}A_s)$ is effectively not correlated to other parameters, and the anti-correlation of μ_i and the η_i for the same value of the index i is present in the first three bins. The anti-correlation between these two sets of parameters is expected, since WL is sensitive to the Weyl potential Σ , which is a product of μ and η .

Table ?? shows the corresponding 1σ marginalized errors on $\ln(10^{10}A_s)$ and on the μ_i and η_i , both in the linear and non-linear cases for a Euclid Redbook WL survey. As in the case of GC, linear WL cannot constrain alone any of the amplitudes of the Modified Gravity parameters μ_i and η_i for any redshift bin. Being able to include non-linear scales improves constraints on the amplitude $\ln(10^{10}A_s)$ by a factor 100. The 1σ errors on μ_i and η_i improve up to one order of magnitude, with the FoM increasing by 17 nits, although remaining quite unconstraining for Modified Gravity parameters in all redshift bins. Notice, however, that the 1σ error on μ_1 from WL in the linear case is slightly smaller than in the non-linear case. This can be attributed to the fact that in the linear case, μ_1 is uncorrelated to any other parameter, as shown in Figure 4.5 and on that specific bin ($0 < z < 0.5$) non-linearities don't seem to improve the constraints on this parameter.

4.5.3 Combining Euclid Galaxy Clustering and Weak Lensing, with Planck data

The combination of Galaxy Clustering and Weak Lensing is expected to be very powerful for Modified Gravity parameters as they measure two different combinations of μ and η , thus breaking their degeneracy as illustrated in Fig. 4.14. This

is shown in Table ??, where the sensitivity drastically increases with respect to the two separate probes, especially in the low redshifts bins ($0. < z < 1.5$), where the lensing signal is dominant. Adding non-linearities further doubles the FoM. The *Planck* data constrains mostly the standard Λ CDM parameters and has only a limited ability to constrain the MG sector. However, the additional information breaks parameter degeneracies and in this way significantly decreases the uncertainties on all parameters, so that the linear GC+WL+*Planck* is comparable to the non-linear GC+WL. Also, quantitatively, the correlation among parameters is reduced by combining GC+WL with *Planck* data. The FoC in this case is of ≈ 22 . We also see in Table ?? that the differences between the non-linear prescription adopted here (nl-HS) and a straightforward application of Halofit to the MG case (nl-Halofit) is not very large. We will investigate further the impact of the parameters used in the non-linear prescription in section 4.6.3.

4.5.4 Decorrelation of covariance matrices and the Zero-phase Component Analysis

In the previous subsections we highlighted how the MG parameters and the amplitude of the primordial power spectrum exhibit significant correlations and showed how including non-linearities helps to decorrelate them. Even without including non-linearities, however, it is interesting to investigate how we can completely decorrelate the parameters, identifying in this way those parameter combinations which are best constrained by data.

Given again a d -dimensional vector p of random variables (our originally correlated parameters), we can calculate its covariance matrix \mathbf{C} defined in Eqn. (4.24). The process of decorrelation is the process of making the matrix \mathbf{C} a diagonal matrix.

Let us define some important identities. The covariance matrix can be decomposed in its eigenvalues (the elements of a diagonal matrix Λ) and eigenvectors (the rows of an orthogonal matrix U).

$$\mathbf{C} = U \Lambda U^T \quad \Leftrightarrow \quad \mathbf{F} = U \Lambda^{-1} U^T , \quad (4.33)$$

where \mathbf{F} is the Fisher Matrix.

It is possible to show that applying a transformation matrix W to the p parameter vector, thus obtaining a new vector of variables $q = Wp$, the covariance matrix of the transformed vector q is whitened (i.e. it is the identity matrix, and whitening is defined as the process of converting the covariance matrix into an identity matrix)

$$\begin{aligned} \tilde{\mathbf{C}} &= W \langle \Delta \hat{p} \Delta \hat{p}^T \rangle W^T = \langle \Delta \hat{q} \Delta \hat{q}^T \rangle \\ &= \mathbb{I} . \end{aligned} \quad (4.34)$$

This means that the transformed q parameters are decorrelated, since their correlation matrix is diagonal. The choice of W is not unique as several possibilities exist; we focus on a particular choice in the rest of the paper referred to as Zero-phase Component Analysis (ZCA, first introduced by Bell and Sejnowski, 1997 in the context of image processing), but we show two other possible choices and their effect on the analysis in Appendix 4.10.

Zero-phase Component Analysis (sometimes also called Mahalanobis transformation Kessy, Lewin, and Strimmer, 2015) is a specific choice of decorrelation

method that minimizes the squared norm of the difference between the q_i and the p_i vector $\|\vec{p} - \vec{q}\|$, under the constraint that the vector \vec{q} should be uncorrelated Kessy, Lewin, and Strimmer, 2015. In this way the uncorrelated variables q will be as close as possible to the original variables p in a least squares sense. This is achieved by using the W matrix:

$$W \equiv F^{1/2}. \quad (4.35)$$

Then in this case, the covariance matrix is whitened, by following Eqn. (4.34):

$$\tilde{C} = F^{1/2} F^{-1} F^{1/2} = \mathbb{1}. \quad (4.36)$$

In our case, since we do not want to whiten, but just decorrelate the covariance matrix, we renormalize the W matrix by multiplying with a diagonal matrix $N_{jj} \equiv \sum_j (W_{ij}^{-2})$, such that the sum of the square of the elements on each row of the new weighting matrix $\tilde{W} \equiv NW$, is equal to unity; therefore the final transformed covariance is still diagonal but is not the identity matrix:

$$\tilde{C} = \tilde{W} C \tilde{W} = N^2 \mathbb{1} \quad (4.37)$$

and at the same time we ensure that the vector of new variables q_i will have the same norm as the old vector of variables p_i .

4.5.4.1 ZCA for Galaxy Clustering

From Fig. 4.4 we can see that the correlations are present in sub-blocks, one for the standard Λ CDM parameters and another one for the Modified Gravity parameters. The exception lies in the linear case where $\ell\mathcal{A}_s \equiv \ln(10^{10} A_s)$ is strongly anti-correlated with all the μ_i and positively correlated with the η_i . To use a more objective criterion, we choose the 10×10 block of MG parameters μ_i and η_i with parameter indices 6 to 15, and only add to this block a Λ CDM parameter with index a if the following condition is satisfied:

$$\sum_{i=6}^{i=15} (P_{ai})^2 \geq 1$$

where the index a corresponds to one of the first five standard parameters. For Galaxy Clustering, the only index satisfying this condition is $a = 4$ in the linear case, corresponding to $\ell\mathcal{A}_s \equiv \ln(10^{10} A_s)$: i.e. the standard parameter corresponding to the amplitude is, as said, degenerate with Modified Gravity parameters μ_i and η_i . In the non-linear case no parameter satisfies this condition (because, as we have seen, non-linearities are able to eliminate correlation with the amplitude), but for consistency we will use the same vector of 11 parameters $p_i = \{\ell\mathcal{A}_s, \mu_i, \eta_i\}$ for our decorrelation procedure. Therefore we will also have 11 transformed uncorrelated q_i parameters, function of the original p_i parameters, in all the cases presented below.

Figure 4.6 shows the coefficients that relate the q_i parameters to the original p_i ones, in the linear (left panel) and the non-linear (right panel) cases, also shown explicitly in Tables 4.10 and 4.11 of Appendix 4.11. We plot in Figure 4.7 a comparison between the 1σ errors on the primary parameters p_i (represented by circles connected with dark green dashed lines) and the decorrelated parameters q_i (represented by squares connected with orange solid lines). In the linear case (left

panel), we can see that the errors on the q_i parameters are 2 orders of magnitude better than the errors on the p_i parameters. In the non-linear case (right panel) the improvement is of at most 1 order of magnitude and that for a completely decorrelated parameter like $\ell\mathcal{A}_s$, the error on its corresponding q_i is exactly the same. This shows that a decorrelation procedure is still worth to do, even when including the non-linear regime, even if the degeneracy with the amplitude is already completely broken thanks to the non-linear prescription. The fact that the curve of 1σ errors for the q_i follows the same pattern as the curve for the p_i errors, is due to the fact that we have used a ZCA decomposition (see Section 4.5.4) and therefore the q_i are as similar as possible to the p_i .

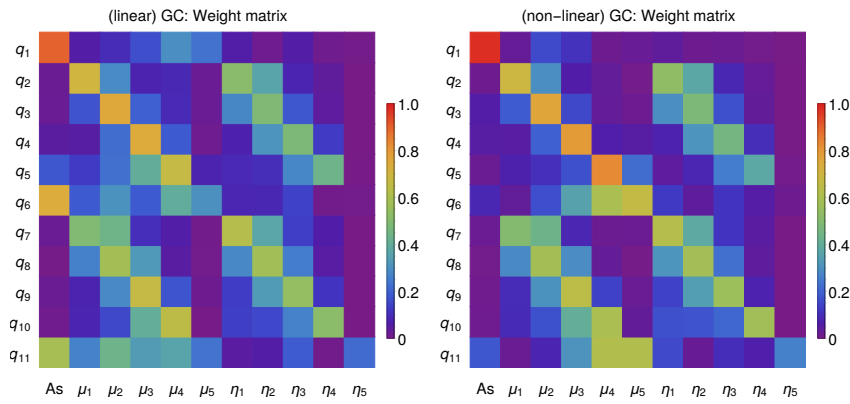


FIGURE 4.6: Entries of the matrix W that relates the q_i parameters to the original p_i ones, after applying the ZCA decorrelation of the covariance matrix in the linear and non-linear GC cases. This matrix shows for each new variable q_i on the vertical axis, the coefficients of the linear combination of parameters μ_i, η_i and A_s that give rise to that variable q_i . The red (blue) colors, indicate a large (small) contribution of the respective variable on the horizontal axis. **Left panel:** linear forecast for Euclid Redbook specifications. **Right panel:** non-linear forecast for Euclid Redbook specifications, using the HS prescription. In both cases one can observe that most q_i parameters have only small or negligible contributions from μ_5 and η_5 , which are found to be the less constrained bins.

We are interested in finding the best combination of primary parameters p_i giving rise to the best constrained uncorrelated parameters q_i . In order to find the errors on the parameters q_i , we need to look at the diagonal of the decorrelated covariance matrix $\tilde{\mathbf{C}}$ expressed in Eqn. (4.37) and identify the q_i parameters with the smallest relative errors (σ_{q_i}/q_i): we find that in the linear GC case, the best constrained combinations of primary parameters (ordered from most to least constrained) are given approximately by:

$$\begin{aligned} q_1 &= +0.9\ell\mathcal{A}_s + 0.32\mu_4 \\ q_3 &= +0.75\mu_2 - 0.29\eta_1 + 0.50\eta_2 \\ q_4 &= -0.25\mu_2 + 0.74\mu_3 - 0.32\eta_2 + 0.49\eta_3 \\ q_2 &= +0.70\mu_1 - 0.30\mu_2 + 0.52\eta_1 - 0.36\eta_2 . \end{aligned} \tag{4.38}$$

In contrast, for the non-linear GC case, the parameter $\ell\mathcal{A}_s \equiv \ln(10^{10}A_s)$ is not correlated to any other, and therefore it is well constrained on its own. The best 4 constrained parameters (ordered from most to least constrained) in the non-linear

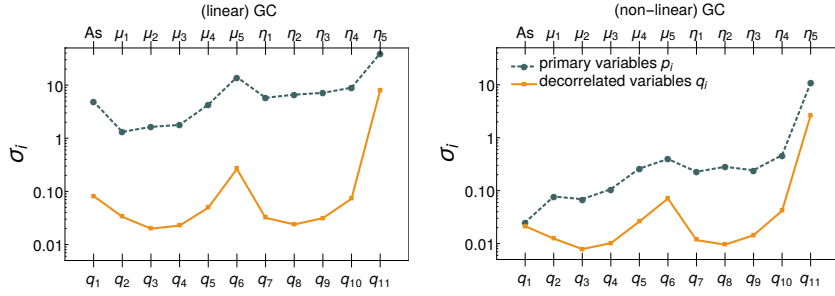


FIGURE 4.7: Results for a Euclid Redbook GC survey, with redshift-binned parameters, before and after applying the ZCA decorrelation. Each panel shows the 1σ fully marginalized errors on the primary parameters p_i (green dashed lines), and the 1σ errors on the decorrelated parameters q_i (orange solid lines). **Left:** linear forecasts, performed using linear power spectra up to a maximum wavenumber $k_{\max} = 0.15h/\text{Mpc}$. **Right:** non-linear forecasts using non-linear spectra with the HS prescription up to a maximum wavenumber $k_{\max} = 0.5h/\text{Mpc}$. In the linear case, the errors on the decorrelated q_i parameters are about 2 orders of magnitude smaller than for the primary parameters, while in the non-linear HS case, the improvement in the errors is of one order of magnitude. This means that applying a decorrelation procedure is worth even when non-linearities are considered. In both cases for GC, the least constrained parameters are μ_5 and η_5 , corresponding to $2.0 < z < 2.5$.

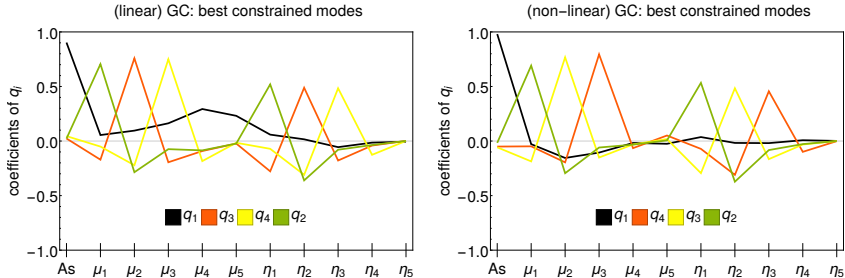


FIGURE 4.8: Best constrained modes for a Euclid Redbook GC survey, with μ and η binned in redshift, after transforming into uncorrelated q parameters via ZCA. Each of the four best constrained parameters q_i , shown in the panels, is a linear combination of the primary parameters p_i . The q_i in the legends are ordered from left to right, from the best constrained to the least constrained.

case, are:

$$\begin{aligned} q_1 &= +0.99\ell\mathcal{A}_s \\ q_4 &= -0.28\mu_2 + 0.76\mu_3 - 0.33\eta_2 + 0.47\eta_3 \\ q_3 &= +0.73\mu_2 - 0.32\eta_1 + 0.49\eta_2 \\ q_2 &= +0.68\mu_1 - 0.35\mu_2 + 0.52\eta_1 - 0.37\eta_2 . \end{aligned} \tag{4.39}$$

The best constrained decorrelated parameters q_i for a Euclid GC survey, expressed in the set of Equations (4.38) (linear) and (4.39) (non-linear HS), can be seen graphically in Fig. 4.8 for the linear (left panel) and non-linear HS (right panel) cases respectively. From these combinations we see that a survey like Euclid, using GC only, will be sensitive to Modified Gravity parameters μ and η mainly in the first

three redshift bins, corresponding to a range $0. < z < 1.5$. The complete matrix W of coefficients relating the q_i to the p_i parameters, can be found in Tables 4.10 and 4.11 of Appendix 4.11.

4.5.4.2 ZCA for Weak Lensing

We apply the same decorrelation procedure to the WL case, obtaining the q vectors shown in the weight matrix of Figure 4.9 again reported explicitly in Tables 4.12 and 4.13 in Appendix 4.11.

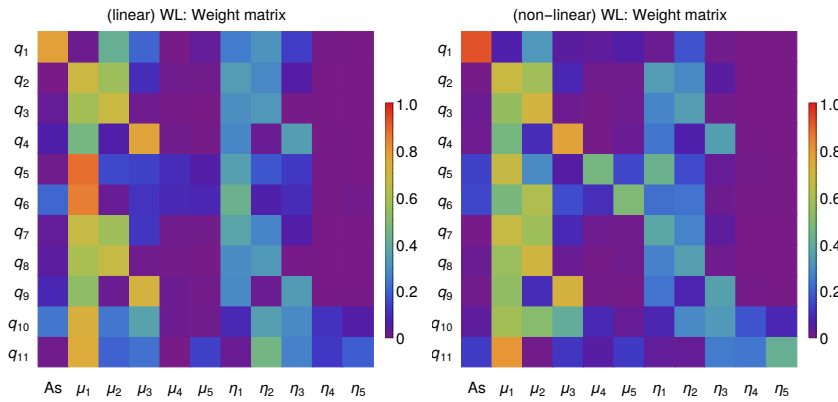


FIGURE 4.9: Entries of the matrix W that relates the q_i parameters to the original p_i ones, after applying the ZCA decorrelation of the covariance matrix in the linear and non-linear WL cases. This matrix shows for each new variable q_i on the vertical axis, the coefficients of the linear combination of parameters μ_i , η_i and A_s that give rise to that variable q_i . The red (blue) colors, indicate a large (small) contribution of the respective variable on the horizontal axis. **Left panel:** linear forecast for Weak Lensing Euclid Redbook specifications. **Right panel:** non-linear forecast for Weak Lensing Euclid Redbook specifications, using the HS prescription. As for GC, most q_i parameters have only small or negligible contributions from μ_5 and η_5 , which are found to be the less constrained bins.

In Figure 4.10 we show the comparison between the errors on the primary parameters p_i and the de-correlated ones q_i . As for the GC case, the errors in the linear case improve by 2 orders of magnitude after applying the decorrelation procedure (left panel). In the non-linear case (right panel) the improvement is smaller, but still worth to do, especially to constrain q_2, q_3, q_7, q_8 .

More generally, as we did for the GC case in the previous section, we look for the q_i parameters with the smallest relative errors (σ_{q_i}/q_i) and find in the linear WL case, that the best constrained combinations (ordered from most to least constrained) of primary parameters are given approximately by:

$$\begin{aligned} q_1 &= +0.76\ell A_s + 0.48\mu_2 + 0.33\eta_2 \\ q_3 &= -0.59\mu_1 + 0.67\mu_2 - 0.30\eta_1 + 0.32\eta_2 \\ q_7 &= +0.65\mu_1 - 0.60\mu_2 + 0.36\eta_1 - 0.28\eta_2 \\ q_2 &= +0.67\mu_1 - 0.59\mu_2 + 0.33\eta_1 - 0.29\eta_2 . \end{aligned} \tag{4.40}$$

This means that WL in the linear case will only be able to constrain combinations of the first two redshift bins in μ and η (corresponding to $0. < z < 1.0$). This can also be observed graphically in the left panel of Figure 4.11. For the non-linear WL case,

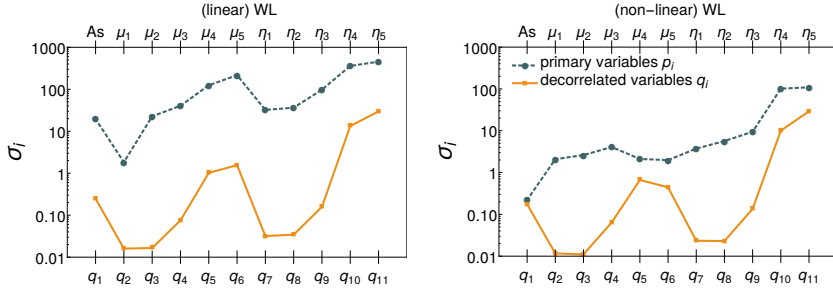


FIGURE 4.10: Results for a Euclid Redbook WL survey, with redshift-binned parameters, before and after applying the ZCA decorrelation. Each panel shows the 1σ fully marginalized errors on the primary parameters p_i (green dashed lines), and the 1σ errors on the decorrelated parameters q_i (orange solid lines). **Left:** Linear forecasts, performed with an $\ell_{\max} = 1000$ and linear matter power spectra. **Right:** Non-linear forecasts using the non-linear spectra with the HS prescription, up to an $\ell_{\max} = 5000$. The errors in the non-linear HS case, are about 1 order of magnitude smaller than in the linear case. For the best constrained q_i parameters, the decorrelated errors are up to 2 orders of magnitude smaller than the corresponding fully marginalized parameters on the parameters p_i .

the combinations remain practically the same, except for q_1 , which will depend much more strongly on the parameter $\ell \mathcal{A}_s$. The best 4 constrained parameters in this case, are (ordered from most to least constrained):

$$\begin{aligned} q_3 &= -0.55\mu_1 + 0.71\mu_2 + -0.27\eta_1 + 0.34\eta_2 \\ q_1 &= +0.93\ell \mathcal{A}_s - 0.32\mu_2 \\ q_2 &= +0.67\mu_1 - 0.60\mu_2 + 0.33\eta_1 - 0.29\eta_2 \\ q_4 &= -0.46\mu_1 + 0.29\mu_2 + 0.73\mu_3 + 0.31\eta_3 . \end{aligned} \quad (4.41)$$

These combinations can also be visualized in the right panel of Figure 4.11. The complete matrix W of coefficients relating the q_i to the p_i parameters, can be found in Tables 4.10 and 4.11 of Appendix 4.11.

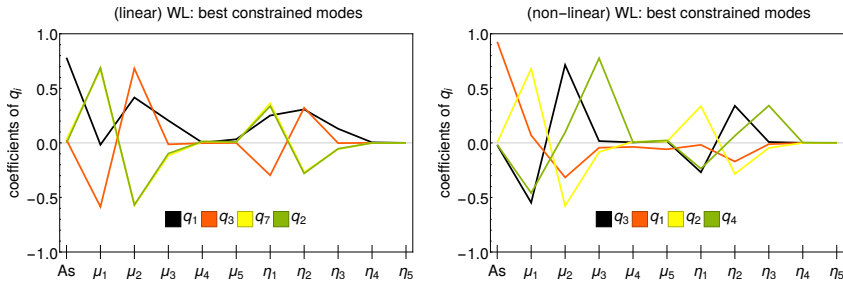


FIGURE 4.11: Best constrained modes for a Euclid Redbook WL survey, with μ and η binned in redshift, after transforming into uncorrelated q parameters via ZCA. Each of the four best constrained parameters q_i , shown in the panels, is a linear combination of the primary parameters p_i . q_i in the label are ordered from the best constrained to the least constrained.

4.5.4.3 ZCA for Weak Lensing + Galaxy Clustering + CMB *Planck* priors

As mentioned earlier, Galaxy Clustering and Weak Lensing are particularly important, combined together, to constrain Modified Gravity parameters, as they probe two independent combinations of the gravitational potentials. We now show results for their combination, using for both the non-linear HS prescription, together with a *Planck* prior (which was obtained by performing an MCMC analysis on *Planck*+BSH background data, as specified in Section 4.4.5). Notice that we neglect here any information coming from the cross correlation of the two probes; we therefore assume that these two observables are independent of each other and we simply add the GC and WL Fisher matrices to obtain our combined results; this appears to be a conservative (pessimistic) choice Lacasa and Rosenfeld, 2016. In Table ??, we can see that the inclusion of the *Planck* prior improves considerably certain parameters, especially the less constrained ones by GC+WL, namely $\mu_{4,5}$ and $\eta_{4,5}$. In terms of correlations, we can observe in the left panel of Fig. 4.12, that the structure of the correlation matrix resembles the one of the linear WL case (Fig. 4.5), except that the block of standard Λ CDM parameters is much less correlated and that the anti-correlation among μ_i and η_i is much stronger now. On the other hand, applying the decorrelation procedure (Section 4.5.4), the weight matrix W (right panel of Fig. 4.12), resembles the W matrix observed in the non-linear GC case, illustrated in Figure 4.6. Notice that now the variables q_i depend quite strongly on only one of the μ_i for $i = \{1, 2, 3, 4\}$, while the q_i for $i = \{6, 7, 8, 9, 10\}$ depend on a balanced sum of μ_i and η_i for $i = \{6, 7, 8, 9, 10\}$.

Finally, in this combined case the best constrained q_i variables, are q_1 , q_2 , q_3 , , q_4 approximately given by:

$$\begin{aligned} q_1 &= +0.93\ell\mathcal{A}_s \\ q_2 &= +0.84\mu_1 + 0.48\eta_1 \\ q_3 &= +0.80\mu_2 - 0.26\eta_1 + 0.45\eta_2 \\ q_4 &= +0.28\ell\mathcal{A}_s + 0.79\mu_3 - 0.29\eta_2 + 0.39\eta_3 . \end{aligned} \tag{4.42}$$

These combinations of primary parameters are illustrated in the right panel of Figure 4.13. The combination q_2 is similar to the combination $2\mu + \eta$ that was also identified in Planck Collaboration, Ade, and others, 2016 as being well-constrained. The best constrained modes q_2 , q_3 and q_4 all contain terms of the form $a\mu_i + b\eta_i$ for $i = \{1, 2, 3\}$, with positive coefficients a and b , where $a \approx 2b$.

All errors are shown in the left panel of Figure 4.13. Notice how in this case, the improvement on the errors of the q_i variables is less than an order of magnitude, thus smaller than what found in GC and WL separately; this is due to combination of GC and WL which, together with the inclusion of the CMB prior, lead to smaller correlations among the parameters. When combining GC+WL in the non-linear HS case, the FoC (defined in 4.29) is ≈ 31 , showing that there is not much gain in decorrelation, compared to GC or WL alone, where this quantity was approximately 32. However, combining GC+WL (non-linear HS) with *Planck* priors yields $\text{FoC} \approx 22$, showing that correlations among parameters are drastically reduced. The fact that the curve of 1σ errors for the q_i (orange line, marked with circles) follows the same pattern as the curve for the p_i errors (green dashed line, marled with circles), is due to the fact that we have used a ZCA decomposition and therefore the q_i are as close as possible to the p_i . The complete matrix of coefficients W can be found in Table 4.14 in appendix 4.11.

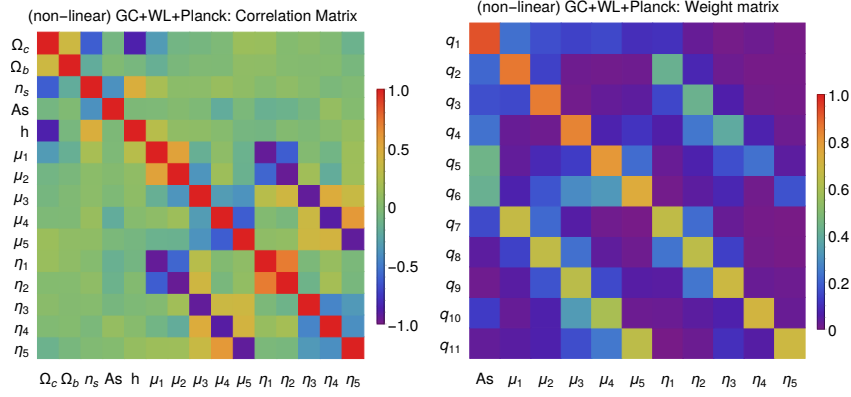


FIGURE 4.12: Results for the combined forecasts of Euclid Redbook GC+WL using the non-linear HS prescription together with the addition of *Planck* CMB priors. **Left panel:** correlation matrix obtained from the covariance matrix in the MG-binning case. Red (purple blue) colors represent strong positive (negative) correlations. The structure of this matrix is considerably diagonal, except for the strong anti-correlations of the pair (μ_i, η_i) for $i = \{1, 2, 3, 4, 5\}$, which resembles the correlations found for the WL case alone (see Figure 4.5). However, the sub-block of standard cosmological parameters is now much more diagonal and shows less correlations than in the GC (Fig. 4.4) or WL cases. The natural FoC (defined in 4.29) in this case is ≈ 22 , showing that the variables are much less correlated than in the two previous cases. **Right panel:** entries of the matrix W for the ZCA decorrelation of the covariance matrix. This matrix shows for each new variable q_i on the vertical axis, the coefficients of the linear combination of parameters μ_i and η_i that give rise to that variable q_i . The red (blue) colors, indicate a large (small) contribution of the respective variable on the horizontal axis.

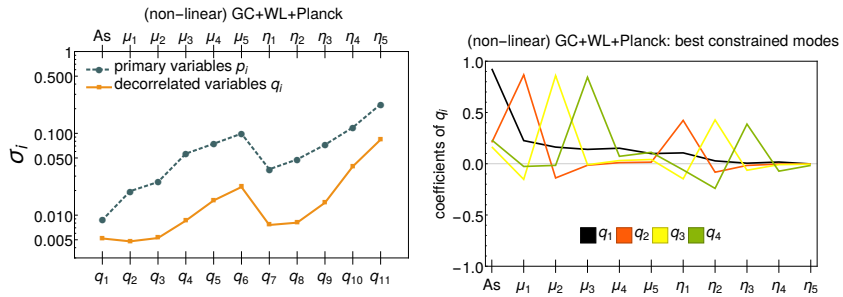


FIGURE 4.13: **Left:** the 1σ fully marginalized errors on the primary parameters p_i (green dashed lines), and the 1σ errors on the decorrelated derived parameters q_i (yellow solid lines). As opposed to the GC or WL cases (figs.4.7,4.10), here the decorrelated errors are much more similar to the standard errors. This is due to the fact that in the GC+WL+*Planck* combination, the cosmological parameters are not so strongly correlated. **Right:** best constrained modes for a Euclid Redbook GC+WL case using the non-linear HS prescription and adding a CMB *Planck* prior. Each panel shows the four best constrained parameters q_i . Each of them is a linear combination of the primary parameters p_i . The best constrained modes are sums $a\mu_i + b\eta_i$ for $i = \{1, 2, 3\}$ and positive values a and b .

4.6 Modified gravity with simple smooth functions of the scale factor

As discussed in Sec. 4.2, μ and η (or an equivalent pair of functions of the gravitational potentials) depend in general on time and space. We will now investigate the time dependence further, starting from the two parameterizations proposed in Planck Collaboration, Ade, and others, 2016 and recalled in Eqns. (4.9-4.12) in this paper. We extend the analysis of the *Planck* paper by testing different prescriptions for the non-linear regime in Modified Gravity (as illustrated in Section 4.3) and further investigate forecasts for future experiments like Euclid, SKA, DESI. In the following subsections we first give results for the late-time parameterization of Eqns. (4.9,4.10) and then for the early time parameterization of Eqns. (4.11,4.12). In both cases we consider Galaxy Clustering and Weak Lensing, neglecting, as in Section 4.5 any information coming from the cross correlation of the two probes.

4.6.1 Modified Gravity in the late-time parameterization

The late-time parameterization is defined in Eqns. (4.9,4.10). We now calculate forecasts for Galaxy Clustering and Weak Lensing, with future surveys, in the linear and mildly non-linear regimes. We also include prior information obtained from the analysis of the *Planck*+BSH datasets (where we recall that BSH stands for BAO + SNe + H_0 prior), as discussed in Section 4.4.5.

4.6.1.1 Galaxy Clustering in the linear and mildly non-linear regime

In Table 4.4 we show forecasts for the Euclid survey Laureijs and others, 2011 for Galaxy Clustering (top part of the table) and three different cases: using only linear scales with a cutoff at $k_{\max} = 0.15h/\text{Mpc}$, labeled GC(lin); extending forecasts in the mildly non-linear regime, obtained using the prescription described in Sec. 4.3.2.2, with a cutoff at $k_{\max} = 0.5 h/\text{Mpc}$, labeled GC(nl-HS); combining the mildly non-linear case with *Planck* priors, as described in Sec. 4.4.5. We take into account the BAO features, redshift space distortions and the full shape of the power spectrum, as well as the survey specifications of the Euclid Redbook, recalled in Section 4.4.2 for convenience. The columns correspond to the marginalized errors on five standard cosmological parameters $\{\Omega_c, \Omega_b, n_s, \ln(10^{10} A_s), h\}$ and three combinations of the gravitational potentials $\{\mu, \eta, \Sigma\}$: the latter are reconstructed in time, according to the late-time parameterization, as defined in Eqns. (4.9,4.10). We recall that only two of these three functions are independent and fully determine cosmological linear perturbations.

In the late-time scenario, for a Galaxy Clustering survey, neither η nor Σ are actually constrained by a linear forecast, while μ is mildly constrained. Adding the non-linear regime improves constraints on μ , while the other parameters remain unconstrained, unless we also include *Planck* priors, which yields an improvement in the FoM of 6.3 nits. In general the observable power spectrum may depend on both μ (explicitely appearing in the last term of the equation for the density perturbation (cf. Eqn.(4.61)) and on η (implicitly contained in the derivatives of the gravitational potential in the same equation). The contribution of the derivative of the potentials is larger in the early-time parameterization, with respect to the late-time one by construction. This is due to the fact that in the late-time case deviations from GR go to zero at large redshifts. In this sense, in the specific case of the late time parameterization, the observed power spectrum mainly depends on μ only,

which explains why this is the only quantity (mildly) constrained by GC alone. In the early-time parameterization, though, modifications can appear also at earlier times, so that both η and μ effectively affect the power spectrum, which explains why they can both be constrained with a smaller uncertainty, as we will discuss in Section 4.6.2.

In Appendix 4.9 we review the equation governing the evolution of cold dark matter density fluctuations, as a function of the Modified Gravity functions $\mu(a)$ and $\eta(a)$ as they are implemented in the code MGCAMB Hojjati, Pogosian, and Zhao, 2011. The inability of GC to constrain η in this parametrization, is also visible in Fig. 4.14 which shows that the GC constraints are degenerate along the η or Σ directions. Therefore, we show how with this parameterization choice Euclid GC will be extremely sensitive to modifications of the Poisson equation for Ψ , while it would require additional information to constrain departures from the standard Weyl potential.

4.6.1.2 Weak Lensing in the linear and mildly non-linear regime

Using the Euclid Weak Lensing specifications described in Section sub:Fisher-Weak-Lensing, we obtain the results displayed in the middle panel of Table 4.4. Also in this case, we use the late-time parameterization, in three different cases: the first uses only linear quantities, with a maximum multipole of $\ell_{\max} = 1000$; the second case uses the non-linear HS prescription of section 4.3.2.2 up to a maximum multipole of $\ell_{\max} = 5000$; the third case combines Weak Lensing with *Planck* priors, as described in 4.4.5.

In the linear case, WL forecast yields constraints on the standard Λ CDM parameters at around 10% of accuracy, with the exception of Ω_b which is poorly constrained at around 26%, and the expansion rate h (19%). This is likely due to the fact that WL is only directly sensitive to the total matter distribution in the Universe and cannot differentiate baryons from dark matter. All constraints improve when adding non-linear information, with Ω_b and h still constrained only at the level of about 20%. When the *Planck* priors are included, though, constraints shrink down to about 1% for all cosmological parameters. The Modified Gravity parameters show the expected trend; in the linear case, only Σ is constrained, at 11%, as this parameter is directly defined in terms of the lensing potential $\Phi + \Psi$; a Weak Lensing probe is however not directly sensitive to μ and η separately, as can be seen in Fig. 4.14. The linear FoM is only slightly weaker than the one from GC for this parameterization, probably because both probes have an effectively unconstrained degeneracy direction. When adding non-linear information, errors on μ and η improve, though still remaining in a poorly constrained interval (25%-44%). Already on its own, however, Weak Lensing could rule out many models of Modified Gravity that change Σ at more than 5% (or even 2.9%, if we include *Planck* priors). The combination GC+*Planck* and WL+*Planck* has a comparable overall constraining power, with GC+*Planck* being about 1 nit stronger and providing smaller errors on μ .

4.6.1.3 Combining Weak Lensing and Galaxy Clustering

After using the two primary probes from Euclid separately, we discuss here the constraints obtained combining Weak Lensing and Galaxy Clustering. The combination between GC and WL can be seen in the bottom panel of Table 4.4. In the late-time parameterization, in the linear case, Weak Lensing combined with a

Euclid (Redbook)	Ω_c	Ω_b	n_s	$\ell\mathcal{A}_s$	h	μ	η	Σ	MG F
Fiducial	0.254	0.048	0.969	3.060	0.682	1.042	1.719	1.416	relative
GC(lin)	1.9%	6.4%	3%	2.8%	4.5%	17.1%	1030%	641%	0
GC(nl-HS)	0.9%	2.5%	1.3%	0.8%	1.7%	1.7%	475%	291%	2.9
GC(nl-HS)+Planck	0.7%	0.6%	0.3%	0.2%	0.3%	1.7%	16.8%	10.3%	6.3
WL(lin)	7.8%	25.7%	9.9%	10.3%	19.1%	58.2%	106%	9.3%	3.2
WL(nl-HS)	6.3%	20.7%	4.6%	5.8%	13.8%	23.3%	40.9%	4.6%	4.5
WL(nl-HS)+Planck	2.1%	1.1%	0.4%	0.7%	0.7%	11.8%	21.8%	2.8%	5.7
GC+WL(lin)	1.8%	5.9%	2.8%	2.3%	4.2%	7.1%	10.6%	2%	6.6
GC+WL(lin)+Planck	1.0%	0.7%	0.4%	0.4%	0.4%	6.2%	9.8%	1.5%	7.0
GC+WL(nl-HS)	0.8%	2.2%	0.8%	0.7%	1.5%	1.6%	2.4%	1.0%	8.8
GC+WL(nl-HS)+Planck	0.7%	0.6%	0.2%	0.2%	0.3%	1.6%	2.4%	0.9%	8.9
GC+WL(nl-Halofit)+Planck	0.6%	0.5%	0.2%	0.2%	0.2%	0.8%	1.7%	0.8%	9.0

TABLE 4.4: 1σ fully marginalized errors on the cosmological parameters in the late-time parameterization of Modified Gravity for a Euclid Galaxy Clustering forecast (top), a Weak Lensing forecast (middle) and the combination of both probes (bottom): Modified Gravity is encoded in two of the three functions μ , η , Σ , which are reconstructed in the late-time parameterization defined in Eqns. (4.9,4.10). For each case, we also list the forecasted errors using a *Planck*+BSH prior. Linear forecasts are labeled by “lin”, and correspond to a cut-off $k_{\max} = 0.15h/\text{Mpc}$ for GC and $\ell_{\max} = 5000$ for WL; non-linear forecasts use the prescription described in sec. 4.3.2.2, are labeled by “nl-HS” and correspond to a cutoff of $k_{\max} = 0.5h/\text{Mpc}$ for GC and $\ell_{\max} = 5000$ for WL. in both cases, power spectra have been computed using the MGCAmb Boltzmann code. For completeness, we also show the GC+WL+*Planck* case using the non-linear power spectra computed using Halofit only (nl-Halofit). In the last column, we show for each observation the Figure of Merit (FoM) relative to our base observable in this parametrization, which is GC(linear). GC(linear) has an absolute FoM of -0.94 in ‘nits’. We can see that in both GC and WL there is a considerable gain when including non-linear scales and *Planck* priors. The difference in the FoM between the non-linear HS prescription and the standard Halofit approach is quite small.

galaxy clustering for a Euclid survey (Redbook specifications) constrains the standard Λ CDM parameters in the range $2\% - 6\%$, and below 1% when *Planck* priors are included. Modified Gravity parameters μ and η are now also constrained below 10% , reaching 1% when adding non-linear scales. The remarkable improvement can be attributed to the fact that the combination of GC and WL Fisher matrices breaks many degeneracies in the parameter space. This is shown in Figure 4.14, where it is possible to notice how the two probes are almost orthogonal both in the μ - η - and μ - Σ -plane. Weak Lensing measures the changes in the Weyl potential, parametrized by Σ , while μ is related to the Poisson equation, and therefore to the potential Ψ , modified by peculiar velocities and sensitive to Galaxy Clustering; η can also be written as a combination of μ and Σ (see Eqn. 4.5).

Euclid (Redbook)	Ω_c	Ω_b	n_s	$\ell\mathcal{A}_s$	h	μ	η	Σ
Fiducial	0.256	0.048	0.969	3.091	0.682	0.902	1.939	1.326
GC(lin)	3.7%	19.2%	9.1%	16.6%	16.5%	16.7%	758%	489%
GC(nl-HS)	1.1%	2.3%	1.3%	0.7%	1.6%	1.8%	7.9%	4.8%
GC(nl-HS)+Planck	0.8%	0.7%	0.3%	0.3%	0.3%	1.7%	7.6%	4.6%
WL(lin)	12.1%	28.9%	11.3%	13.3%	24%	6.8%	11.1%	11.9%
WL(nl-HS)	6.5%	21.9%	6.6%	5.9%	15.8%	2.8%	8.0%	3.4%
WL(nl-HS)+Planck	2.1%	1.3%	0.5%	0.9%	0.7%	2.2%	7.2%	2.9%
GC+WL(lin)	1.8%	6.6%	3.4%	5.6%	5.2%	3.0%	6.8%	3.4%
GC+WL(lin)+Planck	1.2%	0.9%	0.6%	2.3%	0.4%	2.4%	6.5%	2.8%
GC+WL(nl-HS)	1.0%	2.2%	1.2%	0.7%	1.6%	1.3%	4.4%	1.9%
GC+WL(nl-HS)+Planck	0.8%	0.7%	0.3%	0.3%	0.3%	1.3%	4.4%	1.9%
GC+WL(nl-Halofit)+Planck	0.7%	0.7%	0.3%	1.3%	0.3%	0.9%	2.3%	1%

TABLE 4.5: Same as Table (4.4) but for the early-time parameterization. Note that the last column (MG FoM) cannot be compared to the one for a different parameterization (Table 4.4) since the reference value is different (GC(lin)) and the two parameterizations have a different number of primary parameters). In this case the absolute MG FoM of GC(lin) is ≈ -0.47 nits.

Further improvement is brought by the sensitivity of Galaxy Clustering to standard Λ CDM parameters; even though GC constraints on Σ and η are not as good as the ones for Weak Lensing, the better measurement of standard parameters provided by Galaxy Clustering breaks degeneracies in the Modified Gravity sector of the parameter space, leading to narrower bounds for η and Σ with respect to both probes taken separately. WL is instead not sensitive to modifications of the Poisson equation for matter and this explains why constraints on μ are not improved by the combination of the two probes, but are rather dominated by GC. The correlation among parameters can also help us explain the observed results. The Figure of Correlation, defined in Eq. (4.29), for GC (non-linear HS) alone is 4.9, while for WL (non-linear HS) the correlation is higher, with FoC = 16.9. When combining both probes (GC+WL (non-linear HS)) the FoC goes to an intermediate point of 7.6.

Given the constraining power of the GC+WL combination on MG functions, adding the *Planck* priors does not lead to significant improvements on the dark energy related parameters. On the other hand, standard parameters significantly benefit from the inclusion of CMB and background priors and we can expect this to be a relevant factor for MG models with degeneracies with Λ CDM parameters, e.g. models affecting also the expansion history of the universe. An overview of the constraints on Modified Gravity described in this section is shown in Fig.4.14, with Euclid GC, Euclid WL and Euclid GC+WL combined with *Planck* priors.

4.6.1.4 Forecasts in Modified Gravity for SKA1, SKA2 and DESI

For the SKA1 and SKA2 surveys (whose specifications are explained in detail in Section 4.4.1), previous work on forecasting cosmological parameters has been done, among others, by Baker and Bull, 2015 and Bull, 2015. In the latter work, the author

	Ω_c	Ω_b	n_s	$\ell\mathcal{A}_s$	h	μ	η	Σ	MG FoM
Fiducial	0.254	0.048	0.969	3.060	0.682	1.042	1.719	1.416	relative
GC(nl-HS)									
Euclid	0.9%	2.5%	1.3%	0.8%	1.7%	1.7%	475%	291%	2.9
SKA1-SUR	5%	15.3%	8.7%	3.8%	10.8%	18.1%	165%	108%	1.7
SKA2	0.5%	1.3%	0.4%	0.4%	0.8%	0.7%	86.8%	53.2%	5.5
DESI-ELG	1.6%	4.1%	2.3%	1.3%	2.9%	3.3%	899%	552%	1.8
WL(nl-HS)									
Euclid	6.3%	20.7%	4.6%	5.8%	13.8%	23.3%	40.9%	4.6%	4.5
SKA1	30.8%	109%	35%	36.5%	77.6%	220%	405%	36.8%	0.5
SKA2	6%	22.5%	5.9%	6.8%	15.9%	19%	33.2%	3.7%	4.9
GC+WL(lin)									
Euclid	1.8%	5.9%	2.8%	2.3%	4.2%	7.1%	10.6%	2%	6.6
SKA1	10.1%	47.6%	25.4%	21.7%	40.4%	26.4%	28.8%	13.6%	3.7
SKA2	1.2%	4.5%	2.2%	1.9%	3.3%	4.1%	5.5%	1.6%	7.5
GC+WL(lin)+Planck									
Euclid	1.0%	0.7%	0.4%	0.4%	0.4%	6.2%	9.8%	1.5%	6.9
SKA1	2.4%	1.2%	0.4%	1.2%	0.7%	12%	19.8%	3.8%	5.3
SKA2	0.7%	0.6%	0.3%	0.4%	0.3%	3.6%	5.2%	1.2%	7.8
GC+WL(nl-HS)									
Euclid	0.8%	2.2%	0.8%	0.7%	1.5%	1.6%	2.4%	1.0%	8.7
SKA1	4.7%	14.3%	6.2%	3.6%	9.6%	12.8%	11%	7.3%	5.5
SKA2	0.4%	1.3%	0.3%	0.4%	0.8%	0.7%	0.9%	0.6%	10.3
GC+WL(nl-HS)+Planck									
Euclid	0.7%	0.6%	0.2%	0.2%	0.3%	1.6%	2.4%	0.9%	8.9
SKA1	2.0%	1.0%	0.4%	0.8%	0.6%	3.5%	6%	2.7%	6.9
SKA2	0.4%	0.5%	0.2%	0.1%	0.2%	0.6%	0.9%	0.5%	10.3

TABLE 4.6: 1σ fully marginalized errors on the cosmological parameters $\{\Omega_m, \Omega_b, h, \ell\mathcal{A}_s, n_s, \mu, \eta, \Sigma\}$ in the late-time parameterization comparing different surveys in the linear and non-linear case. In the last column, we show for each observation the Modified Gravity Figure of Merit (MG FoM) relative to our base observable, which is the Euclid Redbook GC(linear), see Table 4.4. We can see that in general terms, SKA2 is the most powerful survey, followed by Euclid and SKA1. In the case of GC alone, DESI-ELG is more constraining than SKA1-SUR. Notice that in this parameterization, a GC survey would only constrain μ with a high accuracy, while a WL survey would constrain Σ with a very good accuracy. The combination of both is much more powerful than the single probes. Adding *Planck* priors (last row) improves considerably the constraints on the Λ CDM parameters but has an almost negligible effect on the MG parameters (MG FoM remain almost constant when adding *Planck* priors to the GC+WL (non-linear HS) case. The marginalized contours for the μ - η plane , comparing these surveys, can be seen in the left panel off Fig.4.16.

	Ω_c	Ω_b	n_s	$\ell\mathcal{A}_s$	h	μ	η	Σ	MG FoM
Fiducial	0.256	0.0485	0.969	3.091	0.682	0.902	1.939	1.326	relative
GC(nl-HS)									
Euclid	1.1%	2.3%	1.3%	0.7%	1.6%	1.8%	7.9%	4.8%	6.6
SKA1-SUR	7.9%	14.2%	13.4%	4.2%	11%	12.6%	82.7%	52.6%	2.2
SKA2	0.6%	1.3%	0.7%	0.4%	0.9%	0.9%	3.4%	1.8%	8.3
DESI-ELG	2.0%	4.3%	2.7%	1.4%	3.0%	8.2%	32%	28.6%	4.3
WL(nl-HS)									
Euclid	6.5%	21.9%	6.6%	5.9%	15.8%	2.8%	8.0%	3.4%	6.6
SKA1	32%	106%	37.2%	33%	79.3%	13.1%	37.1%	16.4%	3.4
SKA2	5.9%	22.1%	6.7%	6.1%	16.1%	2.4%	7.0%	2.9%	6.9
GC+WL(lin)									
Euclid	1.8%	6.6%	3.4%	5.6%	5.2%	3.0%	6.8%	3.4%	6.4
SKA1	10.3%	46.4%	24.2%	33.6%	40.2%	14.4%	29.6%	15.5%	3.3
SKA2	1.3%	4.9%	2.5%	4.2%	3.9%	2.5%	5.7%	2.7%	6.8
GC+WL(lin)+Planck									
Euclid	1.2%	0.9%	0.6%	2.3%	0.4%	2.4%	6.5%	2.8%	6.8
SKA1	2.5%	1.5%	0.8%	2.9%	0.8%	8.8%	22.2%	8.5%	4.5
SKA2	0.9%	0.7%	0.6%	2.1%	0.3%	2.1%	5.4%	2.3%	7.2
GC+WL(nl-HS)									
Euclid	1.0%	2.2%	1.2%	0.7%	1.6%	1.3%	4.4%	1.9%	8.1
SKA1	7.1%	13.4%	10.7%	4%	10%	8.2%	24.4%	10.5%	4.4
SKA2	0.6%	1.3%	0.7%	0.4%	0.9%	0.8%	2.7%	1.3%	8.8
GC+WL(nl-HS)+Planck									
Euclid	0.8%	0.7%	0.3%	0.3%	0.3%	1.3%	4.4%	1.9%	8.1
SKA1	2.1%	1.3%	0.5%	0.9%	0.7%	7%	20.8%	8.2%	4.9
SKA2	0.5%	0.5%	0.3%	0.2%	0.2%	0.8%	2.7%	1.3%	8.8

TABLE 4.7: Same as Table 4.6 but for the early-time parameterization. The last 4 columns correspond to the projection of the errors on E_{11} and E_{22} onto μ , η and Σ , respectively. We have marginalized over E_{12} and E_{21} since at $z = 0$ they don't contribute to the Modified Gravity parameters. Notice that in this parameterization, a GC survey alone is able to constrain both μ and Σ to a good level for all surveys, better than with the late time parameterization, more often used in literature. The combination of GC+WL is however less constraining in the early time parametrization than in late time parameterization one. The reference case for the MG FoM is the Euclid (Redbook) GC linear forecast (Table 4.5). The non-linear forecast for GC+WL+*Planck* would yield, for Euclid and SKA2, constraints at the 1-2% accuracy on μ , Σ , while for SKA1 the constraints would be at the 8% level. The marginalized contours for the μ - η plane, comparing these surveys, can be seen in the right panel of Fig.4.16.

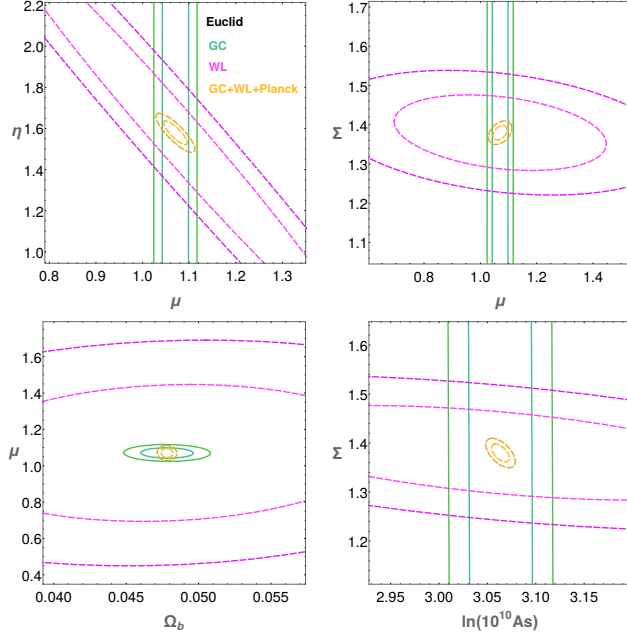


FIGURE 4.14: Fisher Matrix marginalized contours ($1, 2 \sigma$) for the Euclid space mission in the late-time parameterization using mildly non-linear scales and the HS prescription. Green lines represent constraints from a Galaxy Clustering survey, pink lines stand for the Weak Lensing observables, and orange lines represent the GC+WL+*Planck* combined confidence regions. **Upper Left:** contours for the fully marginalized errors on η and μ . **Upper Right:** contours for the fully marginalized errors on Σ and μ . **Lower Left:** contours for the fully marginalized errors on μ and Ω_b . **Lower Right:** contours for the fully marginalized errors on Σ and $\ln(10^{10} A_s)$. The fact that the combination of GC, WL and *Planck* breaks many degeneracies in the 7-dimensional parameter space, explains why the combined contours (yellow) have a much smaller area. Notice that in this parametrization, GC measures mostly μ and WL constrains mostly just Σ .

parameterizes the evolution of $\mu(a)$ using the late-time parameterization, but also adds an extra parameter allowing for a scale dependence in $\mu(a)$ and including a *Planck* prior. For a fixed scale, the 1σ errors on the amplitude of μ lie between 0.045 and 0.095, depending on the details of the SKA1 specifications, while for SKA2, this error is of about 0.017. This setting would correspond to our GC+WL(linear) + *Planck* case (see Table 4.6) where we find for SKA1 a 1σ error on μ of 0.12 and for SKA2 the forecasted error is 0.036. Our errors are somewhat larger, but we also have extended our analysis to let the gravitational slip η be different from 1 at present time, our departure from $\mu = 1$ at present time is larger by a factor 4 and our linear forecast is conservative in the sense that it includes less wavenumbers k at higher redshifts, compared to theirs.

In Figure 4.15 we show the 1σ fully marginalized forecasted errors on the parameters $\{\Omega_m, \Omega_b, h, \ell A_s, n_s, \mu, \Sigma\}$ for different Weak Lensing (left panel) and Galaxy Clustering (right panel) surveys in the late-time parameterization. In the GC case, the surveys considered are DESI-ELG (yellow), SKA2 (green), SKA1-SUR (orange) and Euclid (blue). For the WL forecast, we considered Euclid (blue), SKA1 (orange) and SKA2 (green). These constraints correspond to the ones listed in Table 4.6. The marginalized confidence contours for the μ - η plane , comparing all these surveys,

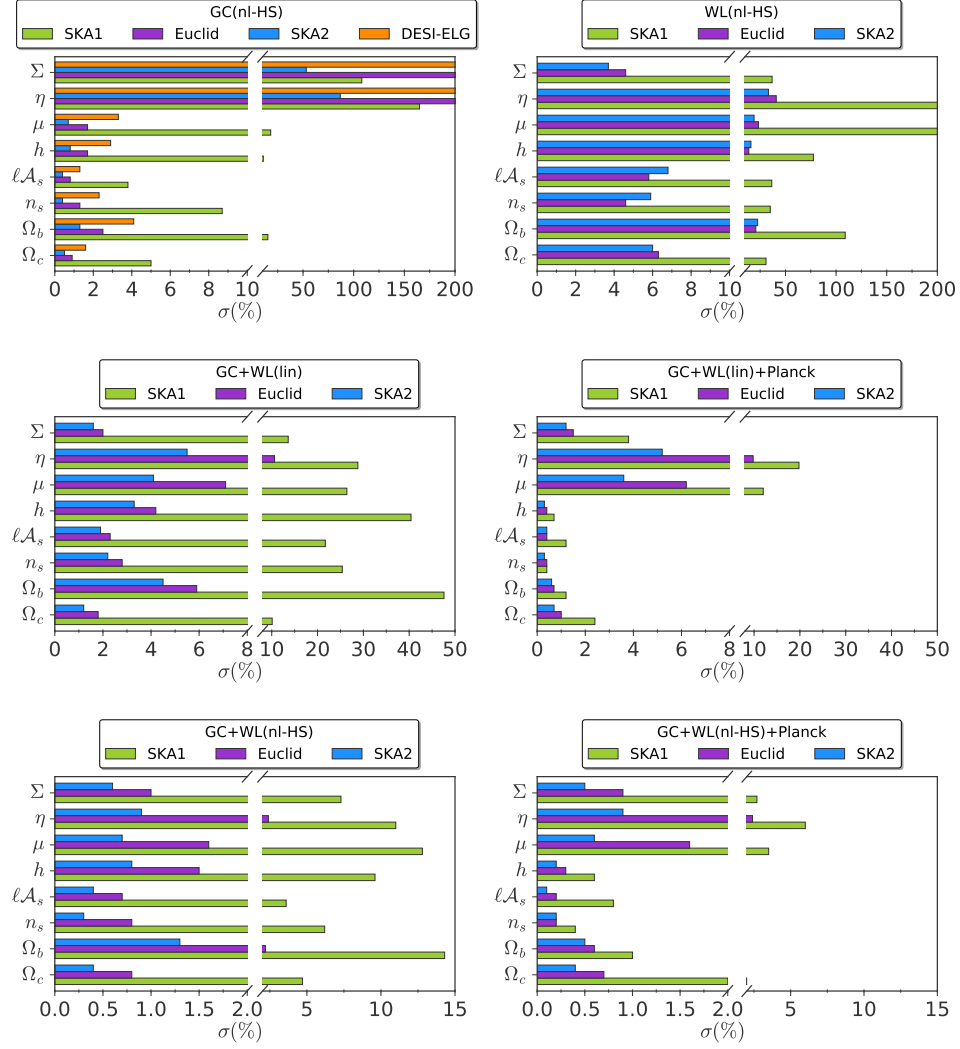


FIGURE 4.15: 1σ fully marginalized errors on the parameters $\{\Omega_m, \Omega_b, h, \ell\mathcal{A}_s, n_s, \mu, \eta, \Sigma\}$ for the late-time parameterization of MG obtained by forecasts on Galaxy Clustering (non-linear HS) (top left panel), Weak Lensing (non-linear HS) (top right panel), the combinations GC+WL (linear) (middle left) and GC+WL+Planck (linear) (middle right) and the combinations GC+WL (non-linear HS) (bottom left) and GC+WL+Planck (non-linear) (bottom right). In the GC case, the surveys considered are SKA2 (blue), SKA1-SUR (green), Euclid Redbook (purple) and DESI-ELG (orange). For forecasts including WL, only Euclid, SKA1 and SKA2 are included. Although the 1σ constraints on the standard parameters are overall weaker for WL than for GC, Weak Lensing surveys perform better on Modified Gravity parameters. Comparing the different surveys, Euclid and SKA2 perform similarly well for the WL observable alone, if non-linearities are included. Notice that SKA1-SUR performs better than Euclid on the η and Σ parameters, because it can measure better at lower redshifts. Including the Planck prior, the GC+WL combination for Euclid and SKA2 constrains all parameters at much better than percent accuracy. Detailed specifications of the different surveys are explained in the text.

can be seen in the left panel of Fig. 4.16. The 1σ fully marginalized constraints on the parameters are weaker for WL than for GC, which may be a consequence of the higher correlation among variables for the Weak Lensing observable, described in the previous section 4.6.1.3. Comparing the different surveys, the general trend is that Euclid and SKA2 perform at a similar level for WL at both linear and non-linear level; for GC and when combining both probes, SKA2 gives the strongest constraints, followed by Euclid, SKA1 and DESI (for GC). Notice that in this parameterization, a SKA1-SUR GC survey constrains the Σ parameter alone better than a Euclid Galaxy Clustering survey (although Euclid is overall much stronger as can be seen with the FoM). This is due to the fact that SKA1-SUR probes much lower redshifts (from $z = 0.05 - 0.85$) than Euclid and is therefore suitable to better constrain those parameterizations in which the effect of the Modified Gravity parameters is stronger at lower redshifts; this is the case of the late-time parameterization, which is proportional to the dark energy density, dominating at low redshifts only. This result is reversed in the early time parameterization, in which Modified Gravity can play a role also at earlier redshifts.

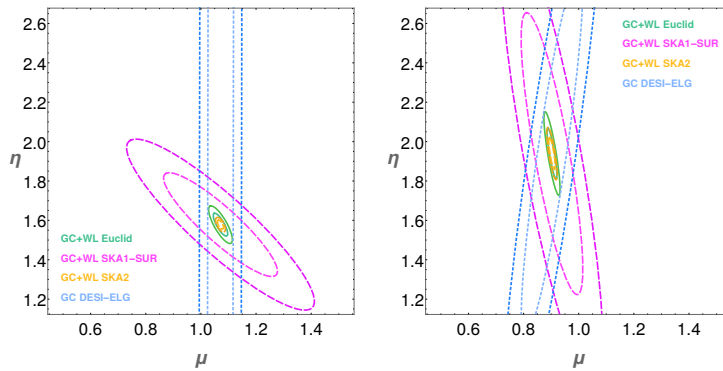


FIGURE 4.16: 1σ and 2σ fully marginalized confidence contours on the parameters μ and η , for 3 different surveys combining Galaxy Clustering (GC) and Weak Lensing (WL): Euclid, SKA1-SUR and SKA2 and for GC only: DESI-ELG, all in the late-time (left panel) and early-time (right panel) parameterizations of sections 4.6.1 and 4.6.2, respectively. As explained in the main text, the constraints are parameterization-dependent, especially on η , where in the late-time scenario GC alone is not able to constrain it, while in the early-time scenario GC can constrain both μ and η .

4.6.2 Modified Gravity in the early-time parameterization

4.6.2.1 Galaxy Clustering, Weak Lensing and its combination

We extend our analysis now to an alternative choice, the early time parameterization specified in Eqns. (4.11) and (4.12). As before, we use Euclid Redbook specifications for WL and GC and the cut in scales discussed previously for the two observables, i.e. a maximum wavelength cutoff at $k_{\max} = 0.15$ for GC and a maximum multipole of $\ell_{\max} = 1000$ for WL in the linear case, and a cutoff $k_{\max} = 0.5h/\text{Mpc}$ and a maximum multipole of $\ell_{\max} = 5000$ for WL in the non-linear regime, which is analyzed using the prescription described in Sec. 4.3.2.2. We use the two observables both separately and in combination, without accounting for cross correlation of the two (as discussed in section 4.5 this seems to correspond to a conservative choice), with and without *Planck* priors.

Results are shown in Table 4.5 and Figure 4.17. The general behaviour of the constraints is similar to the one in the late-time parameterization, with the combination of GC and WL able to break the degeneracies with standard cosmological parameters, leading to a significant improvement of the constraints on MG parameters, constraining μ and Σ at the 1-2% level. There are some other interesting differences with the late-time scenario. First, the addition of *Planck* priors does not really improve much the constraints obtained by GC or WL alone, which was not the case in the late-time parameterization. This is related to the fact that in the early-time parameterization, GC and WL (non-linear) on their own are already good at constraining both μ (at 2-3 %) and η (at around 8%), with consequently small errors on Σ ($\approx 3\%$). In Appendix 4.9 we show the derivatives of the matter power spectrum with respect to the MG parameters μ and η in both parameterizations. We can observe that in the early-time scenario, the derivative $dP(k)/d\eta$ is larger than in the late-time parameterization, leading therefore to better constraints. Another difference lies in the correlation among parameters, which for WL and GC+WL is considerably smaller than in the late-time scenario. The Figure of Correlation (defined in Eqn. 4.29) for GC (non-linear HS) alone is 4.7, while for WL (non-linear HS) the correlation is somewhat higher, with FoC = 7.3. When combining both probes (GC+WL (non-linear HS)) the FoC goes to an intermediate point of 5.2.

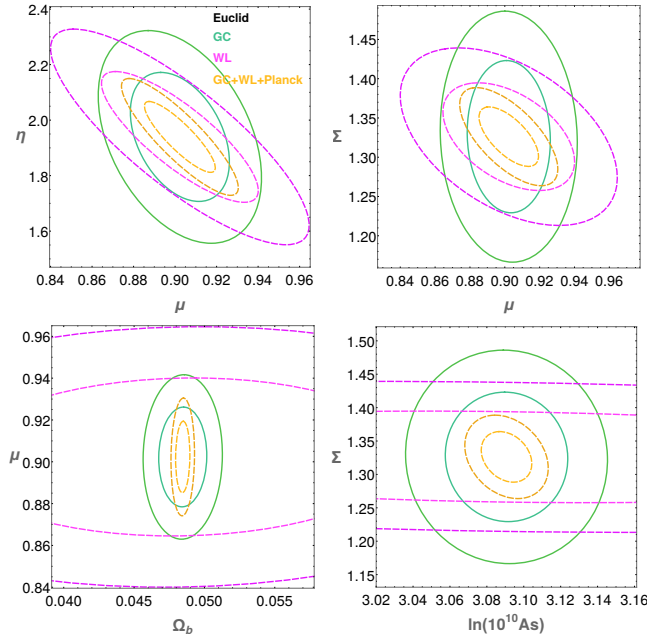


FIGURE 4.17: Fisher Matrix marginalized forecasted contours (1σ , 2σ) for the Euclid Redbook satellite in the early-time parameterization using mildly non-linear scales and the HS prescription. Green lines represent constraints from the Galaxy Clustering survey, pink lines stand for the Weak Lensing observables, and orange lines represent the GC+WL+*Planck* combined confidence regions. **Upper left:** contours for the fully marginalized errors on η and μ . **Upper right:** contours for the fully marginalized errors on Σ and μ . **Lower left:** contours for the fully marginalized errors on μ and Ω_b . **Lower right:** contours for the fully marginalized errors on Σ and $\ln 10^{10} A_s$. Notice that in this parameterization, GC and WL are able to constrain both μ and η or Σ on their own.

4.6.2.2 Other Surveys: DESI-ELG, SKA1 and SKA2

Also in the early time parameterization we obtain the 1σ fully marginalized errors for Galaxy Clustering (top left panel of Figure 4.18) considering DESI-ELG (yellow), SKA2 (green), SKA1-SUR (orange) and Euclid (blue), and for Weak Lensing (top right panel of Figure 4.18) using Euclid (blue), SKA1 (orange) and SKA2 (green). We also report the results in Table 4.7, where it is possible to notice how the conclusions drawn on the hierarchy of the considered experiments do not change with respect to the late-time parameterization. The main difference is that in this case the full SKA1-SUR GC survey does not constrain the Σ parameter better than the Euclid survey; this is due to the fact that in the early time parametrization, deviations from Λ CDM are present also at high redshift, therefore we do expect the information present at small redshift to be as relevant as the one coming from higher z , where Euclid performs significantly better than SKA1-SUR. The marginalized contours for the μ - η plane, comparing all these surveys, can be seen in the right panel of Fig. 4.16.

4.6.3 Testing the effect of the Hu-Sawicki non-linear prescription on parameter estimation

In this section we show the effect of changing the parameters c_{nl} and s used in the HS prescription (specified in Eq. 4.13) for the mildly non-linear matter power spectrum. As mentioned already in Section 4.3.2.2, previous works (see Zhao, 2014; Zhao, Li, and Koyama, 2011; Koyama, Taruya, and Hiramatsu, 2009), have fitted the values of c_{nl} and s to match N-body simulations in specific Modified Gravity models. In all these cases the HS parameters c_{nl} and s have been found to be of order unity, with c_{nl} ranging usually from 0.1 to 3 and s from about 1/3 to a value of around 2. In the absence of N-body simulations for our models, we selected our benchmark HS parameters to be $c_{\text{nl}} = 1$ and $s = 1$, as discussed in Section 4.3.2.2, which we used for all the analysis presented above. However, in order to test the effect of a change of c_{nl} and s non-linear parameters on our estimation of errors on the cosmological parameters, we perform our GC and WL forecasts on the MG late-time model (Section 4.6.1) also changing one at a time the values of both HS parameters. We use the following values for our test: $c_{\text{nl}} = \{0.1, 0.5, 1, 3\}$ and $s = \{0, 1/3, 2/3, 1\}$.

In Figure 4.19 we show the percentage discrepancy between the 1σ marginalized error obtained on parameters in the GC non-linear HS benchmark case (see Table 4.4 for the exact values) and the corresponding error obtained by performing the same forecast with a different value of the $c_{\text{nl}}\text{-}s$ parameters. In general terms we see that for the MG parameter μ (left panel of Figure 4.19) the relative difference in the estimation of the 1σ forecasted errors can lie between 90% (at $c_{\text{nl}} = 3, s = 0.33$) and -30% for $c_{\text{nl}} = 0.1$ and $s = 1.0$. The behavior of the contour lines shows us that for a fixed value of c_{nl} , the forecasted error on the parameter μ remains unaffected. For η (right panel) the relative discrepancy lies between 40% and -2%. Here, to get the same 1σ errors on η , one would have to vary both c_{nl} and s . We also tested the effect on the standard Λ CDM parameters and found it to be smaller than 4% for all choices of c_{nl} and s . In the case of WL forecasts, we perform the same tests, which are shown in Figure 4.20. We can observe that the relative discrepancies in the case of the μ parameter lie between $\sim 60\%$ and $\sim -15\%$, while for Σ the discrepancy is considerably smaller. The 1σ error on Σ varies only between $\pm 6\%$. This is however a particular effect of choosing Σ , which is the true WL observable. If we perform

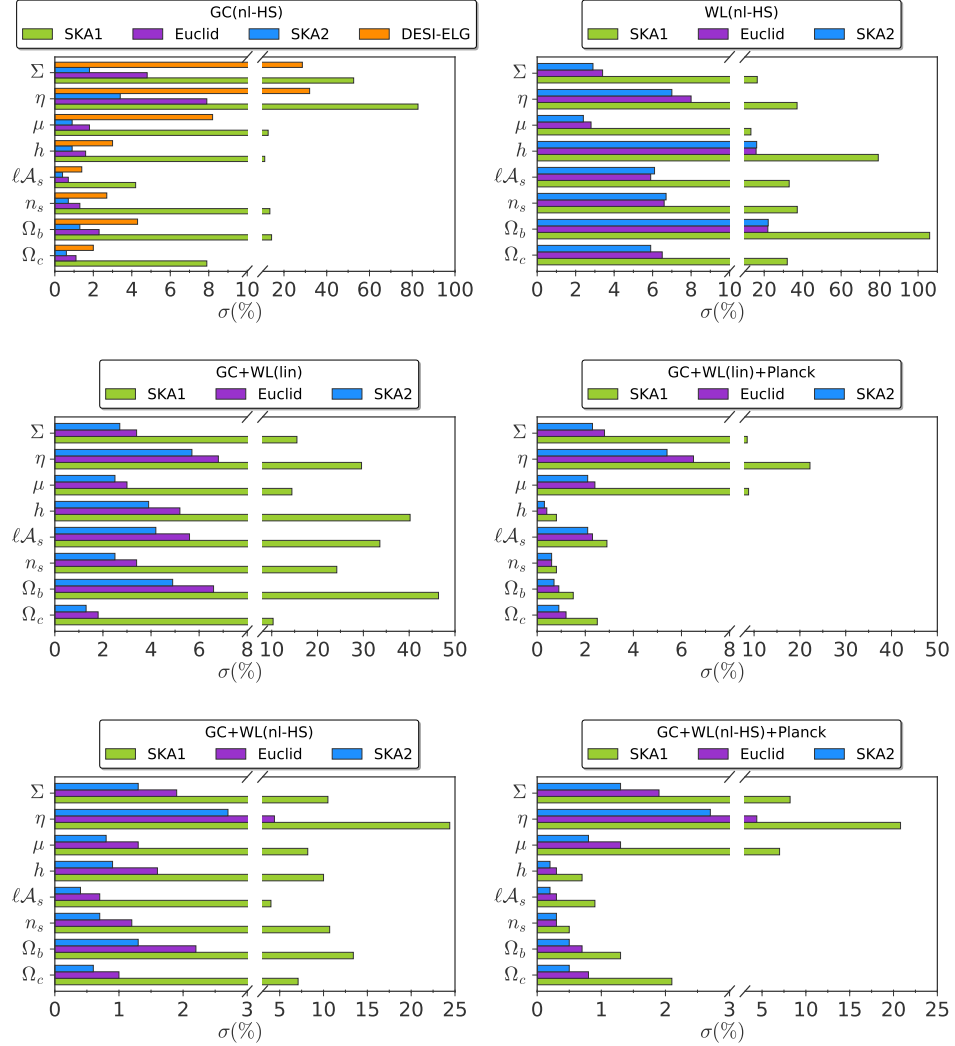


FIGURE 4.18: Same as Fig.4.15 but for the early-time parameterization (Eqns. 4.11,4.12) The 1σ fully marginalized constraints on the parameters are weaker for WL than for GC, which is a consequence of the higher correlation among variables for the Weak Lensing observable.

this test on η using WL, we will find a stronger discrepancy, that lies in between $\sim 50\%$ and $\sim 15\%$, similar to the one found for μ .

We can also test the effect of adding these two HS parameters as extra nuisance parameters to our model of the non-linear power spectrum; therefore, by taking derivatives of the observed power spectrum with respect to these parameters, we can forecast what would be the estimated error on c_{nl} and s . Then, marginalizing over c_{nl} and s would yield more realistic constraints on our cosmological parameters, and take into account our ignorance on the correct parameters of the HS prescription. In Table 4.8 we list the 1σ marginalized constraints on c_{nl} and s for our benchmark fiducial ($c_{nl} = 1$, $s = 1$) and using the standard fiducial for the cosmological parameters used previously for the MG late time parametrization.

Taking these HS parameters into account in our Fisher forecast, will automatically change the constraints on the other parameters. For our method to be consistent, we would like this effect to remain as small as possible. In Table 4.8, we list

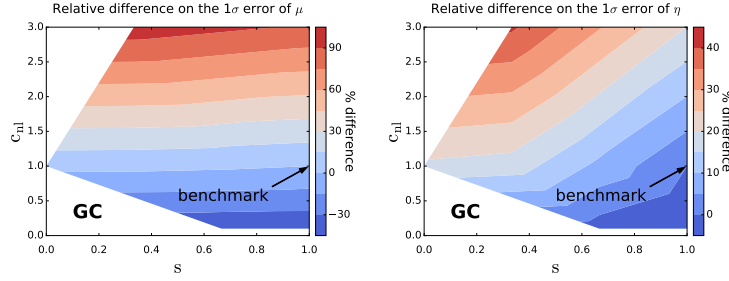


FIGURE 4.19: Effect of the c_{nl} and s parameters on the 1σ marginalized error of the μ (left panel) and the η (right panel) parameters in the MG late-time parametrization for a Euclid Galaxy Clustering forecast with Redbook specifications. The colored contours show the percentage discrepancy when departing from the benchmark case $c_{\text{nl}} = 1$ and $s = 1$ (marked with a black arrow) to all other points in the $c_{\text{nl}}\text{-}s$ space. The red (blue) contours signal the regions of maximum positive (negative) discrepancy. For example in the left panel, choosing c_{nl} and s in the red region, will yield a 1σ marginalized error on μ which is 90% larger than in the benchmark case (see Table 4.4 for the benchmark forecast). For the standard Λ CDM cosmological parameters (not shown here) the discrepancy is smaller than 4% for all choices of c_{nl} and s .

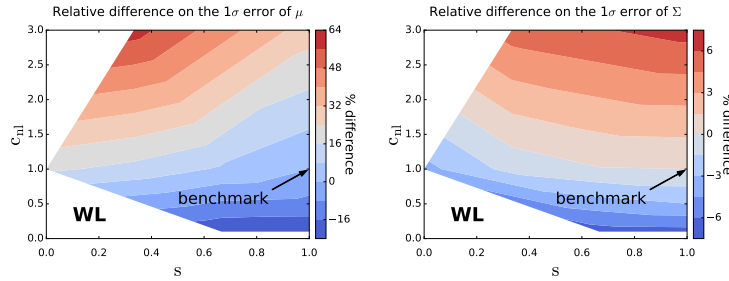


FIGURE 4.20: Same as Fig.4.19 but for a Weak Lensing Euclid forecast using Redbook specifications. In the left panel, choosing c_{nl} and s in the red region, will yield a 1σ marginalized error on μ which is 60% larger than in the benchmark case (see Table 4.4 for the benchmark forecast). In the right panel we see that for the MG parameter Σ the maximum positive and negative discrepancy is only of about 6%. The maximum and minimum discrepancy for the MG parameter η is of -15% and 50%. This means that the parameter Σ (defined as the lensing Weyl potential, and therefore directly constrained by Weak Lensing) is much less sensitive to changes in the non-linear prescription parameters.

the same constraints reported in Table 4.4, but obtained marginalizing over c_{nl} and s at the benchmark fiducial $c_{\text{nl}} = 1$, $s = 1$. Comparing the two tables, we can see that for GC the errors on the cosmological parameters remain quite stable, except for η and Σ ; this is understandable since those parameters are not well constrained by GC alone. For WL, we see a difference of 4 to 7 percent points in the errors on h , n_s and Ω_b , while all other errors remain stable, with Σ varying less than 2 percent points. Remarkably, the combined constraints from GC+WL are even less affected by the two nuisance parameters. Comparing the Modified Gravity FoM between the two tables, shows the expected behavior, the MG FoM is reduced when adding two extra parameters, but the change is very small, of just 0.3-0.5 nits.

Euclid (Redbook)	Ω_c	Ω_b	n_s	$\ell\mathcal{A}_s$	h	μ	η	Σ	c_{nl}	s
Fiducial	0.254	0.048	0.969	3.060	0.682	1.042	1.719	1.416	1	1
GC(nl-HS)	1.0%	2.8%	1.3%	1.1%	2.0%	1.7%	784%	480%	372%	236%
WL(nl-HS)	6.5%	25%	8.3%	9.1%	19%	25%	46%	6.0%	1680%	899%
GC+WL(nl-HS)	1%	2.8%	1.2%	1%	1.9%	1.6%	2.6%	1.2%	333%	166%

TABLE 4.8: $1-\sigma$ fully marginalized errors on the cosmological parameters and the two HS parameters c_{nl} and s for a Euclid Galaxy Clustering forecast, a Weak Lensing forecast and the combination of both in the late-time parameterization of Modified Gravity using non-linear scales and the HS prescription. In contrast to Table 4.4 (where c_{nl} and s had been fixed to the benchmark value) here we include c_{nl} and s as free parameters and marginalize over them. The MG FoM is computed relative to the same Euclid Redbook GC linear case, used previously. The errors and the MG FoM show the expected behavior of adding two nuisance parameters, and remain quite stable. All other naming conventions are the same as for Table 4.4. Remarkably, the combination of GC and WL is still able to constrain all Modified Gravity parameters at the level of 1-2 % after marginalizing over the non-linear parameters.

Model	Description	Results
Redshift Binned μ and η	Section 4.2.1, Eqns. (4.6)-(4.8)	Table ??; Figs. 4.4-4.13
Late-time parameterization	Section 4.2.2, Eqns. (4.9)-(4.10)	Tables 4.4,4.6; Figs. 4.14, 4.15,
Early-time parameterization	Section 4.2.2, Eqns. (4.11)-(4.12)	Tables 4.5,4.7; Figs. 4.17, 4.18,
Effect of non-linear prescription	Section 4.3.2.2, Eqns. (4.13),(4.14)	Table 4.8; Figs. 4.19, 4.20

TABLE 4.9: Summary of results for this work. For each studied model, we indicate where to find the explanations and where to find the main Fisher forecast results.

4.7 Conclusions

We study in this paper the constraining power of upcoming large scale surveys on Modified Gravity theories, choosing a phenomenological approach that does not require to specify any particular model. To this purpose we consider the two functions μ and η that encode general modifications to the Poisson equation and the anisotropic stress. We study three different approaches to MG: redshift-binning, where we discretize the functions $\mu(z)$ and $\eta(z)$ in 5 redshift bins and let the values of μ and η in each of the bins vary independently with respect to the others; an early-time parameterization, where μ and η are allowed to vary at early times and their amplitude can be different from unity today; a late-time parameterization where μ and η are linked to the energy density of dark energy and therefore they are very close to unity in the past, but they can vary considerably at small redshifts. For convenience, we summarize all results in Table 4.9, with a direct link to the section and tables related to each scenario.

We use the predictions of linear perturbation theory to compute the linear power spectrum in Modified Gravity and then use a prescription to add the non-linearities, by interpolating between Halofit non-linear corrections computed for the linear power spectrum for the MG model and for the corresponding GR model ($\eta = \mu =$

1). We find that the non-linear power spectrum is sensitive to changes in μ and η ; limiting the analysis to linear scales significantly reduces the constraining power on the anisotropic stress. Using this prescription, we perform Fisher forecasts for Galaxy Clustering and Weak Lensing, taking into account linear and non-linear scales. We use the specifications for Euclid (using Redbook specifications), SKA1 & SKA2 and DESI (only ELG). In addition to these surveys we also include *Planck* priors obtained by performing an MCMC analysis with *Planck* data for the MG parametrizations considered here.

In the redshift-binned case, we find that in the linear case the μ_i and η_i parameters are strongly correlated, while including the information coming from non linear scales reduces this correlation. We compute a figure of merit (FoM), given by the determinant of the μ - η part of the Fisher matrix, for the cases examined, finding that the combination of Galaxy Clustering and Weak Lensing is able to break the degeneracies among Modified Gravity parameters; as an example the error obtained with the non-linear prescription on μ (η) in the first redshift bin changes from 7% (20%) for Galaxy Clustering to 2.2% (3.6%) when this is combined with Weak Lensing, even if Weak Lensing alone is not very constraining for the same parameters. Overall, constraints are stronger at low redshifts, with the first two bins ($0 < z < 1$) being constrained at better than 5% for both μ and η if non-linearities are included (while the constraints are half as good, < 10%, if we only consider linear scales).

Given the significant correlation between the μ_i and η_i parameters, we apply the ZCA decorrelation method, in order to find a set of uncorrelated variables, which gives us information on which redshift dependence of μ and η will be best constrained by future surveys. If one combines GC+WL (Euclid Redbook)+*Planck*, the best constrained combinations of parameters (effectively $2\mu + \eta$ in the lowest redshift bin) will be measured with a precision of better than 1%. In the linear case, the errors on the decorrelated q_i parameters are about 2 orders of magnitude smaller than for the primary parameters, while in the non-linear HS case, the improvement in the errors is of one order of magnitude. This also shows that applying a decorrelation procedure is worth even when non-linearities are considered.

In addition to binning Modified Gravity functions in redshift, we also forecast the constraining power of the same probes in the case where we assume a specific time evolution for the μ and η functions. We choose two different and complementary time evolutions, used in Planck Collaboration, Ade, and others, 2016 and to which we refer as late-time and early-time evolution. We investigate also in this case the impact of the non-linear prescription interpolating between Halofit and the MG power spectrum. For these parameterizations we extract constraints on the present reconstructed value of μ , η and Σ , where the latter is the parameter actually measured directly by Weak Lensing. In the late time parameterization, in the linear case, μ is mainly constrained by GC (although poorly, at the level of 17%) while WL constrains directly Σ , the modification of the lensing potential, at the level of 9%. Adding non-linear scales allows to significantly improve constraints down to less than 2% for GC (on μ) and to less than 5% on Σ for those two probes. Combining probes allows to reach 1 – 2% on all Modified Gravity values of the μ , η and Σ functions at $z = 0$.

In the early-time parameterization, we find that including non-linearities allows to constrain also the η and Σ functions with GC alone at the level of 8% and 5%, respectively. This is related to the early time deviations from GR allowed by this parameterization, which are not present in the late time case: a variation in η can yield a variation of the amplitude of the power spectrum, which can then be measured in the mildly non-linear regime. Overall, also in this case the combination

of Weak Lensing and Galaxy Clustering leads to errors of the order of 1% on the values of these functions at present.

Finally, we test the impact on the forecasts given by uncertainties appearing in the non linear HS prescription, related in particular to the parameters c_{nl} and s . We find that the errors on the parameters μ and η can vary by up to 90% for the Galaxy Clustering case and up to 65% for Weak Lensing when we change the fiducial values of the HS parameters in a region between 0 and 3 for c_{nl} and 0 and 1 for s . The effect on Σ is quite small, with a discrepancy of $\pm 6\%$ compared to the benchmark case. Interestingly, when we include these two parameters as extra nuisance parameters in our forecast formalism and marginalize over them, the effect is very small and the errors found previously remain stable both for GC, WL and their combination.

It is clear that limiting the analysis to linear scales discards important information encoded in structure formation. On the other hand, a realistic analysis of non-linear scales would have to include several further effects (baryonic effects, higher order RSD's, damping of BAO peaks, corrections to peculiar velocity perturbations, higher order perturbation theory in Modified Gravity, just to name a few), which make our non-linear case an optimistic limit. Therefore, the quantitative true constraints given by a survey like Euclid will probably lie in between these two limiting cases.

4.8 Transformation of primary variables in Modified Gravity

4.8.1 Late time parameterization

Our main observables are parameterized in terms of the primary variables E_{11} and E_{22} from Equation 4.11; we are however interested in forecasting the constraints on the pair of secondary variables $\{\mu, \eta\}$ or on the pair $\{\mu, \Sigma\}$.

Therefore we need to transform the variables using a Jacobian $J_{ij} = \frac{\partial \theta_i}{\partial \theta_j}$, where θ_i is the set of primary variables and $\tilde{\theta}_i$ is the vector of secondary variables. Eqns. (4.5, 4.9, 4.10) allow us to express the $\tilde{\theta}_i$ as a function of the variables θ_i and to obtain the non-vanishing derivatives of μ and η w.r.t to all cosmological parameters:

$$\frac{\partial \mu}{\partial \Omega_c} = -E_{11}, \quad \frac{\partial \eta}{\partial \Omega_c} = -E_{22} \quad (4.43)$$

$$\frac{\partial \mu}{\partial \Omega_b} = -E_{11}, \quad \frac{\partial \eta}{\partial \Omega_b} = -E_{22} \quad (4.44)$$

$$\frac{\partial \mu}{\partial E_{11}} = 1 - \Omega_b - \Omega_c - \Omega_\nu, \quad \frac{\partial \eta}{\partial E_{22}} = 1 - \Omega_b - \Omega_c - \Omega_\nu . \quad (4.45)$$

With these derivatives we can construct the inverse of the Jacobian $J_{ij}^{-1} = \frac{\partial \tilde{\theta}_j}{\partial \theta_i}$. The Fisher matrix in the secondary variables \tilde{F}_{ij} is then given by

$$\tilde{F} = J^T F J \quad (4.46)$$

For the parameter set containing $\tilde{\theta}_i = \{\mu, \Sigma\}$ we obtain the following non-vanishing derivatives

$$\frac{\partial \mu}{\partial \Omega_c} = -E_{11}, \quad \frac{\partial \Sigma}{\partial \Omega_c} = -\frac{1}{2}E_{22}(1 + E_{11}(1 - \Omega_b - \Omega_c - \Omega_\nu)) \quad (4.47)$$

$$-\frac{1}{2}E_{11}(2 + E_{22}(1 - \Omega_b - \Omega_c - \Omega_\nu)) \quad (4.48)$$

$$\frac{\partial \mu}{\partial \Omega_b} = -E_{11}, \quad \frac{\partial \Sigma}{\partial \Omega_b} = -\frac{1}{2}E_{22}(1 + E_{11}(1 - \Omega_b - \Omega_c - \Omega_\nu)) \quad (4.49)$$

$$-\frac{1}{2}E_{11}(2 + E_{22}(1 - \Omega_b - \Omega_c - \Omega_\nu)) \quad (4.50)$$

$$\frac{\partial \mu}{\partial E_{11}} = 1 - \Omega_b - \Omega_c - \Omega_\nu, \quad \frac{\partial \Sigma}{\partial E_{11}} = \frac{1}{2}(2 + E_{22}(1 - \Omega_b - \Omega_c - \Omega_\nu))(1 - \Omega_b - \Omega_c - \Omega_\nu) \quad (4.51)$$

$$\frac{\partial \Sigma}{\partial E_{22}} = \frac{1}{2}(1 + E_{11}(1 - \Omega_b - \Omega_c - \Omega_\nu))(1 - \Omega_b - \Omega_c - \Omega_\nu) \quad (4.52)$$

4.8.2 Early time parameterization

In the early time case, we have two parameters for each $\mu(a)$ and $\eta(a)$ function as in Eq. (4.11). If we are interested in the parameters μ , η and Σ today ($a = 1$), then the parameters E_{12} and E_{21} are not important anymore and we can simply marginalize over them in our Fisher matrix. Then the relation between μ and η is very simple $\{\mu, \eta\} = 1 + \{E_{11}, E_{22}\}$. The corresponding Jacobian is simply a 7×7 identity matrix and we can apply it to the Fisher matrix after we marginalize over the two unimportant parameters.

For the transformation to the pair μ - Σ we use the definition of Σ of Eq. (4.5) and then find the derivatives with respect to E_{ij} . We obtain

$$\frac{\partial \Sigma}{\partial E_{11}} = \frac{1}{2}(2 + E_{22}) \quad (4.53)$$

$$\frac{\partial \Sigma}{\partial E_{22}} = \frac{1}{2}(2 + E_{11}), \quad (4.54)$$

while all other derivatives remain the same.

4.9 Derivatives of the Power Spectrum with respect to μ and η

In this section we investigate the derivatives of the power spectrum with respect to the MG parameters. Using the Jacobians from the previous Appendix 4.8, we can convert our fundamental derivatives $\partial P(k, z)/\partial E_{ij}$ to derivatives of $\partial P(k, z)/\partial(\mu, \eta)$ evaluated at $z = 0$.

We can see from the previous figures that in the early-time parametrization the derivative of the power spectrum with respect to η has a similar shape as the derivative with respect to μ , making η detectable by a Galaxy Clustering survey. To explain this, we derive the equation governing the evolution of density fluctuations for a cold dark matter (CDM) species, based on the equations implemented on the code MGCAMB presented in Hojjati, Pogosian, and Zhao, 2011, expressed here in the conformal Newtonian gauge. In the following, a dot represents derivative with

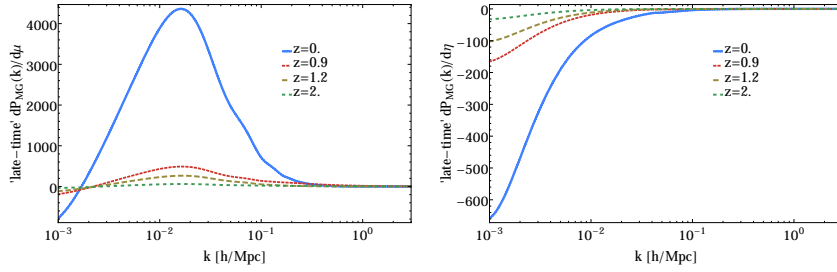


FIGURE 4.21: Derivatives of the matter power spectrum $P(k, z)$ w.r.t. the MG parameters μ and η in the late-time parametrization.

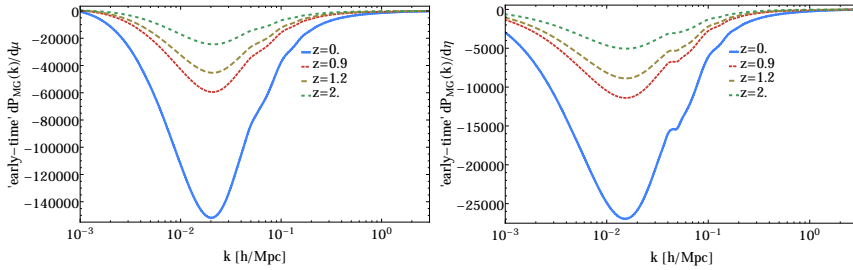


FIGURE 4.22: Derivatives of the matter power spectrum $P(k, z)$ w.r.t. the MG parameters μ and η in the early-time parametrization.

respect to conformal time τ :

$$\dot{\delta} = -(1+w)(\theta - 3\dot{\Phi}) - 3\mathcal{H}\left(\frac{\delta P}{\delta \rho} - w\right)\delta \quad (4.55)$$

$$\dot{\theta} = -\mathcal{H}(1-3w)\theta - \frac{\dot{w}}{1+w}\theta + \frac{\delta P/\delta \rho}{1+w}k^2\delta - k^2\sigma + k^2\Psi \quad (4.56)$$

For CDM we have $\sigma = w = c_s^2 = \delta P/\delta \rho = 0$, then:

$$\dot{\delta} = -(\theta - 3\dot{\Phi}) \quad (4.57)$$

$$\dot{\theta} = -\mathcal{H}\theta + k^2\Psi \quad (4.58)$$

We have parameterized the solution to Ψ as:

$$k^2\Psi = -4\pi Ga^2\mu(\tau)\rho(\tau)\delta(\tau) , \quad (4.59)$$

and since we are also requiring gravitational slip $\eta = \Phi/\Psi$, we then have the Poisson equation for Φ :

$$k^2\Phi = -4\pi Ga^2\mu(\tau)\eta(\tau)\rho(\tau)\delta(\tau) \quad (4.60)$$

Taking the time derivative of (4.57) and using (4.58) and (4.57) to replace $\dot{\theta}$ and θ , and substituting Ψ from (4.59), we obtain:

$$\ddot{\delta} + \mathcal{H}\dot{\delta} = 3\mathcal{H}\dot{\Phi} + 3\ddot{\Phi} + 4\pi Ga^2\mu\rho\delta \quad (4.61)$$

In general, derivatives of Φ appearing on the right hand side will depend on both μ and η . Their contribution is larger in the early-time parameterization with respect to the late-time one.

4.10 Other Decorrelation Methods

In section 4.5.3 we have worked with a special decorrelation method, ZCA (Zero-phase component analysis, first introduced by Bell and Sejnowski, 1997 in the context of image processing), which allows us to find a new vector of decorrelated variables q that is as similar as possible to the original vector of variables p . Other decorrelation methods do not share this property, so in this section we want to illustrate their difference with respect to ZCA. In the next subsections we show for the Principal Component Analysis and Cholesky decomposition methods, a subset of our previous results, namely the Galaxy Clustering non-linear case, using the HS prescription for a Euclid survey with Redbook specifications.

4.10.0.1 Principal Component Analysis

Principal Component Analysis (PCA) Friedman, 1987 is a well known method, which rotates the vector of variables p into a new basis, using the eigenmatrix of the covariance matrix C . At the same time, it is the method that maximizes the compression of all components of p into the components of q using as measure the cross-covariance between q and p (see Kessy, Lewin, and Strimmer, 2015 for more details and references). This method is useful for dimensional reduction or data compression, since the information is stored in as few components as possible. This is achieved by using the W matrix

$$W = \Lambda^{-1/2} U^T \quad (4.62)$$

where Λ and U represent the eigensystem of C (defined in Eqn. 4.33).

Then, it follows that the transformed covariance matrix \tilde{C} is whitened:

$$\tilde{C} = \Lambda^{-1/2} U^T C \Lambda^{-1/2} U^T \quad (4.63)$$

$$= \Lambda^{-1/2} U^T U \Lambda U^T \Lambda^{-1/2} U^T \quad (4.64)$$

$$= \mathbb{I} \quad (4.65)$$

As done previously, we renormalize W in such a way that the sum of the square of the elements of each row sum up to unity. In Figure 4.23 we show in the left panel the weight matrix W and in the right panel the 1σ errors for the original and decorrelated variables. We see that the most constrained q variables are the last components q_8-q_{11} , where most of the information has been compressed into. These 4 variables are complicated linear combinations of A_s , $\mu_{1,2,3}$ and $\eta_{1,2,3}$. This is the same we found for ZCA (cf. Fig. 4.8 and Eqns. (4.8)). However, the interpretation in terms of the old variables p is not so simple anymore. We can see from the weight matrix and the 1σ errors, that the most unconstrained parameter is q_1 , which is basically equivalent to η_5 . This means that this parameter can be eliminated from the analysis if one wants to do dimensional reduction.

4.10.0.2 Cholesky decomposition

Cholesky decomposition of the Fisher matrix $F = LL^T$, allows us to define a decorrelation method that compresses all components of p into an upper triangular matrix of components of q . This is achieved by using the W matrix:

$$W = L^T \quad (4.66)$$

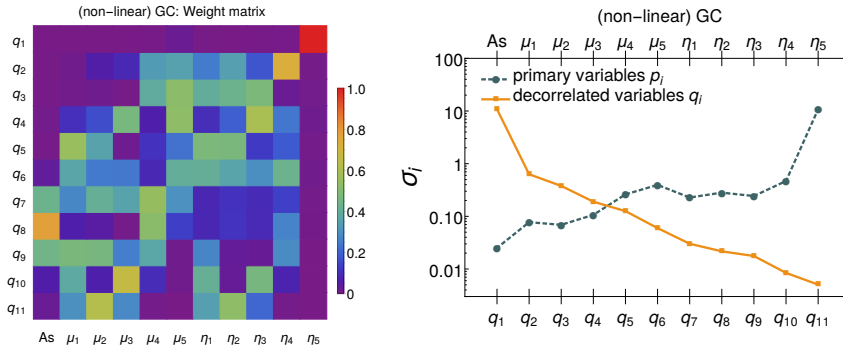


FIGURE 4.23: **Left:** weight matrix W for PCA. **Right:** 1σ fully maximized errors on the primary parameters p (blue lines) and the errors on the uncorrelated derived parameters q (orange lines). Notice how all the important information is constrained in as few variables as possible, namely the last elements of q_i .

Then the covariance matrix will be whitened:

$$\tilde{C} = L^T (LL^T)^{-1}L \quad (4.67)$$

$$= L^T (L^T)^{-1}L^{-1}L \quad (4.68)$$

$$= \mathbb{1} \quad (4.69)$$

As done previously, we renormalize W in such a way that the sum of the square of the elements of each row sum up to unity. In Cholesky decomposition, since we are constructing it via an upper triangular matrix (see left panel of Fig. 4.24), the new parameter q_{11} will be identical to the parameter η_5 , which is, as we have seen before (section 4.5.4.1), the less constrained parameter. This decorrelation method is useful if one wants to have an ordering of the variables (see Kessy, Lewin, and Strimmer, 2015 and references therein). On the other hand q_1 is almost identical to A_s , since as we have seen in section 4.5.4.1, it becomes decorrelated from the MG parameters in the non-linear case.

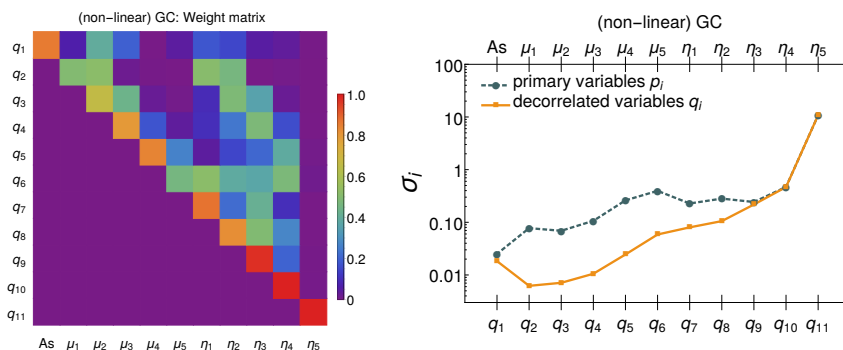


FIGURE 4.24: **Left:** weight matrix W for the Cholesky decorrelation. **Right:** 1σ fully maximized errors on the primary parameters p (blue lines) and the errors on the uncorrelated derived parameters q (orange lines). Notice how in this case, because of the upper triangular construction, the new variables $q_{9,10,11}$ are equivalent to $\eta_{3,4,5}$. The parameter A_s is decorrelated in the non-linear HS case for GC, therefore it is almost equivalent to q_1 as was also the case in ZCA (compare with Fig. 4.6)

4.11 Weight matrices coefficients

Here we explicitly show the coefficient of the W matrices illustrated in Figures 4.6, 4.9 and 4.12. Tables 4.10 and 4.11 contain the coefficient matrices obtained for Galaxy Clustering in the linear and non-linear HS prescription cases respectively, while Tables 4.12 and 4.13 contain the coefficients obtained for WL. Finally, Table 4.14 reports the coefficients for the combination of GC, WL and *Planck* priors, in the non-linear HS case.

$$q_i = \begin{pmatrix} 0.899 & 0.003 & -0.020 & 0.109 & 0.315 & 0.250 & 0.097 & 0.021 & -0.083 & -0.022 & -0.007 \\ 0.001 & 0.695 & -0.304 & -0.089 & -0.084 & -0.026 & 0.519 & -0.362 & -0.082 & -0.033 & 0.001 \\ -0.003 & -0.186 & 0.745 & -0.211 & -0.090 & -0.027 & -0.285 & 0.491 & -0.181 & -0.036 & 0.001 \\ 0.022 & -0.065 & -0.252 & 0.737 & -0.174 & -0.019 & -0.075 & -0.320 & 0.486 & -0.116 & 0.001 \\ 0.148 & -0.142 & -0.250 & -0.405 & 0.666 & 0.070 & -0.094 & -0.102 & -0.268 & 0.439 & -0.002 \\ 0.654 & -0.246 & -0.420 & -0.240 & 0.388 & 0.290 & 0.098 & 0.086 & -0.159 & 0.003 & -0.008 \\ 0.026 & 0.494 & -0.444 & -0.098 & -0.053 & 0.010 & 0.621 & -0.375 & -0.129 & -0.055 & -0.000 \\ 0.004 & -0.265 & 0.588 & -0.320 & -0.044 & 0.007 & -0.288 & 0.578 & -0.248 & -0.045 & -0.000 \\ -0.023 & -0.082 & -0.295 & 0.664 & -0.158 & -0.017 & -0.135 & -0.338 & 0.545 & -0.102 & 0.001 \\ -0.015 & -0.082 & -0.147 & -0.399 & 0.651 & 0.001 & -0.146 & -0.155 & -0.257 & 0.525 & -0.000 \\ -0.519 & 0.308 & 0.510 & 0.346 & -0.348 & -0.239 & -0.061 & -0.070 & 0.181 & -0.004 & 0.193 \end{pmatrix} \cdot \begin{pmatrix} \ln(10^{10} A) \\ \mu_1 \\ \mu_2 \\ \mu_3 \\ \mu_4 \\ \mu_5 \\ \eta_1 \\ \eta_2 \\ \eta_3 \\ \eta_4 \\ \eta_5 \end{pmatrix}$$

TABLE 4.10: Coefficients of the Matrix W for the Euclid Redbook GC forecasted covariance matrix, using linear power spectra. The entries marked with red are those whose absolute values are larger than 0.25.

$$q_i = \begin{pmatrix} 0.986 & -0.064 & -0.112 & -0.093 & -0.037 & -0.038 & -0.002 & 0.005 & -0.002 & 0.005 & 0.002 \\ -0.021 & 0.677 & -0.349 & -0.091 & -0.042 & -0.008 & 0.516 & -0.367 & -0.086 & -0.021 & 0.001 \\ -0.025 & -0.233 & 0.731 & -0.194 & -0.051 & -0.011 & -0.317 & 0.492 & -0.166 & -0.021 & 0.001 \\ -0.030 & -0.088 & -0.281 & 0.755 & -0.061 & 0.036 & -0.073 & -0.331 & 0.465 & -0.086 & -0.001 \\ -0.032 & -0.108 & -0.197 & -0.161 & 0.820 & 0.238 & -0.023 & -0.092 & -0.240 & 0.357 & -0.007 \\ -0.086 & -0.058 & -0.110 & 0.252 & 0.637 & 0.659 & 0.224 & -0.001 & -0.143 & -0.046 & -0.018 \\ -0.001 & 0.492 & -0.452 & -0.071 & -0.008 & 0.031 & 0.617 & -0.391 & -0.113 & -0.038 & -0.001 \\ 0.001 & -0.296 & 0.593 & -0.275 & -0.029 & -0.000 & -0.331 & 0.575 & -0.209 & -0.031 & -0.000 \\ -0.001 & -0.115 & -0.329 & 0.635 & -0.124 & -0.028 & -0.157 & -0.344 & 0.558 & -0.065 & 0.001 \\ 0.008 & -0.092 & -0.136 & -0.390 & 0.614 & -0.030 & -0.176 & -0.167 & -0.216 & 0.581 & 0.001 \\ 0.140 & 0.126 & 0.180 & -0.194 & -0.645 & -0.608 & -0.218 & -0.029 & 0.137 & 0.049 & 0.199 \end{pmatrix} \cdot \begin{pmatrix} \ln(10^{10} A) \\ \mu_1 \\ \mu_2 \\ \mu_3 \\ \mu_4 \\ \mu_5 \\ \eta_1 \\ \eta_2 \\ \eta_3 \\ \eta_4 \\ \eta_5 \end{pmatrix}$$

TABLE 4.11: Coefficients of the Matrix W for the Euclid Redbook GC forecasted covariance matrix, using the non-linear HS prescription. The entries marked with red are those whose absolute values are larger than 0.25.

$$q_i = \begin{pmatrix} 0.760 & -0.005 & 0.475 & 0.131 & 0.005 & 0.034 & 0.247 & 0.329 & 0.095 & 0.004 & -0.000 \\ -0.000 & 0.673 & -0.592 & -0.055 & 0.013 & 0.008 & 0.328 & -0.290 & -0.034 & -0.001 & -0.000 \\ 0.033 & -0.594 & 0.674 & 0.013 & -0.003 & -0.000 & -0.302 & 0.318 & 0.010 & 0.000 & 0.000 \\ 0.075 & -0.457 & 0.112 & 0.754 & 0.002 & 0.004 & -0.310 & 0.039 & 0.326 & 0.001 & 0.000 \\ 0.022 & 0.892 & -0.187 & 0.017 & 0.102 & 0.064 & 0.326 & -0.208 & -0.064 & -0.000 & 0.000 \\ 0.251 & 0.859 & -0.030 & 0.048 & 0.098 & 0.090 & 0.414 & -0.078 & -0.029 & 0.004 & 0.009 \\ 0.034 & 0.654 & -0.600 & -0.074 & 0.009 & 0.008 & 0.356 & -0.280 & -0.037 & -0.000 & 0.000 \\ 0.047 & -0.606 & 0.662 & 0.010 & -0.006 & -0.002 & -0.293 & 0.324 & 0.013 & 0.001 & 0.001 \\ 0.108 & -0.576 & 0.167 & 0.655 & -0.015 & -0.005 & -0.311 & 0.105 & 0.304 & 0.003 & 0.002 \\ 0.256 & -0.718 & 0.380 & 0.136 & -0.003 & 0.032 & -0.010 & 0.448 & 0.197 & 0.111 & 0.061 \\ -0.029 & -0.734 & 0.253 & 0.068 & 0.000 & 0.166 & 0.084 & 0.506 & 0.218 & 0.122 & 0.197 \end{pmatrix} \cdot \ln$$

TABLE 4.12: Coefficients of the Matrix W for the Euclid Redbook WL forecasted covariance matrix, using linear power spectra. The entries marked with red are those whose absolute values are larger than 0.25.

$$q_i = \begin{pmatrix} 0.926 & -0.004 & -0.323 & -0.039 & -0.040 & -0.066 & -0.043 & -0.168 & -0.004 & -0.000 & 0.001 \\ -0.000 & 0.669 & -0.595 & -0.051 & 0.012 & 0.013 & 0.332 & -0.291 & -0.031 & -0.001 & -0.000 \\ -0.021 & -0.552 & 0.711 & 0.029 & 0.005 & 0.016 & -0.270 & 0.339 & 0.014 & 0.001 & 0.000 \\ -0.025 & -0.460 & 0.288 & 0.725 & 0.016 & 0.040 & -0.238 & 0.150 & 0.312 & 0.002 & 0.000 \\ -0.159 & 0.657 & 0.289 & 0.102 & 0.476 & 0.156 & 0.418 & 0.155 & -0.007 & 0.006 & 0.001 \\ -0.168 & 0.455 & 0.622 & 0.158 & 0.100 & 0.486 & 0.223 & 0.236 & -0.016 & -0.001 & -0.002 \\ -0.006 & 0.667 & -0.585 & -0.053 & 0.015 & 0.012 & 0.366 & -0.274 & -0.026 & 0.000 & -0.000 \\ -0.023 & -0.560 & 0.704 & 0.032 & 0.005 & 0.013 & -0.263 & 0.345 & 0.017 & 0.001 & 0.000 \\ -0.005 & -0.576 & 0.277 & 0.636 & -0.002 & -0.008 & -0.238 & 0.165 & 0.319 & 0.004 & 0.001 \\ -0.026 & -0.506 & 0.670 & 0.239 & 0.110 & -0.037 & 0.114 & 0.359 & 0.209 & 0.169 & 0.096 \\ 0.180 & -0.799 & 0.053 & 0.033 & 0.069 & -0.140 & -0.055 & 0.044 & 0.134 & 0.271 & 0.452 \end{pmatrix} \cdot \ln$$

TABLE 4.13: Coefficients of the Matrix W for the Euclid Redbook WL forecasted covariance matrix, using the non-linear HS prescription. The entries marked with red are those whose absolute values are larger than 0.25.

$$q_i = \begin{pmatrix} 0.932 & 0.033 & 0.149 & 0.220 & 0.202 & 0.138 & -0.005 & -0.026 & -0.001 & 0.010 & -0.003 \\ 0.029 & 0.839 & -0.214 & -0.085 & -0.035 & -0.021 & 0.476 & -0.119 & -0.021 & 0.002 & -0.000 \\ 0.138 & -0.222 & 0.800 & -0.083 & 0.016 & 0.028 & -0.256 & 0.452 & -0.118 & -0.011 & -0.002 \\ 0.284 & -0.123 & -0.115 & 0.791 & 0.076 & 0.108 & -0.106 & -0.286 & 0.387 & -0.067 & -0.010 \\ 0.506 & -0.097 & 0.043 & 0.148 & 0.753 & 0.248 & -0.059 & -0.089 & -0.144 & 0.222 & -0.032 \\ 0.545 & -0.092 & 0.120 & 0.331 & 0.390 & 0.626 & -0.027 & -0.088 & -0.089 & -0.009 & 0.104 \\ -0.006 & 0.621 & -0.322 & -0.096 & -0.028 & -0.008 & 0.656 & -0.261 & -0.048 & -0.009 & -0.001 \\ -0.032 & -0.166 & 0.605 & -0.276 & -0.044 & -0.028 & -0.277 & 0.654 & -0.148 & -0.006 & 0.000 \\ -0.003 & -0.049 & -0.270 & 0.634 & -0.122 & -0.048 & -0.088 & -0.252 & 0.659 & -0.023 & 0.010 \\ 0.067 & 0.015 & -0.082 & -0.358 & 0.614 & -0.017 & -0.055 & -0.034 & -0.074 & 0.688 & 0.027 \\ -0.072 & -0.002 & -0.060 & -0.179 & -0.286 & 0.591 & -0.027 & 0.008 & 0.108 & 0.088 & 0.713 \end{pmatrix} \cdot \ln$$

TABLE 4.14: Coefficients of the Matrix W for the Euclid Redbook GC+WL case using the non-linear HS prescription and adding a CMB *Planck* prior. The entries marked with red are those whose absolute values are larger than 0.25.

4.12 The Kullback-Leibler divergence

In Section 4.4.4 we exploited the determinant of the covariance matrix C as a Figure of Merit for our forecasts. Here we summarize a possible alternative, the Kullback-Leibler divergence Kullback and Leibler, 1951, also called relative entropy or information gain. It has been used in the field of cosmology for model selection, experiment design and forecasting, see among others Kunz et al., 2006; Raveri et al., 2016; Seehars et al., 2014; Verde, Protopapas, and Jimenez, 2013; Zhao et al., 2017. The KL-divergence $\mathcal{D}(p_2||p_1)$ measures for a continuous, d -dimensional random variable θ , the relative entropy between two probability density functions $p_1(\theta)$ and $p_2(\theta)$ and it is given by

$$\mathcal{D}(p_2||p_1) \equiv \int p_2(\theta) \ln \left(\frac{p_2(\theta)}{p_1(\theta)} \right) d\theta. \quad (4.70)$$

Although it is not symmetric in p_1 and p_2 it can be interpreted as a distance between the two distributions and measures the information gain since it is non-negative ($\mathcal{D}(p_2||p_1) \geq 0$), non-degenerate ($\mathcal{D}(p_2||p_1) = 0$ if and only if $p_1 = p_2$) and it is invariant under re-parametrizations of the distributions as $p_1(\theta)d\theta = p_1(\tilde{\theta})d\tilde{\theta}$. In the form given here the information gain is measured in nits as in section 4.4.4, to convert nits to bits it is enough to divide the result by $\ln(2)$.

For the special case of $p_1(\theta)$ and $p_2(\theta)$ being multivariate Gaussian distributions, with the same mean values and covariance matrices \mathcal{A} and \mathcal{B} respectively, we obtain

$$\mathcal{D}(p_2||p_1) = -\frac{1}{2} \left[\ln \left(\frac{\det(\mathcal{A})}{\det(\mathcal{B})} \right) + \text{Tr} [\mathcal{B}^{-1} \mathcal{A}] \right]. \quad (4.71)$$

We then define a Kullback-Leibler matrix \mathcal{K} composed of the KL-divergence measure among our observables, defined as:

$$\mathcal{K}_{ij} = \mathcal{D}(p_j||p_i). \quad (4.72)$$

where p_i and p_j represent our observables: GC(lin), GC(nl-HS), WL(lin), WL(nl-HS), GC+WL(lin) and GC+WL(nl-HS) in the redshift binned parameterization of section 4.5. In this way we can quantitatively see how much information is gained when going from one probe like Galaxy Clustering to another probe like Weak Lensing. In Figure 4.25 we plot in the left panel the KL matrix \mathcal{K}_{ij} when no *Planck* priors are added and in the right panel the KL matrix when *Planck* priors are added to all probes. For visualization purposes, we plot the logarithm of the KL matrix: $\log_{10} \mathcal{K}_{ij}$. Blue (red) colours represent small (large) information gain, while black represents no information gain at all, which is by construction the case on the diagonal, $\mathcal{K}_{ii} = 0$. The rows of the matrix represent the reference observable of p_1 and the columns, the new observable p_2 . The information gain when going from a linear WL observable to a non-linear GC observable or to a combined GC+WL (linear and non-linear) observable is considerably high at about $\approx 10^6$ - 10^7 . However, when adding a *Planck* prior, this gets reduced by at least 2 orders of magnitude, since the prior is strong and then there is not as much new information gained in the new observables. On the opposite case, we can see that the row corresponding to GC+WL(nl-HS) is mostly blue, meaning that there is little gain of information when going to one of the other observables.

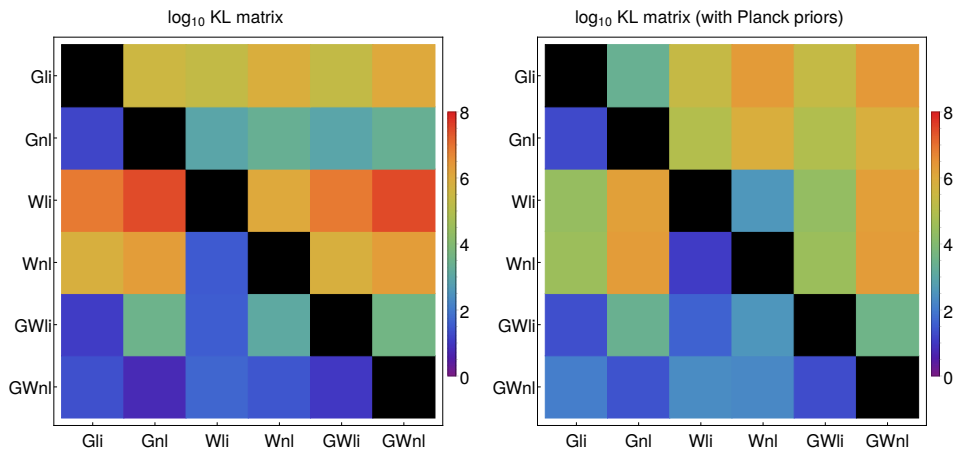


FIGURE 4.25: Kullback-Leibler divergence matrices \mathcal{K}_{ij} . This matrix represents graphically the information gain between all possible observables in the redshift binned parameterization of section 4.5. We have plotted here the logarithm of the KL-divergence matrix, for illustrative purposes. Therefore the diagonal is $-\infty$ and it is represented by a black color. **Left:** KL matrix without *Planck* priors. The maximum gain is about 10^7 when going from WL(lin) to GC+WL(non-linear) and we can observe that GC+WL does not gain extra information when complemented with the other observables, which is expected. **Right:** In this case we compare the observables, when a *Planck* prior is added beforehand. The overall information gain is now smaller, with a maximum of about 10^6 . The maximum gain comes when comparing WL (linear and non-linear) to GC and GC+WL (non-linear).

Chapter 5

Fitting and forecasting coupled dark energy in the non-linear regime

5.1 Introduction

Cosmological data have reached a level of precision that forces us to address effects which may have been safely neglected in the past. Among them, predicting the behaviour of theoretical models at non-linear scales gives a more concrete chance to disentangle Λ CDM from alternative scenarios. The non-linear power spectrum contains useful information encoded in the clustering of galaxies and the weak lensing correlations, which can help to constrain more tightly the cosmological parameters and remove certain degeneracies between them. The drawback relies in the fact that the full estimate of the non-linear power spectrum requires time-demanding and computationally expensive N-body simulations. As a consequence, there exist simulations only for a handful of models beyond Λ CDM on a very limited subset of the parameter space of dark energy theories. This makes it hard to use the non-linear power spectrum in forecasts (see e.g.), both when doing cosmological parameter estimation via Monte Carlo simulations and with the simpler approximation of the Fisher matrix formalism. The alternative is to employ fitting functions for the non-linear power spectrum, like Halofit (Smith et al., 2003; Takahashi et al., 2012) or machine learning estimators like the cosmological emulator (CosmicEmu) (Heitmann et al., 2010; Lawrence et al., 2010; Heitmann et al., 2014) and the interpolator PkANN Agarwal et al., 2012; Agarwal et al., 2014 based on artificial neural networks. All these methods are calibrated or trained using large sets of N-body simulations and typically permit an exploration of the parameter space just around a fiducial Λ CDM cosmology or w CDM cosmology with a constant w . An extension of Halofit to account for massive neutrinos was realised in (Bird, Viel, and Haehnelt, 2011), which was then used in (Audren et al., 2013) to perform a parameter estimation using a Markov Chain Monte Carlo technique. Other authors have recently used polynomial fits to take into account systematic effects in the non-linear regime like baryonic effects such as in Bielefeld, Huterer, and Linder, 2014 or to parametrize the cosmological dependence of non-linear clustering, beyond the Zeldovich approximation (see Mohammed and Seljak, 2014). These fitting functions have, however, an intrinsic error that usually increases when scales become highly non-linear; therefore one has to be aware of the range in scales and redshifts they were designed to work on, in order to keep the errors induced on the power spectrum under control.

As an alternative to fitting formulae and N-body simulations, there has been in recent years a substantial progress in semi-analytical methods to calculate the

non-linear power spectrum at mildly non-linear scales, such as for example renormalized perturbation theory (Crocce and Scoccimarro, 2006b) and all other resummation methods derived from it (for example Anselmi2012), the time renormalisation group (TRG) (Pietroni_2008) and effective field theories of large scale structure Baumann et al., 2010. Most of these approaches claim to reach percent accuracy at the baryon acoustic oscillation (BAO) scale and a bit beyond the second BAO peak, but they are still not able to predict what happens at highly non-linear scales, when the single stream approximation does not hold any longer.

In this paper, we will use N-Body simulations to find fitting functions for a class of models beyond Λ CDM usually referred to as coupled Dark Energy (CDE). These models, widely discussed in literature (Wetterich_1995; Amendola_2000; Amendola_2004; pettorino_baccigalupi_2008), involve an extra degree of freedom, associated to a scalar field that provides acceleration and mediates a fifth force, in addition to gravity, which is felt by dark matter particles only. Semi-analytical non-linear analysis Saracco_etal_2010; Wintergerst and Pettorino, 2010 and cosmological N-body simulations within coupled Dark Energy have been performed by many different groups (baldi_eta1_2010; Li_Barrow_2011; 2015arXiv150407243P; Maccio et al., 2004; Carlesi et al., 2014; Baldi, 2012) and their effects on large scale structure formation have been identified and characterised. The power spectrum, halo mass functions and concentration, halo spin and sphericity, voids and amount of substructures show noticeable differences compared to a simple Λ CDM model (see for example (Mainini and Bonometto, 2006; Macciò, Dutton, and Bosch, 2008; Baldi, 2011; Cui, Baldi, and Borgani, 2012; Baldi, Lee, and Maccio, 2011; Sutter et al., 2014) and the review article (Baldi_2012b)). For a constant coupling, constraints have been found for a variety of probes (Xia_2009; Pettorino et al., 2012; Pettorino, 2013; Amendola and Quercellini, 2004), with the latest ones discussed by the Planck collaboration in (planckcollaboration_planck2015_2015). Recently there have been attempts to constrain more general couplings between dark matter (DM) and dark energy (DE) using large-scale structure (Creminelli et al., 2014), CMB (morris_cosmicmicrowave_2014) or laboratory experiments (hamilton_atominterferometry_2015). Forecasts on coupled dark energy using galaxy clustering (GC) and weak lensing (WL) measurements for future surveys like Euclid have been discussed in (amendola2012testing), but have been performed using only linear power spectra for the CDE models. The TRG method has been extended to coupled Dark Energy (Saracco et al., 2010) and to massive neutrinos (Lesgourgues et al., 2009). However the TRG method does not produce a reliable estimation of the power spectrum for scales larger than $k \approx 0.3h/\text{Mpc}$, which makes them less suitable for forecasts which attempt to extract information on highly non-linear scales.

The CoDECS (Coupled Dark Energy Cosmological Simulations) set of N-body simulations (Baldi, 2012) has shown that CDE models have characteristic and measurable features in the morphology and history of non-linear structures, such as halos, subhalos and voids, and therefore in the non-linear power spectrum.

The aim of this paper is to create fitting functions which are valid in the observable regime of non-linear perturbations at all interesting redshifts and reproduce the subtle effects of coupled dark energy on the non-linear power spectrum while allowing us to vary the different parameters of the model. We use this to perform forecasts of cosmological parameters assuming coupled dark energy as the fiducial model, using galaxy clustering and weak lensing as observational tools, as expected for future surveys like Euclid amendola_cosmology_2012-short; Laureijs and others, 2011. We do a careful treatment of errors and systematics, so that

we take into account all errors induced by our fitting functions, the cosmic emulators and the extraction of the power spectrum from the N-body simulation into the analysis, systematics related to non-linear effects that affect the redshift space distortions and the lensing signals. In this way we obtain a conservative estimate on how well a probe like Euclid, will be able to measure a DM-DE coupling.

5.2 Coupled Dark Energy

In this section we briefly review the main equations governing the coupled DE models that will be investigated in the present work. For a more detailed and extended discussion and for the full derivation of the equations we refer the interested reader to some of the original publications on the subject (**Amendola_2000; Amendola_2004; pettorino_baccigalupi_2008; baldi_eta****l_2010**).

The background evolution for the coupled DE scenario model is described by the following equations, in which the subscripts r , b , c and ϕ , indicate radiation, baryons, cold dark matter (CDM) and the dark energy scalar field, respectively:

$$\ddot{\phi} + 3H\dot{\phi} + \frac{dV}{d\phi} = \sqrt{\frac{2}{3}}\beta(\phi)\frac{\rho_c}{M_{Pl}}, \quad (5.1)$$

$$\dot{\rho}_c + 3H\rho_c = -\sqrt{\frac{2}{3}}\beta(\phi)\frac{\rho_c\dot{\phi}}{M_{Pl}}, \quad (5.2)$$

$$\dot{\rho}_b + 3H\rho_b = 0, \quad (5.3)$$

$$\dot{\rho}_r + 4H\rho_r = 0, \quad (5.4)$$

$$3H^2 = \frac{1}{M_{Pl}^2}(\rho_b + \rho_c + \rho_r + \rho_\phi). \quad (5.5)$$

We express from now on the scalar field ϕ in units of the Planck mass $M_{pl} \equiv 1/\sqrt{8\pi G}$, and choose as potential $V(\phi)$ an exponential $V(\phi) = Ae^{-\alpha\phi}$ (**Lucchin_Matarrese_1984; Wetterich_1988**). The coupling function $\beta(\phi)$ defines the strength of the interaction between the DE fluid and CDM particles and in the present work we will restrict our analysis to the simplified case of a constant coupling $\beta(\phi) = \beta$, although in general it could be a field-dependent quantity **Amendola_2004; Baldi_2011a**

The current constraints on a coupling to ordinary matter are very tight. The “post-Einstein” coupling parameter $\bar{\gamma}$ that measures the local admixture of a spin-0 field to gravity is constrained in Solar System experiments (see e.g. the PDG review **Agashe:2014kda** and also (**Will_2005; Bertotti_Iess_Tortora_2003**)) roughly to $|\bar{\gamma}| \leq 4 \cdot 10^{-5}$. This parameter enters the modification of the effective Newton constant as $G_{eff} = G_N(1 - \bar{\gamma}/2)$; in our notation, this is $G_{eff} = G_N(1 + 4\beta^2/3)$ (see below) and therefore $\beta^2 = -3\bar{\gamma}/8$. A coupling $\beta_{baryons}^2$ appears then constrained to be smaller than 10^{-5} roughly, and we assume therefore that is completely negligible. As a consequence, baryons follow the usual geodesics of a FLRW cosmology, which allows coupled DE to pass the stringent local gravity constraints without the need to employ any screening mechanism (**2015arXiv150203888H**).

Due to the exchange of energy between DE and CDM, the energy density of the latter will no longer scale as the cosmic volume, and by assuming the conservation of the CDM particle number one can derive the time evolution of the CDM particle mass by integrating Eq.(5.2) between the present time ($z = 0$) and any other redshift z :

Parameter	Explanation	Value	Reference Λ CDM
A	Potential normalization	0.0218	–
α	Potential slope	0.08	–
$\phi(z = 0)$	Scalar field normalization	0	–
β	Coupling parameter	{0.05, 0.10, 0.15}	–
$w_\phi(z = 0)$	DE equation of state	{−0.997, −0.995, −0.992}	−1
$\sigma_8(z = 0)$	Power spectrum amplitude	{0.825, 0.875, 0.967}	0.809

TABLE 5.1: The main parameters and normalizations of the three coupled DE models of the Codecs suite considered in the present work. The last column displays the corresponding value for the reference Λ CDM cosmology.

$$m_c(z) = m_{c,0} e^{-\beta(\phi(z) - \phi(0))} . \quad (5.6)$$

5.3 The CoDECS simulations

5.4 Extracting the power spectrum at small scales

5.5 Fitting functions

5.5.1 The net effect of the DM-DE coupling at non-linear scales

5.5.2 Generating the fitting functions

5.5.3 Fitting functions and cosmological parameters

5.6 Non-linear power spectrum and error estimation

5.7 Fisher Matrix method

The Fisher matrix formalism ([seo2007improved](#); [seo2005baryonic](#); Tegmark et al., 1998) is one of the most popular tools to forecast the outcome of an experiment, because of its speed and its versatility when the likelihood is approximately Gaussian (see Sellentin, Quartin, and Amendola, 2014 for a method on how to improve this approximation). Here we apply the Fisher matrix formalism to two different probes, galaxy Clustering (GC) and weak lensing (WL), which are the ones that a future satellite like Euclid [amendola_cosmology_2012-short](#) will carry on board.

5.7.1 Galaxy Clustering

The Fisher matrix for the galaxy power spectrum has the following form ([seo2007improved](#); [amendola2012testing](#)):

$$F_{ij} = \frac{V_{\text{survey}}}{8\pi^2} \int_{-1}^{+1} d\mu \int_{k_{\min}}^{k_{\max}} dk k^2 \frac{\partial \ln P_{\text{obs}}(k, \mu, z)}{\partial \theta_i} \frac{\partial \ln P_{\text{obs}}(k, \mu, z)}{\partial \theta_j} \left[\frac{n(z)P_{\text{obs}}(k, \mu, z)}{n(z)P_{\text{obs}}(k, \mu, z) + 1} \right]^2 . \quad (5.7)$$

Here V_{survey} is the volume covered by the survey and contained in a redshift slice Δz , $n(z)$ is the galaxy number density as a function of redshift, $P_{\text{obs}}(k, \mu, z)$ is

the observed power spectrum as a function of the redshift z , the wavenumber k and of $\mu \equiv \cos \alpha$, where α is the angle between the line of sight and the 3D-wavevector \vec{k} .

The derivatives in eq. (5.7) are taken with respect to a vector of cosmological parameters, $\theta_i = \{\beta^2, h, \log \mathcal{A}_s, n_s, \omega_c, \omega_b, b(z)\}$, where $b(z)$ is the galaxy bias. When we perform the numerical derivatives of $P_{obs}(k, \mu, z)$, we have to take into account that not only the power spectrum and the background functions change, when the cosmological parameters are modified, but also μ and k are changed by a geometrical factor depending on $H(z)$ and $D_A(z)$, due to the Alcock-Paczinsky effect (alcock1979anevolution).

The observed power spectrum contains all the cosmological information about the background and the matter perturbations as well as corrections due to redshift-space distortions and observational uncertainties. In this work we write it in the following form:

$$P_{obs}(k, \mu, z) = \frac{D_{A,f}^2(z)H(z)}{D_A^2(z)H_f(z)} b^2(z) (1 + \beta_d(z)\mu^2)^2 e^{-k^2\mu^2(\sigma_r^2 + \sigma_v^2)} P(k, z) \quad (5.8)$$

In the above formula, the subscript f denotes the fiducial value of each quantity, $P(k, z)$ is the matter power spectrum, $D_A(z)$ is the angular diameter distance, $H(z)$ the Hubble function and $\beta_d(z)$ is the redshift space distortion factor, which in linear theory is given by $\beta_d(z) = f(z)/b(z)$, with $f(z) \equiv d \ln G / d \ln a$ representing the linear growth rate of matter perturbations. The exponential factor represents the damping of the observed power spectrum, due to two different effects: σ_z an error induced by spectroscopic redshift measurement errors, which translates into a damping scale $\sigma_r = \sigma_z/H(z)$ and σ_v which is the dispersion of pairwise peculiar velocities which are present at non-linear scales and also introduce a damping scale in the mapping between real and redshift space.

5.7.1.1 Including sources of error in the Fisher formalism

In section 5.6 we discussed several sources of error affecting the non-linear power spectrum, the intrinsic errors of the coupled DE fitting functions, mode-binning errors in the N-body power spectrum and the estimation and interpolation error of the Λ CDM non-linear power spectrum obtained from the CosmicEmulator. We will take these sources of error into account in our Fisher forecast analysis by including them as extra noise affecting the observed power spectrum. The term in square brackets in eq. (5.7) corresponds to the inverse of the covariance $C = P(k, z) + n(z)^{-1}$. The “noise term” $n(z)^{-1}$ is the number density of sampling points for the matter power spectrum (galaxies in a survey), which gives us an estimate of the signal-to-noise ratio we can expect from the forecast: for a higher number density, the power spectrum is better sampled and more information can be extracted from it. In order to take into account the theoretical and numerical errors on $P(k, z)$, we decrease $n(z)$ by a factor that contains the relative errors on $P(k, z)$. In eq. (5.7), instead of $n(z)$, we then have an “effective” number density:

$$n_{eff}(k, z) = n(z)/(1 + n(z)\tilde{\sigma}_p(k, z)) \quad (5.9)$$

The term $\tilde{\sigma}_p(k, z)$ is a scale- and redshift-dependent term which is the square root of the sum of the relative errors squared. We take into account all error sources which affect $P(k, z)$ due to different reasons, as explained in section 5.6. One of them is

the difference between our power spectrum estimator and the N-body simulation: $\sigma_p(k, z) = (P_{\text{numerical}}(k, z) - P_{\text{true}}(k, z))/P_{\text{true}}(k, z)$. If $\tilde{\sigma}_p(k, z) = 0$ or it is negligible, the effective number density will be the observed one $n_{\text{eff}}(z) = n(z)$; otherwise, $n_{\text{eff}}(z) < n(z)$, the effective number of sampling points being reduced, together with the amount of information one can extract from the power spectrum. As long as $n(z)P(k, z) \gg 1$ for all z and k , the sampling will be always good enough to extract cosmological information from the power spectrum even in the presence of noise. For the specifications used in this work (see table 5.3 below), $n(z)P(k, z)$ is larger than 1 in all scales of interest and therefore the theoretical and numerical error on $P(k, z)$ does not have such a considerable effect on the parameter estimation, as one would expect naively. We test the inclusion of the effective number density $n_{\text{eff}}(z)$ on the Fisher forecast analysis and we find that the relative 1- σ marginalised errors on each cosmological parameter are between 8% and 15% higher when using the estimated uncertainties on the power spectrum.

5.7.1.2 Systematic bias on cosmological parameters

In this section we will quantify the effect of the systematic errors due to the uncertainties on the non-linear power spectrum. We will show how big this systematic bias would be, if we used for our forecasts a power spectrum which is not the “correct” one, for example one obtained from a single N-body realization. For the following discussion on systematic biases, we will use the expressions derived in the Appendix B of Taylor et al., 2007.

The linear bias on a cosmological parameter $\delta\theta_i$ due to the bias $\delta\psi$ in a parameter of the model which we assume fixed and cannot be measured is given by:

$$\delta\theta_i = - \left[F^{\theta\theta} \right]_{ik}^{-1} F_{kj}^{\theta\psi} \delta\psi_j \quad (5.10)$$

In our case we will have only one systematic parameter ψ , which controls the difference between the “true” power spectrum P_{true} and our simulated power spectrum P_{num} :

$$P_\psi = \psi P_{\text{num}} + (1 - \psi) P_{\text{true}}$$

ψ can vary continuously so that for $\psi = 1$ we recover P_{num} , while for $\psi = 0$ we obtain P_{true} . We can define the relative difference between P_{true} and P_{num} as:

$$\sigma_p(k, z) \equiv \frac{P_{\text{num}}(k, z) - P_{\text{true}}(k, z)}{P_{\text{true}}(k, z)} \quad (5.11)$$

The $F^{\theta\theta}$ in eqn.5.10 above is simply the usual Fisher matrix:

$$F^{\theta\theta} = \frac{1}{2} \text{tr} \left(C^{-1} \partial_i^\theta C C^{-1} \partial_j^\theta C \right)$$

while the pseudo-Fisher matrix between measured and assumed parameters $F^{\theta\psi}$ is:

$$F_{ij}^{\theta\psi} = \frac{1}{2} \text{tr} \left(C^{-1} \partial_i^\theta C C^{-1} \partial_j^\psi C \right) \quad (5.12)$$

which for one systematic parameter only, is just a column vector.

In the case of galaxy Clustering we will compute $F^{\theta\psi}$ in the following way, using the fact that for $\psi = 1$, $C = P_{\text{num}}(k, z) + n^{-1}(z)$ and $P_\psi|_{\psi=1} = P_{\text{num}}$:

$$F_i^{\theta\psi} \propto \int dk k^2 \left(\frac{n_{eff}(z)P_{num}(k,z)}{n_{eff}(z)P_{num}(k,z) + 1} \right)^2 \left(\frac{1}{P_{num}(k,z)} \right)^2 \frac{\partial P_\psi}{\partial \psi} \Big|_{\psi=1} \frac{\partial P_{num}}{\partial \theta_i} \quad (5.13)$$

in this step we have assumed that we have no systematic parameters affecting the galaxy number density $n(z)$ and therefore, its derivative w.r.t ψ vanishes. Also, for notational simplicity we left out the integral over μ and the form of the observed power spectrum.

We have then $\partial_\psi P_\psi = -P_{true} + P_{num} = P_{true}\sigma_p(k,z)$ and we just need to perform eqn. 5.13 with eqn. 5.10 in order to obtain the systematic biases on the cosmological parameters.

In the following table 5.2 we present the results on the systematic bias, for a standard Λ CDM forecast, for different maximum k coverages, up to a maximum k of 1.1h/Mpc. We will regard as a “true” power spectrum P_{true} , the one obtained by the Cosmic (Franken) Emulator Heitmann et al., 2014, since they have performed a careful analysis of resolution effects using a large set of simulations and claim to be accurate for $k < 1.0$ h/Mpc at the 1% percent level compared to state of the art N-body simulations. On the other hand, the numerical “biased” power spectrum P_{num} , is the one obtained from the CoDECS Λ CDM run, which consists on only one realization. We have left out the CDE coupling parameter β , since in that case we do not have any other prediction in the non-linear regime to compare with.

Parameter	h	$\ln \mathcal{A}_s$	n_s	ω_b	ω_c
fiducial	0.7036	2.42	0.966	0.04503	0.2256
$k_{max} = k_{Ny}/2 = 1.1h/\text{Mpc}$					
syst. bias with $\delta\psi = 1$	-0.0016	-0.15	0.061	0.0028	-0.0031
$k_{max} = 0.35h/\text{Mpc}$					
syst. bias with $\delta\psi = 1$	-0.0094	-0.11	0.045	0.0021	-0.0039
$k_{max} = 0.15h/\text{Mpc}$					
syst. bias with $\delta\psi = 1$	-0.0032	-0.04	0.018	0.00026	-0.0024

TABLE 5.2: Systematic bias on the Λ CDM cosmological parameters evaluated at our fiducial model. The systematic bias is higher when probing smaller scales, where uncertainties in the non-linear power spectrum are higher. This highlights the importance of modelling correctly the non-linear power spectrum in order to analyze data. Using the wrong non-linear power spectrum produces statistical errors which are larger or of the same order as the statistical results.

The results of table 5.2 show how important it is to model accurately the non-linear power spectrum in order to make forecasts and to analyze the upcoming data of large scale structure surveys like Euclid **amendola_cosmology_2012-short**. The systematic errors on the cosmological parameters can be bigger than the statistical errors (compare to table 5.4 and figure 5.1 in the results section below). This is the case if, as in our example scenario, we would use a non-linear power spectrum that is inaccurate by about 10-15% in the non-linear regime at higher redshifts (which was shown in figure ??). Therefore, it is well justified to choose for our Fisher forecasts the Cosmic Emulator as the “true” Λ CDM non-linear power spectrum estimator, since this is the most accurate predictor up to date. It would still be interesting to know how robust is the signal of the coupling parameter β with respect to changes in the other parameters or in the Λ CDM non-linear prediction, but

as long as we do not have better and faster semianalytic methods applicable to general models of dark energy, the estimation of systematic biases of extra parameters is an impossible task.

5.7.1.3 Choice of the k_{max} integration limit in the Fisher formalism

There are at least three ways of setting the maximum k mode used in the Fisher forecast integration (eqn. 5.7). One common choice is to set a hard cut in k at all redshifts, and depending if one wants to include or not non-linear effects, this cut can be taken at linear scales, smaller than $k = 0.1h/\text{Mpc}$, or at non-linear scales $k > 0.1h/\text{Mpc}$. In the latter case if one is using a power spectrum calculated in linear theory, one needs to use some Lagrangian damping correction, as introduced originally in [seo2007improved](#); Seo et al., 2008, in order to take into account broadening effects on the BAO peak induced by the non-linear evolution of densities and velocities. Another option to cut off the power spectrum is to demand that the variance $\sigma_8(z; k)$ stays below a specified value at each redshift, therefore implicitly changing the cutoff in k as a function of z . An usual choice for this is $\sigma_8(z; k_{cut}) = 0.25$, as was done previously in Amendola et al., 2012. Since we are assuming to have a knowledge of the non-linear power spectrum up to the Nyquist frequency, we implement for our forecasts a hard-cut method, at k_{Ny} and at $k_{Ny}/2$, without the need of any Lagragian damping correction. However, to be conservative, we cite as our main results the ones in which the cut is performed at $k_{Ny}/2$ in order to eliminate any possible unknown contribution from the numerical high-frequency noise entering the estimation of $P(k)$ at the Nyquist frequency (see e.g. [Fosalba2013](#); Colombi et al., 2009 for similar prescriptions on where to cut the non-linear power spectrum).

5.7.2 Weak Lensing

For the weak lensing power spectrum the Fisher matrix is just a sum over all possible correlations at different redshift bins (Tegmark et al., 1998), namely :

$$F_{\alpha\beta} = f_{sky} \sum_{\ell}^{\ell_{max}} \sum_{i,j,k,m} \frac{(2\ell+1)\Delta\ell}{2} \frac{\partial P_{ij}(\ell)}{\partial \theta_{\alpha}} C_{jk}^{-1} \frac{\partial P_{km}(\ell)}{\partial \theta_{\beta}} C_{mi}^{-1} \quad (5.14)$$

With the power spectrum of the shear field given by:

$$P_{ij}(\ell) = \frac{9}{4} \int_0^{\infty} dz \frac{W_i(z)W_j(z)H^3(z)\Omega_m^2(z)}{(1+z)^4} P_m(\ell/r(z)) \quad (5.15)$$

where P_m is the matter power spectrum discussed above, the indices i, j stand for each of the \mathcal{N} redshift bins and the window functions are given by:

$$W(z) = \int_z^{\infty} d\tilde{z} \left(1 - \frac{r(z)}{r(\tilde{z})}\right) n(\tilde{z}) \quad (5.16)$$

where the normalized galaxy distribution function is:

$$n(z) = z^2 \exp\left(-(z/z_0)^{3/2}\right) \quad (5.17)$$

Here the median redshift and z_0 are related by $z_{med} \approx 1.412z_0$. The corresponding covariance matrix has the following form:

$$C_{ij}(\ell) = P_{ij}(\ell) + \delta_{ij}\gamma_{int}^2 n_i^{-1} + K_{ij}(\ell) \quad (5.18)$$

where γ_{int} is the intrinsic galaxy ellipticity and the shot noise term contains

$$n_i = 3600 \left(\frac{180}{\pi} \right)^2 n_\theta / \mathcal{N} \quad (5.19)$$

with n_θ the total number of galaxies per arcmin² assuming that the redshift bins have been chosen such that each contain the same amount of galaxies (equi-populated bins). The matrix $K_{ij}(\ell)$ is a diagonal “cutoff” matrix whose entries increase to very high values at the scales where the power spectrum $P(k)$ has to be cut to avoid the inclusion of numerical noise errors. Since $K_{ij}(\ell)$ depends on the multipole ℓ , which itself depends on k and z through: $\ell = k r(z)$, each of the entries K_{ii} increase with the multipole in a different way. For our purposes we chose a very sharp cutoff, such that multipoles containing wavenumbers k beyond the Nyquist frequency (or half of the Nyquist frequency, for our reference case) at the center of the redshift bin i , do not contribute to the Fisher matrix at all after the corresponding ℓ_{cut} (specified in table 5.6 below).

5.7.3 Adding non-linear corrections to the power spectrum

We are interested in a Fisher forecast that includes information from non-linearities. In this case we cannot separate the power spectrum, into a power spectrum at redshift zero multiplied by the square of the normalized growth factor, but we need to evaluate directly the non-linear power spectra $P(k, z)$ at different redshifts. A full non-linear correction for the redshift space distortions would be also desirable, but since the modelling of that effect is yet to be understood in general cases, we use as a first approximation an exponential damping of the form $\exp(-k^2 \mu^2 \sigma_v^2)$, where σ_v is the pairwise peculiar velocity of galaxies induced by non-linearities in the matter and velocity power spectrum. This is the first term of a set of corrections that can be applied to the Kaiser formula (Kaiser, 1987) for the clustering in redshift space (see e.g. Torre and Guzzo, 2012, Scoccimarro, 2004, Taruya, Nishimichi, and Saito, 2010, Wang, Chuang, and Hirata, 2012). We use a value of $\sigma_v = 300$ km/s which is an approximate and conservative value based on the estimations by (Torre and Guzzo, 2012), in which the authors test a variety of redshift-space distortion models.

As already mentioned, the damping term, introduced by (`seo2007improved`), which should correct the linear $P(k)$, especially the position of the BAO peaks, for non-linearities, is not included here, since we assume that we have a complete model of the non-linear power spectrum and therefore all possible corrections are already included in our fitting functions and power spectrum emulators.

In order to implement our model of coupled Dark Energy, we use for $H(z)$ and $D(z)$ tables precomputed using a modified version of CAMB, that includes the exponential and inverse-power law potentials for coupled dark energy Amendola et al., 2012; Pettorino, 2013. We calculate these tables for each of the parameters $\theta_i \pm \epsilon$, where $\epsilon = 0.03$. We do the same for the linear perturbation quantity $G(z)$, whose logarithmic derivative with respect to $\ln(a)$, known as the growth rate $f(z)$ enters the redshift space distortion term in 5.8. The background quantities $H(z)$ and $D(z)$ are important in the Fisher forecast for the Alcock-Paczynski geometrical term, which we take into account in the observed power spectrum.

The full non-linear power spectrum we use in our method is then obtained as follows.

- At linear scales $k \lesssim 0.1h/\text{Mpc}$ the linear power spectrum is obtained from our modified version of CAMB which includes the effect of the DM-DE coupling.
- At non-linear scales, $k \gtrsim 0.1h/\text{Mpc}$, we use a combination of the power spectrum calculated with the cosmic emulator *FrankenEmu* and our fitting formulas for CDE that account for the non-linear dynamics in presence of a fifth force.
- The matching at $k \approx 0.1h/\text{Mpc}$ is performed using different interpolation methods, either averaging on both sides and smoothing out or allowing for a small discontinuity. The matching point is left out of the Fisher integral and we check for this effect, showing that the different methods have a negligible effect (less than 2 percent) on the final absolute errors on the parameters.
- In order to be conservative in terms of numerical errors and noise, we cut the power spectra at half of the Nyquist frequency (we also test and compare with a cutoff at k_{Ny}) and we include all sources of errors specified in section 5.7.1.1, as effective noise terms into our Fisher estimation.

5.8 Results

We now present results for galaxy clustering and weak lensing, using the specifications for a Euclid-like survey as described in tables 5.3 and 5.5 below. We use the Fisher formalism described in section 5.7 to forecast the errors in the cosmological parameters, using information from the non-linear power spectrum for coupled Dark Energy models, as obtained with the procedure described in section 5.4 together with the fitting functions obtained in section 5.5. To make our estimation more realistic, we also take into account all sources of error and systematics for the power spectrum which were discussed in section 5.6. As a way of testing our improvement on the parameter estimation, we also perform two extra Fisher forecasts, first using only linear power spectra for the CDE model and then correcting these linear $P(k)$ with the latest version of Halofit Takahashi et al., 2012, which was designed for ΛCDM only.

The fiducial parameters are $\omega_c = 0.1117$, $\omega_b = 0.0223$, $n_s = 0.966$, $\log \mathcal{A}_s = -19.8395$, $h = 0.7036$, $\beta^2 = 0.0025$, which are consistent with WMAP7 results (see table ??). The fiducial values for the galaxy bias $b(z)$ used for the GC probe are taken from the Euclid specifications (see [amendola_cosmology_2012-short](#); [orsi2010probing](#); Laureijs and others, 2011) For our final results, we convert these parameters into the set $p_i = \{\beta^2, h, 10^9 \mathcal{A}_s, n_s, \Omega_c, \Omega_b\}$ marginalizing over the bias $b(z)$ (for the GC case) and using a Jacobian transformation to convert into the new set of parameters, which is allowed by the Fisher matrix formalism. We choose to forecast the error on the square of the coupling parameter β^2 , because this is the quantity entering the modified gravitational Newton constant G_{eff} in the limit of linear perturbations (cf. eq. ??), therefore giving the strength of the “fifth force”. The corresponding fiducial value for the coupling, $\beta = 0.05$, is still compatible with recent limits set by analyzing the data from the Planck Satellite (see [planckcollaboration_planck2015_2015](#); Pettorino, 2013).

5.8.1 Galaxy clustering

Table 5.3 shows the specifications of a Euclid-like survey, which are used in our Fisher forecast. While Euclid specifications use 14 redshift bins of a width $\Delta z = 0.1$

Parameter	Value	Description
A_{survey}	15000 deg^2	Survey area in the sky
σ_z	0.001	Photometric redshift error
σ_v	300 km/s	Fiducial pairwise velocity dispersion
Δz	0.2	Redshift bin width
$\{z_{\min}, z_{\max}\}$	{0.6, 2.0}	Min. and max. limits for redshift bins

TABLE 5.3: Specifications for the Fisher Matrix of an Euclid-like galaxy clustering survey.

Parameter	β^2	h	$10^9 \mathcal{A}_s$	n_s	Ω_b	Ω_c
fiducial	0.0025	0.7036	2.42	0.966	0.04503	0.2256
$k_{\max} = k_{Ny}/2$						
abs. error	0.000346	0.00160	0.01855	0.00267	0.00084	0.00088
relative error	14%	0.23%	0.77%	0.28%	1.9%	0.39%
$k_{\max} = k_{Ny}$						
abs. error	0.000305	0.00151	0.01808	0.00249	0.00081	0.00085
relative error	12%	0.22%	0.75%	0.26%	1.8%	0.38%

TABLE 5.4: $1-\sigma$ fully marginalized errors on the cosmological parameters of the model for a galaxy clustering Fisher forecast. Two cases are presented, a hard cutoff of the power spectrum at $k_{\max} = k_{Ny}/2$, and a hard cut at k_{Ny} .

(see **amendola_cosmology_2012-short** table 3 in that work), we use only 6 bins of a width of 0.2. We check in the case of Λ CDM, that this re-binning (done using the specified number of galaxies and the corresponding comoving volumes in our cosmology) has a very small effect (of a few percent) on the estimation of the $1-\sigma$ errors on the parameters.

In table 5.4 we show the fully marginalized $1-\sigma$ errors on the final cosmological parameters $p_i = \{\beta^2, h, 10^9 \mathcal{A}_s, n_s, \Omega_c, \Omega_b\}$, performing the non-linear power spectrum cut-off at two different scales: $k_{\max} = k_{Ny}/2$ and $k_{\max} = k_{Ny}$. As explained above, we take as a reference result the one corresponding to a cutoff at $k_{Ny}/2$. The gain in constraining the β^2 parameter when going from $k_{Ny}/2$ to k_{Ny} is of two percent points in the relative errors, while for the other cosmological parameters the improvement is negligible.

5.8.1.1 Variation of the k_{\max} integration limit

We now test the gain in information obtained by including progressively more non-linear wavemodes k into the Fisher integration. We perform the same Fisher forecast, each time increasing the maximum mode k_{\max} at which the integration is cut off. In figure 5.1 we show how the $1-\sigma$ fully marginalized error on the cosmological parameters p_i changes with an increase of k_{\max} . The error decreases steadily with an increase of k_{\max} , where the biggest gain is achieved when going from linear ($k \approx 0.1h/\text{Mpc}$) to mildly non-linear ($k \approx 0.3h/\text{Mpc}$) scales. For parameters like h and Ω_b , an approximate plateau is reached already before $k_{\max} \approx 1.0$, while for β^2 there is still a considerable gain in parameter constraints when going into smaller scales, even beyond $k_{Ny}/2$ (consistent with table 5.4 above). This happens, qualitatively, because at small scales we have a well-defined characteristic signal coming from non-linear interactions including the fifth force which itself involves

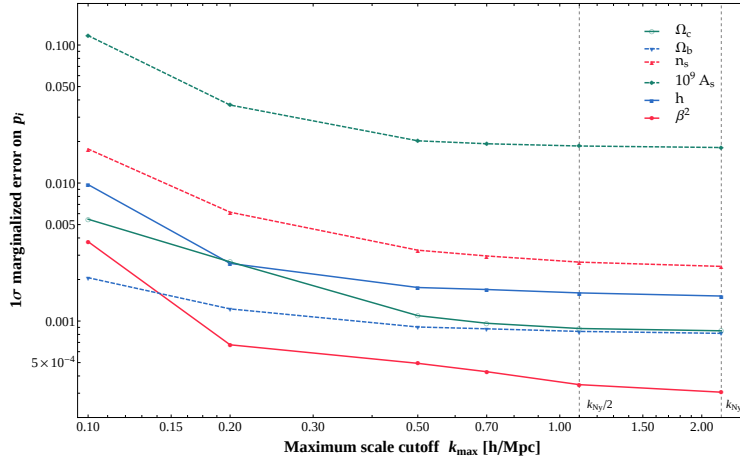


FIGURE 5.1: Change of the $1-\sigma$ fully marginalized error on the set of cosmological parameters p_i for a galaxy clustering Fisher forecast, as a function of the maximum mode k_{max} used as a cutoff in the Fisher matrix integration. When increasing the maximum k_{max} the errors on the parameters get steadily smaller, especially when going from linear ($k \approx 0.1h/\text{Mpc}$) to mildly non-linear ($k \approx 0.3h/\text{Mpc}$) scales. The vertical dashed grey lines, mark the half and the full Nyquist frequencies.

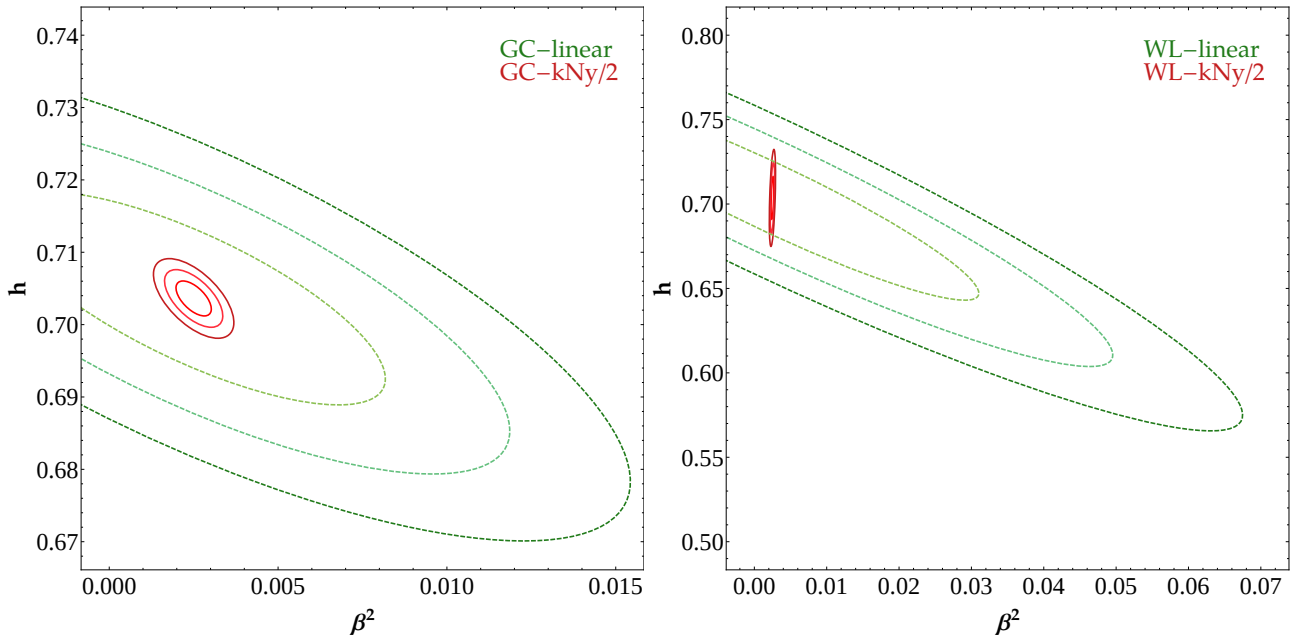


FIGURE 5.2: Marginalized confidence contour regions $1,2,3-\sigma$ for β^2 and h . The plots correspond to a comparison between linear (green-dashed) and non-linear (red-solid) scales for GC (left) and WL (right) using the scale cutoff at $k_{Ny}/2$.

the β coupling, while the information on the background cosmological parameters gets washed out (c.f. section 5.5.3 above).

Parameter	Value	Description
f_{sky}	0.364	Observed sky fraction
γ_{int}	0.22	Intrinsic alignment
n_θ	30	Galaxy density per $arcmin^2$
σ_{pz}	0.05	Photometric redshift error

TABLE 5.5: Specifications for the Fisher Matrix of an Euclid-like weak lensing survey.

Parameter	Value	Description
N	6	Number of redshift bins
z_{peak}	$\{0.59, 0.75, 0.90, 1.06, 1.28, 1.57\}$	z -position of peak of the bin
w_z	$\{0.22, 0.23, 0.25, 0.27, 0.32, 0.51\}$	full width at half maximum of the peak
ℓ_{cut, k_1}	$\{1686, 2070, 2410, 2753, 3155, 4344\}$	cutoff in multipole ℓ at the center of each bin for $k_1 = k_{Ny}/2$
ℓ_{cut, k_2}	$\{3372, 4141, 4820, 5506, 6311, 8689\}$	cutoff in multipole ℓ at the center of each bin for $k_2 = k_{Ny}$
z_{range}	$0.5 \leq z \leq 3$	Total range in redshift of each bin

TABLE 5.6: Redshift bins specifications for an Euclid-like weak lensing survey using equipopulated redshift bins in the range $0 \leq z \leq 3$ and the corresponding values for the cutoff applied in the multipoles ℓ at each redshift bin, for two different cases: scales larger than $k_1 = k_{Ny}/2$ and scales larger than $k_2 = k_{Ny}$.

5.8.2 Weak lensing

Table 5.5 show the specifications for a weak lensing probe in an Euclid-like survey. The redshift bins are chosen in such a way that they contain an equal number of galaxies (equipopulated bins). The bins are then given by:

$$n_i(z) = \frac{1}{2} n(z) \left[\text{Erf} \left(\frac{\tilde{z}_{i+1} - z}{\sigma_{pz} \sqrt{2}} \right) - \text{Erf} \left(\frac{\tilde{z}_i - z}{\sigma_{pz} \sqrt{2}} \right) \right] \quad (5.20)$$

where \tilde{z}_i are the values of the bin intervals in the range $z_{range} = 0.5 \leq z \leq 3$ chosen such that for each interval the integral over the galaxy distribution function $n(z)$ (eqn. 5.17) is equal. The resulting peaks of the bins and their full width at half maximum are specified in table 5.6.

Analogously to the galaxy clustering case, we show in table 5.7 the fully marginalised $1-\sigma$ errors on the parameters p_i . The sum over multipoles ℓ in eq. (5.14) is performed from $\ell_{min} = 5$ up to a maximum of $\ell_{max} = 20000$, but as explained in section 5.7.2, we perform a cutoff at each redshift bin, so that no scales in the non-linear power spectrum beyond the half of the Nyquist (for our reference case) or beyond the Nyquist frequency (for our second case) contribute to the WL signal. The values of these cutoffs, ℓ_{cut} for the two different cases $k_1 = k_{Ny}/2$ and $k_2 = k_{Ny}$ are listed in table 5.6. In contrast to the GC case, going from $k_{Ny}/2$ to k_{Ny} in a WL survey does bring a noticeable improvement on the estimation of parameters.

The dependence of the $1-\sigma$ fully marginalized error on each parameter p_i with respect to ℓ_{max} is shown in figure 5.3. When using just linear power spectra information, the error on the parameters does not improve if one increases the scale ℓ_{max} , while in the case where non-linear information is used, increasing the maximum multipole ℓ_{max} improves considerably the $1-\sigma$ error on the parameters, especially on the coupling β^2 and on the initial amplitude of scalar fluctuations $10^9 A_s$.

Parameter	β^2	h	$10^9 A_s$	n_s	Ω_b	Ω_c
fiducial	0.0025	0.7036	2.42	0.966	0.04503	0.2256
$\ell_{\text{cut}, k_{Ny}/2}$						
abs. error	0.000125	0.00835	0.112	0.0105	0.0032	0.0046
relative error	5.0%	1.2%	4.6%	1.1%	7.1%	2.0%
$\ell_{\text{cut}, k_{Ny}}$						
abs. error	0.000097	0.0068	0.058	0.0085	0.0022	0.0032
relative error	3.9%	0.97%	2.4%	0.88%	4.9%	1.4%

TABLE 5.7: $1-\sigma$ fully marginalized errors on the cosmological parameters of the model for a weak lensing Fisher forecast. Two cases are presented, a redshift-dependent cutoff $\ell_{\text{cut}, k_{Ny}/2}$ and a cutoff $\ell_{\text{cut}, k_{Ny}}$, corresponding to cutting off the non-linear power spectrum at the half and at the full Nyquist frequency (analogously to the GC case) as explained in the main text. As opposed to the GC case, going into smaller scales in a WL survey does bring a noticeable improvement.

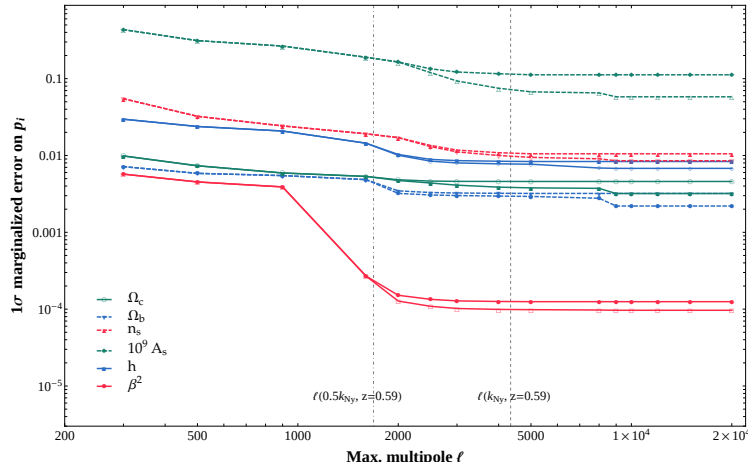


FIGURE 5.3: Variation in the $1-\sigma$ fully marginalized errors for each cosmological parameter p_i as a function of the maximum multipole used in the weak lensing Fisher forecast. Increasing the observed multipole range improves considerably the determination of a parameter, especially on the coupling β^2 (red solid line) and the initial amplitude of perturbations $10^9 A_s$ (dashed green line). The double lines corresponding to each parameter, show how the error changes if a cut in the matter power spectrum $P(k)$ is performed at k_{Ny} (lower line) instead of a cut at $k_{Ny}/2$ (upper line, respectively). The vertical dashed grey lines mark the ℓ_{cut} at the peak of the first redshift bins for the cases $\ell_{\text{cut}, k_{Ny}/2}$ and $\ell_{\text{cut}, k_{Ny}}$.

This is due to the fact that the extra signal on the coupling coming from the non-linear part of the power spectrum, the so called “bump”, greatly enhances the constraints on the parameter estimation. The double lines corresponding to each parameter in figure 5.3, show how the error estimation is changed if scales up to k_{Ny} are included (lower line) compared to the upper line where only scales up to $k_{Ny}/2$ contribute. At small ℓ both lines are on top of each other and only start diverging at around $\ell = 2000$, when the extra amount of information contained in highly non-linear scales starts becoming important. The most significant gains occur again on the parameters β^2 and $10^9 A_s$.

5.8.3 Combined results

In figure 5.4 we show the 1-, 2- and 3- σ confidence contours from the Fisher forecast for WL and GC. These confidence regions for each pair of parameters are obtained after marginalizing over all the other parameters. As it can be seen, some degeneracies are broken when combining the confidence ellipses from two different observations, for example in the case of the plane Ω_b, β^2 . Other parameter combinations, as n_s, β^2 , show the same orientation of the ellipses for WL and GC, so that the combination of both probes does not help to disentangle the degeneracies. While GC constraints much better the usual parameters $\{h, 10^9 A_s, n_s, \Omega_c, \Omega_b\}$, WL constrains the coupling parameter β^2 much better which can be seen in the vertical orientation of the ellipses that correspond to β^2 . Therefore combining the observations on GC and WL, as a future survey like Euclid will do, is a powerful way of constraining degenerate parameters in cosmology.

In table 5.8, we cite the 1- σ fully-marginalised errors on the parameters p_i for three different cases: a) using only linear CDE power spectra computed from our modified version of CAMB; b) applying a non-linear correction to these linear CDE power spectra using the latest version of Halofit from Takahashi et al., 2012, which was designed for Λ CDM-only; c) using the full coupled DE non-linear power spectra computed with our fitting functions following the procedure explained in section 5.7.3.

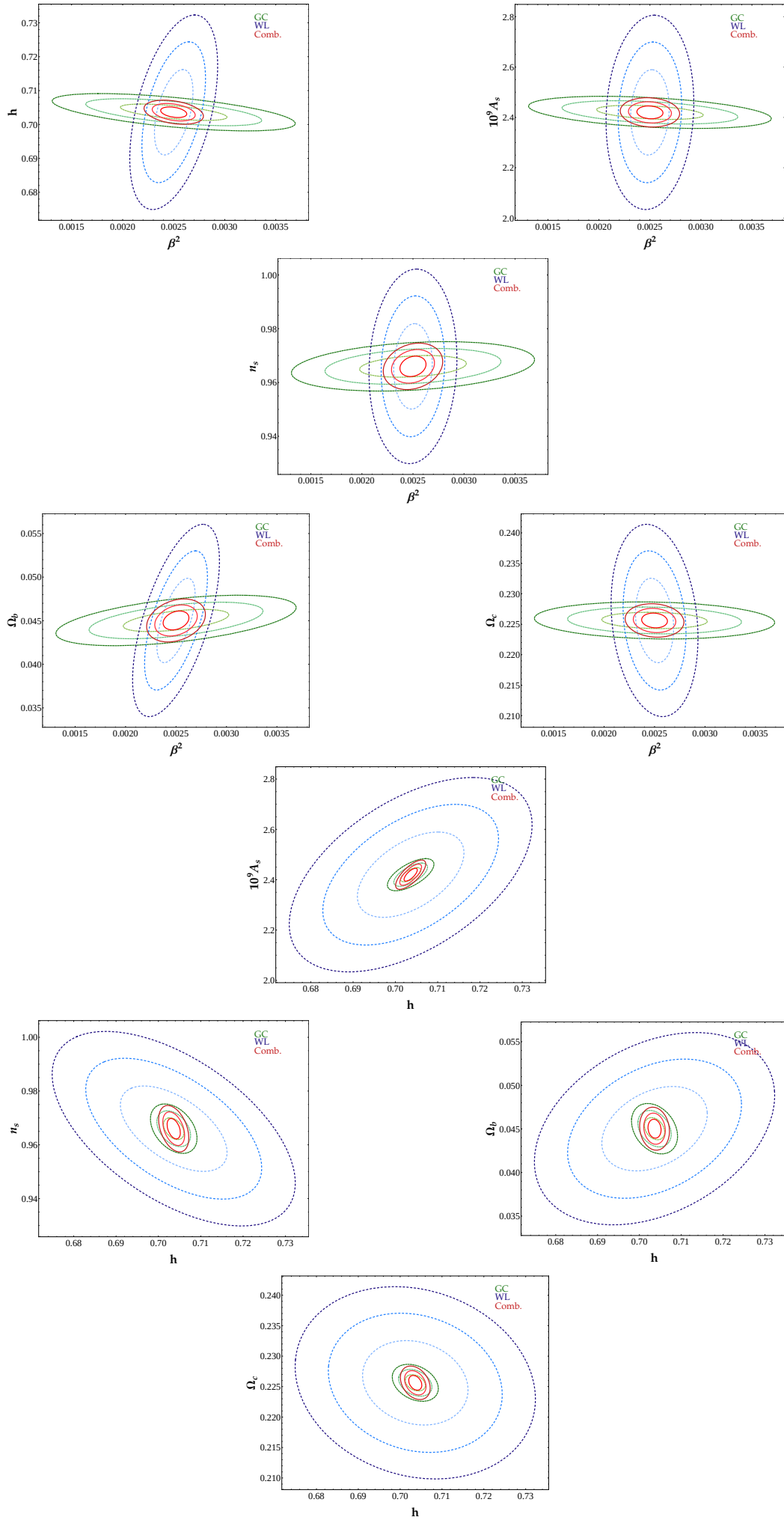
This shows the value of using the N-body-calibrated fitting functions on the coupling β^2 . Using the proper β -dependent non-linear correction instead of the standard Halofit correction, the constraints on β^2 improve by more than an order of magnitude for WL and by a factor of order three for GC. This makes very clear the importance of applying non-linear corrections that depend on the parameter to be tested.

5.9 Conclusions

The goal of this paper is to exploit the cosmological information contained in the non-linear regime in order to improve parameter estimation from future large-scale observations. The main obstacle along this road is that we have accurate non-linear corrections for the matter power spectrum only for Λ CDM and a few other relatively simple variants, but not for the large variety of modified gravity models that have been proposed in recent years.

The first part of this paper has then been devoted to the task of finding corrections to the linear power spectrum in the range of $k \approx 0.1 - 1 h/\text{Mpc}$ for a selected class of modified gravity models, namely coupled dark energy. This model is indeed one of the simplest possible extensions of Einstein's gravity and depends entirely on a single parameter, the coupling constant β (in addition to the standard ones). Employing the CoDECS suite of simulations (Baldi, 2012) we build different fitting function models, such that when multiplied by the Λ CDM non-linear power spectrum (we use the estimator provided in ref. (Heitmann et al., 2014)) they reproduce the N-body results to an accuracy of 1%, for scales k between 0.1 and 5 h/Mpc and a range in z , between 0 and 1.8. To achieve this accuracy in the fitting functions we need to perform a careful extraction and interpolation of the power spectrum from the simulation mesh.

The accurate fitting functions have been then employed to extend the regime of validity of the forecasts for future experiments. We focused on a Euclid-like survey that includes weak lensing and redshift-space distortions (galaxy clustering) and



Parameter	β^2	h	$10^9 \mathcal{A}_s$	n_s	Ω_b	Ω_c
fiducial	0.0025	0.7036	2.42	0.966	0.04503	0.2256
WL: 1-σ abs. error, using:						
linear CDE	0.0189	0.040	0.221	0.0139	0.0062	0.0127
linear CDE+Halofit	0.0184	0.044	0.256	0.0109	0.0066	0.0079
non-linear CDE fitting functions	0.000125	0.00835	0.112	0.0105	0.0032	0.0046
GC: 1-σ abs. error, using:						
linear CDE	0.0038	0.0097	0.117	0.0176	0.0021	0.0055
linear CDE+Halofit	0.0011	0.0029	0.024	0.0023	0.0007	0.0006
non-linear CDE fitting functions	0.00035	0.0016	0.018	0.0027	0.0008	0.0009
comb. WL+GC: 1-σ error, using:						
non-linear CDE fitting functions (abs.)	0.000084	0.0010	0.0169	0.00251	0.00072	0.00080
non-linear CDE fitting functions (rel.)	3.4%	0.16%	0.7%	0.26%	1.6%	0.35%

TABLE 5.8: $1-\sigma$ fully marginalized errors on the cosmological parameters for WL, GC and the combined Fisher matrix WL+GC, using three different power spectra. **Linear CDE:** Using only information from the linear power spectrum for the CDE model up to a scale of $k = 0.1h/\text{Mpc}$. **Linear CDE+Halofit:** Using the linear power spectrum for CDE plus a non-linear correction using the latest Halofit from Takahashi et al., 2012. **Non-linear CDE fitting functions:** Using the fully non-linear power spectra for CDE obtained from the fitting functions and the emulator as explained in 5.5, which we regard as the most reliable description of the model in this range of scales. In all these cases we are using our reference Fisher forecasts corresponding to the cutoff at $k_{Ny}/2$.

predicted the constraints in the cosmological parameters, with particular emphasis on the dark matter-dark energy coupling β . We find that β is better constrained by weak lensing than by galaxy clustering (contrary to all the other standard parameters). We find that the extension into non-linear scales improves the constraints by more than an order of magnitude compared to previous results using only linear power spectra, but also by more than an order of magnitude in WL and a factor of three in GC compared to using a wrong Λ CDM Halofit non-linear correction. We also show that using the wrong non-linear power spectrum, can bias systematically the estimation of errors on the cosmological parameters, yielding systematic errors of the same order of magnitude as the statistical ones. This makes very clear that it is important to include the proper non-linear corrections to the parameter to be tested, especially for models beyond Λ CDM in which the small-scale gravitational dynamics are modified.

To make our forecast more realistic, we take into account all known sources of error entering the estimation of the power spectra and the fitting functions in the way of a reduced effective number density of galaxies and then perform a conservative cut of the power spectrum at half of the simulation Nyquist frequency, to avoid other sources of unknown numerical noise affecting the results. In the case of GC we include also a first approximation to the correction to redshift space distortions, caused by peculiar pairwise velocities at non-linear scales. We find that a space probe like Euclid will be able to constrain the coupling parameter β^2 around the fiducial value 0.0025 at $1-\sigma$ with a relative accuracy of 14% when using weak lensing alone, 5% when using only galaxy clustering and at 3.4% when combining both probes.

It is interesting to note that the most stringent constraint we obtain amounts to

$\Delta\beta^2 \approx 8 \cdot 10^{-5}$; this level of precision on the dark matter-dark energy coupling is not far from the current best limits reached with Solar System observations on a coupling to baryons **Agashe:2014kda** which can be translated in our notation as $\beta^2 \leq 2 \cdot 10^{-5}$ at $1-\sigma$.

5.10 Parameters of the fitting models M2 and M7

Model M2 and M7 have each 5 coefficients, which are third order polynomial function of β and z :

$$\begin{aligned} a_i(\beta, z) = & q_{i1} + q_{i2}\beta + q_{i3}z + q_{i4}\beta z \\ & + q_{i5}\beta^2 + q_{i6}z^2 + q_{i7}z^3 + q_{i8}\beta^3 \end{aligned} \quad (5.21)$$

Since we have 5 coefficients and 8 free parameters for each coefficient, we have a total of 40 free parameters. They can be represented in a matrix q_{ij} by: $A_i = q_{ij}B_j$, where the vector $A_i = a_i(\beta, z)$ is the vector of coefficients and $B_j = (1, \beta, z, \beta z, \beta^2, z^2, \beta^3, z^3)$ the vector of independent variables and the indices are defined in the ranges: $i = 1, \dots, 5$, $j = 1, \dots, 8$. The corresponding matrix q_{ij} for model M7 is:

$$q_{ij}(M7) = \begin{pmatrix} 0.00689754 & -0.200001 & -0.0112943 & 0.157222 & -1.40171 & 0.0129681 & -3.99345 & -0.00629434 \\ -0.0706221 & 1.45187 & 0.236402 & -1.26467 & 9.13266 & -0.300832 & 9.81754 & 0.120649 \\ 0.069102 & -1.44396 & -0.24268 & 1.26135 & -9.23052 & 0.311995 & -12.1568 & -0.12561 \\ 1.19797 & 0.632936 & -1.74767 & 0.920634 & -8.47056 & 1.46434 & 42.7015 & -0.471948 \\ 0.684838 & 1.15722 & -2.15405 & 3.93688 & -5.29011 & 3.42683 & -43.9295 & -1.18691 \end{pmatrix} \quad (5.22)$$

and the coefficient matrix for model M2 is:

$$q_{ij}(M2) = \begin{pmatrix} 0.00301472 & -0.0961879 & -0.00897697 & 0.0389941 & -0.860642 & 0.0131329 & -4.73786 & -0.00555 \\ -0.028584 & 0.615003 & 0.111671 & -0.371008 & 4.94379 & -0.138279 & 20.3258 & 0.05123 \\ 0.0132728 & -0.345125 & -0.0701132 & 0.115389 & -3.11777 & 0.102871 & -16.9949 & -0.0408 \\ 2.91757 & 1.03545 & -5.16595 & 1.69976 & -22.1649 & 4.33453 & 120.513 & -1.350 \\ 0.867566 & 2.92363 & -1.14174 & 3.4356 & -2.96193 & 1.91413 & -113.348 & -0.684 \end{pmatrix} \quad (5.23)$$

Applying a singular value decomposition on both matrices, shows that they have a very similar structure, therefore since the sigmoidal functions M2 and M7 have a related functional form, the matrices describe roughly the same information.

Chapter 6

The non-linear evolution of matter perturbations

6.1 Standard perturbation theory and higher orders

- Vlasov-Poisson system
- System of equations in Fourier space
- Velocity divergence and vorticity
- Stress tensor and higher order hierarchy terms
- Field variable doublet and 1-loop expansion

6.2 The non-linear standard equations in Fourier space

For studying large scale structure formation we will treat the Dark Matter distribution as a perfect fluid coupled to gravity, described by the continuity, Euler and Poisson's equations. This amounts to neglecting higher moments of the Vlasov equation, such as the stress tensor and velocity dispersions Bernardeau et al., 2001. This is equivalent to the single stream approximation and is one of the main limitations of Eulerian perturbation theory, since the theory breaks down as soon as shell crossing and multi-streaming start being important.

In the Einstein frame we have the following fluid equations for a general modification of gravity or a coupling to other scalar degrees of freedom Pietroni, 2008:

$$\frac{\partial \delta_c}{\partial \tau} + \nabla \cdot [(1 + \delta_c) \mathbf{v}] = 0 \quad (6.1)$$

$$\frac{\partial \mathbf{v}}{\partial \tau} + \mathcal{H}(\mathbf{v} + [\mathcal{A}\mathbf{v}]) + (\mathbf{v} \cdot \nabla) \mathbf{v} = -\nabla \Psi \quad (6.2)$$

$$\nabla^2 \Psi = \frac{3}{2} \mathcal{H}^2 \Omega_c(\tau) (\delta_c + [\mathcal{B}\delta_c]) \quad (6.3)$$

Here τ is the conformal time, $\delta_c(\mathbf{x}, \tau)$ and $\mathbf{v}(\mathbf{x}, \tau)$ are respectively the matter density contrast and the peculiar velocity, $\mathcal{H} = d \log a / d\tau$ is the conformal Hubble parameter, $\Psi(\mathbf{x}, \tau)$ the gravitational potential and the functions $\mathcal{A}(\mathbf{x}, \tau)$ and $\mathcal{B}(\mathbf{x}, \tau)$ are general functions of space and time that parametrize different cosmologies, when particles' geodesics are modified, i.e. the Poisson and Euler equations. This can happen due to couplings with a scalar field or more general modifications of gravity (MG), such as any Horndeski theory or massive bigravity theories [amendola_observables_2012](#). However, in the Jordan frame (where most MG theories are formulated) the Euler

equation is not modified and there is only a space-time dependent modification to the Poisson equation, which can be expressed as in eqn. 2.6 once we go to Fourier space. In this work $\Omega_m(\tau) \equiv \Omega_c(\tau)$ are the time functions representing the cold dark matter (CDM) or the full matter density of the Universe, since we are not considering baryonic matter nor non-universal couplings.

The last term in the left hand side of eqns. 6.1 and 6.2 is what causes the nonlinearities in the evolution of the fluid. This can be seen in Fourier space as a mode-mode coupling or expressed as a nonlocality of the equations. This is the property that describes how a specific Fourier mode is able to depend on another mode at a different wave vector. We now go to Fourier space and will express equations 6.1-6.3 in a compact form introduced by **scoccimarro_new_2000**

The density is a scalar degree of freedom and the velocity can be decomposed such that:

$$\mathbf{v}(\mathbf{k}) = \mathbf{v}_\theta(\mathbf{k}) + \mathbf{v}_\omega(\mathbf{k}) \quad (6.4)$$

where:

$$\begin{aligned} \mathbf{k} \cdot \mathbf{v}_\omega(\mathbf{k}) &= 0 \\ \mathbf{k} \times \mathbf{v}_\theta(\mathbf{k}) &= 0 \end{aligned}$$

According to linear theory the vorticity component $\mathbf{v}_\omega(\mathbf{k})$ decays with the expansion of the Universe as a^{-1} , so if we assume non-vortical initial conditions, we can neglect this term and look only at the velocity divergence $\theta = i\mathbf{k} \cdot \mathbf{v}$, which is now a scalar function. Inverting this last relation to get: $\mathbf{v} = -\frac{i\mathbf{k}}{k^2}\theta$, allows us to perform the Fourier transforms explicitly:

$$\begin{aligned} FT \{ \nabla \cdot (\delta_m \mathbf{v}) \} &= +i\mathbf{k} \int d^3q d^3p \delta_D(\mathbf{p} + \mathbf{q} - \mathbf{k}) \frac{-i\mathbf{p}}{p^2} \delta_m(\mathbf{q}, \tau) \theta(\mathbf{p}, \tau) \\ &= \int d^3q d^3p \delta_D(\mathbf{k} - \mathbf{p} - \mathbf{q}) \underbrace{\frac{(\mathbf{p} + \mathbf{q}) \cdot \mathbf{p}}{p^2}}_{\alpha(\mathbf{p}, \mathbf{q})} \delta_m(\mathbf{q}, \tau) \theta(\mathbf{p}, \tau) \\ \\ FT \{ \nabla \cdot [(\mathbf{v} \cdot \nabla) \cdot \mathbf{v}] \} &= i\mathbf{k} \cdot \int d^3q d^3p \delta_D(\mathbf{q} + \mathbf{p} - \mathbf{k}) \left(\frac{-i\mathbf{q}}{q^2} \cdot i\mathbf{p} \right) \frac{-i\mathbf{p}}{p^2} \theta(\mathbf{q}, \tau) \theta(\mathbf{p}, \tau) \\ &= \mathbf{k} \cdot \int d^3q d^3p \delta_D(\mathbf{k} - \mathbf{q} - \mathbf{p}) \left(\frac{\mathbf{p} \cdot \mathbf{q}}{p^2 q^2} \right) \mathbf{p} \theta(\mathbf{q}, \tau) \theta(\mathbf{p}, \tau) \\ &= \int d^3q d^3p \delta_D(\mathbf{k} - \mathbf{q} - \mathbf{p}) \underbrace{\frac{(\mathbf{p} \cdot \mathbf{q})^2 \mathbf{p} \cdot \mathbf{q}}{2p^2 q^2}}_{\beta(\mathbf{q}, \mathbf{p})} \theta(\mathbf{q}, \tau) \theta(\mathbf{p}, \tau) \end{aligned}$$

where in the last step we used the symmetry between \mathbf{p} and \mathbf{q} . The terms marked with an underbrace, are the ones responsible for the mode-mode coupling:

$$\alpha(\mathbf{q}, \mathbf{p}) = \frac{(\mathbf{p} + \mathbf{q}) \cdot \mathbf{q}}{q^2} = \alpha(-\mathbf{q}, -\mathbf{p}); \quad \beta(\mathbf{q}, \mathbf{p}) = \frac{(\mathbf{p} + \mathbf{q})^2 \mathbf{p} \cdot \mathbf{q}}{2p^2 q^2} = \beta(-\mathbf{q}, -\mathbf{p}) \quad (6.5)$$

6.2.0.1 The field notation

In the perturbation theory literature [crocce_renormalized_2005](#); Bernardeau et al., 2001; Pietroni, 2008, eqns. 6.1-6.3 are written in a more compact way (also called field notation):

$$\partial_\eta \varphi_a(\mathbf{k}, \eta) = -\Omega_{ab}(\mathbf{k}, \eta) \varphi_b(\mathbf{k}, \eta) + e^\eta \gamma_{abc}(\mathbf{k}, -\mathbf{p}, -\mathbf{q}) \varphi_b(\mathbf{p}, \eta) \varphi_c(\mathbf{q}, \eta) \quad (6.6)$$

Where the field doublet is defined as:

$$\varphi_a(\mathbf{k}, \eta) = e^{-\eta} \begin{pmatrix} \delta_m(\mathbf{k}, \eta) \\ -\theta(\mathbf{k}, \eta)/\mathcal{H} \end{pmatrix} \quad (6.7)$$

and we define a new time variable which will prove to be very convenient in this notation

$$\eta \equiv \log \frac{a}{a_{in}}$$

On the l.h.s. of eqn. 6.6 the second term represents all the nonlinearities and non-localities, if we neglect this term we go back to linear perturbation theory. The γ_{abc} functions in this formalism can be understood as interaction vertices and its only non-vanishing components are precisely given by the mode-mode coupling functions 6.5 :

$$\begin{aligned} \gamma_{121}(\mathbf{k}, \mathbf{p}, \mathbf{q}) &= \frac{1}{2} \delta_D(\mathbf{k} + \mathbf{p} + \mathbf{q}) \alpha(\mathbf{p}, \mathbf{q}) & \gamma_{121}(\mathbf{k}, \mathbf{q}, \mathbf{p}) &= \gamma_{112}(\mathbf{k}, \mathbf{p}, \mathbf{q}) \\ \gamma_{222}(\mathbf{k}, \mathbf{p}, \mathbf{q}) &= \delta_D(\mathbf{k} + \mathbf{p} + \mathbf{q}) \beta(\mathbf{p}, \mathbf{q}) \end{aligned} \quad (6.8)$$

in this notation and throughout this work, an integration over \mathbf{p}, \mathbf{q} is understood and \mathbf{k} is always the “external” momentum. The integral signs will be added only when there could be a confusion.

Due to mode-mode coupling, there is a loss of information about the initial conditions in the limit of high- \mathbf{k} , since density perturbations get mixed Crocce and Scoccimarro, 2006a. This has as a consequence that highly-nonlinear corrections to the power spectrum become cosmology-independent in a rough way.

The information about the cosmological background is contained in:

$$\Omega_{ab}(\mathbf{k}, \eta) = \begin{pmatrix} 1 & -1 \\ -\frac{3}{2} \Omega_m(\eta)(1 + \mathcal{B}(\mathbf{k}, \eta)) & 2 + \frac{\mathcal{H}'}{\mathcal{H}} + \mathcal{A}(\mathbf{k}, \eta) \end{pmatrix} \quad (6.9)$$

Where we have the usual definitions: $\mathcal{H} = aH$, $a d\tau = dt$, $a' = \frac{da}{d \ln a} = a$, $\frac{\mathcal{H}'}{\mathcal{H}} = \frac{H'}{H} + 1$, where $' := \frac{d}{d \ln a}$ and $N \equiv \ln a$ is what is typically called the e-foldings time.

For details on how to go back to the usual fluid equations 6.1-6.3 in Fourier space starting from the field equation 6.6, see Appendix ??.

Equation 6.6 is the starting point for all renormalization and resummation methods [crocce_renormalized_2005](#); [bernardeau_constructing_2012](#); [valageas_matter_2013](#); [anselmi_next-leading_2010](#); Bernardeau, 2013; Anselmi and Pietroni, 2012. The linear part can be easily solved and the function relating the initial primordial density perturbations to the final one, is called the linear propagator and will be studied in section 6.2.1. The nonlinear part, cannot be solved exactly analytically, nor numerically. But a perturbative approach using all tools from Quantum Field Theory

can be used to regularize its divergences which are caused by the fact that the density perturbations (which is at the same time the perturbation variable) grows with time and increasing wave vector. For this part we will use the resummation technique of Anselmi and Pietroni, 2012 and this will be explained in detail in section 6.3.

Renormalized perturbation theory (RPT) can help in finding the evolution of the nonlinear power spectrum at small scales and late times, but even if we could calculate exactly its result at all loop orders, there are still intrinsic limitations given by the starting equations 6.1-6.3. Apart from neglecting vorticity in the later stages of evolution, the initial equations are derived in the single-stream-approximation. This means that at a single point in space, there can be only one velocity direction. This clearly breaks down in the virialization regime and even before. The RPT approach can be extended and improved by including these other sources of density power into the equations in an effective way, see the discussion in Manzotti et al., 2014; Pietroni et al., 2011 and recent results in the effective field theory of large scale structures pajar_renormalization_2013; senatore_ir-resummed_2014; Baumann et al., 2012; Carrasco, Hertzberg, and Senatore, 2012.

6.2.1 Solving for the general scale dependent linear propagator

As was explained above, in eqn. 6.6 the non-linearity of the Vlasov-Poisson system of equations is fully encoded in the vertex γ_{abc} which represents the mode-mode coupling. Without this term, we recover the linear equation:

$$\partial_\eta \varphi_a(\mathbf{k}, \eta) = -\Omega_{ab}(\mathbf{k}, \eta) \varphi_b(\mathbf{k}, \eta) \quad (6.10)$$

which is valid for a fully scale and time dependent Ω_{ab} .

The linear propagator is just the function that connects the initial density perturbations with the final ones, or in other words solves the above equation crocce_renormalized_2005 If this equation has solutions of the form Pietroni, 2008:

$$\varphi_{sol}(\mathbf{k}, \eta) = \begin{pmatrix} 1 \\ f(\mathbf{k}, \eta) \end{pmatrix} \varphi(\mathbf{k}, \eta)$$

then we can find an equation that describes the evolution of the growth of perturbations.

For the index $a = 1$:

$$\partial_\eta \varphi = -\Omega_{11}\varphi - \Omega_{12}f\varphi = -(\Omega_{11} + \Omega_{12}f)\varphi \quad (6.11)$$

For the index $a = 2$:

$$\partial_\eta(f\varphi) = f\partial_\eta\varphi + \varphi\partial_\eta f = -\Omega_{21}\varphi - \Omega_{22}f\varphi \quad (6.12)$$

$$\Rightarrow \partial_\eta f = \Omega_{12}f^2 + (\Omega_{11} - \Omega_{22})f - \Omega_{21} \quad (6.13)$$

$$\Rightarrow \partial_\eta f = \Omega_{12}(f - \bar{f}_+)(f - \bar{f}_-) \quad (6.13)$$

Equation 6.12 is what we usually know as the growth rate equation for $f = d \ln D / d \ln a$, being D the growth factor of density perturbations and in this general case it can have a time and scale dependent solution.

The zeros of eqn. 6.13 are given by:

$$\bar{f}_\pm(\mathbf{k}, \eta) = \frac{(\Omega_{22} - \Omega_{11}) \mp \sqrt{(\Omega_{22} - \Omega_{11})^2 + 4\Omega_{21}\Omega_{12}}}{2\Omega_{12}} \quad (6.14)$$

The solution of eqns. 6.11 and 6.13 is then given by:

$$\begin{aligned} \varphi(\eta) &= e^{-\int_{\eta'}^{\eta} (\Omega_{11} + \Omega_{12} f) dx} \varphi(\eta') \\ f(\eta)\varphi(\eta) &= e^{-\int_{\eta'}^{\eta} (\Omega_{21} + \Omega_{22} f) dx} f(\eta')\varphi(\eta') \\ &= e^{-\int_{\eta'}^{\eta} (\Omega_{11} + \Omega_{12} f) dx} \varphi(\eta') f(\eta') \frac{f(\eta)}{f(\eta')} \end{aligned}$$

One can identify the basis solutions by setting their initial conditions as:

$$f_\pm^{in} = \bar{f}_\pm(\mathbf{k}, \eta_i)$$

where η_i is an initial time that can be set at high redshift where the Universe is approximately Einstein-deSitter (E-dS) or strongly matter dominated.

For E-dS, $\Omega_m = 1$ we have very simple background quantities: $\mathcal{H}'/\mathcal{H} = -1/2 - 3w_{eff}/2 = -1/2$, so that the Ω_{ab} from equation 6.9 is simply:

$$\Omega_{ab} = \begin{pmatrix} 1 & -1 \\ -\frac{3}{2} & \frac{3}{2} \end{pmatrix}$$

which gives the following initial conditions for the growing u and decaying v modes:

$$u_a = \begin{pmatrix} 1 \\ f_+^{in} \end{pmatrix} = \begin{pmatrix} 1 \\ 1 \end{pmatrix}$$

$$v_a = \begin{pmatrix} 1 \\ f_-^{in} \end{pmatrix} = \begin{pmatrix} 1 \\ -\frac{3}{2} \end{pmatrix}$$

The growing mode will be the mode of interest that we will use in section 6.3, when we want to calculate the evolution of the power spectrum.

The instantaneous projectors on the two basis solutions are defined as:

$$\mathbf{M}^+(\mathbf{k}, \eta) \begin{pmatrix} 1 \\ f_+(\mathbf{k}, \eta) \end{pmatrix} = \begin{pmatrix} 1 \\ f_+(\mathbf{k}, \eta) \end{pmatrix}$$

$$\mathbf{M}^+(\mathbf{k}, \eta) \begin{pmatrix} 1 \\ f_-(\mathbf{k}, \eta) \end{pmatrix} = 0$$

$$\mathbf{M}^-(\mathbf{k}, \eta) \begin{pmatrix} 1 \\ f_-(\mathbf{k}, \eta) \end{pmatrix} = \begin{pmatrix} 1 \\ f_-(\mathbf{k}, \eta) \end{pmatrix}$$

$$\mathbf{M}^-(\mathbf{k}, \eta) \begin{pmatrix} 1 \\ f_+(\mathbf{k}, \eta) \end{pmatrix} = 0$$

The growing projector can be written explicitly by subtracting the decaying projector from the unity matrix:

$$\mathbf{M}^+(\mathbf{k}, \eta) = \mathbb{1} - \mathbf{M}^-(\mathbf{k}, \eta) = \frac{1}{f_- - f_+} \begin{pmatrix} f_- & -1 \\ f_- f_+ & -f_+ \end{pmatrix}$$

For the Einstein-deSitter case, the projectors do not evolve in time, since u_a and v_a are constant, and they are given by:

$$\mathbf{M}^+ = \frac{1}{5} \begin{pmatrix} 3 & 2 \\ 3 & 2 \end{pmatrix}$$

$$\mathbf{M}^- = \frac{1}{5} \begin{pmatrix} 2 & -2 \\ -3 & 3 \end{pmatrix}$$

The linear propagator is defined as the operator giving the linear evolution of the field φ_a , or in other words, solves eqn.6.10 :

$$\varphi_a(\mathbf{k}, \eta) = g_{ab}(\mathbf{k}, \eta, \eta') \varphi_b(\mathbf{k}, \eta')$$

and it has to fulfill following properties:

$$\partial_\eta g_{ab}(\mathbf{k}, \eta, \eta') = -\Omega_{ac}(\mathbf{k}, \eta) \cdot g_{cb}(\mathbf{k}, \eta, \eta')$$

$$\lim_{\eta' \rightarrow \eta} g_{ab}(\mathbf{k}, \eta, \eta') = \mathbb{1}_{ab}$$

$$g_{ab}(\mathbf{k}, \eta, \eta') \cdot g_{bc}(\mathbf{k}, \eta', \eta'') = g_{ac}(\mathbf{k}, \eta, \eta'')$$

Using these properties and the projectors, the propagator can be written in general as:

$$g(\mathbf{k}, \eta, \eta') = \Theta(\eta - \eta') \left[e^{-\int_{\eta'}^\eta (\Omega_{11} + \Omega_{12} f_+) dx} \begin{pmatrix} 1 & 0 \\ 0 & \frac{f_+(\mathbf{k}, \eta)}{f_+(\mathbf{k}, \eta')} \end{pmatrix} \mathbf{M}^+(\mathbf{k}, \eta') \right. \\ \left. + e^{-\int_{\eta'}^\eta (\Omega_{11} + \Omega_{12} f_-) dx} \begin{pmatrix} 1 & 0 \\ 0 & \frac{f_-(\mathbf{k}, \eta)}{f_-(\mathbf{k}, \eta')} \end{pmatrix} \mathbf{M}^-(\mathbf{k}, \eta') \right] \quad (6.15)$$

In the E-dS case, this would reduce to simply (since there is no k -dependence in any quantity and the growing mode is constant):

$$g(\eta, \eta') = \Theta(\eta - \eta') \left[\frac{1}{5} \begin{pmatrix} 3 & 2 \\ 3 & 2 \end{pmatrix} + \frac{1}{5} \begin{pmatrix} 2 & -2 \\ -3 & 3 \end{pmatrix} e^{-5/2(\eta - \eta')} \right]$$

Using the same procedure, we will calculate the linear propagator for the Horndeski case, in which the growth factor D is now scale and time dependent. Then the linear propagator can be used to calculate its fully nonlinear renormalized version, which then is a crucial ingredient of the evolution equation in section 6.3.

6.2.2 The linear propagator in the Horndeski case

Using eqn. 2.6 as the modification of the Poisson equation we can write the general Ω_{ab} matrix as:

$$\Omega_{ab}(\mathbf{k}, \eta) = \begin{pmatrix} 1 & -1 \\ -\frac{3\mu(k)\Omega_m(\eta)}{2} & \frac{\mathcal{H}'}{\mathcal{H}} + 2 \end{pmatrix} \quad (6.16)$$

in this case, the initial conditions from eqn.6.14 are:

$$\begin{aligned} f_-^{in} &= -\frac{1}{2}(\Sigma + \omega) \\ f_+^{in} &= \frac{1}{2}(\Sigma - \omega) \end{aligned} \quad (6.17)$$

where $\omega = 1 + \frac{\mathcal{H}'}{\mathcal{H}} = \frac{1}{2} - \frac{3}{2}w_{eff}$ and $\Sigma = \sqrt{6Y\Omega_m + \omega^2}$ are quite general functions of scale and time. Inserting this into eqn.6.15, one can find the most general form of the propagator for the Horndeski theory. However, this is not so practical, since we would have to solve for a scale and time dependent growth rate f and evaluate the \mathcal{H} function at each step.

For models which are close to Λ CDM, it is more convenient to change the time variable from $\eta = \ln \frac{a}{a_{in}}$ to $\mathcal{X} = \ln \frac{D(\tau)}{D(\tau=\tau_{in})}$, where $D(\tau)$ is the growth function usually written as the growing solution of the linear density perturbation equation : $\delta_c(\tau) = D_+(\tau)\delta_c^{in}$. In our case, however, the time variable \mathcal{X} would itself be scale dependent, since the growth rate equation in the Horndeski case is scale dependent, so that $\mathcal{X}(k) = \ln \frac{D(\tau_{in}, k)}{D(\tau=\tau_{in}, k)}$. Using $\frac{\partial}{\partial \eta} = \frac{d \ln D}{d \ln a} \frac{\partial}{\partial \ln D} = f \frac{\partial}{\partial \mathcal{X}}$, we can rewrite eqns.6.11-6.12 as (where $' := \frac{\partial}{\partial \mathcal{X}}$):

$$f(\mathbf{k}, \mathcal{X})\delta'_c(\mathbf{k}, \mathcal{X}) + \frac{\theta(\mathbf{k}, \mathcal{X})}{\mathcal{H}} + \frac{\mathbf{k} \cdot \mathbf{q}}{q^2}\delta_c(\mathbf{q}, \mathcal{X})\frac{\theta(\mathbf{p}, \mathcal{X})}{\mathcal{H}} = 0 \quad (6.18)$$

$$f(\mathbf{k}, \mathcal{X})\frac{\theta(\mathbf{k}, \mathcal{X})'}{\mathcal{H}} + \frac{\theta(\mathbf{k}, \mathcal{X})}{\mathcal{H}} + \frac{1}{2}\frac{\mathbf{k}^2 \mathbf{q} \cdot \mathbf{p}}{q^2 p^2}\frac{\theta(\mathbf{q}, \mathcal{X})}{\mathcal{H}}\frac{\theta(\mathbf{p}, \mathcal{X})}{\mathcal{H}} = -\frac{3}{2}\Omega_m(\mathcal{X})\mu(\mathbf{k})\mathcal{H}^2\delta_c(\mathbf{k}, \mathcal{X}) \quad (6.19)$$

The doublet 6.7 can now be redefined as:

$$\tilde{\varphi}_a = \begin{pmatrix} \tilde{\varphi}_1 \\ \tilde{\varphi}_2 \end{pmatrix} = \begin{pmatrix} e^{-\mathcal{X}}\delta_c \\ -e^{-\mathcal{X}}\frac{\theta}{\mathcal{H}f} \end{pmatrix} \quad (6.20)$$

Substituting in the previous equations the values for δ_c , θ and $\delta'_c = e^{\mathcal{X}}(\varphi'_1 + \varphi_1)$, $\theta' = -e^{\mathcal{X}}f(\mathcal{X})\mathcal{H}\left(\tilde{\varphi}_2\left(1 + \frac{f'(\mathcal{X})}{f(\mathcal{X})} + \frac{\mathcal{H}'}{\mathcal{H}}\right) + \tilde{\varphi}'_2\right)$ we get:

$$\tilde{\varphi}'_1 + \tilde{\varphi}_1 - \tilde{\varphi}_2 - \alpha e^{\mathcal{X}}\tilde{\varphi}_1\tilde{\varphi}_2 = 0 \quad (6.21)$$

$$-\tilde{\varphi}'_2 - \tilde{\varphi}_2\left(1 + \frac{f'}{f} + \frac{1}{f} + \frac{\mathcal{H}'}{\mathcal{H}}\right) + \beta e^{\mathcal{X}}\tilde{\varphi}_2\tilde{\varphi}_2 = -\frac{3}{2}\Omega_m\mu\frac{\tilde{\varphi}_1}{f^2}$$

$$\Rightarrow -\tilde{\varphi}'_2 - \frac{3}{2}\frac{\Omega_m\mu}{f^2}\tilde{\varphi}_2 + \frac{3}{2}\frac{\Omega_m\mu}{f^2}\tilde{\varphi}_1 + \beta e^{\mathcal{X}}\tilde{\varphi}_2\tilde{\varphi}_2 = 0 \quad (6.22)$$

where we have omitted for notational simplicity the momentum and time dependence. In the last step we used the growth rate equation $\ddot{\delta}_m + \dot{\delta}_m\left(1 + \frac{\dot{\mathcal{H}}}{\mathcal{H}}\right) = \frac{3}{2}\Omega_m\delta_m\mu$, where in this case an overdot represents a derivative with respect to $\eta = \ln \frac{a}{a_{in}}$, since the ' $'$ -symbol is now reserved for the \mathcal{X} time variable.

Comparing eqns. 6.21-6.22 with 6.6, we get the following Ω matrix:

$$\tilde{\Omega}(\mathbf{k}, \mathcal{X}) = \begin{pmatrix} 1 & -1 \\ -\frac{3}{2}\frac{\Omega_m(\mathcal{X})}{f_+^2(\mathcal{X})}\mu(k) & \frac{3}{2}\frac{\Omega_m(\mathcal{X})}{f_+^2(\mathcal{X})}\mu(k) \end{pmatrix} \quad (6.23)$$

It is of great importance to note that in the Horndeski case, the quantity $\frac{\Omega_m(\mathcal{X})}{f_+^2(\mathcal{X})}$ cannot be approximated to 1 as it is done in LCDM for all times, since in this case it can have a much greater or lower value during structure formation, but more importantly it is scale-dependent through the scale dependence of $\mathcal{X}(k)$. This can be seen clearly in plot ??.

6.2.3 Assuming a constant $\mu \neq 1$ for the 1-loop quantities

Assuming a constant μ different from 1 and the approximation that $\frac{\Omega_m(\mathcal{X})}{f_+^2(\mathcal{X})} = 1$ throughout the history of the Universe (which is valid only for E-dS but turns out to be a good approximation (much more accurately than 1%) for the nonlinear Λ CDM power spectrum), we can follow the steps given above in section 6.2.1 and obtain the initial growing and decaying modes:

$$u_a = \begin{pmatrix} 1 \\ 1 \end{pmatrix}$$

$$v_a = \frac{-2}{3Y} \begin{pmatrix} 1 \\ -\frac{3Y}{2} \end{pmatrix}$$

and with this the projectors:

$$\mathbf{M}^+ = \frac{1}{2+3Y} \begin{pmatrix} 3Y & 2 \\ 3Y & 2 \end{pmatrix}$$

$$\mathbf{M}^- = \frac{1}{2+3Y} \begin{pmatrix} 2 & -2 \\ -3Y & 3Y \end{pmatrix}$$

The propagator would then look like:

$$g(\mathcal{X}, \mathcal{X}') = \Theta(\mathcal{X} - \mathcal{X}') \left[\frac{1}{2+3Y} \begin{pmatrix} 3Y & 2 \\ 3Y & 2 \end{pmatrix} + \frac{1}{2+3Y} \begin{pmatrix} 2 & -2 \\ -3Y & 3Y \end{pmatrix} e^{-\frac{(2+3Y)}{2}(\mathcal{X}-\mathcal{X}')} \right] \quad (6.24)$$

For the rest of this work, eqn. 6.24 will be the linear propagator we will use, even if we are treating more general cases where $\mu(k)$ is an arbitrary function and $\Omega_m/f^2 \neq 1$. This approximation can be justified better in the next section, when we will see that g only enters in the evolution equation of the power spectrum inside the integral of the self-energy and mode-coupling 1-loop quantities, which should contribute only sub-dominantly in the final power spectrum.

6.3 The Evolution Equation for the Power Spectrum

We are interested in solving the general scale and time dependent evolution equation from the resummation method presented in Anselmi and Pietroni, 2012 (eqn. 53):

$$\begin{aligned}\partial_{\mathcal{X}} \tilde{P}_{ab}(k; \mathcal{X}) = & -\tilde{\Omega}_{ac}(\mathbf{k}; \mathcal{X}) \tilde{P}_{cb}(\mathbf{k}; \mathcal{X}) - \tilde{\Omega}_{bc}(\mathbf{k}; \mathcal{X}) \tilde{P}_{ac}(\mathbf{k}; \mathcal{X}) \\ & + H_{\mathbf{a}}(k; \mathcal{X}, \mathcal{X}_{in}) \tilde{P}_{\mathbf{ab}}(\mathbf{k}; \mathcal{X}) + H_{\mathbf{b}}(k; \mathcal{X}, \mathcal{X}_{in}) \tilde{P}_{\mathbf{ab}}(\mathbf{k}; \mathcal{X}) \\ & + \int ds \left[\tilde{\Phi}_{ad}(k; \mathcal{X}, s) G_{bd}^{eik}(k; \mathcal{X}, s) + G_{ad}^{eik}(k; \mathcal{X}, s) \tilde{\Phi}_{db}(k; \mathcal{X}, s) \right]\end{aligned}\quad (6.25)$$

where $\mathcal{X} = \ln(D(a)/D(a_{in}))$ (notice that in ref. Anselmi and Pietroni, 2012, η is the time variable and represents the growth factor). The first line of this equation corresponds to the linear evolution equation of the power spectrum already discussed before. The second and third lines contain the 1PI (one-particle-irreducible) functions, the self-energy Σ_{ab} and the mode-coupling term $\tilde{\Phi}G_{ab}^{AB}$ accounting for the contributions at the large- and small-k limit at 1-loop order.

Massimo: Can you check from eqns. 33–36?

If we transform this equation to $\eta = \ln \frac{a}{a_{in}}$, using the variable transformation $\partial \mathcal{X}/\partial \eta = \frac{d \ln D(a)}{d \ln a} = f(\eta)$, where $f(\eta) \equiv f(N(\eta))$ and the relation between N and η is given by $N = \eta + \ln(a_{in})$, we have to transform also the power spectrum since the field has been redefined (see 6.20):

$$\tilde{P}_{ab} = e^{-2\mathcal{X}(\eta)} e^{2\eta} (\delta_{a1} + \frac{1}{f(\eta)} \delta_{a2})(\delta_{b1} + \frac{1}{f(\eta)} \delta_{b2}) P_{ab}(\eta) \quad (6.26)$$

where we can call this transformation Ξ_{ab} :

$$\tilde{P}_{ab} = \Xi_{ab} P_{ab}(\eta)$$

and its inverse would be:

$$\Xi_{ab}^{-1} = e^{2\mathcal{X}(\eta)} e^{-2\eta} (\delta_{a1} + f(\eta) \delta_{a2})(\delta_{b1} + f(\eta) \delta_{b2}) \quad (6.27)$$

However, eqn. 6.25 is only invariant under the transformation:

$$\Upsilon_{ab}(\eta) = f(\eta) \Xi_{ab}^{-1} = f(\eta) e^{2\mathcal{X}(\eta)} e^{-2\eta} (\delta_{a1} + f(\eta) \delta_{a2})(\delta_{b1} + f(\eta) \delta_{b2}) \quad (6.28)$$

since we also have to transform the derivatives and the Ω_{ab} functions.

Inserting these transformations into eqn. 6.25, and generalizing to the case where the growth rate is k-dependent, $f(\eta, k)$, we obtain:

$$\partial_{\eta} P_{ab}(k; \eta) = -\Omega_{ac}(\mathbf{k}; \eta) P_{cb}(\mathbf{k}; \eta) - \Omega_{bc}(\mathbf{k}; \eta) P_{ac}(\mathbf{k}; \eta) \quad (6.29)$$

$$+ [H_{\mathbf{a}}(k; \mathcal{X}(\eta, k), \mathcal{X}(\eta_{in}, k)) f(\eta, k) P_{\mathbf{ab}}(k; \eta)$$

$$+ H_{\mathbf{b}}(k; \mathcal{X}(\eta, k), \mathcal{X}(\eta_{in}, k)) f(\eta, k) P_{\mathbf{ab}}(k; \eta)]$$

$$+ \Upsilon_{ab}(\eta, k) \times \int ds \left[\tilde{\Phi}_{ad}(k; \mathcal{X}(\eta, k), s) G_{bd}^{eik}(k; \mathcal{X}(\eta, k), s) + G_{ad}^{eik}(k; \mathcal{X}(\eta, k), s) \tilde{\Phi}_{db}(k; \mathcal{X}(\eta, k), s) \right]$$

The quantities such as $H_{\mathbf{a}}(k; \eta, \eta_{in})$ and $\tilde{\Phi}_{ad}(k; \eta, s)$, shown in eqns 6.33–6.36, which are actually calculated in the \mathcal{X} variable, are now indirectly a function of η through the relation $\mathcal{X}(\eta) = \ln(D(N(\eta))/D(N(\eta_{in})))$.

The evolution equation as it is written in eqn. 6.25 relies on three different assumptions: the power spectrum is well behaved for $k \rightarrow 0$, which is in our cosmology a good assumption, since it behaves just a power law k^n ; there is a clear separation of scales between “hard” and “soft” modes, or in other words, the eikonal limit is fulfilled. This means that the modes k we are interesting in are much bigger than the internal coupling modes p, q . The third assumption is of course the single-stream approximation, which is used in all forms of resummed and renormalized perturbation theories in cosmology as was explained already in section 6.2.0.1.

In this work we want to solve eqn. ?? for the simple Horndeski models stated above. We will test two approaches, first we will include inside the $\Omega_{ac}(\mathbf{k}; \eta)$ functions, the full scale and time dependence of the parametrized Horndeski models. These terms will have a dominant effect on the evolution of $P(\mathbf{k})$ and we will calculate the 1-loop integrals using the usual Λ CDM model. Since the $H_a(k; \eta, \eta_{in})$ and $\tilde{\Phi}_{ab}(k; \eta, s)$ functions are calculated for a scale-dependent growth factor, we will have to test if this scale dependence has a big effect on the result.

As a second approach we will calculate the 1PI functions using the linear Horndeski propagator in the case that μ is a constant different from one. Once these integrals are calculated, we can then solve the evolution equation completely. In this case we have to test how much a change in $\mu(k)$ affects the result, i.e. if assuming a constant μ is a good approximation or not. In the next section we will show the explicit expressions for these integrals.

6.3.1 The 1PI functions in the Horndeski constant $\mu \neq 1$ case

The Horndeski variable is Y for compatibility with the code for now, but it can be changed to μ later on.

Now we give the general expression for the 1PI functions $\Sigma_{ab}^{(1)}(k; \mathcal{X}, \mathcal{X}')$ and $\Phi_{ab}^{(1)}(k; \mathcal{X}, \mathcal{X}')$ computed at 1-loop in eRPT. The general expression for $\Sigma_{ab}^{(1)}(k; \mathcal{X}, \mathcal{X}')$ is given by:

$$\begin{aligned} \Sigma_{ab}^{(1)}(k; \mathcal{X}, \mathcal{X}') = & \\ & 4e^{\mathcal{X}+\mathcal{X}'} \int d^3q \gamma_{acd}(\mathbf{k}, -\mathbf{q}, \mathbf{q} - \mathbf{k}) u_c P^0(q) u_e \gamma_{feb}(\mathbf{k} - \mathbf{q}, \mathbf{q}, -\mathbf{k}) g_{df}(\mathcal{X}, \mathcal{X}') \end{aligned} \quad (6.30)$$

If we insert for g_{ab} the linear propagator from 6.24 and the coupling vertices γ_{abc} from 6.8 we have to perform an angular integration of d^3q , see Appendix ?? for the explicit terms.

The $H_1(k; \mathcal{X}, -\infty), H_2(k; \mathcal{X}, -\infty)$ functions are a time integration of the $\Sigma_{ab}^{(1)}(k; \mathcal{X}, \mathcal{X}')$ quantities in the internal time from minus infinity to the external time η :

$$H_1(k; \mathcal{X}, -\infty) = \int_{-\infty}^{\eta} ds \Sigma_{1b}^{(1)}(k; \mathcal{X}, \mathcal{X}') u_b \quad (6.31)$$

$$H_2(k; \mathcal{X}, -\infty) = \int_{-\infty}^{\eta} ds \Sigma_{2b}^{(1)}(k; \mathcal{X}, \mathcal{X}') u_b \quad (6.32)$$

They have the following form after performing the time integration:

$$H_{1Y}(k; \mathcal{X}, -\infty) = -\frac{\pi k^3 e^{2\mathcal{X}}}{3(3Y+4)} \int dr \left[16 + 3Y(3r^4 - 8r^2 + 1) - \frac{9Y}{2r} (r^2 - 1)^3 \log \left| \frac{1+r}{1-r} \right| \right] P^0(kr) \quad (6.33)$$

$$H_{2Y}(k; \mathcal{X}, -\infty) = -\frac{\pi k^3 e^{2\mathcal{X}}}{3(3Y+4)} \int dr \left[-\frac{9Y}{r^2} + 9r^2\mu + 4(9Y+4) - \frac{9Y}{2r^3} (r^2 - 1)^3 \log \left| \frac{1+r}{1-r} \right| \right] P^0(kr) \quad (6.34)$$

The third line of the evolution equation 6.25 contains the mode-coupling function, which is obtained by integrating the counter-term 1-loop quantity:

$$\tilde{\Phi}_{ad}^{(1)}(k; \mathcal{X}, \mathcal{X}') = 2e^{\mathcal{X}+\mathcal{X}'} \int d^3q \gamma_{acd}(\mathbf{k}, -\mathbf{q}, \mathbf{p}) u_c P^0(q) u_d \quad (6.35)$$

$$\times u_e P^0(p) u_f \gamma_{bef}(\mathbf{k}, -\mathbf{q}, \mathbf{p}) \quad (6.36)$$

where $\mathbf{p} = \mathbf{k} - \mathbf{q}$, together with the renormalized propagator from Crocce-Scoccimarro $\bar{G}_{bd}^L(k; \eta, s)$:

$$\int ds \left[\tilde{\Phi}_{ad}(k; \mathcal{X}, s) \bar{G}_{bd}^L(k; \mathcal{X}, s) + \bar{G}_{ad}^L(k; \mathcal{X}, s) \tilde{\Phi}_{db}(k; \mathcal{X}, s) \right] = \tilde{\Phi} G_{ab}^A(k; \mathcal{X}) + \tilde{\Phi} G_{ab}^B(k; \mathcal{X}) \quad (6.37)$$

where for all a, b , the B terms are:

$$\tilde{\Phi} G_{ab}^B(k; \mathcal{X}) = u_a u_b y^2 \left(\frac{\sqrt{\pi}}{2} (2y^2 + 1) \text{Erf}(y) + (e^{-y^2} - 2) y \right) P^0(k) \quad (6.38)$$

The $\tilde{\Phi} G_{ab}^B(k; \eta)$ expression has to be switched off in the small k -limit since it contains 2-loop expressions valid only at large k , therefore it has to be “filtered” by a momentum-cutoff function:

$$\tilde{\Phi} G_{ab}^A(k; \eta) + \frac{(k/\bar{k})^4}{1 + (k/\bar{k})^4} \tilde{\Phi} G_{ab}^B(k; \eta)$$

The \bar{k} quantity can be set to a reasonable scale at which the large scale expression starts to be applicable, usually we can set here $\bar{k} = 0.2h/\text{Mpc}$. The A terms read (a new variable $W = \frac{3}{2}Y$ has been defined for simplicity):

$$\tilde{\Phi} G_{11}^A = y(\Phi_{11}^{(1)} - \Phi_{11}^{(1)}) \mathcal{B}(y^2; W) \quad (6.39)$$

$$+ \frac{\sqrt{\pi} \text{Erf}(y)}{W+1} (\Phi_{11}^{(1)} W + \Phi_{12}^{(1)})$$

$$\tilde{\Phi} G_{12}^A = \frac{y \mathcal{B}_{12}(y^2; W)}{(1+W)^2(2+W)} (\Phi_{12}^{(1)} - \Phi_{22}^{(1)} - W(\Phi_{11}^{(1)} - \Phi_{12}^{(1)})) \quad (6.40)$$

$$+ \frac{\sqrt{\pi} \text{Erf}(y)}{2(W+1)} (W(\Phi_{11}^{(1)} + \Phi_{12}^{(1)}) + \Phi_{12}^{(1)} + \Phi_{22}^{(1)}) \quad (6.41)$$

$$\tilde{\Phi}G_{22}^A = \frac{yW}{(W+1)^2}(\Phi_{22}^{(1)} - \Phi_{12}^{(1)})\mathcal{B}(y^2; W) + \frac{\sqrt{\pi}}{(W+1)}\text{Erf}(y)(\Phi_{12}^{(1)}W + \Phi_{22}^{(1)}) \quad (6.42)$$

and where we have used the combination of generalized Hypergeometric functions:

$$\begin{aligned} \mathcal{B}(y^2; W) &= {}_2F_2\left(\frac{1}{2}, 1; \frac{W}{2} + 1, \frac{W}{2} + \frac{3}{2}; -y^2\right) \\ &\quad + \frac{W+1}{W+2} {}_2F_2\left(\frac{1}{2}, 1; \frac{W}{2} + \frac{3}{2}, \frac{W}{2} + 2; -y^2\right) \\ &\quad - \frac{1}{W+2} {}_2F_2\left(1, \frac{3}{2}; \frac{W}{2} + \frac{3}{2}, \frac{W}{2} + 2; -y^2\right) \\ \mathcal{B}_{12}(y^2; W) &= (2+W) {}_2F_2\left(\frac{1}{2}, 1; \frac{W}{2} + 1, \frac{W}{2} + \frac{3}{2}; -y^2\right) \\ &\quad - {}_2F_2\left(1, \frac{3}{2}; \frac{W}{2} + \frac{3}{2}, \frac{W}{2} + 2; -y^2\right) \end{aligned}$$

Assuming a general scale-dependent function $\mu(k)$ would turn out impossible an analaytic calculation of the intermediate quantities, which would render a practical implementation of this method to be numerically prohibitive. Therefore, using the fact that the μ function behaves as a step function in $\log k$, having a well defined minimum and maximum value we can use simply a constant and check its effect on the 1-loop and 2-loop corrections. Besides, in any viable model compatible with observations μ can differ from 1 by about 15-20%. So that we can be sure that the overall effect will be just a perturbation around the LCDM value and should reduce to it in the limit $\mu \rightarrow 1$.

Issue: In the LCDM case from Massimo's paper, all three $\tilde{\Phi}G_{ab}^A$ functions can be written using the same combination of Hypergeometric Functions. In this case, this is only possible for $\tilde{\Phi}G_{11}^A$ and $\tilde{\Phi}G_{22}^A$.

6.3.2 Method of implementation

Equation ?? is the final and main equation we want to solve and it represents a differential equation in time, for each external momentum k that we are interested in. This means that if we want to compute the power spectrum on a grid with 100 points in k -space, we need to solve 100 times the same differential equation. That is why parallelism plays an important role here to speed up the computational calulation.

First we compute the linear growth function for a specific Horndeski model, using the linear part of 6.19. With this we obtain the growth rate and the growth factor, which are then used to calculate the loop integrals.

The initial power spectrum is obtained from CAMB and its evaluated at 100 points in k -space. This is used to compute analytically eqns. 6.33, 6.34. These integrals can be stored as long as the cosmological parameters are not modified.

Finally we compute the 6.25 for each k mode in parallel, which using 8 cores on a normal machine, takes about 15 seconds until redshift $z = 0$.

6.4 Numerical approaches

6.4.1 N-body simulations

- The Vlasov-Poisson system can be discretized on a grid and the density can be represented with particles
- Particle-Mesh method
- Tree method
- Extraction of information: The power spectrum and Halo catalogs

6.4.2 Fitting formulae and prescriptions

Chapter 7

Growing Neutrino Quintessence

7.1 Introduction

The observed accelerated expansion of the Universe is currently well described by the standard Λ CDM scenario, where a cosmological constant leads the background of the Universe to a final de Sitter state. Such a scenario, however, raises a “coincidence” (or “why-now”) problem, as it is not understood why dark energy becomes important just recently, marking the present cosmological epoch as a special one within cosmic history. Alternative models of dynamical dark energy or modified gravity should address the “why now problem” and the associated fine tuning of parameters. At the same time they need to explain why dark energy is almost static in the present epoch, such that the present dark energy equation of state w is close to the observed range near -1 .

Growing neutrino quintessence [wetterich_growing_2007](#); Amendola, Baldi, and Wetterich, [2008](#) explains the end of a cosmological scaling solution (in which dark energy scales as the dominant background) and the subsequent transition to a dark energy dominated era by the growing mass of neutrinos, induced by the change of the value of the cosmon field which is responsible for dynamical dark energy. The dependence of the mass of neutrinos on the cosmon (dark energy) field ϕ ,

$$m_\nu = m_\nu(\phi) \propto \hat{m}_\nu e^{-\int \beta(\phi) d\phi}, \quad \beta(\phi) = -\frac{\partial \ln m_\nu(\phi)}{\partial \phi} \quad (7.1)$$

involves the cosmon-neutrino coupling $\beta(\phi)$ which measures the strength of the fifth force (additional to gravity). The constant \hat{m}_ν is a free parameter of the model which determines the size of the neutrino mass. (We take for simplicity all three neutrino masses equal - or equivalently m_ν stands qualitatively for the average over the neutrino species.) The special role of the neutrino masses (as compared to quark and charged lepton masses) is motivated at the particle physics level by the way in which neutrinos get masses [wetterich_growing_2007](#) Growing neutrino quintessence with a sufficiently large negative value of β successfully relates the present dark energy density and the mass of the neutrinos. The evolution of the cosmon is effectively stopped once neutrinos become non-relativistic. Dark energy becomes important now because neutrinos become non-relativistic in a rather recent past, at typical redshifts of about $z = 5$ [mota_neutrino_2008](#) In this way, the “why now problem” is resolved in terms of a “cosmic trigger event” induced by the change in the effective neutrino equation of state, rather than by relying on the fine tuning of the scalar potential. This differs from other mass varying neutrino cosmologies (usually known as MaVaN’s) [brookfield_cosmology_2007](#); [la_vacca_mass-varying_2013](#); [bi_cosmological_2005](#); [fardon_dark_2004](#); [kaplan_neutrino_2004](#); [spitzer_stability_2006](#); [takahashi_speed_2006](#) Some of the observational consequences of those models were studied in [la_vacca_mass-varying_2013](#); [kaplan_neutrino_2004](#)

and more recently a new scalar field - neutrino coupling that produces viable cosmologies was proposed in [simpson_dark_2016](#) A viable cosmic background evolution of growing neutrino quintessence offers interesting prospects of a possible observation of the neutrino background.

The case in which the coupling β is constant has been largely investigated in literature at the linear level [mota_neutrino_2008](#) in semi-analytical non-linear methods [wintergerst_very_2010](#); Wintergerst and Pettorino, [2010](#); Brouzakis et al., [2011](#), joining linear and non-linear information to test the effect of the neutrino lumps on the cosmic microwave background Pettorino et al., [2010](#) and within N-Body simulations [ayaita_neutrino_2013](#); [ayaita_structure_2012](#); [ayaita_nonlinear_2016](#); Baldi et al., [2011](#). For the values of β ($\beta \gtrsim 10^3$) needed for dark energy to dominate today, the cosmic neutrino background is clumping very fast. Large and concentrated neutrino lumps form and induce very substantial backreaction effects. These effects are so strong that the deceleration of the evolution of the cosmon gets too weak, making it difficult to obtain a realistic cosmology [fuhrer_backreaction_2015](#)

In this paper we instead consider the case in which the neutrino-cosmon coupling $\beta(\phi)$ depends on the value of the cosmon field and increases with time. In a particle physics context this has been motivated [wetterich_growing_2007](#) by a decrease with ϕ of the heavy mass scale (B-L-violating scale) entering inversely the light neutrino masses. In this scenario $\beta(\phi)$ has not been large in all cosmological epochs - the present epoch corresponds to a crossover where β gets large. A numerical investigation Baldi et al., [2011](#) of this type of model has revealed compatibility with observations for the case of a present neutrino mass $m_{\nu,0} = 0.07$ eV. In the present paper we investigate the dependence of cosmology on the value of the neutrino mass by varying the parameter \hat{m}_ν in eq. 7.1. For large neutrino masses we find a qualitative behavior similar to the case of a constant neutrino-cosmon coupling β , with difficulties to obtain a realistic cosmology. In contrast, for small neutrino mass, the neutrino lumps form and dissolve, with small influence on the overall cosmological evolution. In this case, the neutrino-induced gravitational potentials are found to be much smaller than the ones induced by dark matter. As we will discuss in this paper, it will not be easy to find observational signals for the neutrino lumps. In-between the regions of small and large neutrino masses we expect a transition region for intermediate neutrino masses where, by continuity, observable effects of the neutrino lumps should show up.

7.2 Growing neutrinos with varying coupling

We consider here cosmologies in which neutrinos have a mass that varies in time, along the framework of “varying growing neutrino models” [wetterich_growing_2007](#) As long as neutrinos are relativistic, the coupling is inefficient and the dark energy scalar field ϕ rolls down a potential, as in an early dark energy scenario. As the neutrino mass increases with time, neutrinos become non-relativistic, typically at a relatively late redshift $z \approx 4 - 6$ Pettorino et al., [2010](#). This influences the evolution of ϕ , which feels the effect of neutrinos via a coupling to the neutrino mass $m_\nu(\phi)$. The evolution of the scalar field slows down and practically stops, such that the potential energy of the cosmon behaves almost as a cosmological constant at recent times. In other words, in these models the cosmological constant behavior observed today is related to a cosmological trigger event (i.e. neutrinos becoming non-relativistic) and the present dark energy density is directly connected to

the value of the neutrino mass. In the following we will detail the formalism and equations used to describe the cosmological evolution of the model.

We start with the linearized Friedman-Lemaitre-Robertson-Walker metric in the Newtonian gauge:

$$ds^2 = -(1 + 2\Psi)dt^2 + a^2(1 - 2\Phi)d\mathbf{x}^2 . \quad (7.2)$$

Moreover, we use a quasi-static approximation for sub-horizon scales ($H/k \ll 1$) which allows us to neglect time derivatives with respect to spatial ones. Then the quasi-static, first-order perturbed Einstein equations, are the Poisson equation [ma_cosmological_1994](#)

$$k^2\Phi = 4\pi G a^2 \delta T_0^0 , \quad (7.3)$$

and the “stress” equation

$$k^2(\Phi - \Psi) = 12G a^2 (\bar{\rho} + \bar{P})\sigma , \quad (7.4)$$

where δT_0^0 is the perturbation of the $0 - 0$ component of the energy momentum tensor $T_{\mu\nu}$ and σ is the anisotropic stress of the fluid which depends on the traceless component of the spatial part of the energy-momentum tensor, $T_j^i - \delta_j^i T_k^k/3$. This stress tensor is in our case only important for relativistic particles (i.e. the neutrinos). The source term of the Poisson equation 7.3 will contain contributions from all matter species (dark matter & neutrinos) and from the cosmon field. It is proportional to the total density contrast $\delta\rho_t = \delta\rho_\nu + \delta\rho_m + \delta\rho_\phi$.

The cosmon field can be described through a Lagrangian in the standard way

$$-\mathcal{L}_\phi = \frac{1}{2}\partial^\nu\phi\partial_\nu\phi + V(\phi) \quad (7.5)$$

where for this work we choose an exponential potential $V(\phi) \propto e^{-\alpha\phi}$. The field dependent mass (eq.7.1) allows for an energy-momentum transfer between neutrinos and the cosmon, which is proportional to the trace of the energy momentum tensor of neutrinos $T_{(\nu)}$ and to a coupling parameter $\beta(\phi)$

$$\nabla_\eta T_{(\phi)}^{\mu\eta} = +\beta(\phi)T_{(\nu)}\partial^\mu\phi , \quad (7.6)$$

$$\nabla_\eta T_{(\nu)}^{\mu\eta} = -\beta(\phi)T_{(\nu)}\partial^\mu\phi . \quad (7.7)$$

The cosmon is the mediator of a fifth force between neutrinos, acting at cosmological scales. Its evolution is described by the Klein-Gordon equation sourced by the trace of the energy-momentum tensor $T_{(\nu)}$ of the neutrinos,

$$\nabla_\mu\nabla^\mu\phi - V'(\phi) = \beta(\phi)T_{(\nu)}. \quad (7.8)$$

As long as the neutrinos are relativistic ($T_{(\nu)} = 0$) the source on the right hand side vanishes. During this time, the coupling has no effect on the evolution of ϕ . While the potential term $\sim V'$ drives ϕ towards larger values, the term $\sim \beta$ has the opposite sign and stops the evolution effectively once $\beta T_{(\nu)}$ equals V' . The trace of the energy momentum tensor T_ν , entering eq.7.8 is equal to:

$$T_\nu = m_\nu(\phi)\tilde{n}(\phi) \quad (7.9)$$

where $\tilde{n}_\nu(\phi) = n_\nu(\phi)/\gamma$ is the ratio of the number density of neutrinos n_ν , divided

by the relativistic γ factor. Eq.7.9 is valid for both relativistic and non-relativistic neutrinos. Here we consider a coupling β between neutrino particles and the quintessence scalar field ϕ as a field dependent quantity:

$$\beta(\phi) \equiv -\frac{1}{\phi_c - \phi}. \quad (7.10)$$

From eq.7.1 the neutrino mass is then given by:

$$m_\nu(\phi) = \frac{\bar{m}_\nu}{\phi_c - \phi}. \quad (7.11)$$

Here ϕ_c denotes the asymptotic value of ϕ for which β and $m_\nu(\phi)$ would formally become infinite. By an additive shift in ϕ it can be set to an arbitrary value, e.g. $\phi_c = 0$. We consider the range $\phi < \phi_c$. The divergence of β for $\phi \rightarrow \phi_c$ in eq.7.10 is not crucial for the results of the present paper - β and m_ν never increase to large values, such that the immediate vicinity of ϕ_c plays no role.

The coupling induces a total force acting on neutrinos given by $\nabla(\Phi_\nu + \beta\delta\phi)$ and appearing in the corresponding Euler equation Pettorino et al., 2010, as usual in coupled cosmologies Baldi et al., 2010. For values $2\beta^2 > 1$ the fifth force induced on neutrinos by the cosmon becomes larger than the gravitational attraction. For the large values of $|\beta| \approx 10^2$ reached during the cosmological evolution, the attraction induced by the cosmon gives rise to the formation of neutrino lumps. As shown in [mota_neutrino_2008](#); Pettorino et al., 2010 this represents the major difficulty encountered within growing neutrino models and also, simultaneously, one of its clearest predictions with respect to alternative dark energy models: the presence of neutrino lumps at scales of ≈ 10 Mpc or even larger, depending on the details of the model [mota_neutrino_2008](#). Since the attractive force between neutrinos is 10^4 times bigger than gravity, therefore also the dynamical time scale of the clumping of neutrino inhomogeneities is a factor 10^4 faster than the gravitational time scale. Even the tiny inhomogeneities in the cosmic neutrino background grow very rapidly non-linear. The impact of such structures, has been shown to depend crucially on the strength of backreaction effects [ayaita_structure_2012](#); [ayaita_nonlinear_2016](#). For constant coupling, the effect of backreaction is strong and can lead to neutrino lumps with rapidly growing concentration, reaching values of the gravitational potential which exceed observational constraints. The effect is so strong that it is able to destroy the oscillatory effect first encountered in Baldi et al., 2010, in which neutrino lumps were forming and then dissipating. No realistic cosmology has been found in this case [fuhrer_backreaction_2015](#). With the varying coupling of eq.7.10 a similar behavior will be found for large neutrino masses. For small neutrino masses the oscillatory effects will be dominant and realistic cosmologies seem possible [ayaita_nonlinear_2016](#).

7.3 Numerical treatment of growing neutrino cosmologies

7.3.1 Modified Boltzmann code

For the early stages of the evolution of the growing neutrino quintessence model, neutrinos behave as standard relativistic particles and the coupling to the cosmon field is suppressed. Therefore the Klein-Gordon equation can be linearized and no important backreaction effects are present. The Einstein-Boltzmann system of equations for the relativistic neutrinos and all other species has been solved using a

modified version of the code CAMB Lewis, Challinor, and Lasenby, 2000 (hereafter referred to as nuCAMB), used and developed already in previous papers on mass-varying and growing neutrino cosmologies. We refer the reader to previous publications **mota_neutrino_2008; wintergerst_very_2010; brookfield_cosmology_2007**; Pettorino et al., 2010 for details about its implementation. These equations are valid until neutrinos become non-relativistic and as long as perturbations are still linear. The neutrinos can be seen as a weakly-interacting gas of particles in thermal equilibrium with a phase space distribution $f(p)$ with p denoting the momentum. The statistical description is in the case of neutrinos a Fermi-Dirac distribution, given by

$$f_{FD}(p) = \frac{1}{e^{(E(p)-\mu)/T} + 1}, \quad (7.12)$$

where μ is the chemical potential and $E(p) = \sqrt{m^2 + p^2}$ the particle energy. Then, the number density of neutrinos, the energy density and the pressure are given respectively by

$$n_\nu = \frac{2}{(2\pi)^3} \int d^3p f_{FD}(p), \quad (7.13)$$

$$\rho_\nu = \frac{2}{(2\pi)^3} \int d^3p E(p) f_{FD}(p), \quad (7.14)$$

$$P_\nu = \frac{2}{(2\pi)^3} \int d^3p \frac{p^2}{E(p)} f_{FD}(p). \quad (7.15)$$

The solution of the Boltzmann hierarchy of neutrinos coupled to the perturbed Einstein equations 7.3 and 7.4, together with the solution of the background Klein-Gordon equation 7.8, form the basis of the modification of nuCAMB with respect to the standard code CAMB, which handles dark matter, photons and baryons altogether. We recall that for growing neutrino quintessence, the neutrino mass depends on the cosmon field ϕ and therefore on the scale factor a .

The ratio of the initial mass of the neutrinos to their temperature (given in eV), is calculated in nuCAMB as follows

$$\hat{r}_{\nu eV} \equiv \left(\frac{m}{T}\right)_{\nu, camb} = \frac{(7/8)(\pi^4/15)}{(3/2)\zeta(3)} \times \frac{\rho_{cr}\Omega_{\nu, input}}{\rho_\nu}. \quad (7.16)$$

The first fraction comes from the relation $m_\nu \approx \rho_\nu/n_\nu = ((7\pi^4/8\cdot 15)/3/2\zeta(3))T_\nu$, which is valid in the non-relativistic limit of eqns. 7.12-7.15; the critical density is defined as usual: $\rho_{cr} = \frac{3H_{0,input}^2}{8\pi G}$. The second fraction is a re-scaling that corrects the neutrino density in order to match the wanted $\Omega_{\nu, input}$ given as input value. The code performs an iterative routine that varies initial conditions in such a way that the input parameters are obtained at present time. Since this is not exact, the final values of H_0 and Ω_ν might vary slightly with respect to the given input values. The ratio $\hat{r}_{\nu eV}$ depends on the input parameters $H_{0,input}$ (via the critical density) and on $\Omega_{\nu, input}$ ¹. Furthermore, the neutrino energy density ρ_ν and the photon energy density ρ_γ at relativistic times are related as

$$\rho_\nu = N_\nu \times \frac{7}{8} \times \left(\frac{4}{11}\right)^{4/3} \rho_\gamma \quad (7.17)$$

¹ $\hat{r}_{\nu eV}$ is also the conversion factor between the mass units in the N-Body code and units in eV.

where $N_\nu = 3$ is the number of neutrino species. The use of these formulae is valid if initial conditions are set when neutrinos are non-relativistic, where the linear regime still applies. For initial conditions set at earlier time relativistic corrections have to be taken into account. After solving the Einstein-Boltzmann system, realizations of the fields $\delta_\nu(\mathbf{k})$ and $v_{pec,\nu}(\mathbf{k})$ at an early time are obtained from nuCMB and are then used as the initial conditions for the neutrino distribution in the growing neutrino quintessence N-body simulation. This will be explained more in detail at the end of the following section.

7.3.2 N-body simulation

For N-body simulations, we use here the code developed in `ayaita_neutrino_2013`; `ayaita_nonlinear_2016`; `ayaita_structure_2012` and then refined in `fuehrer_backreaction_2015` and in the present work, which uses a particle-mesh approach for the neutrino and dark matter particle evolution and a multi-grid approach for solving the non-linear scalar field equations. In table 7.1 we describe the parameters of the models discussed in this paper. We consider 5 models with different neutrino masses.

Our N-body simulation differs from standard Newtonian N-body codes in many ways, the most important one being that we evolve the cosmon ϕ and the gravitational potentials Φ and Ψ separately. While neutrinos, dark matter and the cosmon are non-linear in the N-body simulations, we assume that the gravitational potentials Φ and Ψ are small, which is valid in cosmological applications, even for large deviations of standard Λ CDM and at small scales. The perturbation in the dark energy scalar field $\delta\rho_\phi$ can be calculated from the perturbation of the energy density of the cosmon field

$$\delta\rho_\phi = \frac{\bar{\phi}'\delta\phi}{a^2} + V(\bar{\phi})\delta\phi . \quad (7.18)$$

The evolution of the homogeneous potential of the cosmon field can be obtained through its energy density and pressure in the following way

$$V_\phi(a) = \frac{1}{2}(\rho_\phi(a) - p_\phi(a)) , \quad (7.19)$$

while the perturbations in the potential can be approximated by

$$\delta V_\phi(a) = -\frac{1}{2}(\delta\rho_\phi(a) + 3\delta p_\phi(a)) . \quad (7.20)$$

The cosmon field can cluster and therefore its spatial gradients are non-vanishing, so that after averaging over the volume of the box the energy density of the cosmon field is

$$\bar{\rho}_\phi = \frac{1}{2}\overline{\dot{\phi}^2} + \frac{1}{2a^2}\overline{(1+2\Phi)\partial_i\phi\partial_j\phi\delta^{ij}} + \overline{V(\phi)} , \quad (7.21)$$

while its pressure reads

$$\bar{P}_\phi = \frac{1}{2}\overline{\dot{\phi}^2} - \frac{1}{6a^2}\overline{(1+2\Phi)\partial_i\phi\partial_j\phi\delta^{ij}} + \overline{V(\phi)} . \quad (7.22)$$

We will use for the following a convention in which bars denote spatial averages, while angular brackets denote time averaged quantities. The evolution of the cosmon field is solved using a multigrid relaxation algorithm, known as the Newton-Gauß-Seidel solver, which was originally developed for $f(R)$ modified gravity simulations `puchwein_modified-gravity-gadget_2013` and has also been implemented into the growing neutrino N-body simulations in `ayaita_nonlinear_2016`

Cosmological parameters	Growing neutrino models					
Linear values	M1	M2	M3	M4	M5	M6
$\Omega_{\nu 0} + \Omega_{\phi 0}$	0.686	0.688	0.692	0.701	0.693	0.695
$\Omega_{\nu 0}$	3.8×10^{-3}	2.6×10^{-2}	1.64×10^{-2}	4.7×10^{-2}	6.1×10^{-2}	9.4×10^{-3}
h	0.671	0.673	0.6818	0.701	0.722	0.741
$m_{\nu 0}$ [eV]	0.060	0.407	0.239	0.730	1.000	1.100
$\langle m_{\nu} \rangle [0.4 : 0.6]$ [eV]	0.040	0.067	0.134	0.277	0.399	0.700
$\langle m_{\nu} \rangle [0.8 : 1.0]$ [eV]	0.099	0.152	0.318	0.661	0.907	1.100
$\langle w_{\nu\phi} \rangle [0.9 : 1.0]$	-0.97	-0.97	-0.95	-0.92	-0.90	-0.88
N-body values						
$\Omega_{\nu 0} + \Omega_{\phi 0}$	0.688	0.690	-	-	-	-
$\Omega_{\nu 0}$	2.5×10^{-2}	1.9×10^{-2}	-	-	-	-
$m_{\nu 0}$ [eV]	0.038	0.078	-	-	-	-
$\langle m_{\nu} \rangle [0.4 : 0.6]$ [eV]	0.048	0.069	0.1436	0.280	0.401	0.600
$\langle m_{\nu} \rangle [0.8 : 1.0]$ [eV]	0.120	0.164	-	-	-	-
$\langle w_{\nu\phi} \rangle [0.9 : 1.0]$	-0.95	-0.96	-	-	-	-
a_{final}	1.0	1.0	0.84	0.70	0.65	0.60

TABLE 7.1: Table of parameters for the six models considered in this work. The top part refers to the output values computed with the linear nuCMB code. The bottom part refers to values computed within the N-body simulation. Quantities denoted with a subscript 0 are values at present time, $a = 1.0$. The $\langle m_{\nu} \rangle [a_1 : a_2]$ is the root mean squared (RMS) value of the neutrino mass in units of eV computed between $a = a_1$ and $a = a_2$. The same notation is also valid for $\langle w_{\nu\phi} \rangle [a_1, : a_2]$ corresponding to the equation of state of the combined cosmon and neutrino fluid which represents dynamical dark energy. a_{final} is the final time at which simulations were computed accurately. Therefore, for the models M3-M6 we cannot cite values of present time quantities or averages at times beyond a_{final} . The input values for nuCMB corresponding to all models can be found in table 7.2 of appendix 7.9.

The bottom part of table 7.1 lists the results of the six models computed using the N-body simulations.

In the case of neutrinos, the mass is a time-varying quantity following eq.7.11. Neutrinos obey a modified geodesic equation

$$\frac{du^{\mu}}{d\tau} + \Gamma_{\nu\lambda}^{\mu} u^{\nu} u^{\lambda} = \beta(\phi) \partial^{\mu} \phi + \beta(\phi) u^{\nu} u^{\mu} \partial_{\nu} \phi , \quad (7.23)$$

in which the right hand side gets a contribution from the coupling.

Simulations start at an initial value of $a_{\text{in}} = 0.02$. Until $a \approx 0.30$ the dark matter particles, the cosmon field and the gravitational potentials are evolved on the grid. For dark matter particles we take standard initial conditions from nuCMB and start the particle-mesh algorithm that solves the Poisson equation 7.3 at an initial redshift of $z = 49$. This is not the most accurate way of setting initial conditions for cosmological dark matter simulations (see for example recent N-body comparisons by schneider_matter_2016), but since in this work we are not interested in detailed substructures of dark matter halos or a percent-accurate power spectrum, we find that our approach gives a correct description at the scales of interest. Neutrinos

are first treated differently from other particles, as a distribution of relativistic particles in thermal equilibrium and no backreaction effects from neutrino structures are taken into account. Starting from a scale factor of approximately $a_{ini} \approx 0.30$ (depending on the exact parameters of each model), which is when neutrinos become non-relativistic, neutrinos are also projected on the grid: their phase-space distribution is sampled using effective particles. Since their equation of state is non-relativistic, we can approximate the phase-space distribution by

$$f_\nu(\mathbf{x}, \mathbf{v}) = \bar{n}_\nu f_{FD}(|\mathbf{v}_\nu - \mathbf{v}_{pec,\nu}(\mathbf{x})|)(1 + \delta_v(\mathbf{x})) , \quad (7.24)$$

where f_{FD} is the Fermi-Dirac distribution (7.12). The thermal velocities of the neutrinos are the difference between their total velocities and their peculiar velocities $\mathbf{v}_{th,\nu} = \mathbf{v}_\nu - \mathbf{v}_{pec,\nu}$. We obtain $\delta_v(\mathbf{x})$ and $\mathbf{v}_{pec,\nu}(\mathbf{x})$ by Fourier transforming the momentum-space realization of those fields obtained at the time a_{ini} from nuCMB. Equation 7.24 is solved for $\mathbf{v}_{th,\nu}$ in order to obtain the correct thermal distribution of particles and we duplicate the number of neutrino particles in each grid, assigning to each of them a thermal velocity which is equal in magnitude but opposite in direction, to avoid a distortion of the distribution of peculiar velocities at larger scales than a single grid cell size. For a large enough number of effective neutrino particles (i.e. when there is much more than one particle per cell), the distortion of the peculiar velocities by thermal velocities should be negligible. The correct neutrino density one would obtain from the Fermi-Dirac distribution for a non-relativistic particle reads

$$\langle \rho_\nu(\mathbf{x}) \rangle_{f_\nu} = \int d^3v m_\nu f_\nu(\mathbf{x}, \mathbf{v}) = m_\nu \bar{n}_\nu (1 + \delta_v(\mathbf{x})) . \quad (7.25)$$

Since we need to enforce the right hand side of 7.25 at each grid cell of comoving volume $a^3 \Delta V$, where the mass of the neutrinos is given by the scalar field, we have a condition on the number of particles N_{part} , such that

$$\frac{M_\nu \langle N_{part} \rangle}{a^3 \Delta V} = m_\nu \bar{n}_\nu (1 + \delta_v(\mathbf{x})) , \quad (7.26)$$

is fulfilled (more details of these method can be found in [ayaita_structure_2012](#)). When neutrinos enter as particles into the N-body simulation and therefore backreaction effects from neutrino structures start becoming important, the calculation of the fields and the potentials becomes computationally demanding, due to the non-linearity of the terms sourcing the continuity 7.7 and Klein-Gordon equations 7.8. Since these equations cannot be linearized due to the large values of the coupling parameter $\beta(\phi)$, the multigrid Newton-Gauß-Seidel solver is of crucial importance. For the parallelization of the code, we use a simple *OpenMP* approach, which calculates in parallel, for the available processing cores, the equations of motion of the particles and the fast Fourier transforms. In Tab.7.3 we describe all parameters related to the N-body simulations, including box and grid size.

7.4 Lump dynamics and the low mass - high mass divide

We find two different regimes for the non-linear evolution of neutrino lumps, depending on the average value of the neutrino mass. For light neutrino masses, during the lump formation process, the neutrinos are accelerated to relativistic velocities. Subsequently, the lumps dissolve and form again periodically, as described

in detail in ref. [ayaita_nonlinear_2016](#); Baldi et al., 2011. We demonstrate this behavior in the left panel of fig. 7.1. The repeated acceleration epochs heat the neutrino fluid to a huge effective temperature, such that neutrinos have again an almost relativistic equation of state during alternating periods of time.

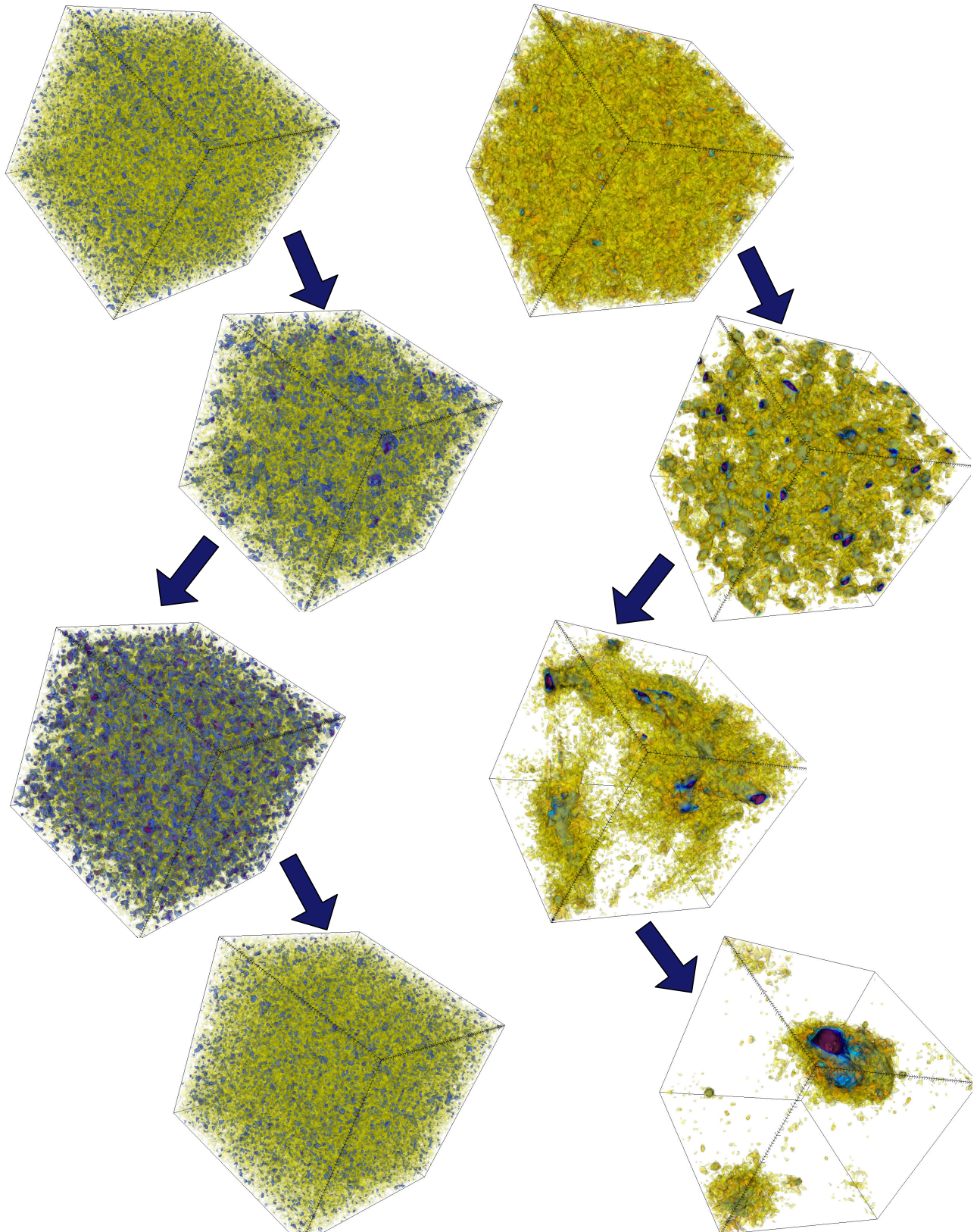


FIGURE 7.1: Snapshots of the number density contrast of neutrinos $\delta n_\nu(\vec{x}) \equiv n_\nu(\vec{x})/\bar{n}_\nu - 1$ at different times. **Left:** Model M2, at scale factors $a = 0.45, 0.7, 0.75$ and 0.95 from top to bottom. The overdensity oscillates between values close to 1 (represented as yellow tones) at early times, where there are no lumps, to values close to 10 (dark blue and purple tones), where several concentrated lumps form at intermediate times. At later times lumps dissolve and the overdensity decreases back to values close to unity. **Right:** Model M4, at scale factors: $a = 0.35, 0.42, 0.53$ and 0.64 from top to bottom. The neutrino lumps start growing at early times and merge progressively into larger and more concentrated structures. At the

In contrast, the behavior for large neutrino masses is qualitatively different. The concentration of the lumps continues to grow after their first formation. Lumps merge, and typically do not dissolve. The neutrino number density contrast reaches high values at late times. This is demonstrated on the right panel in fig.7.1 for an average value of the neutrino mass $m_{\nu,av} = 0.4\text{eV}$ in the range $0.4 < a < 0.6$. This behavior resembles the one found for a constant cosmon-neutrino coupling in [ayaita_neutrino_2013](#); [ayaita_structure_2012](#); [Baldi et al., 2011](#).

Due to the increasing value of the concentration and the increasing cosmon-neutrino coupling, the characteristic time scale becomes very short and gradients very large. This exceeds the present numerical capability of our simulations, typically at a value of the scale factor somewhat larger than $a = 0.6$. In fig.7.2 we show snapshots for two different values of neutrino masses shortly before the simulation breaks down.

The transition between the “heating regime” for small neutrino masses and the “concentration regime” for large neutrino masses occurs in the range $\langle m_\nu \rangle [0.4 : 0.6] \approx 0.07\text{eV} - 0.14\text{eV}$, where the time average is taken for $0.4 < a < 0.6$. The present value of the neutrino mass can be substantially larger due to oscillations and the continued increase of the mass and the temperature. For example, the phenomenologically viable model with $\langle m_\nu \rangle [0.4 : 0.6] = 0.07\text{eV}$ corresponds to a present neutrino mass of around 0.08eV , but the time oscillations grow the neutrino mass to values of up to 0.5eV for very short intervals in the scale factor a . (compare with fig. 7.5 below).

In fig.7.1 we show the distribution of the number (over)density contrast $\delta n_\nu(\vec{x}) \equiv n_\nu(\vec{x})/\bar{n}_\nu - 1$ at four different times and for two different models considered here, namely M2 (left panels) and M5 (right panels). For M2 as well as for models with smaller masses (not shown here), the neutrino lumps form and dissolve very quickly. The lumps are never stable and neutrinos accelerate to relativistic velocities when they fall into the gravitational potentials. The small lumps are also distributed homogeneously across the simulation box (see the third panel from above on the right of fig.7.1). The lumps reach maximal number density contrasts of about $\delta n_\nu \approx 10$. For M5 and for bigger masses, the neutrino lumps become stable, accreting more and more particles with the passing of time and increasing their concentrations. This leads to strong backreaction effects, changing the background cosmological evolution. After some time all neutrinos are concentrated in very big lumps, reaching very high values of $\delta_\nu \approx 50 - 100$, where $\delta_\nu \equiv \rho_\nu(\vec{x})/\bar{\rho}_\nu - 1$, see fig.7.2. After this point, the numerical framework for the growing neutrino quintessence evolution breaks down and we can no longer solve reliably the coupled system of equations.

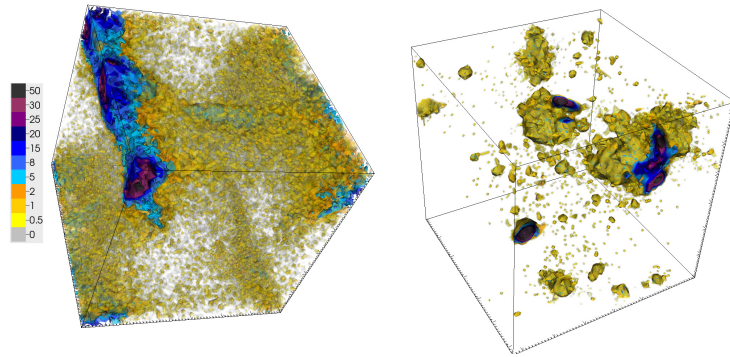


FIGURE 7.2: Snapshots of the neutrino overdensity field $\delta_\nu(\vec{x})$ for models M4 (top left) and M6 (bottom left) at scale factors of $a = 0.64$, and 0.62 , respectively. In these models, neutrino lumps cluster into large stable structures with a high concentration, starting from a bottom-up approach, as was shown for model M4 in fig. 7.1. Neutrino structures occupy large parts of the simulation box, corresponding to scales of ~ 50 Mpc. At these scale factors, the forces introduced by the cosmon coupling are too strong to be resolved by our numerical approach and our simulation breaks down.

7.5 Cosmological evolution in the light neutrino regime

As we have seen in the previous section, there is a qualitative difference between the cosmological evolution of a model with a light or a heavy neutrino mass, the boundary being a present neutrino mass value of roughly ≈ 0.5 eV (calculated in linear theory). In this section we explore more in detail the evolution of background quantities in the light mass model M2 whose parameters are shown in detail in table 7.1 for the linear calculation in nuCMB (top panel) and for the N-body computation (bottom panel). We study in detail the differences appearing in the evolution of background quantities, when non-linear physics and backreaction are taken into account.

The standard definition for the homogeneous energy density fraction of the cosmon field ϕ is

$$\Omega_\phi = \frac{8\pi G}{3H^2} \bar{\rho}_\phi , \quad (7.27)$$

where $\bar{\rho}_\phi$ is the background energy density of a homogeneous scalar field $\bar{\rho}_\phi = K(\phi) + V(\phi)$ and $K(\phi)$ its kinetic energy. In linear theory, the homogeneous term would be the only term entering into Ω_ϕ ; on the contrary, within the N-body simulation, the field is non-homogeneous and the combined energy density of the coupled neutrino-cosmon fluid receives also a contribution from the perturbations $\delta\rho_\phi$ of the non-homogeneous cosmon field, given by eq. 7.18. The important quantity determining the evolution of a dynamical dark energy is not the energy density of the cosmon alone, but the energy density of the combined cosmon-neutrino fluid, given by

$$\Omega_{\phi+\nu} = \frac{8\pi G}{3H^2} (\bar{\rho}_\phi + \bar{\rho}_\nu) . \quad (7.28)$$

The average energy density of the neutrinos is not individually conserved and its evolution is given by the continuity equation with a coupling term on the r.h.s. [ayaita_structure_2012](#); Baldi et al., 2010

$$\rho_\nu + 2\mathcal{H}\rho_\nu = -\beta(\phi)\phi'\rho_\nu , \quad (7.29)$$

where ϕ' is the time derivative of the field with respect to conformal time τ . The corresponding equation of state of the coupled fluid can then be defined as the sum of the pressure components divided by the sum of the density components

$$w_{\nu+\phi} = \frac{\bar{p}_\phi + \bar{p}_\nu}{\bar{\rho}_\phi + \bar{\rho}_\nu} . \quad (7.30)$$

In the literature [brookfield_cosmology_2007](#); [das_super-acceleration_2006](#); [perrotta_extended_1999](#); [perrotta_dark_2002](#) there are several definitions of the effective equation of state or the observed equation of state in the case in which the scalar field is coupled to other particles. We argue that 7.30 is actually the equation of state one would observe from the evolution of the Hubble function (i.e. with Supernovae and standard candle methods of redshift distance measurements). In appendix 7.10 we comment further on this and show a comparison between the “observed” and theoretical equation of state of dark energy in fig.7.10.

In fig.7.3 we plot for model M2 the background evolution of the neutrino energy density Ω_ν (orange lines) and the combined cosmon+neutrino fluid energy density $\Omega_{\nu+\phi}$ (blue lines) as defined in eq.7.28. The dashed lines correspond to the linear computation in nuCMB, while the solid lines correspond to the results of the N-body simulation. One can see that the effect of non-linearities and backreaction is quite small and it is mostly just visible as a phase shift in the oscillations of Ω_ν , which is due to the dynamics of the oscillating lumps, that alter the field-dependent mass of the neutrinos as a function of time and space. The same trend is observed in model M1 (not shown here). This behavior tells us that for small neutrino masses, the effects of backreaction on the background evolution are practically negligible and a linear computation is enough to analyze those models further, with a considerable simplification with respect to a joint linear and non-linear analysis done in [Pettorino et al., 2010](#).

We show in fig.7.4 the neutrino equation of state w_ν (orange lines) as well as the combined cosmon-neutrino fluid equation of state $w_{\nu+\phi}$ as defined in equation 7.30 (blue lines), both for the case of the linear computation with nuCMB (dashed lines) and the non-linear computation (solid lines). In the linear analysis, the neutrinos are treated initially as relativistic particles: as the mass increases, they become more and more non-relativistic, reaching a w_ν of exactly zero at late times. On the contrary, the N-body simulation is able to follow the oscillations in the equation of state of neutrinos, which are caused by the fact that neutrinos get accelerated to relativistic velocities when they fall into deep gravitational and cosmon potentials. Once they are in these lumps, and they have acquired high speeds, their pressure increases and they tend to escape again from these lumps, causing the oscillating neutrino structures. When they are far away from the cosmon potentials, their velocities decrease and they become non-relativistic again. The fifth force acting among neutrinos attracts them again to the cosmon potential wells and the whole cycle repeats itself.

For the combined equation of state $w_{\nu+\phi}$, we find that the simulation predicts a slightly higher value than the linear one; this can be explained by studying how the neutrino fluid is heated due to the strong oscillations of the lumps. By falling repeatedly in the cosmon potential wells and increasing their kinetic energy, the neutrinos temperature increases and therefore neutrinos do not manage to become again completely non-relativistic. This can be seen in the dashed orange lines of

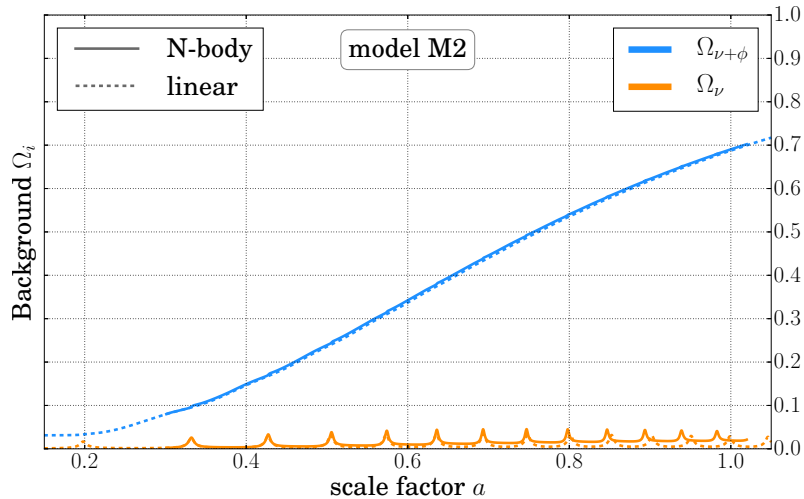


FIGURE 7.3: Evolution of $\Omega_{\phi+\nu}$ (blue lines) and Ω_ν (orange lines) for Model M2, compared between the linear output from nuCMB (dashed lines) and the non-linear calculation of the N-body simulation (solid lines). The total cosmon-neutrino fluid has the same background evolution in the simulation as in the linear calculation. The neutrino energy density is somewhat larger in the simulation and shows a phase-shift in its oscillations, as discussed in the text.

plot 7.4, where the curve of w_ν does not touch the zero axis after $a \approx 0.5$. We will see in section 7.6 that neutrinos depart from their initial Fermi-Dirac distributions and reach temperatures which are high compared to the photon background.

In fig.7.5, we show the evolution of the spatial average of the neutrino mass in the N-body simulation as a function of the scale factor a . One can see that the value of \bar{m}_ν varies along an order of magnitude, from approx. 10^{-2} to 10^{-1} , throughout a cosmological time interval. Due to a phase shift in the oscillation pattern, which sets in at around $a \approx 0.8$, the present day value of the average neutrino mass can be quite different to the one estimated with the linear analysis (and this change depends on the precise parameters of the model), so that the best estimate for the average cosmological neutrino mass today, is a time average of $\bar{m}_\nu(\phi)$ at late times, between $a = 0.8 - 1.0$. We can see that the big discrepancies between the masses of model M1 and M2 calculated in linear theory (e.g. 7.1) are washed away when non-linearities and backreaction effects are taken into account i.e. for small neutrino masses. Even if the present neutrino masses for model M1 and M2 differ by an order of magnitude in linear theory, we find a very similar time averaged value between the two models in the N-body simulation: respectively $\langle m_\nu \rangle[0.8 : 1.0] = 0.120$ and $\langle m_\nu \rangle[0.8 : 1.0] = 0.164$. The oscillation pattern of the neutrino mass for the more massive model (M2) contains higher peaks and has a smaller frequency than compared to the oscillations in the less massive model M1. For other models, this comparison can be seen in table 7.1.

7.6 heating of the neutrino fluid

The repeated acceleration of neutrinos to relativistic velocities during the periods of lump formation and dissolution lead to an effective heating of the neutrino fluid. While we do not expect a thermal equilibrium distribution of neutrino momenta and energies it is interesting to investigate how close the distribution is to the

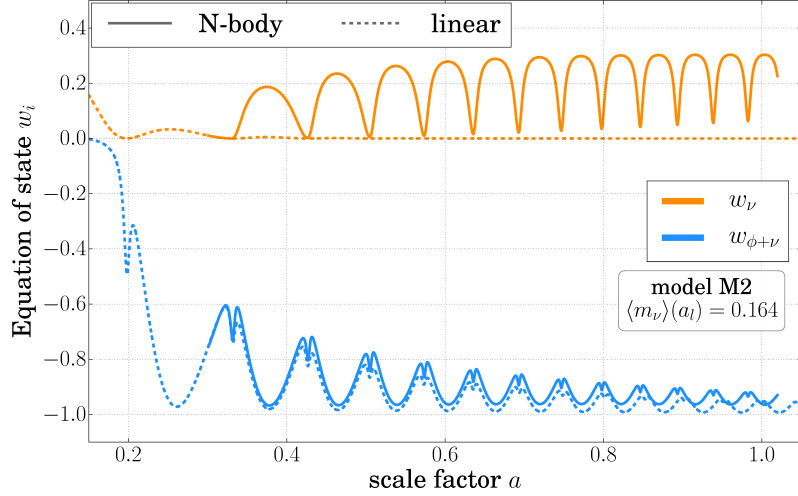


FIGURE 7.4: Equation of state of the combined neutrino-cosmon fluid $w_{\phi+\nu}$ (blue) and equation of state of neutrinos w_ν (orange). We compare the linear output (dashed lines) to the non-linear one obtained from the N-body simulation (solid lines) for model M2. This model has a time averaged RMS mass $\langle m_\nu \rangle(a_l) = 0.164$, where $a_l = 0.9$ in the label denotes the center of the time interval $a = [0.8 - 1.0]$ used to take the average. For w_ν , the linear output does not capture the oscillating equation of state of neutrinos due to the formation of structures, while for $w_{\phi+\nu}$, both codes agree relatively well. At late times the equation of state predicted by the simulation has a somewhat higher value and is phase-shifted due to the heating of the neutrino fluid.

Fermi-Dirac distribution of a free gas of massive neutrinos. This distribution depends on only two parameters, the neutrino mass and the temperature. At a given time we associate the neutrino mass to the space averaged neutrino mass. The temperature can be associated to the mean value of the momentum.

The energy of a relativistic particle is given by

$$E(p, m) = \sqrt{p^2 + m^2}, \quad (7.31)$$

while its kinetic energy $E_k = E(p, m) - m$. Equivalently, the kinetic energy is defined by

$$E_k = \int \vec{v} \cdot d\vec{p}, \quad (7.32)$$

which yields $E_k = m(\gamma - 1)$ and reduces in the limit of very small velocities ($v \ll c$) to the usual $E_k = mv^2/2$. From there the Fermi-Dirac distribution as a function of momentum $p = |\vec{p}|$ can be obtained in the standard way. It depends on m and T . For $m \ll T$ it can be approximated by the relativistic distribution while for $m \gg T$ we recover the Maxwell-Boltzmann distribution. The distribution of particle momenta is then given by

$$\mathcal{P}(p)dp = \frac{4\pi p^2}{(1 + e^{(E(p,m)-\mu)/T}}dp \quad (7.33)$$

where the factor 4π comes from the angular integration of the three-dimensional

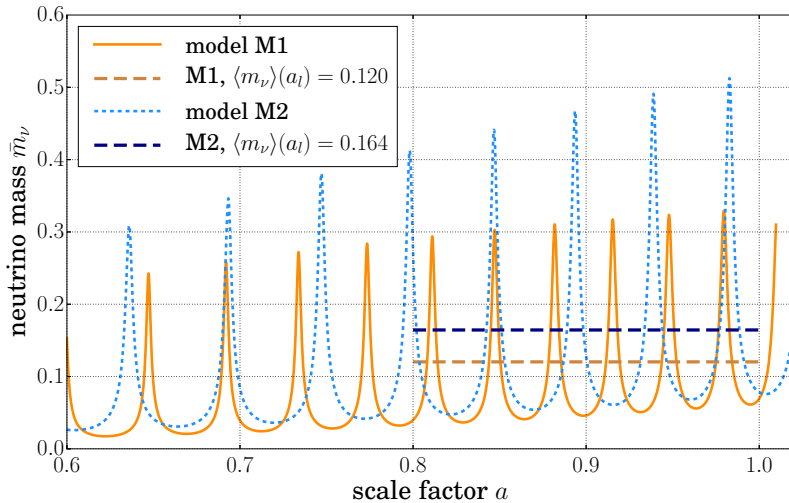


FIGURE 7.5: Neutrino mass \bar{m}_ν (average over simulation volume) in model M2 (firebrick red line) and model M1 (dodger blue line), as a function of the scale factor a , for the N-body simulation. The horizontal lines, show the time averaged RMS value at a late time $a_l = 0.9$, denoting the center of the time interval of $[0.8 : 1.0]$ considered for taking the average. For model M2, the time averaged neutrino mass is $\langle m_\nu \rangle(a_l) = 0.164$ (blue dashed lines), while for model M1 it is somewhat smaller $\langle m_\nu \rangle(a_l) = 0.120$ (red dashed lines). One can observe that the oscillation frequency is higher for the smaller $\langle m_\nu \rangle$ mass and the peaks are higher for the larger $\langle m_\nu \rangle$. The present neutrino masses of the two models calculated in linear theory differ by an order of magnitude, on the contrary the time averaged masses are very close to each other.

momentum. In the ultra-relativistic limit we can analytically integrate the momentum p over its distribution eq.7.33 and invert $\bar{p}(\bar{T})$ to yield the mean temperature as a function of the mean momentum

$$\bar{T} = \frac{180\zeta(3)}{7\pi^4} \bar{p} \quad (7.34)$$

We neglect the chemical potential in 7.33, because the exponential term in the denominator is 2 or 3 orders of magnitude larger than unity. Since in our case, the average momentum and mass of the neutrinos are of the same order, we cannot use either a non-relativistic or an ultra-relativistic limit. We need to consider both the mass and the momentum in the relativistic energy equation 7.31. Therefore for each model and each time, we numerically find \bar{T} as a function of the mean momentum \bar{p} .

We extract for $a = 1$ the temperatures

$$\bar{T} = 0.077\text{eV (M1, } \bar{m}_\nu = 0.2404\text{)}, \quad \bar{T} = 0.065\text{eV (M2, } \bar{m}_\nu = 0.2327\text{)} . \quad (7.35)$$

They are higher by a factor 327 (M1) or 276 (M2) as compared to the CMB photon temperature $2.35 \times 10^{-4}\text{eV}$. This demonstrates the unconventional heating of the neutrino fluid due to the formation and dissolution of lumps. The high temperatures are connected with the almost relativistic equation of state of the neutrinos seen in fig. 7.4. Overall, the observed momentum distributions come rather close to the thermal equilibrium distribution. This also holds for the distribution of kinetic

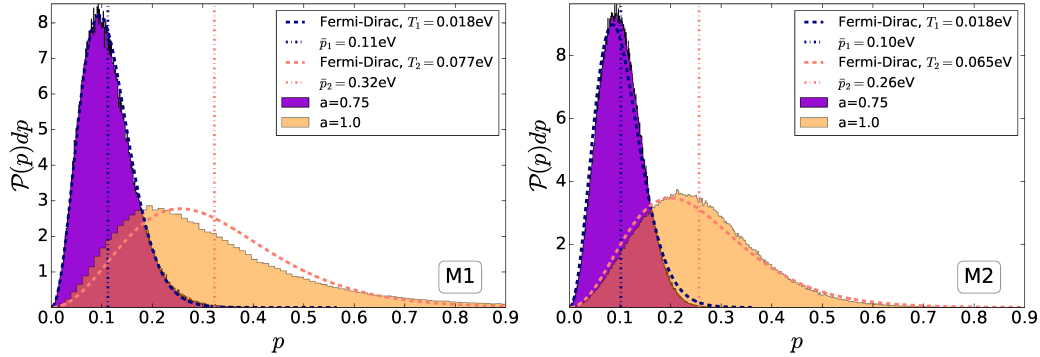


FIGURE 7.6: Distribution of the momenta of the neutrino particles in the simulation, for two different times, $a = 0.75$ (purple shade) and $a = 1.0$ (orange shade), compared against a Fermi-Dirac distribution with a temperature given by the mean of the distribution (dashed lines). **Left:** For model M1 the Fermi-Dirac fits very well for temperatures of $\bar{T} = 0.018\text{eV}$ and $\bar{T} = 0.077\text{eV}$ for each scale factor respectively. **Right:** For model M2 the fit is also good, the corresponding temperatures being $\bar{T} = 0.018\text{eV}$ and $\bar{T} = 0.065\text{eV}$. The CMB photon temperature is $2.35 \times 10^{-4}\text{eV}$, this means that the non-linear cosmon-neutrino interactions heat the neutrino background by more than a factor 100.

energies. With the bulk quantities as momenta and kinetic energies roughly distributed thermally this is an example of prethermalization [berges_prethermalization_2004](#)

In fig. (7.6) we fit the distribution of momenta of the neutrino particles on the grid (shown with an histogram) with a Fermi Dirac distribution. The actual distribution of momenta fits the thermal equilibrium distribution very well. At later times (orange shade), the fit is slightly less good: neutrinos might be accelerating towards or away from lumps giving them an extra kick that shifts the peak of the distribution of momenta.

When comparing the equation of state of neutrinos obtained from the N-body simulation to a neutrino equation of state $w_\nu = p_\nu / \rho_\nu$, using our Fermi-Dirac fit to the particle distribution and eqns.7.15 and 7.14, we get a very good agreement, taking into account that for the Fermi-Dirac fit, we are neglecting the spatial variation of the neutrino mass $m_\nu(\phi)$. For model M2 at the scale factor $a = 0.75$ we obtain from the N-body simulation a neutrino equation of state of $w_\nu = 0.081$ while using the Fermi-Dirac fit to the distribution of particles with a mean temperature of $\bar{T} = 0.018\text{eV}$ and an average neutrino mass $\bar{m}_\nu = 0.1835$, the proper calculation yields $w_\nu = 0.086$. For a later time, at $a = 1.0$ the N-body simulation gives us a value of $w_\nu = 0.207$ while the Fermi-Dirac fit with a mean temperature of $\bar{T} = 0.065\text{eV}$ and an average neutrino mass $\bar{m}_\nu = 0.2327$ amounts to a neutrino equation of state of $w_\nu = 0.182$.

To visualize the evolution of w_ν , we can observe from fig.7.4 that neutrinos in the N-body simulation start as non-relativistic particles and oscillate between being almost relativistic and completely non-relativistic in the interval $a = [0.3, 0.6]$. However, at later times $a \gtrsim 0.7$ the neutrino equation of state still oscillates but never reaches a value of zero again. This is in agreement with our description of the heating of the neutrino fluid. Since the mean temperature of the neutrino fluid is increasing with time and therefore its mean kinetic energy and pressure, the minimum of the oscillations of the neutrino equation of state increases also in time and departs from zero, once neutrinos are heated to very high temperatures

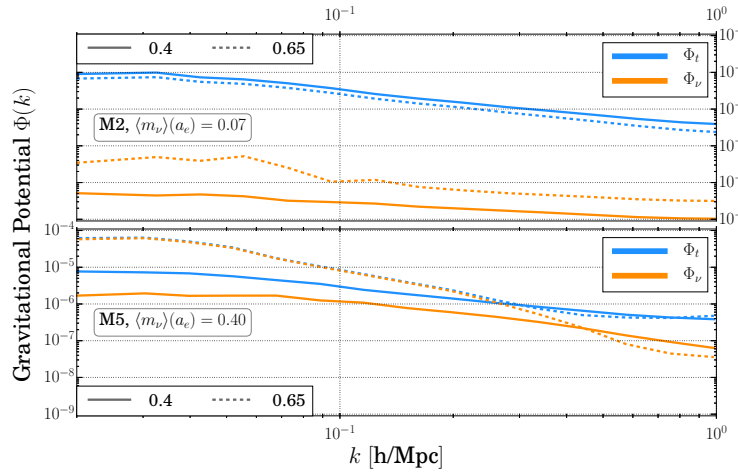


FIGURE 7.7: Power spectra of the total gravitational potential Φ_t (blue lines) and of the neutrino contribution Φ_ν (orange lines) for model M2 and model M5 at the scale factors $a = 0.40$ (solid lines) and $a = 0.65$ (dashed lines), as a function of scale. Model M2 has an RMS time averaged neutrino mass $\langle m_\nu \rangle(a_e) = 0.07$, where $a_e = 0.5$ stands for the central time in the interval $a = [0.4 - 0.6]$ used to take the average. Model M5 has in the same interval a higher RMS mass of $\langle m_\nu \rangle(a_e) = 0.40$. In the first model, Φ_t at large scales is of the order of 10^{-5} , while Φ_ν is 3 to 4 orders of magnitude smaller at both cosmological times. For model M5, in which neutrino lumps are stable and growing, one sees that at large scales, the total Φ_t starts with a value of 10^{-5} at $a = 0.4$, but reaches 10^{-4} at later times. At $a = 0.65$ the neutrino contribution is dominant and neutrino structures have migrated from small scales to large scales, as can be seen from the dip in Φ_ν at modes between $k = 0.2 - 1.0$ h/Mpc.

due to the collapsing and dissolving of the neutrino-cosmon lumps.

7.7 Gravitational Potentials of Neutrino Lumps

The gravitational potential Φ is a good measure of the physics going on in structure formation. We know from observational constraints, that Φ is of the order of 10^{-5} on cosmological scales Pettorino et al., 2010; Brouzakis et al., 2011. In Λ CDM, the gravitational potential is sourced mainly by dark matter perturbations. In figures 7.7 and 7.8 we show that for models with small neutrino masses, the neutrino contribution to Φ remains several orders of magnitude smaller than the CDM contribution, at all scales and at all times. Moreover, one can observe an oscillation in time of the neutrino gravitational potential. For models with large neutrino masses, the neutrino contribution grows monotonically with time. At large scales $k \lesssim 0.3h/\text{Mpc}$ and at late times the neutrino lump induced potential dominates over the cold dark matter gravitational potential. This renders the total potential Φ_{tot} too big to be compatible with present cosmological constraints.

We show the scale dependence of the total gravitational potential and the neutrino induced gravitational potential Φ_ν at two different cosmic time scales $a = 0.4$ and $a = 0.65$ in fig. 7.7. While for $a = 0.4$ (solid lines) the neutrino contribution is still subdominant for both models M2 and M5, this changes at $a = 0.65$ for model M5 (bottom panel). For model M2 the total gravitational potential decreases in

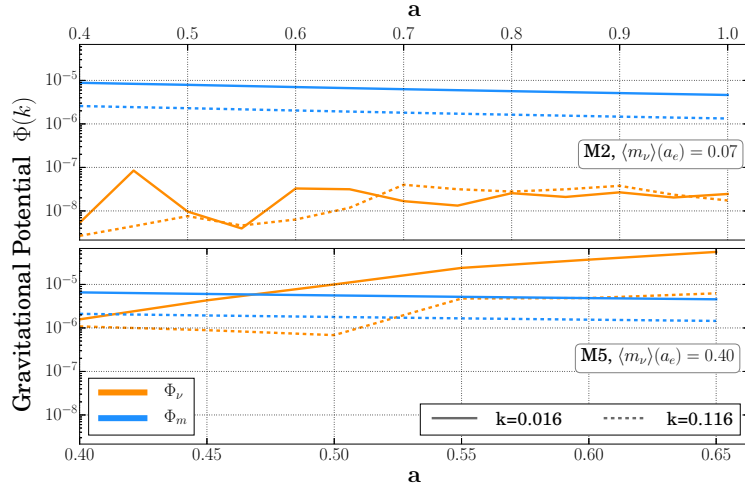


FIGURE 7.8: Power spectra of the matter gravitational potential Φ_m (blue lines) and of the neutrino contribution Φ_ν (orange lines) at two different scales, $k = 0.016$ (solid lines) and $k = 0.116$ (dashed lines) as a function of scale factor a with two different scales on the top and bottom axis. For model M2 the matter gravitational potential Φ_m is at most 10^{-5} at all times, while the neutrino contribution is 2-3 orders of magnitude smaller and displays time oscillations. In clear contrast, the neutrino contribution from model M5 for very large scales, reaches and dominates over the matter contribution for $a \gtrsim 0.5$ and pushes the total Φ to high values that would be ruled out by observations, see also fig. 7.7. The RMS neutrino mass has been taken in the same interval range as for fig. 7.7, where $a_e = 0.5$.

time, as it is expected due to the effect of dark energy, while Φ_ν increases especially at large scales. For model M5, since the neutrino contribution dominates at $a = 0.65$, the total gravitational potential is raised to values of 10^{-4} at large scales, while at small scales ($k \gtrsim 0.4$) the neutrino contribution is still subdominant.

In fig. 7.8 we show the power spectra of the total gravitational potential Φ (blue lines) and of the neutrino contribution to it (orange lines) at two different scales, $k = 0.016$ (solid lines) and $k = 0.116$ (dashed lines) as a function of the scale factor a . For model M2, corresponding to an average early time neutrino mass of 0.07 eV, the total gravitational potential $\Phi(k)$ is 10^{-5} at all times, while the neutrino contribution is 2-3 orders of magnitude smaller and shows time oscillations. In clear contrast, the neutrino contribution from model M5 (corresponding to an average early time neutrino mass of 0.40 eV)) for very large scales reaches and dominates over the matter contribution (at $a \gtrsim 0.5$) and pushes the total Φ to high values that would be ruled out by observations. This is due to the fact that neutrino lumps do not dissolve, but rather grow with continuously growing concentration and higher gravitational potential.

There is also anticorrelation between the neutrino structures and the neutrino induced gravitational potential, as expected from the fact that neutrinos will tend to fall into gravitational potential wells. In the left panel of fig. 7.9, we plot the values of the neutrino number density contrast $\delta n_\nu = n_\nu(\vec{x})/\bar{n}_\nu - 1$ and the negative neutrino induced gravitational potential Φ_ν , along a diagonal line through the simulation box. The correlation of peaks and troughs (corresponding to an anticorrelation of δn_ν and Φ_ν) is very clear and it is valid for even small substructures of the order of a few Mpc. By plotting the neutrino density contrast δ_ν , we also show

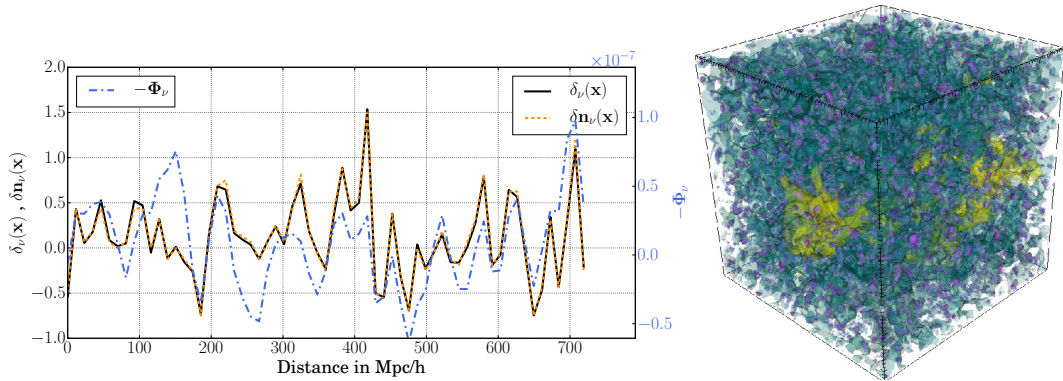


FIGURE 7.9: **Left:** Line plot through the main diagonal of the simulation box, for model M2 at $a = 0.75$. The negative of the neutrino contribution to the gravitational potential Φ_ν (blue dot-dashed lines) oscillates between $\pm 1.0 \times 10^{-7}$. This is correlated to the neutrino density contrast (black lines) and the number density contrast $\delta n_\nu = n_\nu(\vec{x})/\bar{n}_\nu - 1$ (orange dashed lines) reaching values of up to 1.5. **Right:** Snapshot of the same simulation, showing a equipotential contour of the gravitational potential, for $\Phi_\nu = +1.0 \times 10^{-7}$ in yellow, and the small but dense neutrino lumps in blue, purple and red, corresponding to density contrasts δn_ν of 1.5, 2.0 and 4.0 respectively.

that at this time $a = 0.75$, the neutrino number density and the energy density are proportional, meaning that neither local mass variations or relativistic speeds are having any effect in the neutrino total energy. In the right panel of fig.7.9 we visualize the neutrino induced gravitational potential as a yellow region marking the equipotential surface $\Phi_\nu = +1.0 \times 10^{-7}$ and the neutrino number overdensity structures colored blue, purple and red, corresponding to density contrasts δn_ν of 1.5, 2.0 and 4.0 respectively. For this model (M2) and at this specific time, the neutrino structures are spread almost homogeneously throughout the simulated volume.

7.8 Conclusions

We have investigated the dynamics of neutrino lumps in growing neutrino quintessence and how it depends on the mass of neutrinos. As a main result of this paper we found a characteristic divide in the qualitative behavior between small and large neutrino mass.

For light neutrino masses the combined effects of oscillations in the neutrino masses and the cosmon-neutrino coupling lead to rapid formation and dissociation of the neutrino lumps. The concentration in the neutrino structures never grows to very large overdensities. As a consequence, backreaction effects remain small. The effects of lump formation and dissociation lead to an effective heating of the neutrino fluid to temperatures much higher than the photon temperature. Due to this heating, the neutrino equation of state becomes again close to the one for relativistic particles. For a small present average neutrino mass $m_\nu = 0.06\text{eV}$ it has been found earlier Pettorino et al., 2010 that the cosmology of growing neutrino quintessence resembles very closely a cosmological constant, making differences to the ΛCDM model difficult to detect. We extend this qualitative feature to a whole range of light neutrino masses.

For large neutrino masses, one finds a qualitatively different behavior. Big neutrino lumps form, due to the strong cosmon-mediated fifth-force between neutrinos. These lumps are stable and keep growing in concentration and density. The strong clumping of the cosmic neutrino background induces large backreaction effects on the overall cosmic evolution. As a result, the combined cosmon-neutrino fluid does not act effectively as a cosmological constant anymore and compatibility with observations is difficult to achieve. This situation is similar to the case of a constant cosmon-neutrino coupling [fuhrer_backreaction_2015](#)

The divide in the characteristic behavior reflects the competition between heating of the neutrino fluid and lump concentration. We have not yet established a quantitatively accurate value of the parameter \tilde{m}_ν , where the divide is located, since the numerics are rather time consuming. In principle, this divide will lead to an upper bound on the present neutrino mass, as seen in terrestrial experiments. For models in the vicinity of model M2, which seem compatible with observations so far, spatial average neutrino masses as large as 0.5eV can occur at the peak of oscillations, c.f. fig.[7.5](#). We note that if we live inside a neutrino lump the neutrino mass will be reduced as compared to the cosmological value.

We have further computed the strength of the neutrino-induced gravitational potential. For light masses, this potential is found to be rather small, rendering a detection of the neutrino lumps difficult. As neutrino masses increase towards an intermediate mass region, before reaching the heavy mass range incompatible with observation, the neutrino-induced gravitational potentials will get stronger. By continuity we expect that in the intermediate mass region the clumped neutrino background becomes observable.

7.9 Initial parameters for generating the models in nuCAMB and in the N-Body simulation

CAMB values	M1	M2	M3	M4	M5	M
input: $\Omega_\nu h^2$	0.048	0.048	0.075	0.018	0.038	0.0
\tilde{m}_ν amplitude factor	8.35×10^{-5}	2.0×10^{-4}	6.0×10^{-4}	9.9×10^{-3}	8.8×10^{-3}	$8.8 \times$
input $\hat{r}_{\nu eV}$ factor	1.5045	1.5045	2.3508	0.5642	1.1911	3.07
V_i	0.99×10^{-7}	$0.99 \times$				

TABLE 7.2: Table of initial parameters for each model computed with nuCAMB. \tilde{m}_ν is the neutrino mass amplitude used in the simulations, $\hat{r}_{\nu eV}$ is the neutrino mass units conversion factor between the simulations and nuCAMB. V_i is the initial value of the cosmon potential.

N-body parameters	Values	Meaning
L	428	Box side length in Mpc/h
N_g	64	Grid size per dimension
N_{pdm}	262144	Number of dark matter particles in the simulation
$N_{p\nu}$	524288	Number of neutrino particles in the simulation
$n_{\text{ngs}}^{\text{acc}}$	1.0×10^{-5}	Numerical accuracy for the NGS solver

TABLE 7.3: Table of numerical parameters for each N-body simulation run. Several tests were performed varying these parameters, but the overall behavior for the purposes of this paper was the same. We also tested model M2 with grid sizes of 128 and 8 times the number of particles, not noticing any qualitative difference in the dynamics. Only deviations of the order of 10% in perturbation quantities were observed when varying the grid size or the number of particles.

7.10 The effective and observed equation of state of dark energy

The equation of state w of a species is defined in terms of its pressure and density as

$$w = \frac{p}{\rho} . \quad (7.36)$$

For the case of coupled species, there have been several definitions in the literature (c.f. `brookfield_cosmology_2007`; `das_super-acceleration_2006`; `perrotta_extended_1999`; `perrotta_dark_2002`). This is due to the fact that when there is an exchange of energy and momentum between a particle and a scalar field, the time evolution of matter does not correspond anymore to the volume dilution rule $\rho(a) = \rho_0 a^{-3}$. Therefore the equation of state of the dark energy field will not be as simple as the equation of state of a homogeneous scalar field, namely

$$w_\phi = \frac{p_\phi}{\rho_\phi} = \frac{(1/2a^2)\dot{\phi}^2 + V(\phi)}{(1/2a^2)\dot{\phi}^2 - V(\phi)} . \quad (7.37)$$

In `das_super-acceleration_2006`; `brookfield_cosmology_2007` two definitions of the equation of state (e.o.s) of dark energy were investigated. The first one, called the effective e.o.s. w_{eff} , given by

$$w_{eff} \equiv w_\phi + \frac{\beta \dot{\phi}}{3H} \frac{\rho_\nu}{\rho_\phi} \quad (7.38)$$

and the second one named “apparent” e.o.s. w_{ap} , defined by

$$w_{ap} \equiv \frac{w_\phi}{1+x} , \quad (7.39)$$

with

$$x = -\frac{\rho_{\nu,0}}{a^3 \rho_\phi} \left[\frac{m_\nu(\phi)}{m_\nu(\phi_0)} - 1 \right] , \quad (7.40)$$

where a 0 subscript denotes quantities at $z = 0$. Notice that by construction, w_{ap} at the present epoch is identical to w_ϕ and that w_{ap} can be smaller than -1 . We find that none of these two definitions of e.o.s. describe the dynamical dark energy field present in our model.

Since in our model the neutrino and cosmon field behave together as a tightly coupled fluid, we are interested in the conserved equation of state for the combined fluid. This is given by the sum of both contributions from the pressure, divided by the sum of both densities. Therefore, we define $w_{\nu+\phi}$ as

$$w_{\nu+\phi} \equiv \frac{\bar{p}_\phi + \bar{p}_\nu}{\bar{\rho}_\phi + \bar{\rho}_\nu} . \quad (7.41)$$

This definition should agree with what we can extract directly from observations of the Friedmann equation. The equation of state $w_{DE}(z)$ of a general dark energy component that fulfills the continuity equation (if it is composed by two coupled fluids, the continuity equation is fulfilled for the sum of densities and pressures), appears in the Friedmann equation as

$$E^2(z) \equiv \frac{H^2(z)}{H_0^2} = \left[\Omega_{r,0}(1+z)^4 + \Omega_{m,0}(1+z)^3 + \Omega_{DE,0} \exp \left\{ \int_0^z \frac{3(1+w_{DE}(\tilde{z}))}{1+\tilde{z}} d\tilde{z} \right\} + \Omega_{k,0}(1+z)^2 \right] \quad (7.42)$$

Moreover, in a flat Universe and with a negligible contribution from radiation, we can solve for $w_{DE}(z)$ and obtain Amendola and Tsujikawa, 2010:

$$w_{DE}(z) = \frac{(1+z)(E^2(z))' - 3E^2(z)}{3[E^2(z) - \Omega_{m,0}(1+z)^3]} . \quad (7.43)$$

Thus, from background expansion observations we can obtain a constrain on $w_{DE}(z)$, provided we know from large-scale structure or CMB observations the present value of Ω_m . In the fig. 7.10 we compare $w_{DE}(z)$ obtained from eq.7.43 and $w_{\nu\phi}(z)$ computed both consistently within the N-body simulation. In the former case, numerical noise in the derivatives of $E(z)$ create certain scatter in $w_{DE}(z)$ at late times.

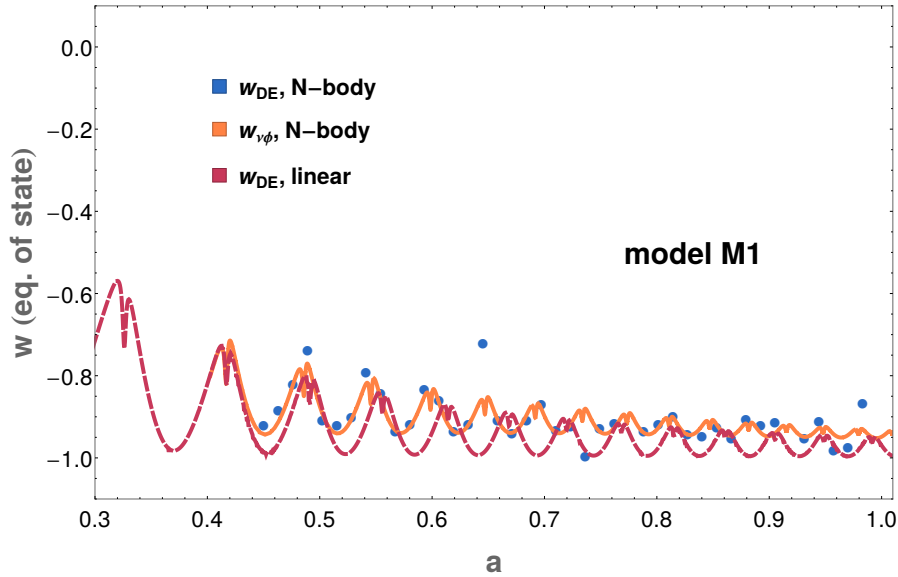


FIGURE 7.10: Different $w(z)$ curves in the case of model M1 computed with the N-body simulation and compared to linear theory. The red dashed lines represent w_{DE} computed from the Hubble function which is an output of the linear code nuCMB. The solid orange line, representing $w_{\nu+\phi}$ is computed using the standard pressure and density outputs from the simulation. The blue dots stand for some set of computed values of $w_{DE}(z)$ obtained from the Hubble function calculated entirely within the N-body simulation. Due to numerical noise in the oscillating derivatives of $E(z)$, there is some scatter in the e.o.s. obtained in this case.

Chapter 8

Conclusions

Appendix A

Appendix Title Here

Write your Appendix content here.

Bibliography

- Agarwal, Shankar et al. (2012). "PkANN - I. Non-linear matter power spectrum interpolation through artificial neural networks". In: *Monthly Notices of the Royal Astronomical Society* 424.2, pp. 1409–1418. ISSN: 00358711. DOI: [10.1111/j.1365-2966.2012.21326.x](https://doi.org/10.1111/j.1365-2966.2012.21326.x). URL: <http://arxiv.org/abs/1203.1695>.
- (2014). "PkANN - II. A non-linear matter power spectrum interpolator developed using artificial neural networks". In: *Monthly Notices of the Royal Astronomical Society* 439.2, pp. 2102–2121. ISSN: 0035-8711, 1365-2966. DOI: [10.1093/mnras/stu090](https://doi.org/10.1093/mnras/stu090). URL: <http://arxiv.org/abs/1312.2101>.
- Alcock, C. and B. Paczynski (1979). "An evolution free test for non-zero cosmological constant". In: *Nature* 281, p. 358. ISSN: 0028-0836. DOI: [10.1038/281358a0](https://doi.org/10.1038/281358a0). URL: <http://adsabs.harvard.edu/abs/1979Natur.281..358A> (visited on 02/12/2017).
- Alonso, David et al. (2016). "The Observational Future of Cosmological Scalar-Tensor Theories". In: *arXiv:1610.09290 [astro-ph, physics:gr-qc, physics:hep-th]*. arXiv: 1610.09290. URL: <http://arxiv.org/abs/1610.09290> (visited on 11/02/2016).
- Amendola, Luca, Marco Baldi, and Christof Wetterich (2008). "Growing Matter". In: *Physical Review D* 78.2. ISSN: 1550-7998, 1550-2368. DOI: [10.1103/PhysRevD.78.023015](https://doi.org/10.1103/PhysRevD.78.023015). URL: <http://arxiv.org/abs/0706.3064> (visited on 10/05/2014).
- Amendola, Luca and others (2013). "Cosmology and fundamental physics with the Euclid satellite". In: *Living Reviews in Relativity* 16. ISSN: 1433-8351. DOI: [10.12942/lrr-2013-6](https://doi.org/10.12942/lrr-2013-6). URL: <http://arxiv.org/abs/1206.1225> (visited on 01/03/2017).
- Amendola, Luca and Claudia Quercellini (2004). "Skewness as a test of the equivalence principle". In: *Phys. Rev. Lett.* 92, p. 181102. DOI: [10.1103/PhysRevLett.92.181102](https://doi.org/10.1103/PhysRevLett.92.181102).
- Amendola, Luca and Shinji Tsujikawa (2010). *Dark Energy: Theory and Observations*. en. Cambridge University Press. ISBN: 978-1-139-48857-0.
- Amendola, Luca et al. (2012). "Testing coupled dark energy with next-generation large-scale observations". In: *Physical Review D* 85.10. ISSN: 1550-7998, 1550-2368. DOI: [10.1103/PhysRevD.85.103008](https://doi.org/10.1103/PhysRevD.85.103008). URL: <http://link.aps.org/doi/10.1103/PhysRevD.85.103008>.
- Amendola, Luca et al. (2013). "Observables and unobservables in dark energy cosmologies". In: *Physical Review D* 87, p. 023501. ISSN: 0556-2821. DOI: [10.1103/PhysRevD.87.023501](https://doi.org/10.1103/PhysRevD.87.023501). URL: <http://arxiv.org/abs/1210.0439> (visited on 02/12/2017).
- Anselmi, Stefano and Massimo Pietroni (2012). "Nonlinear power spectrum from resummed perturbation theory: a leap beyond the BAO scale". In: *Journal of Cosmology and Astroparticle Physics* 2012.12, p. 013. URL: <http://iopscience.iop.org/1475-7516/2012/12/013> (visited on 02/14/2014).
- Audren, Benjamin et al. (2013). "Neutrino masses and cosmological parameters from a Euclid-like survey: Markov Chain Monte Carlo forecasts including theoretical errors". In: *Journal of Cosmology and Astroparticle Physics* 2013.01, pp. 026–026. ISSN: 1475-7516. DOI: [10.1088/1475-7516/2013/01/026](https://doi.org/10.1088/1475-7516/2013/01/026). URL: <http://arxiv.org/abs/1303.5077>

- //stacks.iop.org/1475-7516/2013/i=01/a=026?key=crossref.0594fc507c5faa23a2ba7c9ccb91b7e1.
- Bailoni, Alberto, Alessio Spurio Mancini, and Luca Amendola (2016). "Improving Fisher matrix forecasts for galaxy surveys: window function, bin cross-correlation, and bin redshift uncertainty". In: *ArXiv e-prints* 1608, arXiv:1608.00458. URL: <http://adsabs.harvard.edu/abs/2016arXiv160800458B> (visited on 02/12/2017).
- Baker, Tessa and Philip Bull (2015). "Observational signatures of modified gravity on ultra-large scales". In: *The Astrophysical Journal* 811.2, p. 116. ISSN: 1538-4357. DOI: 10.1088/0004-637X/811/2/116. URL: <http://arxiv.org/abs/1506.00641> (visited on 11/05/2015).
- Baldi, Marco (2011). "Clarifying the effects of interacting dark energy on linear and non-linear structure formation processes". en. In: *MNRAS* 414.1, pp. 116–128. ISSN: 0035-8711, 1365-2966. DOI: 10.1111/j.1365-2966.2011.18263.x. URL: <http://mnras.oxfordjournals.org/content/414/1/116>.
- (2012). "The codecs project: a publicly available suite of cosmological N-body simulations for interacting dark energy models". en. In: *MNRAS* 422.2, pp. 1028–1044. ISSN: 0035-8711, 1365-2966. DOI: 10.1111/j.1365-2966.2012.20675.x. URL: <http://mnras.oxfordjournals.org/content/422/2/1028>.
- Baldi, Marco, Jounghun Lee, and Andrea V. Maccio (2011). "The effect of coupled dark energy on the alignment between dark matter and galaxy distributions in clusters". In: *The Astrophysical Journal* 732.2, p. 112. URL: <http://iopscience.iop.org/0004-637X/732/2/112>.
- Baldi, Marco et al. (2010). "Hydrodynamical N-body simulations of coupled dark energy cosmologies". In: \textbackslash textbackslash mnras 403, pp. 1684–1702. DOI: 10.1111/j.1365-2966.2009.15987.x.
- Baldi, Marco et al. (2011). "Oscillating non-linear large-scale structures in growing neutrino quintessence". en. In: *Monthly Notices of the Royal Astronomical Society* 418.1, pp. 214–229. ISSN: 1365-2966. URL: <http://arxiv.org/abs/1106.2161> (visited on 03/17/2013).
- Ballinger, W. E., J. A. Peacock, and A. F. Heavens (1996). "Measuring the cosmological constant with redshift surveys". In: *Monthly Notices of the Royal Astronomical Society* 282, p. 877. ISSN: 0035-8711. DOI: 10.1093/mnras/282.3.877. URL: <http://adsabs.harvard.edu/abs/1996MNRAS.282..877B> (visited on 02/12/2017).
- Baumann, Daniel et al. (2010). "Cosmological Non-Linearities as an Effective Fluid". In: *arXiv:1004.2488 [astro-ph, physics:gr-qc, physics:hep-th]*. URL: <http://arxiv.org/abs/1004.2488>.
- (2012). "Cosmological non-linearities as an effective fluid". In: *Journal of Cosmology and Astroparticle Physics* 2012.07, p. 051. URL: <http://iopscience.iop.org/1475-7516/2012/07/051>.
- Bell, Anthony J. and Terrence J. Sejnowski (1997). "The "independent components" of natural scenes are edge filters". In: *Vision Research* 37.23, pp. 3327–3338. ISSN: 0042-6989. DOI: [http://dx.doi.org/10.1016/S0042-6989\(97\)00121-1](http://dx.doi.org/10.1016/S0042-6989(97)00121-1). URL: <http://www.sciencedirect.com/science/article/pii/S0042698997001211>.
- Bellini, Emilio and Ignacy Sawicki (2014). "Maximal freedom at minimum cost: linear large-scale structure in general modifications of gravity". In: *arXiv:1404.3713 [astro-ph, physics:gr-qc]*. arXiv: 1404.3713. URL: <http://arxiv.org/abs/1404.3713> (visited on 07/10/2014).

- Bellini, Emilio et al. (2016). "Constraints on deviations from Λ CDM within Horndeski gravity". In: *Journal of Cosmology and Astroparticle Physics* 2016.02. arXiv: 1509.07816, pp. 053–053. ISSN: 1475-7516. DOI: 10.1088/1475-7516/2016/02/053. URL: <http://arxiv.org/abs/1509.07816> (visited on 02/28/2017).
- Bernardeau, F. et al. (2001). "Large-Scale Structure of the Universe and Cosmological Perturbation Theory". In: *arXiv:astro-ph/0112551*. DOI: 10.1016/S0370-1573(02)00135-7. URL: <http://arxiv.org/abs/astro-ph/0112551> (visited on 03/19/2013).
- Bernardeau, Francis (2013). "The evolution of the large-scale structure of the universe: beyond the linear regime". In: *arXiv:1311.2724 [astro-ph]*. URL: <http://arxiv.org/abs/1311.2724> (visited on 07/17/2014).
- Bielefeld, Jannis, Dragan Huterer, and Eric V. Linder (2014). "Cosmological Lever-age from the Matter Power Spectrum in the Presence of Baryon and Nonlinear Effects". In: *SciRate*. URL: <https://scirate.com/arxiv/1411.3725> (visited on 11/30/2015).
- Bird, Simeon, Matteo Viel, and Martin G. Haehnelt (2011). "Massive Neutrinos and the Non-linear Matter Power Spectrum". In: *arXiv:1109.4416*. DOI: 10.1111/j.1365-2966.2011.20222.x. URL: <http://arxiv.org/abs/1109.4416>.
- Blas, Diego et al. (2016). "Time-sliced perturbation theory II: baryon acoustic oscillations and infrared resummation". en. In: *Journal of Cosmology and Astroparticle Physics* 2016.07, p. 028. ISSN: 1475-7516. DOI: 10.1088/1475-7516/2016/07/028. URL: <http://stacks.iop.org/1475-7516/2016/i=07/a=028> (visited on 11/24/2016).
- Brouzakis, N. et al. (2011). "Nonlinear matter spectra in growing neutrino quintessence". In: *JCAP* 1103, p. 049. DOI: 10.1088/1475-7516/2011/03/049.
- Bull, Philip (2015). "Extending cosmological tests of General Relativity with the Square Kilometre Array". In: *arXiv:1509.07562 [astro-ph, physics:gr-qc]*. URL: <http://arxiv.org/abs/1509.07562> (visited on 10/09/2015).
- Bull, Philip et al. (2015). "Measuring baryon acoustic oscillations with future SKA surveys". In: *arXiv:1501.04088 [astro-ph]*. URL: <http://arxiv.org/abs/1501.04088> (visited on 09/22/2015).
- Carlesi, E. et al. (2014). "Hydrodynamical simulations of coupled and uncoupled quintessence models - I. Halo properties and the cosmic web". In: \textbackslash textbackslash mnras 439, pp. 2943–2957. DOI: 10.1093/mnras/stu150.
- Carrasco, John Joseph M., Mark P. Hertzberg, and Leonardo Senatore (2012). "The effective field theory of cosmological large scale structures". In: *Journal of High Energy Physics* 2012.9, pp. 1–40. URL: [http://link.springer.com/article/10.1007/JHEP09\(2012\)082](http://link.springer.com/article/10.1007/JHEP09(2012)082) (visited on 10/10/2013).
- Casas, Santiago et al. (2015). "Fitting and forecasting non-linear coupled dark energy". In: *arXiv:1508.07208 [astro-ph]*. URL: <http://arxiv.org/abs/1508.07208> (visited on 11/30/2015).
- Colombi, Stéphane et al. (2009). "Accurate estimators of power spectra in N -body simulations". In: *Monthly Notices of the Royal Astronomical Society* 393.2, pp. 511–526. ISSN: 00358711, 13652966. DOI: 10.1111/j.1365-2966.2008.14176.x. URL: <http://mnras.oxfordjournals.org/cgi/doi/10.1111/j.1365-2966.2008.14176.x>.
- Creminelli, Paolo et al. (2014). "Single-Field Consistency Relations of Large Scale Structure. Part III: Test of the Equivalence Principle". In: *Journal of Cosmology and Astroparticle Physics* 2014.06, pp. 009–009. ISSN: 1475-7516. DOI: 10.1088/1475-7516/2014/06/009. URL: <http://arxiv.org/abs/1312.6074>.

- Crocce, Martín and Román Scoccimarro (2006a). "Memory of initial conditions in gravitational clustering". In: *Physical Review D* 73.6. ISSN: 1550-7998, 1550-2368. DOI: [10.1103/PhysRevD.73.063520](https://doi.org/10.1103/PhysRevD.73.063520). URL: <http://link.aps.org/doi/10.1103/PhysRevD.73.063520>.
- (2006b). "Renormalized cosmological perturbation theory". In: *Physical Review D* 73.6, p. 063519. DOI: [10.1103/PhysRevD.73.063519](https://doi.org/10.1103/PhysRevD.73.063519). URL: <http://link.aps.org/doi/10.1103/PhysRevD.73.063519> (visited on 07/12/2015).
- Cui, Weiguang, Marco Baldi, and Stefano Borgani (2012). "The halo mass function in interacting Dark Energy models". In: *arXiv:1201.3568*. URL: <http://arxiv.org/abs/1201.3568>.
- DESI Collaboration, Amir Aghamousa, and others (2016a). "The DESI Experiment Part I: Science, Targeting, and Survey Design". In: *arXiv:1611.00036 [astro-ph]*. URL: <http://arxiv.org/abs/1611.00036> (visited on 01/03/2017).
- (2016b). "The DESI Experiment Part II: Instrument Design". In: *arXiv:1611.00037 [astro-ph]*. URL: <http://arxiv.org/abs/1611.00037> (visited on 01/03/2017).
- Feldman, Hume A., Nick Kaiser, and John A. Peacock (1994). "Power Spectrum Analysis of Three-Dimensional Redshift Surveys". In: *The Astrophysical Journal* 426, p. 23. ISSN: 0004-637X, 1538-4357. DOI: [10.1086/174036](https://doi.org/10.1086/174036). URL: <http://arxiv.org/abs/astro-ph/9304022> (visited on 07/20/2015).
- Fosalba, P. et al. (2013). "The MICE Grand Challenge Lightcone Simulation I: Dark matter clustering". In: *arXiv preprint arXiv:1312.1707*. URL: <http://arxiv.org/abs/1312.1707>.
- Friedman, Jerome H. (1987). "Exploratory Projection Pursuit". In: *Journal of the American Statistical Association* 82.397, pp. 249–266. DOI: [10.1080/01621459.1987.10478427](https://doi.org/10.1080/01621459.1987.10478427). eprint: <http://amstat.tandfonline.com/doi/pdf/10.1080/01621459.1987.10478427>. URL: <http://amstat.tandfonline.com/doi/abs/10.1080/01621459.1987.10478427>.
- Gleyzes, Jérôme et al. (2016). "Effective Theory of Dark Energy at Redshift Survey Scales". In: *Journal of Cosmology and Astroparticle Physics* 2016.02. arXiv: 1509.02191, pp. 056–056. ISSN: 1475-7516. DOI: [10.1088/1475-7516/2016/02/056](https://doi.org/10.1088/1475-7516/2016/02/056). URL: <http://arxiv.org/abs/1509.02191> (visited on 05/04/2016).
- Gubitosi, Giulia, Federico Piazza, and Filippo Vernizzi (2013). "The Effective Field Theory of Dark Energy". In: *Journal of Cosmology and Astroparticle Physics* 2013.02. arXiv: 1210.0201, pp. 032–032. ISSN: 1475-7516. DOI: [10.1088/1475-7516/2013/02/032](https://doi.org/10.1088/1475-7516/2013/02/032). URL: <http://arxiv.org/abs/1210.0201> (visited on 02/28/2017).
- Harrison, Ian et al. (2016). "SKA Weak Lensing I: Cosmological Forecasts and the Power of Radio-Optical Cross-Correlations". In: *arXiv:1601.03947 [astro-ph]*. URL: <http://arxiv.org/abs/1601.03947> (visited on 01/18/2016).
- Heitmann, Katrin et al. (2010). "The Coyote Universe. I. Precision determination of the nonlinear matter power spectrum". In: *The Astrophysical Journal* 715.1, p. 104. URL: <http://iopscience.iop.org/0004-637X/715/1/104>.
- Heitmann, Katrin et al. (2014). "The Coyote Universe Extended: Precision Emulation of the Matter Power Spectrum". In: *The Astrophysical Journal* 780.1, p. 111. URL: <http://iopscience.iop.org/0004-637X/780/1/111>.
- Heymans, Catherine and others (2013). "CFHTLenS tomographic weak lensing cosmological parameter constraints: Mitigating the impact of intrinsic galaxy alignments". In: *Mon. Not. Roy. Astron. Soc.* 432, p. 2433. DOI: [10.1093/mnras/stt601](https://doi.org/10.1093/mnras/stt601).

- Hojjati, Alireza, Levon Pogosian, and Gong-Bo Zhao (2011). "Testing gravity with CAMB and CosmoMC". In: *JCAP* 1108, p. 005. DOI: [10.1088/1475-7516/2011/08/005](https://doi.org/10.1088/1475-7516/2011/08/005).
- Hojjati, Alireza et al. (2012). "Cosmological tests of General Relativity: a principal component analysis". In: *Phys. Rev.* D85, p. 043508. DOI: [10.1103/PhysRevD.85.043508](https://doi.org/10.1103/PhysRevD.85.043508). URL: <https://arxiv.org/abs/1111.3960>.
- Hu, Wayne and Ignacy Sawicki (2007). "A Parameterized Post-Friedmann Framework for Modified Gravity". In: *Phys. Rev.* D76, p. 104043. DOI: [10.1103/PhysRevD.76.104043](https://doi.org/10.1103/PhysRevD.76.104043).
- Hu, Wayne and Naoshi Sugiyama (1996). "Small Scale Cosmological Perturbations: An Analytic Approach". In: *The Astrophysical Journal* 471.2, pp. 542–570. ISSN: 0004-637X, 1538-4357. DOI: [10.1086/177989](https://doi.org/10.1086/177989). URL: <http://arxiv.org/abs/astro-ph/9510117> (visited on 07/01/2016).
- Kaiser, Nick (1987). "Clustering in real space and in redshift space". In: *Monthly Notices of the Royal Astronomical Society* 227, pp. 1–21. ISSN: 0035-8711. URL: <http://adsabs.harvard.edu/abs/1987MNRAS.227....1K>.
- Kessy, Agnan, Alex Lewin, and Korbinian Strimmer (2015). "Optimal whitening and decorrelation". In: *arXiv:1512.00809 [stat]*. URL: <http://arxiv.org/abs/1512.00809> (visited on 10/04/2016).
- Kitching, T. D. and others (2014). "3D Cosmic Shear: Cosmology from CFHTLenS". In: *Mon. Not. Roy. Astron. Soc.* 442.2, pp. 1326–1349. DOI: [10.1093/mnras/stu934](https://doi.org/10.1093/mnras/stu934).
- Koyama, Kazuya, Atsushi Taruya, and Takashi Hiramatsu (2009). "Non-linear Evolution of Matter Power Spectrum in Modified Theory of Gravity". In: *Physical Review D* 79.12. ISSN: 1550-7998, 1550-2368. DOI: [10.1103/PhysRevD.79.123512](https://doi.org/10.1103/PhysRevD.79.123512). URL: <http://arxiv.org/abs/0902.0618> (visited on 11/27/2016).
- Kullback, S. and R. A. Leibler (1951). "On Information and Sufficiency". EN. In: *The Annals of Mathematical Statistics* 22.1, pp. 79–86. ISSN: 0003-4851, 2168-8990. DOI: [10.1214/aoms/1177729694](https://doi.org/10.1214/aoms/1177729694). URL: <http://projecteuclid.org/euclid.aoms/1177729694> (visited on 01/02/2017).
- Kunz, M. et al. (2006). "Constraining topology in harmonic space". In: *Physical Review D* 73.2. ISSN: 1550-7998, 1550-2368. DOI: [10.1103/PhysRevD.73.023511](https://doi.org/10.1103/PhysRevD.73.023511). URL: <http://arxiv.org/abs/astro-ph/0510164> (visited on 12/30/2016).
- Kunz, Martin (2012). "The phenomenological approach to modeling the dark energy". In: *Comptes Rendus Physique* 13.6-7, pp. 539–565. ISSN: 16310705. DOI: [10.1016/j.crhy.2012.04.007](https://doi.org/10.1016/j.crhy.2012.04.007). URL: <http://arxiv.org/abs/1204.5482> (visited on 02/01/2017).
- Lacasa, Fabien and Rogerio Rosenfeld (2016). "Combining cluster number counts and galaxy clustering". In: *JCAP* 1608, p. 005. DOI: [10.1088/1475-7516/2016/08/005](https://doi.org/10.1088/1475-7516/2016/08/005), [10.1088/1475-7516/2016/08/005](https://doi.org/10.1088/1475-7516/2016/08/005). URL: <https://arxiv.org/abs/1603.00918> (visited on 02/27/2017).
- Laureijs, R. and others (2011). "Euclid Definition Study Report". In: *arXiv:1110.3193 [astro-ph]*. URL: <http://arxiv.org/abs/1110.3193>.
- Lawrence, Earl et al. (2010). "The coyote universe. III. simulation suite and precision emulator for the nonlinear matter power spectrum". In: *The Astrophysical Journal* 713.2, p. 1322. URL: <http://iopscience.iop.org/0004-637X/713/2/1322>.
- Lesgourgues, Julien et al. (2009). "Non-linear power spectrum including massive neutrinos: the time-RG flow approach". In: *Journal of Cosmology and Astroparticle*

- Physics* 2009.06, p. 017. URL: <http://iopscience.iop.org/1475-7516/2009/06/017>.
- Levi, Michael et al. (2013). "The DESI Experiment, a whitepaper for Snowmass 2013". In: *arXiv:1308.0847 [astro-ph]*. URL: <http://arxiv.org/abs/1308.0847> (visited on 01/03/2017).
- Lewis, Antony (2013). "Efficient sampling of fast and slow cosmological parameters". In: *Phys. Rev.* D87.10, p. 103529. DOI: [10.1103/PhysRevD.87.103529](https://doi.org/10.1103/PhysRevD.87.103529).
- Lewis, Antony and Sarah Bridle (2002). "Cosmological parameters from CMB and other data: A Monte Carlo approach". In: *Phys. Rev.* D66, p. 103511. DOI: [10.1103/PhysRevD.66.103511](https://doi.org/10.1103/PhysRevD.66.103511).
- Lewis, Antony, Anthony Challinor, and Anthony Lasenby (2000). "Efficient Computation of CMB anisotropies in closed FRW models". In: *Astrophys. J.* 538, pp. 473–476. DOI: [10.1086/309179](https://doi.org/10.1086/309179).
- Maccio, A.V. et al. (2004). "Coupled dark energy: Parameter constraints from N-body simulations". In: *Physical Review D* 69.12, p. 123516. DOI: [10.1103/PhysRevD.69.123516](https://doi.org/10.1103/PhysRevD.69.123516). URL: <http://link.aps.org/doi/10.1103/PhysRevD.69.123516> (visited on 03/17/2013).
- Macciò, Andrea V., Aaron A. Dutton, and Frank C. van den Bosch (2008). "Concentration, spin and shape of dark matter haloes as a function of the cosmological model: WMAP 1, WMAP 3 and WMAP 5 results". In: *Monthly Notices of the Royal Astronomical Society* 391.4, pp. 1940–1954. ISSN: 00358711, 13652966. DOI: [10.1111/j.1365-2966.2008.14029.x](https://doi.org/10.1111/j.1365-2966.2008.14029.x). URL: <http://mnras.oxfordjournals.org/cgi/doi/10.1111/j.1365-2966.2008.14029.x>.
- Mainini, Roberto and Silvio Bonometto (2006). "Mass functions in coupled Dark Energy models". In: *arXiv:astro-ph/0605621*. DOI: [10.1103/PhysRevD.74.043504](https://doi.org/10.1103/PhysRevD.74.043504). URL: <http://arxiv.org/abs/astro-ph/0605621>.
- Manzotti, Alessandro et al. (2014). "A coarse grained perturbation theory for the Large Scale Structure, with cosmology and time independence in the UV". In: *arXiv:1407.1342 [astro-ph, physics:gr-qc, physics:hep-th]*. URL: <http://arxiv.org/abs/1407.1342> (visited on 01/27/2015).
- Mohammed, Irshad and Uros Seljak (2014). "Analytic model for the matter power spectrum, its covariance matrix, and baryonic effects". In: *Mon.Not.Roy.Astron.Soc.* 445, pp. 3382–3400. DOI: [10.1093/mnras/stu1972](https://doi.org/10.1093/mnras/stu1972).
- Mukherjee, Pia et al. (2008). "Planck priors for dark energy surveys". In: *Physical Review D* 78.8. ISSN: 1550-7998, 1550-2368. DOI: [10.1103/PhysRevD.78.083529](https://doi.org/10.1103/PhysRevD.78.083529). URL: <http://arxiv.org/abs/0803.1616> (visited on 11/29/2016).
- Pettorino, Valeria (2013). "Testing modified gravity with Planck: the case of coupled dark energy". In: *Phys. Rev. D* 88, 063519.
- Pettorino, Valeria et al. (2010). "Neutrino lumps and the cosmic microwave background". In: *Physical Review D* 82.12, p. 123001. URL: <http://prd.aps.org/abstract/PRD/v82/i12/e123001> (visited on 02/21/2014).
- Pettorino, Valeria et al. (2012). "Constraints on coupled dark energy using CMB data from WMAP and SPT". In: *Phys. Rev.* D86, p. 103507. DOI: [10.1103/PhysRevD.86.103507](https://doi.org/10.1103/PhysRevD.86.103507).
- Pietroni, Massimo (2008). "Flowing with Time: a New Approach to Nonlinear Cosmological Perturbations". In: *JCAP* 0810, p. 036. DOI: [10.1088/1475-7516/2008/10/036](https://doi.org/10.1088/1475-7516/2008/10/036).

- Pietroni, Massimo et al. (2011). "Coarse-Grained Cosmological Perturbation Theory". In: *arXiv:1108.5203 [astro-ph, physics:hep-th]*. URL: <http://arxiv.org/abs/1108.5203>.
- Planck Collaboration, P. A. R. Ade, and others (2016). "Planck 2015 results. XIV. Dark energy and modified gravity". In: *Astronomy and Astrophysics* 594, A14. DOI: [10.1051/0004-6361/201525814](https://doi.org/10.1051/0004-6361/201525814). URL: <http://arxiv.org/abs/1502.01590>.
- Pogosian, L. et al. (2010). "How to optimally parametrize deviations from general relativity in the evolution of cosmological perturbations". In: *Phys. Rev.* D81.10, 104023, p. 104023. DOI: [10.1103/PhysRevD.81.104023](https://doi.org/10.1103/PhysRevD.81.104023). arXiv: [1002.2382 \[astro-ph.CO\]](https://arxiv.org/abs/1002.2382).
- Raccanelli, Alvise et al. (2015). "Measuring redshift-space distortions with future SKA surveys". In:
- Raveri, Marco et al. (2016). "CosmicFish Implementation Notes V1.0". In: *arXiv:1606.06268 [astro-ph, physics:gr-qc]*. URL: <http://arxiv.org/abs/1606.06268> (visited on 12/30/2016).
- Saltas, Ippocratis D. et al. (2014). "Anisotropic Stress as a Signature of Nonstandard Propagation of Gravitational Waves". In: *Phys. Rev. Lett.* 113.19, p. 191101. DOI: [10.1103/PhysRevLett.113.191101](https://doi.org/10.1103/PhysRevLett.113.191101).
- Santos, Mario G. et al. (2015). "HI galaxy simulations for the SKA: number counts and bias". In: *arXiv:1501.03990 [astro-ph]*. URL: <http://arxiv.org/abs/1501.03990> (visited on 09/22/2015).
- Saracco, F. et al. (2010). "Non-linear Matter Spectra in Coupled Quintessence". In: *Physical Review D* 82.2. ISSN: 1550-7998, 1550-2368. DOI: [10.1103/PhysRevD.82.023528](https://doi.org/10.1103/PhysRevD.82.023528). URL: <http://arxiv.org/abs/0911.5396> (visited on 10/05/2014).
- Sawicki, Ignacy et al. (2016). "Non-standard gravitational waves imply gravitational slip: on the difficulty of partially hiding new gravitational degrees of freedom". In:
- Scoccimarro, Román (2004). "Redshift-space distortions, pairwise velocities, and nonlinearities". In: *Phys. Rev. D* 70.8, p. 083007. DOI: [10.1103/PhysRevD.70.083007](https://doi.org/10.1103/PhysRevD.70.083007). URL: <http://link.aps.org/doi/10.1103/PhysRevD.70.083007>.
- Seehars, Sebastian et al. (2014). "Information Gains from Cosmic Microwave Background Experiments". In: *Physical Review D* 90.2. ISSN: 1550-7998, 1550-2368. DOI: [10.1103/PhysRevD.90.023533](https://doi.org/10.1103/PhysRevD.90.023533). URL: <http://arxiv.org/abs/1402.3593> (visited on 01/02/2017).
- Sellentin, Elena, Miguel Quartin, and Luca Amendola (2014). "Breaking the spell of Gaussianity: forecasting with higher order Fisher matrices". In: *Monthly Notices of the Royal Astronomical Society* 441.2, pp. 1831–1840. ISSN: 0035-8711, 1365-2966. DOI: [10.1093/mnras/stu689](https://doi.org/10.1093/mnras/stu689). URL: <http://arxiv.org/abs/1401.6892> (visited on 07/20/2015).
- Seo, Hee-Jong and Daniel J. Eisenstein (2005). "Baryonic acoustic oscillations in simulated galaxy redshift surveys". In: *The Astrophysical Journal* 633.2, pp. 575–588. ISSN: 0004-637X, 1538-4357. DOI: [10.1086/491599](https://doi.org/10.1086/491599). URL: <http://arxiv.org/abs/astro-ph/0507338>.
- (2007). "Improved forecasts for the baryon acoustic oscillations and cosmological distance scale". In: *The Astrophysical Journal* 665.1, pp. 14–24. ISSN: 0004-637X, 1538-4357. DOI: [10.1086/519549](https://doi.org/10.1086/519549). URL: <http://arxiv.org/abs/astro-ph/0701079>.

- Seo, Hee-Jong et al. (2008). "Nonlinear structure formation and the acoustic scale". In: *The Astrophysical Journal* 686.1, p. 13. URL: <http://iopscience.iop.org/0004-637X/686/1/13>.
- Smith, R. E. et al. (2003). "Stable clustering, the halo model and non-linear cosmological power spectra". en. In: *MNRAS* 341.4, pp. 1311–1332. ISSN: 0035-8711, 1365-2966. DOI: [10.1046/j.1365-8711.2003.06503.x](https://doi.org/10.1046/j.1365-8711.2003.06503.x). URL: <http://mnras.oxfordjournals.org/content/341/4/1311>.
- Springel, Volker (2005). "The cosmological simulation code GADGET-2". In: *Mon. Not. Roy. Astron. Soc.* 364, pp. 1105–1134.
- Sutter, P. M. et al. (2014). "On the observability of coupled dark energy with cosmic voids". In: *arXiv:1406.0511 [astro-ph]*. URL: <http://arxiv.org/abs/1406.0511>.
- Takahashi, Ryuichi et al. (2012). "Revising the Halofit Model for the Nonlinear Matter Power Spectrum". In: *arXiv:1208.2701*. URL: <http://arxiv.org/abs/1208.2701>.
- Taruya, Atsushi and Takashi Hiramatsu (2008). "A Closure Theory for Non-linear Evolution of Cosmological Power Spectra". In: *The Astrophysical Journal* 674.2, pp. 617–635. ISSN: 0004-637X, 1538-4357. DOI: [10.1086/526515](https://doi.org/10.1086/526515). URL: <http://arxiv.org/abs/0708.1367> (visited on 10/05/2014).
- Taruya, Atsushi, Takahiro Nishimichi, and Shun Saito (2010). "Baryon acoustic oscillations in 2D: Modeling redshift-space power spectrum from perturbation theory". In: *Phys. Rev. D* 82.6, p. 063522. DOI: [10.1103/PhysRevD.82.063522](https://doi.org/10.1103/PhysRevD.82.063522). URL: <http://link.aps.org/doi/10.1103/PhysRevD.82.063522>.
- Taruya, Atsushi et al. (2014). "Regularized cosmological power spectrum and correlation function in modified gravity models". In: *Physical Review D* 90.12. ISSN: 1550-7998, 1550-2368. DOI: [10.1103/PhysRevD.90.123515](https://doi.org/10.1103/PhysRevD.90.123515). URL: <http://arxiv.org/abs/1408.4232> (visited on 10/08/2015).
- Taylor, A. N. et al. (2007). "Probing dark energy with the shear-ratio geometric test". en. In: *Monthly Notices of the Royal Astronomical Society* 374.4, pp. 1377–1403. ISSN: 0035-8711, 1365-2966. DOI: [10.1111/j.1365-2966.2006.11257.x](https://doi.org/10.1111/j.1365-2966.2006.11257.x). URL: <http://mnras.oxfordjournals.org/content/374/4/1377> (visited on 11/25/2015).
- Tegmark, Max et al. (1998). "Measuring the galaxy power spectrum with future redshift surveys". In: *The Astrophysical Journal* 499.2, pp. 555–576. ISSN: 0004-637X, 1538-4357. DOI: [10.1086/305663](https://doi.org/10.1086/305663). URL: <http://arxiv.org/abs/astro-ph/9708020>.
- Torre, Sylvain de la and Luigi Guzzo (2012). "Modelling non-linear redshift-space distortions in the galaxy clustering pattern: systematic errors on the growth rate parameter". In: *arXiv:1202.5559 [astro-ph]*. URL: <http://arxiv.org/abs/1202.5559>.
- Verde, Licia, Pavlos Protopapas, and Raul Jimenez (2013). "Planck and the local Universe: Quantifying the tension". In: *Physics of the Dark Universe* 2.3, pp. 166–175. ISSN: 2212-6864. DOI: [10.1016/j.dark.2013.09.002](https://doi.org/10.1016/j.dark.2013.09.002). URL: <http://www.sciencedirect.com/science/article/pii/S2212686413000319> (visited on 01/02/2017).
- Vollmer, Adrian, Luca Amendola, and Riccardo Catena (2014). "Efficient implementation of the Time Renormalization Group". In: *arXiv:1412.1650 [astro-ph, physics:physics]*. URL: <http://arxiv.org/abs/1412.1650> (visited on 11/30/2015).

- Wang, Yun, Chia-Hsun Chuang, and Christopher M. Hirata (2012). "Toward More Realistic Forecasting of Dark Energy Constraints from Galaxy Redshift Surveys". In: *arXiv:1211.0532 [astro-ph]*. URL: <http://arxiv.org/abs/1211.0532> (visited on 04/20/2015).
- Wintergerst, Nico and Valeria Pettorino (2010). "Clarifying spherical collapse in coupled dark energy cosmologies". In: *Phys. Rev.* D82, p. 103516. DOI: [10.1103/PhysRevD.82.103516](https://doi.org/10.1103/PhysRevD.82.103516).
- Yahya, S. et al. (2015). "Cosmological performance of SKA HI galaxy surveys". In: *Monthly Notices of the Royal Astronomical Society* 450.3, pp. 2251–2260. ISSN: 0035-8711, 1365-2966. DOI: [10.1093/mnras/stv695](https://doi.org/10.1093/mnras/stv695). URL: <http://arxiv.org/abs/1412.4700> (visited on 10/07/2015).
- Zhao, Gong-Bo (2014). "Modeling the nonlinear clustering in modified gravity models I: A fitting formula for matter power spectrum of f(R) gravity". In: *The Astrophysical Journal Supplement Series* 211.2, p. 23. ISSN: 0067-0049, 1538-4365. DOI: [10.1088/0067-0049/211/2/23](https://doi.org/10.1088/0067-0049/211/2/23). URL: <http://arxiv.org/abs/1312.1291> (visited on 11/24/2016).
- Zhao, Gong-Bo, Baojiu Li, and Kazuya Koyama (2011). "N-body Simulations for f(R) Gravity using a Self-adaptive Particle-Mesh Code". In: *Physical Review D* 83.4. ISSN: 1550-7998, 1550-2368. DOI: [10.1103/PhysRevD.83.044007](https://doi.org/10.1103/PhysRevD.83.044007). URL: <http://arxiv.org/abs/1011.1257> (visited on 11/27/2016).
- Zhao, Gong-Bo et al. (2009). "Searching for modified growth patterns with tomographic surveys". In: *Phys. Rev.* D79, p. 083513. DOI: [10.1103/PhysRevD.79.083513](https://doi.org/10.1103/PhysRevD.79.083513).
- Zhao, Gong-Bo et al. (2017). "The clustering of galaxies in the completed SDSS-III Baryon Oscillation Spectroscopic Survey: Examining the observational evidence for dynamical dark energy". In: